A Structural and Spectroscopic Investigation of Hydrous and Anhydrous Rare Earth Phosphates

A Thesis Submitted to the College of

Graduate and Postdoctoral Studies

In Partial Fulfillment of the Requirements

For the Degree of Doctor of Philosophy

In the Department of Chemistry

University of Saskatchewan

Saskatoon

By

Mohamed Ruwaid Rafiuddin

PERMISSION TO USE

In presenting this thesis/dissertation in partial fulfillment of the requirements for a Postgraduate degree from the University of Saskatchewan, I agree that the Libraries of this University may make it freely available for inspection. I further agree that permission for copying of this thesis/dissertation in any manner, in whole or in part, for scholarly purposes may be granted by the professor or professors who supervised my thesis/dissertation work or, in their absence, by the Head of the Department or the Dean of the College in which my thesis work was done. It is understood that any copying or publication or use of this thesis/dissertation or parts thereof for financial gain shall not be allowed without my written permission. It is also understood that due recognition shall be given to me and to the University of Saskatchewan in any scholarly use which may be made of any material in my thesis/dissertation.

Requests for permission to copy or to make other uses of materials in this thesis/dissertation in whole or part should be addressed to:

Head of the Department of Chemistry

University of Saskatchewan

Saskatoon, Saskatchewan S7N 5C9

Canada

OR

Dean

College of Graduate and Postdoctoral Studies

University of Saskatchewan

116 Thorvaldson Building, 110 Science Place

Saskatoon, Saskatchewan S7N 5C9

Canada

ABSTRACT

Nuclear power plants provide clean energy for generating electricity via neutron induced fission reactions of nuclear fuels and at the end of this energy generation process, radioactive waste is produced. Currently, the waste is chemically incorporated into a glass matrix and the resulting wasteform is destined for storage in geological repositories. Glass based wasteforms, however, might corrode under repository conditions and could potentially release radionuclides to the biosphere. Hence, crystalline wasteforms were proposed as an alternative to glass based wasteforms and among the many materials studied, materials adopting the monazite- ($REPO_4$; RE = La to Gd) and xenotime- (RE'PO_4; RE' = Tb to Lu and Y) type structures were suggested as a potential wasteform. Both monazite and xenotime are naturally abundant rare-earth minerals containing significant amounts of U and Th and have remained stable on a geological time-scale. Hydrous rare-earth phosphates adopting the rhabdophane-type structure ($REPO_4.nH_2O$; RE = La to Dy) also exist in nature and are present on the surface of anhydrous rare-earth minerals (e.g., monazite). The hydrous phase may act as a secondary barrier by preventing the release of actinides from reaching the biosphere. This thesis aims to provide an atomic level understanding of hydrous and anhydrous rare-earth phosphates using X-ray based diffraction and spectroscopic techniques.

A comprehensive account of the rich structural chemistry of rare-earth phosphates are provided in Chapters 2 and 3 using X-ray diffraction (XRD) and X-ray absorption near-edge spectroscopy (XANES). Crystalline materials containing radioactive wastes are prone to undergo radiation-induced structural damage and, in Chapter 4, radiation damage studies on monazite- and xenotime-type materials were conducted by simulating radiation damage events using high-energy ion implantation. The results from this study depict the ability of these materials to recover from the structural damage inflicted by high energy ion-implantation. In Chapter 5, the chemical durability of rare-earth phosphates was studied by investigating leaching behaviour of these materials in deionized water. Preliminary results suggest a faster leaching of hydrous rare-earth phosphates when compared to their anhydrous counterparts. The information presented in this thesis will contribute to the growing body of work on crystalline wasteforms for nuclear waste immobilization.

ACKNOWLEDGEMENTS

I would first like to thank my mom who has played a big part in my life for shaping me into the person I am today. Mom – your love and support has kept me going even on the toughest days of my life and words can't express how grateful I am for all that you have done for me. Next, I would like to thank my Dad for being selfless and for instilling the value of hard-work early on in my life. I also wanted to thank my sister and other members of my extended family for their support throughout my life. Finally, I would like to thank my cousin brothers (Dr. Abdul Rumaiz and Mohammed Nooman) for encouraging me to pursue a Ph.D. in Chemistry as well as for guiding and supporting me in both personal and academic life. Rumaiz – you have been instrumental in my academic career and for this, I am indebted to you forever.

I would like to extend my heartfelt gratitude to my advisor, Dr. Andrew P. Grosvenor, for all his support and guidance throughout my Ph.D. program. Andrew, I consider myself to be fortunate to have you as my Ph.D. advisor and I would like to thank you for patiently answering my questions as well as for providing instant and valuable feedback to my manuscripts, reports, and thesis. I also wanted to thank you for granting academic freedom as well as for making sure that I don't digress from my Ph.D. research objectives. Next, I wanted to thank the members of my Advisory Committee (Drs. Timothy Kelly, Stephen Urquhart, and Yuanming Pan) for their support and valuable suggestions during my Ph.D. program. I would like to thank the current and past members of the Grosvenor group for their help and support during my Ph.D. I would especially like to thank Drs. Esther Rani Aluri, John Hayes, James Walker, Peter Blanchard, and Vince for their help with XANES data collection which was presented in Chapters 2 – 5 of this thesis. I would like to acknowledge Eric Mueller for his contribution to the work presented in Chapter 2. I also wanted to thank Dr. Ester Rani Aluri for her help with the micro-XRD experiments presented in Chapter 4 of this thesis. Finally, I would like to thank my friends in Saskatoon for making my stay in Canada, a memorable one.

I also wanted to acknowledge the help I received from the beamline scientists at the Canadian Light Source and Advanced Photon Source with regard to XAS data collection. Dr. Yongfeng Hu, Dr. Qunfeng Xiao, and Ms. Aimee Maclennan from the SXRMB beamline at the CLS are thanked for their help with XANES and glancing angle XANES experiments which was

presented in Chapters 2 – 5 of this thesis. Dr. Lucia Zuin from the VLS-PGM beamline is thanked for her help with XANES experiments presented in Chapters 2 – 5 of this thesis. Dr. Tom Regier from the SGM beamline at the CLS is thanked for his help with the XANES experiments presented in Chapter 2 of this thesis. Drs. Zou Finfrock, Matthew Ward, and Robert Gordon from the 20 BM beamline at CLS@APS are thanked for their help with the XANES experiments presented in Chapter 3 and 5 of this thesis. Drs. George Sterbinsky and Tianpin Wu from the 9 BM beamline at the APS are thanked for their help with XANES experiments presented in Chapter 5 of this thesis. Dr. Dimitre Karpuzov from the Alberta Centre for Surface Engineering and Science, University of Alberta, is thanked for collecting the XPS spectra presented in Chapter 2 of this thesis. Mr. Jack Hendriks from Interface Science Western, University of Western Ontario is thanked for carrying out the ion-implantation studies which was presented in Chapter 4 of this thesis. Mr. Jianzhong Fan from the Department of Geological Sciences, University of Saskatchewan is thanked for collecting ICP-MS data presented in Chapter 5 of this thesis. Dr. Robert Scott from the Department of Chemistry, University of Saskatchewan is thanked for allowing me to use his TGA instrument to collect TGA data presented in Chapter 3 of this thesis. Dr. Atal Shivhare and Mr. Sudheesh Kumar Veeranmaril are thanked for collecting the TGA data presented in Chapter 3 of this thesis. I also would like to thank Ms. Leah Hildebrandt (Graduate Secretary, Department of Chemistry - University of Saskatchewan) for keeping me apprised of the various deadlines as well as for scheduling my Ph.D. candidacy exams and committee meetings.

The funding agencies are being thanked for providing the funds for the research projects presented in this thesis. I would like to thank University of Saskatchewan for the financial support. The research presented in this thesis was funded by the Natural Sciences and Engineering Council (NSERC) of Canada through a discovery grant awarded to Prof. Andrew P. Grosvenor. The Canadian Foundation for Innovation is thanked for providing funds to purchase the PANalytical Empyrean powder X-ray diffractometer that was used for obtaining XRD data presented in Chapters 2 - 5 of this thesis. Access to Sector 20 beamline was obtained through CLS-APS partnership agreement. Sector 20 operations are supported by the US department of Energy and the Canadian Light Source. The research work presented in this thesis used resources of the Advanced Photon Source, an Office of Science User Facility operated for the US department of Energy (DOE) Office of Science by Argonne National Laboratory, and was

supported by the US DOE under Contract No. DE-AC02-06CH11357, and the Canadian Light Source and its funding partners. The CLS is supported by NSERC, the National Research Council of Canada, the Canadian Institutes of Health Research, Western Economic Diversification Canada, University of Saskatchewan, and the Government of Saskatchewan.

Contents

LIST OF TABLES

LIST OF FIGURES

LIST OF ABBREVIATIONS

α	Helium ion
β	Electron
μ	Absorption Coefficient
σ	Mass Absorption Cross-Section
ρ	Density
ϕ	Work Function
λ	Wavelength
d	Particle diameter
D	Crystallite Size
I_0	Intensity of Incident X-rays
I_t	Intensity of transmitted X-rays
l	Orbital Quantum Number
n	Principal Quantum Number
t	Sample Thickness
APS	Advanced Photon Source
AVM	Atelier de Vitrification de Marcoule
BE	Binding Energy
BM	Bending Magnet
BET	Brunauer-Emmett-Teller

CLS	Canadian Light Source
DAC	Diamond Anvil Cell
DOS	Density of States
ENSP	Electronic to Nuclear Stopping Power
EXAFS	Extended X-ray Absorption Fine Structure
FWHM	Full Width at Half Maxima
GA	Glancing Angle
GeV	Giga Electron Volt
GPa	Giga Pascal
HREE	Heavy Rare-Earth Elements
HWR	Heavy Water Reactor
HDPE	High Density Polyethylene
HLW	High Level Waste
IAEA	International Atomic Energy Agency Test
ICP-MS	Inductively Coupled Plasma – Mass Spectrometry
IR	Infrared Radiation
ISW	Interface Science Western
KE	Kinetic Energy
LCF	Linear Combination Fitting
LINAC	Linear Accelerator
LREE	Light Rare-Earth Elements

LWR	Light Water Reactor
MCC	Materials Characterization Centre Test
MOX	Mixed Oxide Nuclear Fuel
PCT	Product Consistency Test
PFY	Partial Fluorescent Yield
PUREX	Plutonium Uranium Recovery Extraction
RE	Rare-Earth
RF	Radio Frequency
SA	Surface Area
SGM	Spherical Grating Monochromator
SNF	Spent Nuclear Fuel
SPFT	Single Pass Flow Through Test
SRIM	Stopping and Range of Ions in Matter
SXRMB	Soft X-ray Microcharacterization Beamline
SYNROC	Synthetic Rock
TEM	Transmission Electron Microscopy
TEY	Total Electron Yield
TGA	Thermogravimetric Analysis
TB-LMTO-ASA	Tight Binding – Linear Muffin Tin Orbital Model – Atomic Spheres Approximation
VESTA	Visualization for Electronic and Structural Analysis

VLS-PGM	Variable Line Spacing – Plane Grating Monochromator
VUV	Vacuum Ultraviolet
UHV	Ultra-High Vacuum
XAS	X-ray Absorption Spectroscopy
XANES	X-ray Absorption Near-Edge Spectroscopy
XPS	X-ray Photoelectron Spectroscopy
XRD	X-ray Diffraction
WS	Wigner-Seitz

Chapter 1

INTRODUCTION

1.1 Introduction

Since the dawn of the 21st century, the world has been witnessing a tremendous increase in energy demands fueled mainly by the growing population and rapid urbanization of the world.[1–3] The energy requirements of our modern society in the present day scenario have been largely met using a combination of fossil fuel based energy sources such as coal, oil, and natural gas.[2,4] With the world population estimated to reach around 9.7 billion by the year 2050, the global demand for energy will continue to skyrocket and since fossil fuels are non-renewable sources of energy, the continual use of fossil fuels for meeting these energy demands will pose an imminent risk of exhaustion of the world's fossil fuel supply.[2,4,5] However, the biggest concern revolving around the burning of fossil fuel for energy generation is the emission of large amounts of CO_2 into the atmosphere which has now been established to be a major driving force for global climate change.[6,7] In light of these issues, a sustainable future could be envisioned by switching to environmental friendly alternate energy sources to meet our current and future energy demands.[8,9]

Renewable energy sources (e.g., wind, solar, hydrothermal, geothermal etc.) could possibly solve the looming energy crisis of our world and help ensure a sustainable future.[8,10,11] However,

because of various technological and geographical limitations, only a minor fraction of their potential could be tapped and as such, the use of renewable energy technology to meet the projected energy demands of our future is far from reality.[9,12–14] Therefore, reliable and efficient energy sources such as nuclear energy derived from the fission of an atom must be used in addition to renewable energy sources to meet the growing energy requirements. In comparison to the energy obtained using fossil fuels, nuclear energy has a significantly lower carbon footprint due to negligible CO_2 emissions and, as a result, nuclear energy is considered to be a cleaner source of energy.[15–17] As of 2014, nuclear energy accounts for about 10.6% of the world's total electricity supply while fossil fuel accounts for an overwhelming 66.3% of the total electricity production.[18] In order to reduce our increased dependency on fossil fuels and to meet the demands of an increasingly urban society, the contribution of nuclear energy to the world's total electricity supply can be maximized by building more nuclear power plants. However, building new nuclear reactors faces significant political hurdles and this primarily has to do with the fact that although nuclear energy production is considered to be an emission-free process, it does leave behind spent nuclear fuel which is highly radioactive in nature.[19,20] Therefore, in order to overcome the political hurdle associated with future nuclear reactor development, robust scientific and engineering technologies that aim to provide a practical solution for the nuclear waste problem are currently being developed.[9,21–23] The scientific aspect of the proposed solution relies on the atomic level confinement of the radioactive waste elements in an amorphous or crystalline solid matrix.[24–26] In order to design new solid-state materials geared towards radioactive waste storage applications, it is important to first deepen our fundamental understanding of these host matrices and this thesis aims to address this aspect by providing

detailed insight into the structure of crystalline solids proposed for nuclear waste sequestration applications using X-ray based diffraction and spectroscopic techniques.

This chapter begins with a brief introduction of the nuclear fuel cycle followed by a discussion of current and future strategies for high-level radioactive waste disposal. Following this, an overview of amorphous and crystalline radioactive host matrices will be provided. The penultimate section of this chapter will discuss the basic aspects of X-ray based spectroscopic techniques used extensively in this thesis to investigate the structure of crystalline materials. The objectives of this thesis will be presented in the final section of this chapter.

1.2 Nuclear Energy

Nuclear power plants generate electricity in much the same way as fossil-fuel based power plants (i.e., both plants utilize heat to produce steam which in turn drives the turbine connected to an electric generator to generate electricity).[27] However, the processes that govern the production of heat in fossil- and nuclear- fuel based power plants are very different. In a fossil fuel power plant, fossil fuels serve as the primary energy source and heat energy is produced via combustion of these fuels. Nuclear power plants, on the other hand, produce heat by a process called nuclear fission in which an atom, typically uranium (^{235}U), transforms into lighter atoms upon bombardment with a neutron and releases large amounts of energy in the form of heat.[7,27] The various steps associated with the production of nuclear energy will be briefly discussed in the following section.

1.2.1 Nuclear Fuel Cycle: Open Cycle vs Closed Cycle

The process of generating nuclear energy for electricity production proceeds through a sequence of multiple steps and these steps collectively represent the nuclear fuel cycle (Figure 1.1).[28,29] The primary requirement for the extraction of nuclear energy from U-235 atom is a fuel source that is rich in uranium and the first step of this cycle deals with the mining of uranium from uranium-ore deposits.[30] Uranium is one of the many elements that occur in the earth's crust and is typically found as a constituent in various natural resources such as ores, soil, and seawater.[31,32] Uranium-ore deposits are distributed throughout the world with countries like Canada, Australia, and Kazakhstan holding a major stockpile of the world's uranium deposits.[32] The concentration of uranium in these ores could range anywhere from 0.01% to about 20% and depending on the concentration of uranium, the ores are broadly classified as very low- (0.01% U), low- (0.1% U), high- (2% U), and very high-grade (20% U) ores.[32] In Canada, the uranium mines in the northern part of the Province of Saskatchewan holds the world's largest deposits of very high-grade uranium-ores.[32,33] The uranium-ore deposits are generally present in either near-surface regions or in deep underground locations and, accordingly, uranium can be mined in either open-pit or underground mines.[30,32,34] The mined uranium-ore is subsequently transferred to a milling facility in proximity with the mining facility where the ore is crushed and chemically treated in order to isolate uranium from the ore.[30,31] At the end of the milling process, uranium oxide (U_3O_8) solid concentrate is produced which is commonly referred to as 'yellowcake'.[30,31]

Naturally occurring uranium primarily consists of two isotopes namely U-238 (99.3%) and U-235 (0.7%) of which U-235 is the most fissile isotope.[30,31,35,36] Most nuclear plants in the world use energy released from the neutron-initiated fission reactions of U-235 for electricity

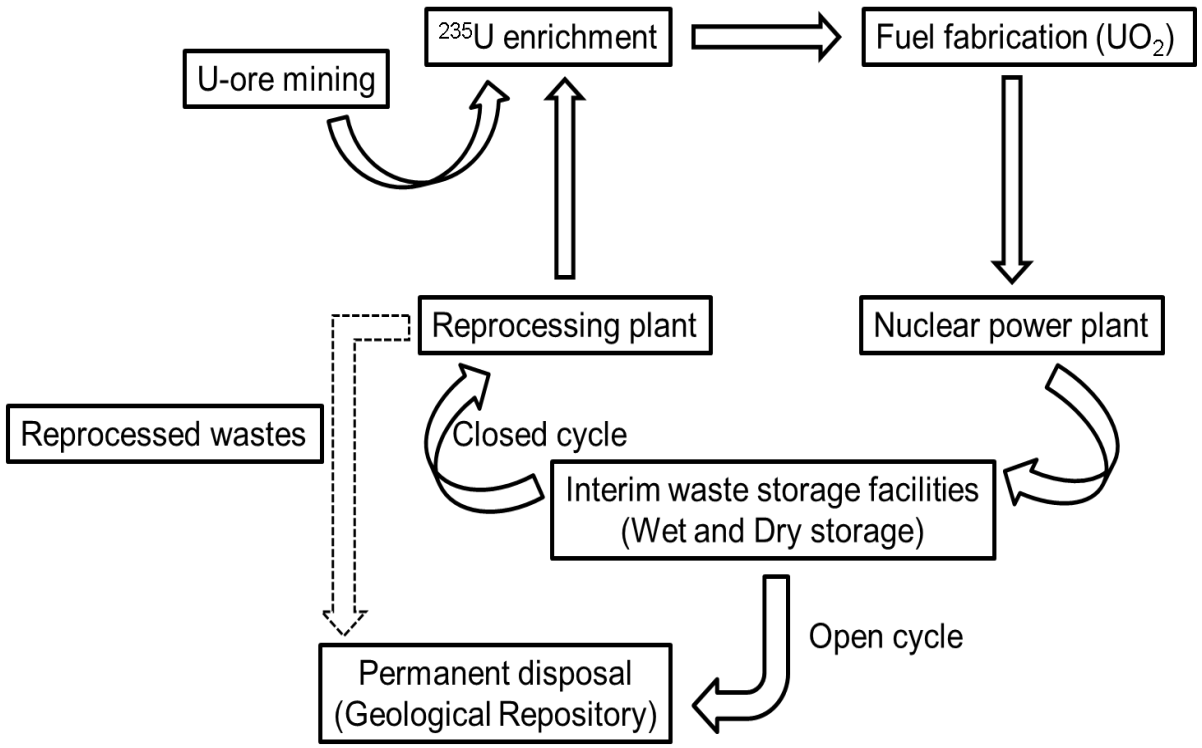

Figure 1.1 A schematic flow chart outlining the various steps involved in an open and closed nuclear fuel cycle.

generation purposes and require about 3-5% of U-235 in the nuclear fuel.[30,31] For this reason, the third step of the nuclear fuel cycle involves the enrichment of U-235 in which the concentration of fissile U-235 will be increased.[31] Since the enrichment step requires gaseous uranium samples, the U_3O_8 obtained from the milling facility is first converted into uranium hexafluoride (UF_6) gas using either a dry or wet process.[30,31,35] In the dry process, the U_3O_8 is purified via heating at high temperatures followed by reduction of calcined U_3O_8 to UO_2.[30,31,35] In the wet process, the U_3O_8 is dissolved in concentrated nitric acid and the resulting uranyl nitrate solution ($UO_2(NO_3)_2.6H_2O$) is calcined to produce UO_3 powder and this, in turn, is reduced to UO_2.[30,31,35] The UO_2 obtained via dry or wet process is reacted with hydrogen fluoride (HF) to form UF_4, which, in turn, is treated with gaseous fluorine (F_2) to produce UF_6.[30,31,35] The UF_6 gas is enriched with U-235 using either a gas diffusion or gas centrifuge method.[30,31,35] Both of these methods separate the isotopes of uranium by taking advantage of the different mass of U-238 and U-235 atoms. The enriched UF_6 gas is stored within a cylinder and is shipped to a nuclear fuel fabrication facility wherein UF_6 is chemically transformed to uranium dioxide (UO_2) powders.[31] This step constitutes the fourth step of fuel cycle and here, pellets of UO_2 are prepared by pressing the powders of UO_2 at high pressures followed by annealing at high temperatures.[30,31] The pellets are packed inside metal tubes made of zirconium alloys and sealed.[30,31] The individual metal tubes hosting these fuel pellets are called fuel rods and several fuel rods form a fuel assembly when packed together.[31]

In the penultimate step of the fuel cycle, the fuel assembly arrives at a nuclear power plant and is employed within a nuclear reactor. Despite the different types of reactors that currently exist in the world, the basic components of a nuclear reactor still remains the same. A nuclear reactor generally consists of a fuel assembly, moderator, coolant, control rods, pressure vessel,

and steam generator.[29] The pressure vessel houses the reactor core which consists of a fuel assembly, moderator, and coolant.[31] The neutron-initiated fission reactions occurring at the reactor core, in addition to releasing energy, also emit high energy neutrons which initiate further fission of U-235 atoms eventually setting off a chain reaction. The function of a moderator is to sustain this chain reaction by slowing down the fast-moving neutrons.[31] Nuclear reactors, based on the type of moderator used, are classified into light water reactors (LWRs) and heavy water reactors (HWRs). In a light water reactor, H_2O serves as a moderator whereas in a heavy water reactor D_2O is used as the moderator. Control rods typically made of a neutron absorbing material (e.g., B, Cd, Hf) are also used to control the reaction rate of the fission process.[31] The role of a coolant is to transfer the heat generated from fission of U-235 atom to the steam generator where steam is produced and is used to drive the turbines used to produce electricity.[31] In LWRs and HWRs, H_2O and D_2O serve as both the coolant and moderator.[31] The nuclear fuel stays in the reactor for a specified time period (e.g., ~ 1 – 3 years) and every year the used fuel is partially replaced with new fuel.

At the end of the fuel service period, the spent nuclear fuel (SNF) rods, which are extremely hot and radioactive, are removed from the reactor core and placed in a water pool located adjacent to the nuclear reactor in order to reduce the radioactivity and heat levels.[37] The spent fuel contains U-238 and U-235 radionuclides along with plutonium and other fission products formed as a result of fission of U-235 and much of the radioactivity in the used fuel originates mainly from the fission products.[38] The spent fuel remains under water for a minimum of one year and is either transferred to a dry storage facility wherein the spent fuel assembly is placed in specially designed casks or to a reprocessing facility where the uranium and plutonium are recovered from the used fuel for further use in reactors.[39] In the former case, the fuel cycle is

said to be an open cycle and the spent fuel assembly awaits disposal in geological repositories.[37] In the latter case, the fuel cycle is called a closed cycle and the recovered uranium can either be converted to UO_2 fuel or can be mixed with plutonium to create a mixed oxide (MOX) nuclear fuel.[31,37,38] The reprocessing of spent nuclear fuel also produces high-level radioactive waste elements (i.e., the radioactive elements have a very long half-life), which are comprised of actinides and other fission products.[40]

1.2.2 Strategies for High-Level Waste (HLW) Disposal

The global inventory of high level waste (HLW) originating from nuclear power plant is continually increasing and appropriate measures need to be taken to safely isolate the HLW from the biosphere.[41] The HLWs originating from open- and closed- fuel cycles are currently stored at interim storage facilities.[42] The proposed strategy for completely isolating the wastes from the biosphere is to permanently dispose the HLWs in geologically stable underground locations.[43] A brief description of different steps involved in the nuclear waste management is presented below.

1.2.2.1 Interim Storage facilities

The first step towards the disposal of HLW is the storage of spent fuel assemblies in interim storage facilities.[42,44] Initially, the used fuel is removed from the reactor and transferred to a wet storage facility where the used fuel is placed under water (~ 20 - 40 feet deep) in a specially designed pool called a spent fuel storage pool.[42] The walls and floors of these pools are made of reinforced concrete and are also lined with stainless steel to prevent the water from seeping through the concrete layer.[39,42] The water serves to cool down the hot spent fuel rods and also to act as a shield against the radiation emanating from these rods.[44] The spent nuclear fuel remains in this wet storage facility for a designated time (e.g., 1 - 10 years), after which, the spent fuel

assembly is withdrawn from the storage pool and transferred to a dry storage facility.[45] Here, the spent fuel assembly is placed inside a steel canister encased within concrete casks.[42] In dry cask storage, the spent fuel assemblies are surrounded by inert gas to prevent the elements present in the used fuel from potential oxidation.[39,42] The dry casks holding the spent fuel are either placed vertically on a concrete pad or horizontally in a concrete bunker.[42] Both the dry and wet storage facilities are monitored regularly to prevent the occurrence of any untoward incidents.[42]

1.2.2.2 HLW Vitrification

In the case of a closed fuel cycle, the spent fuel is withdrawn from the storage pool and transferred to a reprocessing facility where uranium and plutonium are recovered from the spent fuel by a process called PUREX (Plutonium Uranium Recovery Extraction).[46,47] In the PUREX process, the spent fuel rods are initially shredded and dissolved in concentrated nitric acid followed by separation of uranium and plutonium by solvent extraction techniques.[46–48] The resultant solution after isolation of uranium and plutonium now contains highly radioactive fission products (e.g., Cs and Sr) and minor actinides (e.g., Np, Am, and Cm).[47–49] The liquid wastes are conditioned by incorporating the waste elements in a borosilicate glass matrix through a process called vitrification.[49–52] In this process, the liquid wastes are initially calcined to produce dry powder which is then mixed with glass forming additives in a crucible and heated to ~1050°C.[51] The powder comprising HLW reacts with the molten glass and the resulting hot melt is poured into a steel canister and is allowed to cool.[51] After the cooling stage, HLW glass is obtained in which the radioactive elements are present within the glass matrix.[51] Due to the high level of radioactivity of this waste, the steel canister holding the vitrified HLW glass is stored in an interim storage facility and is passively cooled in order to prevent the heat due to radioactive

decay from inducing a glass transition (i.e., transition of glass into viscous state at high temperatures) in the vitrified HLW glass.[51]

1.2.2.3 Geological Disposal

The proposed solution for the permanent disposal of HLW is to store the radioactive wastes in multiple containers and place them in deep geological repositories (>300 m below ground).[22,23,48,53–55] The geological disposal method relies on a multiple-barrier concept in which both engineering and natural barriers prevent/delay the radioactive wastes from reaching the biosphere via groundwater migration.[22,23,48,53–55] There are three engineering barriers and they are as follows:[22,23,48,53–55]

1. HLW Glass and/or spent fuel rods represent the first barrier for the outward movement of radionuclides.

2. The second barrier is the container itself that holds the vitrified waste or spent fuel. The container typically made of stainless steel or corrosion-resistant alloys, prevents the groundwater from reaching the radioactive wastes.

3. The canister which contains HLW glass and/or spent fuel rods are sealed and placed in a geological repository. In order to fill the void between the canister and the geological repository, as well as to restrict the movement of groundwater, a backfill or overpack material (e.g., clay) is used and this material represents the third barrier.

The natural barrier, which consists of crystalline rock that surrounds the backfill material, will eventually slow-down the groundwater movement.[22,23,54,55] In the event of radionuclide release from the container, the rocks and backfill materials tend to decrease the rate of movement

of radionuclides both physically and chemically for longer periods of time.[22,23,54,55] Should the radionuclides reach the biosphere after having been stored for long periods of time, the radioactivity levels of the wastes are expected to be similar to the natural background radiation.[22,23,54,55] Geological repositories are currently viewed by many to be one of the safest methods for the long-term storage of HLW and yet despite this view, no operational geological repositories exist in the world for the disposal of HLW.[23,56] Some countries, however, are in the process of obtaining approval from their respective governments for the construction of geological repositories.[23,56] Recently, the Finnish government has granted approval for the construction of geological repositories for HLW storage and is expected to be operational in the year 2020.[23,56,57]

1.3 Nuclear Wasteforms

For safety concerns and ease of transportation, the liquid HLW arising from the SNF reprocessing facility is converted into a solid wasteform via chemical incorporation of HLW into a durable solid host matrix.[50,58] Solid matrices hosting these radioactive wastes are called nuclear wasteforms and they could be either amorphous or crystalline or a combination of both.[25,52,58–61] Crystalline and glass based nuclear wasteforms are usually synthesized by heating a mixture comprising of nuclear wastes and starting precursors at high temperatures. Both, amorphous and crystalline host matrices have their own advantages and disadvantages as a wasteform and, in the following sections, a brief discussion of glass- and crystalline- based wasteforms will be presented with a major focus being given to crystalline-based wasteforms.

1.3.1 Glass Wasteforms

Radioactive glass wasteforms were first produced via vitrification on an industrial scale at the AVM (*Atelier de Vitrification de Marcoule*) plant, in Marcoule, France, in 1978.[51,59] Since then, a global consensus has been reached on using glass materials, notably borosilicate glasses, as a host matrix for the immobilization of liquid HLW.[25,49,52,62–64] Currently, glass vitrification technology has been used in most countries for the conversion of liquid HLW into durable solid wasteform.[62] The liquid HLWs which are compositionally diverse (i.e., contains a wide range of radionuclides) are homogenously distributed inside a glass matrix.[52] Borosilicate glasses that are being used worldwide as a HLW matrix are generally prepared using varying mass percentages of chemicals such as SiO_2, B_2O_3, Al_2O_3, CaO, MgO, and Na_2O. and accordingly, the waste loading capabilities of these glasses could range anywhere between 25 % to 35 % by mass.[52,59,65,66] In addition to borosilicate glass materials, other materials such as aluminophosphate, silicate, rare-earth oxide, and iron-phosphate glasses are also being considered for the immobilization of HLW.[59,67,68]

Since borosilicate glass wasteforms are destined for permanent disposal in deep geological repositories, several studies discussing the long-term physical and chemical behaviour of borosilicate wasteform have been carried out. Some of the properties of glass that has been investigated are chemical durability, thermal, mechanical, and radiation stability.[52,59,69–74] Among these properties, the chemical durability of borosilicate wasteform has been studied the most.[69–71,74–77] This is because, under a failed container situation, the groundwater in geological repositories could penetrate through multiple containers and ultimately interact with the glass wasteform.[69,76] The glass wasteform-groundwater interaction could potentially lead to the outward diffusion of trapped radionuclides from the glass matrix thereby contaminating the

groundwater.[69,76] In order to address the issue of chemical durability, second-generation wasteforms such as crystalline wasteforms are currently being developed and tested for HLW immobilization applications.[78]

1.3.2 Crystalline Wasteforms

Naturally occurring crystalline minerals containing radionuclides are known to be on Earth for millions of years and have been exposed to extreme environmental conditions.[21,79] Some of the natural minerals have endured these extreme conditions and remained structurally stable on a geological timescale.[21,79] This observation has inspired scientists to propose synthetic analogue of these crystalline minerals for HLW immobilization applications.[50,79,80] Crystalline materials, unlike their amorphous counterparts (e.g., glass), are thermodynamically stable and therefore should possess greater structural stability and chemical durability over long periods of time required for HLW storage.[78,81,82] In a crystalline wasteform, the radionuclides occupy specific atomic sites of the host matrix and become a part of the crystal structure.[50,78] Since the atomic sites in a crystal structure have specific size, charge, and bonding requirements, the crystalline host matrix imposes restriction on the type of radioactive element that can be incorporated into the crystal structure.[50,78] As a result, different crystalline materials are being developed or proposed to host specific type of radioactive elements (e.g., fission products, minor actinides) that are present in liquid HLWs.[50,78]

In 1953, Hatch first proposed the idea of incorporating radionuclides in crystalline clays and since then, various single- and multi-phase crystalline ceramics have been proposed as a host matrix for immobilization of HLW.[80] Among the various crystalline wasteforms that have been studied, multiphase wasteforms called SYNROC (synthetic rock) developed by Ringwood and

coworkers have been investigated extensively in the literature.[83–87] SYNROC is a polyphase assemblage of synthetic analogues of Ti-containing crystalline minerals and generally comprise of hollandite ($BaAl_2Ti_2O_6$), perovskite ($CaTiO_3$), zirconolite ($CaZrTi_2O_7$), and rutile (TiO_2) phases.[78] The minerals constituting the SYNROC wasteform have survived in various geological environments for millions of years and hence, SYNROC wasteform possess higher chemical durability than glass based wasteforms.[85] In addition to high durability, the presence of multiple crystalline phases in SYNROC also allows for the incorporation of a wide variety of radionuclides resulting from the reprocessing of spent fuel.[78] Single phase wasteforms, on the other hand, are tailored for hosting specific radionuclides and some of the proposed crystalline wasteforms include monazite ($CePO_4$), xenotime (YPO_4), brannerite (UTi_2O_6), pyrochlore ($Gd_2Ti_2O_7$), and zircon ($ZrSiO_4$).[88–92] Upon incorporation of radionuclides, the crystalline materials will be exposed to radiatin resulting from various radioactive decay events which in turn causes a breakdown of the crystal structure.[78] In the event of structural breakdown, the crystalline phase is transformed into an amorphous phase and this phase transformation is termed metamictization.[78] Consequently, the radiation stability of crystalline wasteforms has been the most extensively studied property in the literature.[78,89,91,93–98] In the next section, an overview of the radiation damage process in nuclear wasteforms will be presented along with a brief discussion of the experimental technique that is being used to simulate radiation damage events in crystalline solids.

1.4 Radiation Effects in Nuclear Wasteforms

The radiation emanating from HLW is a result of radioactive decay of fission products (e.g., ^{137}Cs and ^{90}Sr) and minor actinides (e.g., Np, Am, Cm) present in the HLW stream.[78,99,100] The

fission products decay via emission of β (e^-) particles and in this process a low-energy recoil nuclei, also called daughter products, are produced.[78,99] The minor actinides, on the other hand, decay by producing energetic α (He^{2+}) particles and high-energy recoil nuclei.[78,99] The fission products and minor actinides have shorter and longer half-lives, respectively.[78,99,101] As a result, for the first ~500 years of HLW storage, the radiation will predominantly arise from the β-decay of fission products after which the radiation will arise primarily from the α-decay of actinides.[50,78,99] When these radionuclides are atomically confined within a solid matrix, the radioactive decay products dissipate their energy into the host matrix via ionization and elastic collision events.[78,99,102] In the case of an ionization event, the energies of the decay products are used to excite and remove electrons from the atoms in the solid whereas in an elastic collision event, the energies are transferred to atoms present in the host matrix.[78,99,102] Both ionization and elastic collision events affect the structures and properties of nuclear wastefoms.[78,99–101]

Among the decay products, α- and β- particles lose energy mainly by ionization processes while the recoil nuclei resulting from α- and β- decay events transfer energy to atoms primarily via an elastic collision process.[78,99] The decay products resulting from β-decay do not possess enough energy (e.g., energy of β-particle ~ 0.5 MeV) to initiate atomic displacements in the host matrix.[78,99] As a result, β-decay events do not cause significant damage to the structure of a nuclear wasteform.[78,99] However, the α-decay event which produces high energy α-particles (4.5 to 5.8 MeV) and α-recoil atoms (70 to 100 keV) brings about the most structural damage in wasteforms.[78,99,103] During an α-decay event, an α-particle can travel over a range of 16 – 22 μm and loses the majority of its energy to inducing ionization events.[78,99] A portion of the energy of an α-particle is also used to produce a few hundred atomic displacements along its path with greater displacements occurring at the end of the particle trajectory.[78,99] The heavier α-recoil

atom, on the other hand, dissipates energy primarily via elastic collision processes over a very short range (30 – 40 nm) and causes 1000 to 2000 atomic displacements.[78,99] Compared to α-recoil, the β-recoil atom only generates about 0.1 atomic displacements per β-decay event.[78,99] As a result, several studies have focused on investigating the radiation damage in solid wasteforms due to α-recoil atoms.[79,93–95,98,103]

The extent of structural damage due to α-decay events varies depending on the dose (i.e., number of α-decay events per gram of actinide) and type of nuclear wasteform that is being studied.[50] Structurally, glass based host matrices in which atoms are arranged in a random fashion are less affected by the atomic rearrangements that occur as a result of α-decay of actinides.[50] The minor changes in the structure of a glass that accompanies the radioactive decay of actinides are usually manifested in a small increase or decrease in the volume of a glass wasteform.[50] The maximum change in the volume of a glass wasteform after α-decay events is on the order of ~1%.[50] As a result, significant changes in the chemical durability of glass wasteforms are not observed after α-decay. Crystalline wasteforms, on the other hand, are structurally more affected by radiation damage events.[50,103] Crystalline materials are characterized by long-range periodic arrangement of atoms and, in the event of an α-decay event, the high energy α-recoil atom tends to disrupt this periodic arrangement either partially or completely.[78,104] In the former case, a disordered crystalline wasteform is produced whereas in the latter the crystalline phase is completely transformed into an amorphous phase.[78] These structural changes are accompanied by a swelling of the wasteform and the change in volume of the crystalline wasteform can range between 5 % - 18%.[78] Swelling of a wasteform results in an increase in its surface area thereby decreasing the chemical durability of crystalline wasteform.[78,105] The structural response of nuclear wasteforms to α-decay induced radiation damage events has been studied in the literature

either via incorporation of actinides in a wasteform (internal irradiation) and/or through simulation of damage by implanting high energy charged particles in a wasteform (external rradiation).[78,95,106] A short account of internal and external irradiation methods is provided in the following section.

1.4.1 Internal Irradiation

Radiation-induced structural damage due to α-decay events is best studied through doping of short-lived actinides (e.g., Pu, Cm) in the wasteform of interest.[78,106] In internal or self-irradiation methods, the radiation resulting from the α-decay of incorporated actinides varies gradually with time and, accordingly, the structural performance of nuclear wasteforms is monitored as a function of time. During an α-decay event, the wasteform is simultaneously exposed to radiation arising from both α-particles and α-recoil atoms.[78,106] Therefore, the internal irradiation method enables determination of structural stability of proposed wasteforms under conditions that are quite similar to those experienced by HLW incorporated wasteforms.[78,106] However, the major disadvantages of employing an internal irradiation method to study radiation-induced damage process in wasteforms are that it is time-consuming and the radioactivity of the wasteform also places a limit on the access to various characterization techniques that could be used for examining the structure of the host matrix.[95,106]

1.4.2 External Irradiation

The limitations faced by internal irradiation can be overcome using an external irradiation method in which the radiation events are simulated under laboratory conditions via high energy ion-implantation.[78,95] In this method, the radiation conditions representing different time periods

of HLW storage is attained in a very short time by irradiating a thin region of the monolithic wasteform (e.g., pellet) with high-energy ion beams (e.g., He^{2+}, Ne^{+}, Kr^{+}, Au^{-}) of varying ion doses (i.e., number of ions/cm^2).[78,94,95,106,107] The externally irradiated solids are also non-radioactive which therefore allows the use of different experimental techniques to characterize the ion-implanted solids.[95,106,107] Since α-decay is the major decay pathway for actinides present in HLW, the wasteforms are irradiated with high-energy light (e.g., He^{2+}) and/or heavy (e.g., Pb^{+}, Au^{-}) ions to simulate radiation effects due to α-particles and/or α-recoil atoms (i.e., daughter products), respectively.[78,106,107]

High energy ion implantation studies are generally carried out using a Tandetron accelerator facility and a schematic highlighting the important parts of this facility is presented in Figure 1.2.[108,109] The positively or negatively charged ion beams from almost any non-radioactive element in the periodic table can be generated using different types of ion sources (e.g., duoplasmatron, sputter ion source).[109] The duoplasmatron and sputter ion sources which operate on different working principles produce ion beams from the element of interest using gaseous and solid samples (powders), respectively. Therefore, charged particles of gaseous elements (e.g., H, He) are obtained from a duoplasmatron source while ion beams of heavier solids (e.g., Au, Pb) are obtained via a sputter ion source.[109] The charged ions from either one of the ion sources are injected into a T-shaped high-current Tandem accelerator wherein the ions are accelerated to higher energies of the order of MeV.[108,109] These high energy ions could be transferred to different end-stations each designed to carry out specific experiments. In the ion-implantation end-station, ion beams of varying dose are implanted on the surface of the monolithic wasteform. The ion-implantation depth in solids varies depending on the energy and dose of incoming ion beam as well as the composition of the wasteform.[107] Typically, the implanted ions can be found

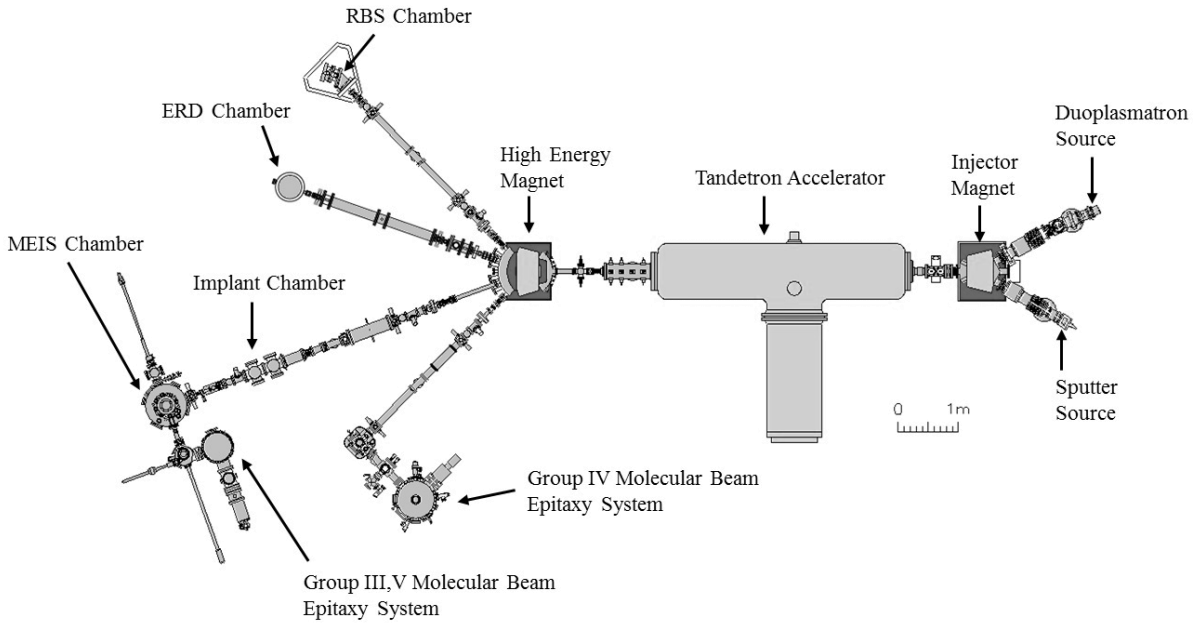

Figure 1.2 A schematic layout of the Tandetron Accelerator facility located at Interface Science Western (ISW), Western University, Canada. This figure was reproduced from the ISW website.[108] The heavy ions obtained via a sputter source are accelerated to high energies (2 MeV) inside a T-shaped Tandetron accelerator. These high energy ions enter the ion-implantation chamber wherein the samples are placed normal to a beam of high energy heavy ions.

in the nanometre regime of the solid and various characterization techniques can be used to study the ion-implanted solids.[107]

1.5 Rare-Earth Phosphate Based Wasteforms

In the search for a suitable crystalline wasteform, synthetic analogues of some of the naturally occurring rare-earth phosphate minerals have been identified as a potential host matrix for HLW storage.[60,81,100] The rare-earth phosphate minerals are both compositionally and structurally diverse and can be found in nature as monazite [(Ce,La,Nd,Th,U)PO_4], xenotime [(Y,HREE,U,Th)PO_4; HREE – heavy rare-earth elements], fluorapatite [$(Ca,Ce)_5(PO_4)_3F$], vitusite [$Na_3(Ce,La,Nd)(PO_4)_2$], rhabdophane [$(Ce,La)PO_4.H_2O$], and brockite [$(Ca,Th,Ce)PO_4.H_2O$].[110] Of the various rare-earth phosphate minerals that exist in nature, the monazite and xenotime minerals contain the highest weight percent of rare-earth elements and these minerals are used commercially for the extraction of rare-earth elements.[111,112] Monazite and xenotime are abundant rare-earth minerals that exist as an accessory phase in rocks such as granitoids, rhyolites, and gneisses.[110–113] The mineral monazite is also found in alluvial deposits and beach sands as a result of the weathering of rocks.[110,113] In addition to accommodating rare-earth elements, the monazite and xenotime minerals also contain varying amounts of radioactive elements such as thorium and uranium which makes these minerals slightly radioactive.[114–116] Due to the presence of thorium and uranium, these minerals have been exposed to radiation events over geological time scales and yet the monazite mineral, in particular, is never found completely in a metamict state (i.e., amorphous).[117–120] This observation suggests that these minerals are structurally resistant to radiation damage events.[121] However, radiation studies on synthetic and natural monazite samples have shown that these minerals are easily damaged by

radiation events but could also recover from structural damage upon annealing at lower temperatures.[122–124] Unlike the monazite mineral, radiation studies of xenotime minerals are not well documented in the literature. Monazite and xenotime minerals are also highly insoluble and possess high chemical durability in aqueous environments and this is demonstrated by the fact that the monazite minerals are still present in beach sands and placer deposits wherein the minerals are frequently exposed to aqueous conditions.[113] Based on this mineralogical evidence, synthetic analogues of monazite and xenotime minerals are being proposed as potential host candidates for nuclear waste sequestration applications.[88,121,125]

Another important mineral that is chemically related to monazite is the rhabdophane mineral.[126,127] Rhabdophane is a naturally occurring hydrous rare-earth phosphate mineral ($REPO_4.nH_2O$; RE = La to Dy) that is formed during the aqueous alteration of monazite minerals and could play a role in controlling the solubility of actinides.[128–130] A few studies have shown the formation of rhabdophane on the surface of synthetic phosphate ceramics as a result of chemical alteration of the latter and have proposed that the rhabdophane material could act as a protective barrier by either delaying or stopping the release of actinides to the environment.[126,128–134] In terms of structural stability, the rhabdophane phase is considered to be metastable and can undergo structural transformations to the monazite- or xenotime- type structure at higher temperatures.[126] It is for this reason that the synthetic analogues of the rhabdophane mineral have not received attention as a nuclear wasteform in the literature. Nevertheless, a detailed investigation of the structure and properties of rhabdophane-type materials is required in order to assess the long term chemical performance of monazite wasteforms in geological repository based conditions.[127]

1.5.1 Crystal Structures of Monazite and Xenotime

The general formula of compounds adopting the monazite and xenotime structure is $REPO_4$, where RE represents a rare-earth element.[135–137] In the case of monazites, the RE site is occupied by the larger, light rare earth elements (LREE – La to Gd) whereas in xenotime, the RE site is occupied by smaller, heavy rare earth elements (HREE – Tb to Lu and Y).[135] Materials adopting the monazite- and xenotime-type structure crystallize in a monoclinic (space group – $P2_1/n$) or tetragonal (space group – $I4_1/amd$) crystal system, respectively.[135,136,138] The crystal structures of monazite (e.g., $CePO_4$) and xenotime (e.g., YPO_4) are shown in Figures 1.3a and 1.3b. The RE ion in the monazite structure is coordinated to nine oxygen atoms and can be visualized as an equatorial pentagon of oxygen atoms interpenetrated by a tetrahedron of oxygen atoms (Figure 1.3a).[138–140] Nine different RE-O bond distances (e.g., In $CePO_4$, Ce-O = 2.460 Å – 2.776 Å) are reported for this structure, thus indicating a significant distortion of the REO_9 polyhedra.[135,140] As a result of this distortion, the monazite structure offers greater structural flexibility and can accommodate cations of differing sizes and charges.[78,140] The ability of a crystalline structure to accommodate various cations is an important property for the nuclear waste form mainly because the nuclear waste stream obtained from the reprocessing of spent fuel and dismantling of nuclear weapons contains a wide variety of radioactive elements.[78] A slightly distorted PO_4 tetrahedron provides the link for connecting the individual REO_9 polyhedra, which leads to the formation of infinite chains of edge sharing REO_9 and PO_4 polyhedra along the c-axis.[135] These chains are connected laterally by edge-sharing of adjacent REO_9 polyhedra.[135]

The xenotime structure (e.g., YPO_4), which is isostructural with the zircon phase ($ZrSiO_4$; Space group: $I4_1/amd$), places the RE ions in an eight fold coordination environment of oxygen

atoms (Figure 1.3b).[135,138] Similar to the monazite structure, edge-sharing chains of alternating REO_8 polyhedra and PO_4 tetrahedra exist in the xenotime structure.[135] The presence of two unique RE-O bond distances (e.g., In YPO_4, 2 x [4 Y-O] = 2.309 Å and 2.381 Å) in the xenotime structure, as opposed to the nine different RE-O bond distances in monazites, suggests that the REO_8 polyhedron in the xenotime structure is more symmetric.[135,138] The presence of a more regular coordination environment around the RE ion could suggest that the xenotime structure will impose severe symmetry, size, and charge restrictions on the cations that could be incorporated in the structure.[78] Therefore, unlike the monazite structure, the xenotime structure is not expected to accommodate a wide variety of cations.

1.5.2 Crystal Structure of Rhabdophane

Evidence for the existence of the rhabdophane-type structure was first reported by Mooney. Mooney found that the phosphates of La, Ce, and Nd crystallized in two forms: monoclinic (monazite) or hexagonal ($REPO_4.nH_2O$) crystal systems.[141,142] The hexagonal structure (Space group – $P6_222$ or $P3_121$) of the hydrated rare-earth phosphates was proposed based on the analysis of diffraction photographs taken from powder samples.[142] Recently, Mesbah et al. reported that the use of a hexagonal model for the Rietveld refinement of synchrotron powder X-ray diffraction data (XRD) data collected from polycrystalline rhabdophane ($SmPO_4.0.667H_2O$) led to a poor refinement.[126,142] The crystal structure of rhabdophane ($SmPO_4.0.667H_2O$) was solved ab-initio by Mesbah et al., with the results indicating that rhabdophane-type materials adopt a monoclinic (Space group – $C2$) structure.[126] It should be noted that a large body of work is available on the luminescent properties of rhabdophanes in which the crystal structure is considered to be hexagonal.[143–147]

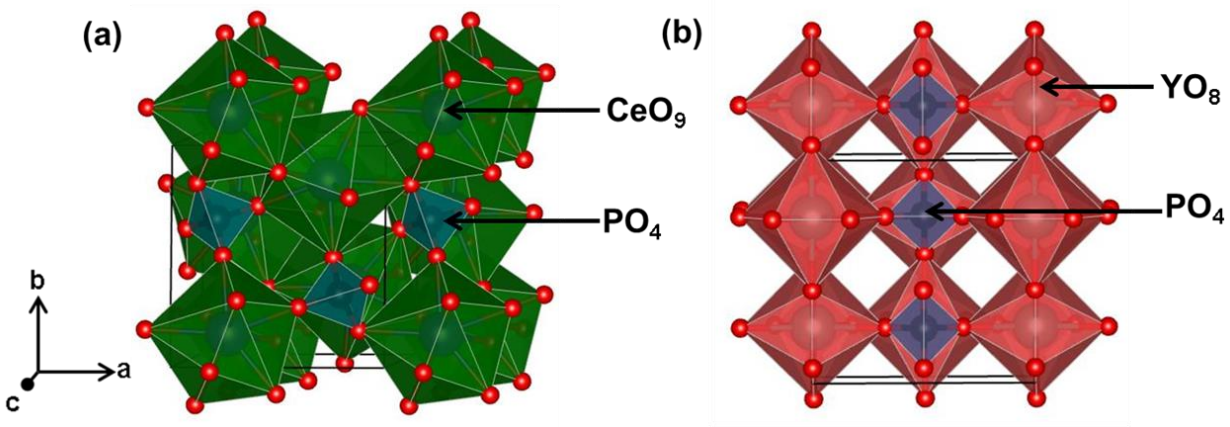

Figure 1.3 Crystal structures of (a) $CePO_4$ (Monazite-type; Space group: $P2_1/n$) and (b) YPO_4 (Xenotime-type; Space group: $I4_1/amd$). The crystal structures were generated using the VESTA (Visualization for Electronic and Structural Analysis) software program.[148]

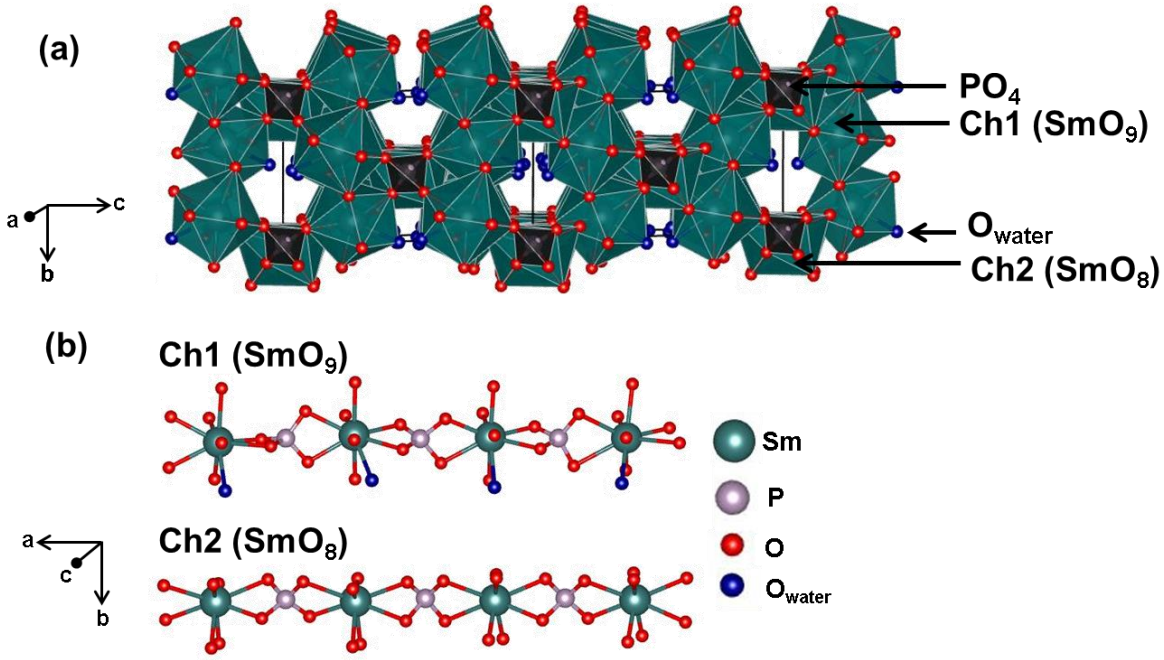

Figure 1.4 (a) Crystal structure of $SmPO_4.0.667H_2O$ (rhabdophane-type; Space group: $C2$). (b) Ball and stick representation of the alternate arrangement of Sm and P atoms in chains 1 (Ch1) and 2 (Ch2). The crystal structure was generated using the VESTA software program.[148]

The crystal structure of monoclinic rhabdophane (e.g., $SmPO_4.0.667H_2O$) is shown in Figure 1.4a.[126] The structure is comprised of two chains referred to as Ch1 and Ch2 (See Figure 1.4b).[126] There is an alternating sequence of Sm-O polyhedra and PO_4 tetrahedra along the 'a' direction in both chains (Figure 1.4b).[126] The alternating PO_4 tetrahedra in Ch1 have four different P-O bond distances (e.g., In $SmPO_4.0.667H_2O$, P-O = 1.535, 1.536, 1.547, 1.549 Å) and P-O-P bond angles whereas in Ch2, the level of distortion in the alternating PO_4 tetrahedra is not uniform (i.e., four distinct P-O bond distances) [e.g., In $SmPO_4.0.667H_2O$, P-O = 1.529, 1.538, 1.545, 1.548 Å] and P-O-P bond angles in the first tetrahedra followed by two distinct P-O bond distances [e.g., In $SmPO_4.0.667H_2O$, P-O = 1.534 Å and 1.537 Å] and P-O-P bond angles in the second tetrahedra).[126] The Sm ions in chains Ch1 and Ch2 differ in terms of their coordination environment. The Sm ions in Ch1 are bonded to nine oxygen atoms (eight provided by the PO_4 groups and one from water) and in Ch2, the Sm atoms are coordinated to only eight oxygen atoms provided by the PO_4 groups (Figure 1.4b).[126] Both SmO_9 and SmO_8 polyhedra are distorted. The connection of the two chains leads to the formation of infinite channels running along the 'a' direction.[126] Each channel is formed by the connection of six chains (4 Ch1 and 2 Ch2) and water resides inside these channels (Figure 1.4a).[126]

1.6 Experimental Techniques

In this thesis, various experimental techniques were used to probe the structure of hydrous and anhydrous rare-earth phosphate materials at different length scales. The long-range structures of rare-earth phosphates were studied using powder X-ray diffraction (XRD) while the electronic and local structures of these materials were investigated using X-ray absorption spectroscopy

(XAS) and X-ray photoelectron spectroscopy (XPS). A brief overview of these techniques is presented in the subsequent sections, with an emphasis given to XAS.

1.6.1 X-ray Absorption Spectroscopy (XAS)

XAS is widely used as a local structural characterization technique in various branches of science such as environmental, material, physical, chemical, and biological sciences.[149–153] The versatility of this technique stems from its ability to provide element-specific local structural information of a wide range of materials which includes, but is not limited to, crystalline, amorphous, and highly disordered materials.[149–151,153,154] The interaction of X-rays with matter can be described mathematically using the Beer-Lambert law (Equation 1.1).[152,155,156]

$$I_t = I_0 e^{-\mu t} \tag{1.1}$$

In Equation 1.1, I_0 represents the intensity of the incoming X-ray beam, I_t is the intensity of the transmitted X-ray beam, μ is the linear absorption coefficient, and t is the thickness of the sample.[152,155,156] According to Equation 1.1, the X-rays of intensity I_0 become attenuated as they pass through the sample and this attenuation in X-ray intensity is a combined result of the absorption of X-rays by the core-electrons of the element of interest as well as the thickness of the sample. The X-ray absorption events are described quantitatively using the linear absorption coefficient term (μ in cm^{-1}) which is defined as the product of mass absorption cross-section (σ in cm^2/g or barns/atom) and density (ρ in g/cm^3) of the sample.[155] The absorption cross-section (σ) signifies the probability of X-ray absorption by the sample.[155] Both, μ and σ are dependent on the type of element that is being studied and varies as a function of the X-ray photon energy.[152,155]

The electrons that are present in various electronic levels of the atom have characteristic well-defined binding energies and X-ray absorption by a sample occurs when the energy of the incoming X-rays is tuned to match the binding energy of electron in the respective core-electronic level.[152] Upon absorption of X-rays, the core-electrons in the element of interest are excited into unoccupied conduction states located above the Fermi level.[152,157] The resulting core-hole is stabilized via a decay process in which the electrons present in a higher energy state is used to fill the vacancy in the lower energy state created by the electronic excitation process.[152] The relaxation of a core-hole can occur via two decay pathways namely fluorescence and electron emission (Auger electrons).[152] In the fluorescence pathway, an X-ray fluorescent photon with energy corresponding to the energy difference between the two electronic states is emitted whereas in the other decay pathway the excess energy is used to eject an electron from the atom.[152] The absorption of X-rays by atoms is accompanied by large changes in the absorption coefficient and in XAS, the absorption coefficient of the desired element is measured at X-ray energies below and above the binding energy of the electron.[154,156,158] The plot of μ (linear absorption coefficient) versus X-ray energy constitutes an XAS spectrum and a representative P K-edge XAS spectra is presented in Figure 1.5. As the energy of the X-rays approaches the binding energy of an electron in the element of interest, an abrupt increase in the mass absorption cross section occurs and this is reflected in the XAS spectra by the appearance of sharp absorption edges (See Figure 1.5).[154] These absorption edges are named after the electronic shells (e.g., K, L, M shells etc.) from which the electrons are excited.[158] Therefore, a K-absorption edge, for example, indicates the excitation of electrons in the K shell (Principal quantum number, n = 1) into unoccupied conduction states. The energies of various absorption edges are unique for each element and, as a result, the XAS technique offers element-specific structural information.[156]

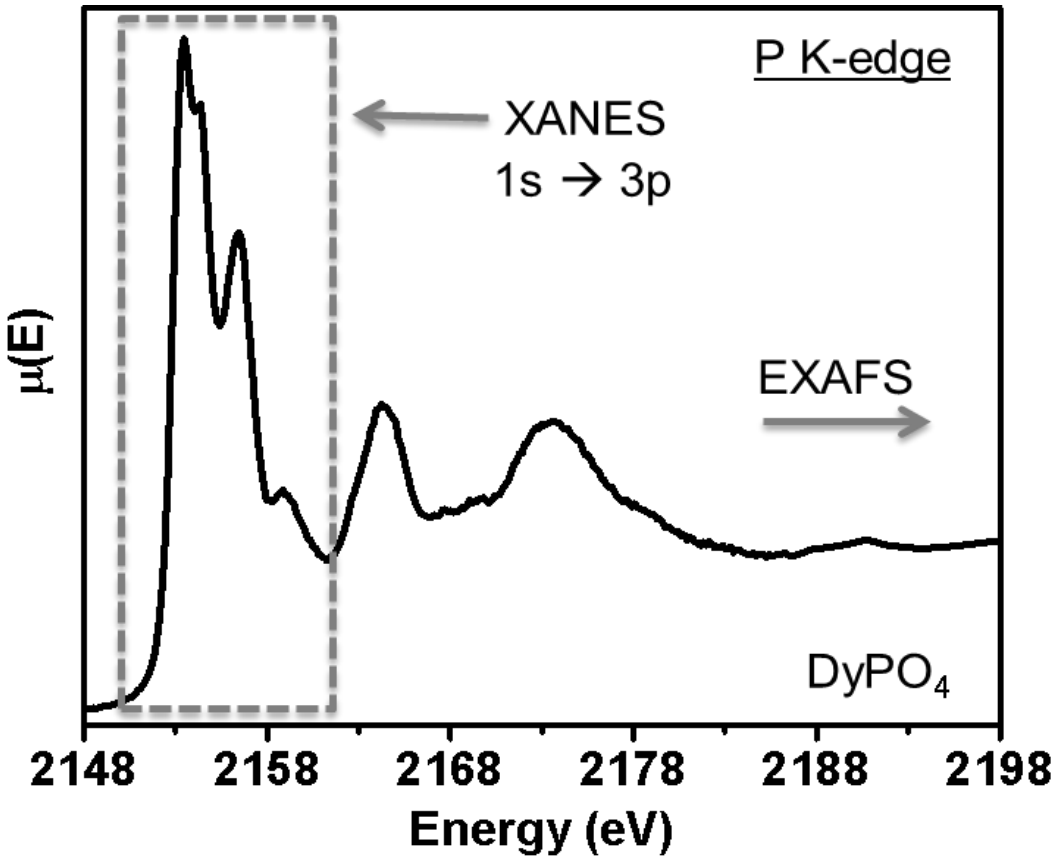

Figure 1.5 A representative P K-edge XAS spectrum from $DyPO_4$ depicting the XANES and EXAFS regions is shown. The sharp absorption edge indicates the dipole allowed transition of electrons from the P 1s state to 3p state.

In the XAS spectrum, the region immediately extending below and above the absorption edge is referred to as the near-edge region and the spectroscopy that extracts information from this near-edge region is called X-ray absorption near-edge spectroscopy (XANES).[152,154,159] The XANES region typically covers upto 20 – 30 eV above the absorption edge. The XANES spectra can provide detailed information about the electronic structure, local coordination environment, and oxidation state of the X-ray absorbing atom.[152,154,158] The intense absorption edge feature (also referred to as the main-edge) that is observed in the XANES spectra is due to X-ray absorption by the atoms and the subsequent promotion of electrons from the occupied electronic states to low lying unoccupied conduction states.[157] A schematic representation of the different electronic transitions representing the K-, L-, and M- absorption edges are presented in Figure 1.6a. These electronic transitions predominantly obey dipole selection rules (i.e., the change in the orbital quantum number (Δl) between two quantum states is equal to ± 1).[158] Thus, the main-edge in P K-edge XANES spectra indicates the excitation of electrons from the P 1s state into the P 3p state. The energy position of the main-edge is highly sensitive to the oxidation state of the X-ray absorbing atom and generally, shifts to higher (or lower) energy with increasing (or decreasing) oxidation state.[158]

In addition to dipole-allowed transitions, dipole-forbidden electronic transitions or quadrupolar transitions ($\Delta l \neq \pm 1$) are also observed in the XANES spectra of certain elements (e.g., transition metals).[158] Peaks due to quadrupolar transitions appear at energies lower than the main-absorption edge energy and are called pre-edge peaks.[159] Representative Sm L_1-edge XANES spectra from $SmPO_4$ and Sm_2O_3 are presented in Figure 1.6b and consist of pre-edge (2s $\rightarrow$ 5d) and main-edge (2s $\rightarrow$ 6p) peaks. In Figure 1.6b, the pre-edge peaks appear as a result of orbital overlap between 5d and 6p states which therefore adds some dipolar character to the

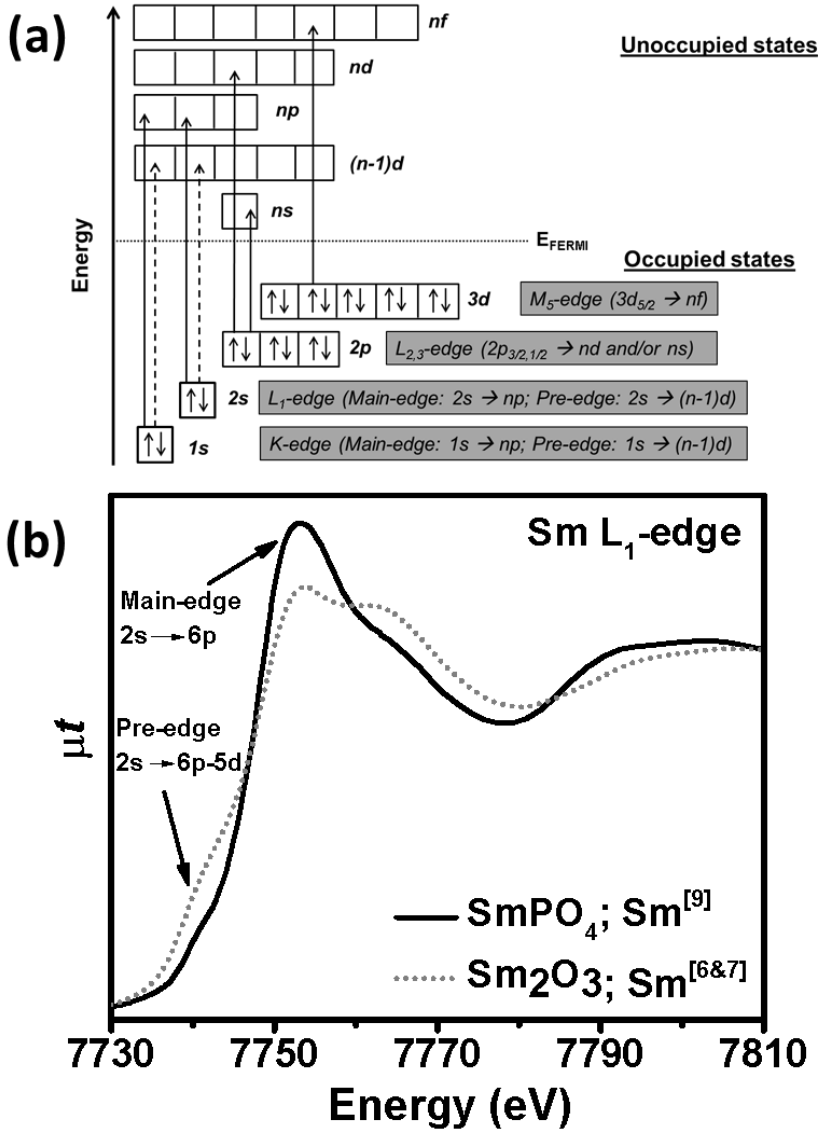

Figure 1.6 (a) A schematic representation of the various electronic transitions associated with K-, L_1-, $L_{2,3}$- and M_5- absorption edges are shown. The solid and dashed arrows indicate the dipole-allowed (main-edge) and dipole-forbidden (pre-edge) electronic transitions, respectively. (b) The Sm L_1-edge XANES spectra of $SmPO_4$ and Sm_2O_3 containing higher (9) and lower (6 & 7) coordinate Sm atoms, respectively, is shown. The pre-edge peak intensity and the spectral lineshape vary with a change in coordination number.

predominantly 2s → 5d quadrupolar transition.[160,161] The intensity of this pre-edge peak is generally sensitive to changes in the local symmetry and coordination environment around the X-ray absorbing atom.[162] In distorted or lower coordination geometries, a greater overlap of d and p states is possible which therefore results in an increase in the intensity of the pre-edge peak.[159] Therefore, the intensity of the Sm L_1-pre-edge peak increases with decreasing coordination number (Sm $^{[9]}$ → Sm $^{[6\&7]}$).

At X-ray energies higher than the main-absorption edge energy, the core-electrons are excited into the continuum wherein the electron behaves as a photoelectron wave.[157,158] In this region, the X-ray energies are higher than the threshold energy of the core-electron and the excess energy of the X-rays is imparted to the photoelectrons in the form of kinetic energy.[154] These low kinetic energy photoelectrons possess large mean free paths and undergo scattering with multiple atoms surrounding the X-ray absorbing atom resulting in peaks (referred to as multiple scattering peaks) in the immediate vicinity above the absorption edge.[158,159] Due to the multiple scattering pathways of the low energy photoelectrons, quantitative analysis of the multiple scattering peaks remains a non-trivial task.[151,154,158,163] At energies well above the absorption edge, the photoelectrons have a significant kinetic energy and undergo scattering with the neighboring atoms primarily via single scattering pathways (i.e., the high energy photoelectrons are scattered by a single atom surrounding the X-ray absorbing atom).[159] These high energy photoelectrons are backscattered by the neighboring atoms and a series of constructive and destructive interference occurs between the photoelectron wave and the backscattered wave thus giving rise to an oscillatory fine structure.[154] This region of the XAS spectrum constitutes the extended X-ray absorption fine-structure (EXAFS).[154,158,163] The EXAFS region provides quantitative structural information such as the coordination number, bond-

distances between the absorber and scatterer as well as the type of ligands that surrounds the absorbing atom.[157,158]

1.6.1.1 Basics of Synchrotron Radiation

The XAS technique requires an energy tunable X-ray source that provides intense X-ray beams. This condition is met using synchrotron radiation and for this reason, the XAS experiments are conducted at synchrotron radiation facilities (e.g., Canadian Light Source - CLS). Synchrotron radiation is produced when electrons travelling near the speed of light are forced to take a circular trajectory via the application of a magnetic field and is emitted in a direction that is tangential to the circular orbit of electrons.[150] The emitted synchrotron radiation encompasses a wide region of the electromagnetic spectrum ranging from Infrared radiation (IR) to X-rays (soft X-rays: <2 keV; hard X-rays: >2 keV) and possess higher flux (photons/second/mrad/unit bandwidth) and brightness (photons/second/unit solid angle/unit source area/unit bandwidth) when compared to conventional laboratory based radiation sources (e.g., vacuum ultraviolet (VUV) lamps, medical X-ray sources etc.).[164]

A simple schematic outlining the steps leading to the production of synchrotron radiation is shown in Figure 1.7. In an electron gun, the electrons are obtained via thermionic emission of electrons from a hot tungsten filament.[164] These electrons then enter into a linear accelerator (also called as LINAC) wherein the electrons are accelerated to energies of the order of mega electron volts (MeV) and travel at 99.9998% of the speed of light ($c = 3.0 \times 10^8$ m/s).[150,164] The accelerated electrons exit the LINAC and enter the booster ring in which the electrons are accelerated to even higher energies on the order of giga electron volts (GeV).[150,164] At the CLS, the energies of the electrons in the booster ring are increased from 250 MeV to 2.9 GeV. Once

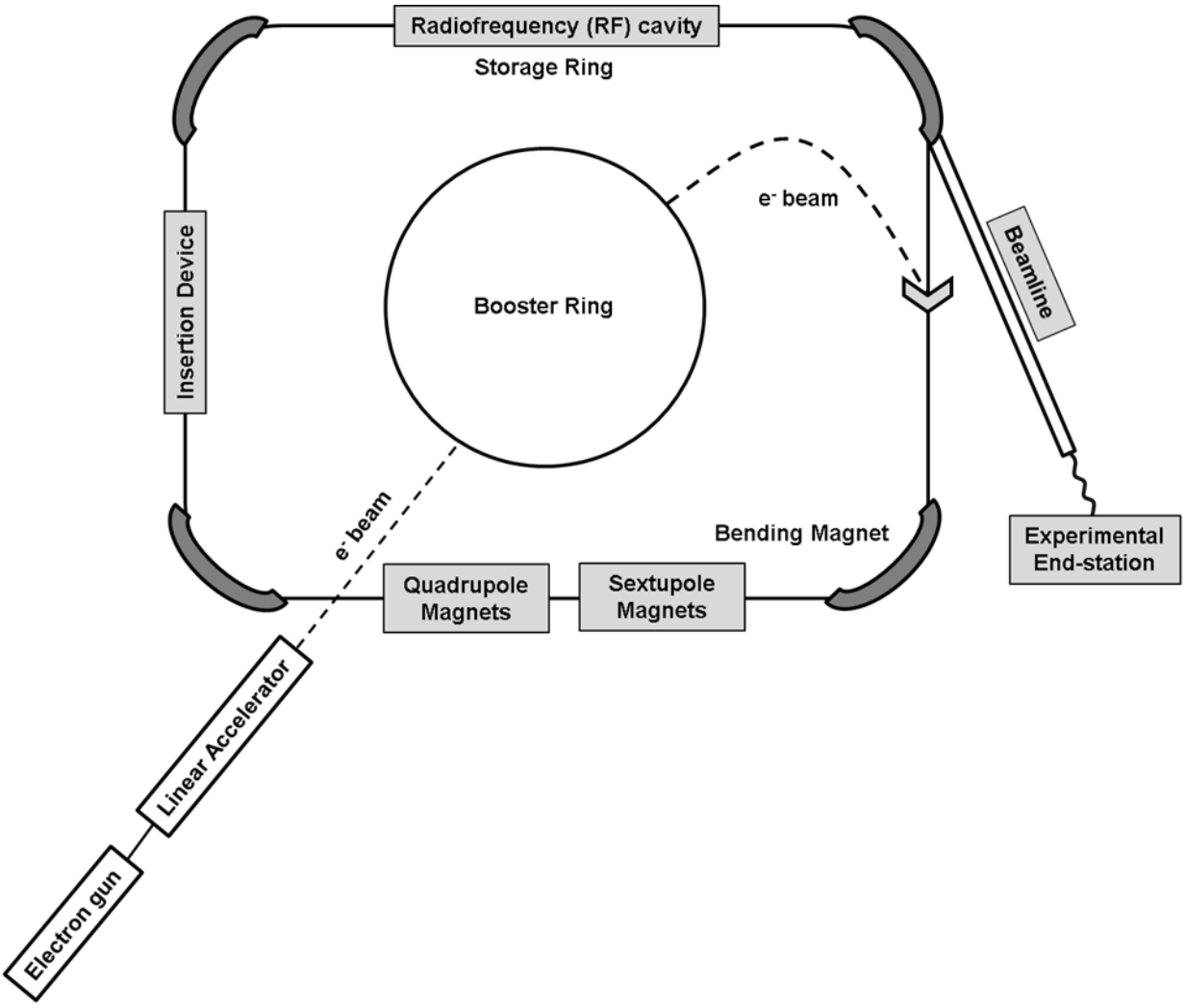

Figure 1.7 A schematic layout of a synchrotron radiation facility is presented. The electrons generated using an electron gun are accelerated to high energies using a linear accelerator. The electrons travel at relativistic speeds once inside the booster ring. The relativistic electrons are fed into a storage ring wherein the electrons maintain a circular path. The magnetic lattice (bending magnets, insertion devices, quadrupole magnets, and sextupole magnets) present in the storage ring ensures the emission of bright and intense synchrotron radiation.

the electrons are accelerated to GeV energies, the electrons are injected into the storage ring inside which the electrons maintain a circular path through the use of a series of magnets (also referred to as the magnetic lattice).[164] The storage ring consists of several straight sections (e.g., the storage ring in the CLS consists of twelve straight sections) and at the corner of every straight section, dipole or bending magnets can be found which are used to bend the high energy electrons into a circular trajectory.[150] Synchrotron radiation is produced every time the electrons are forced to take a circular path by the bending magnet and the emitted synchrotron radiation travels through specially designed vacuum ports (commonly referred to as beamlines) located at a tangent to bending magnets before finally reaching the experimental end-stations which are stationed outside the storage ring.[164] The beamlines are equipped with energy tunable optical elements (e.g., grating and crystal monochromators) that enable the selection of radiation possessing specific wavelengths or energies.[165,166] Hard and soft X-rays with specific energies are generally obtained using crystal monochromators (e.g., Si (111) crystal) or diffraction gratings (e.g., plane and spherical grating monochromators).[165,166]

The energy of the electron beams that is lost in the production of synchrotron light is compensated by the installation of radio frequency (RF) cavities in the straight sections of the storage ring.[150,164] As the electrons pass through these RF cavities, the RF field boosts the energy of the electrons in order to allow the electrons to circulate in the storage ring for specified times or indefinitely in certain synchrotron facilities.[150,164,167] The focusing of the electron beams in the storage ring is done using quadrupole magnets placed in the straight sections of the ring.[164] The focusing error caused by the quadrupole magnets is corrected using sextupole magnets which ensure that the electrons remain in a circular orbit.[164] The brightness of the synchrotron radiation could be further improved by the installation of insertion devices in the linear section of the

ring.[164] Insertion devices consist of a periodic array of magnets of alternating poles and when electrons pass through these regions, the alternating magnetic fields causes the electrons to oscillate in a direction perpendicular to the direction of their motion thereby resulting in the emission of intense and bright synchrotron radiation.[150,164,167]

1.6.1.2 XAS Experimental Setup

In XAS, the measurement of absorption of X-rays by the sample is performed using multiple detection modes namely transmission, fluorescence, and electron yield.[154,159,168] The transmission mode, as the name implies, measures the intensity of the X-rays transmitted by the sample and the absorption of X-rays by the sample (μt) is determined using Equation 1.2.

$$\mu t = \ln\left(\frac{I_O}{I_t}\right) \tag{1.2}$$

In Equation 1.2, I_0 and I_t refers to the intensity of incident and transmitted X-rays, respectively. A basic layout of the experimental setup required for conducting transmission experiments is presented in Figure 1.8. X-rays with specific energies obtained using a monochromator are passed through an ionization chamber (I_0) filled with inert gases (e.g., N_2, Ar, He, Kr) wherein the X-rays will ionize these gases and the intensity of the incident X-ray beam (I_0) is determined by measuring the ionization current.[152] The X-rays, after passing through the first ionization chamber, are now incident on the sample and X-ray absorption by the sample occurs when the energy of the X-rays is at or above the absorption edge of the element of interest. The transmitted X-rays pass through another ionization chamber wherein the intensity of the transmitted X-rays (I_t) is determined.[152] For calibration purposes, XAS spectra are also collected from calibration standards placed between the transmission (I_t) and reference (I_{Ref}) ionization

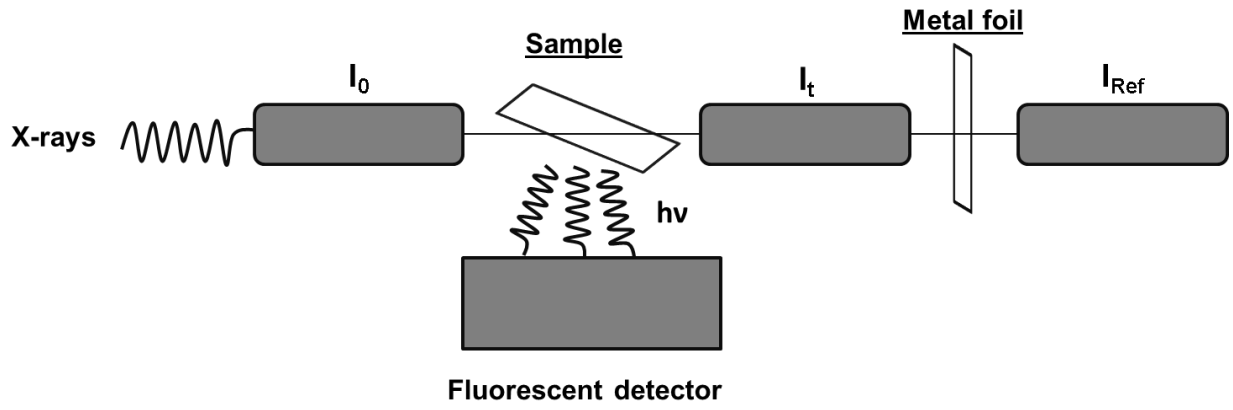

Figure 1.8 A basic layout of the XAS experimental setup. I_0, I_t, and I_{Ref} represent the ionization, transmission, and reference ionization chambers, respectively. Depending on the energy of the X-rays and the detection mode used, the XAS experiments can be conducted in either ambient or ultra-high vacuum (UHV) conditions.

chambers. For thick samples (e.g., > 1 μm), transmission experiments can be performed only using hard X-rays.[159] The high energy of the hard X-rays allows for an easy penetration of X-rays through the sample. Because of the high energy of the X-rays, hard X-ray transmission experiments do not require ultra-high vacuum conditions (UHV) and are generally conducted under ambient conditions. For thin samples (e.g., few nm), transmission experiments can be performed using both soft- and hard- X-rays. The transmission mode is also the preferred detection mode for samples having high concentrations of the element of interest.[152]

XAS spectra are also obtained using indirect methods of detection in which the decay products (fluorescence, photoelectrons, Auger electrons, and secondary electrons) resulting from the core-hole relaxation process are measured.[152,154] The linear relationship between the decay products and absorption cross sections allows for the measurement of XAS spectra in fluorescence and total electron yield (TEY) modes.[159] The fluorescence mode of detection is highly preferred for samples having lower concentrations of the element of interest.[152] As a result, the fluorescence detection mode is most widely used in the study of biological and environmental samples in which the concentrations of the element of interest are usually low. For hard X-ray measurements, fluorescence and transmission data can be collected simultaneously under ambient conditions by placing the fluorescent detector perpendicular to the sample.[152] However, for soft X-ray absorption spectroscopy (e.g., P K-edge), the fluorescence data needs to be collected under UHV conditions.[159] This is because at lower X-ray energies, a fluorescent photon loses the majority of its energy via interactions with air molecules. Measurement of the absorption spectra using the TEY mode can be done only under UHV conditions. The XAS spectra obtained using TEY mode are surface sensitive since the electron attenuation lengths in

solids are much lower when compared to the attenuation lengths of X-ray fluorescent photons.[154,159,168]

1.6.1.3 Glancing Angle XAS

XAS is inherently a bulk-sensitive characterization technique because of the high penetrating power of X-rays into matter.[158] As mentioned in the previous section, local structural information could be obtained from the surface of the material via collection of XAS spectra in TEY mode. However, using the TEY mode of detection would require the samples to be conducting. Therefore, for thick (e.g., pellets) and non-conducting samples, it is possible to obtain surface specific local structural information through the collection of XAS spectra in a glancing (or grazing) angle (GA) mode.[151,154,169] A schematic of the glancing angle XAS (GA-XAS) experimental setup is shown in Figure 1.9. In the glancing angle mode, the X-rays are incident on the surface of a material (e.g., pellet) at an angle 'θ' that is just above the critical angle for total external reflection.[154,169] With this experimental setup, the probing depth of the X-rays into matter decreases thereby rendering the GA-XAS spectra surface sensitive.[154] With regard to the modes of detection, GA-XAS spectra could be obtained using fluorescence and TEY modes. It is also possible to obtain local structural information from different depths of the material by varying the angle 'θ' between the incoming X-ray beam and the sample.[154] The GA-XAS technique is useful for studying materials in which the surface composition of the material is different from the bulk composition of the material.[162]

1.6.2 X-ray Photoelectron Spectroscopy

X-ray photoelectron spectroscopy (XPS) is a technique used in determining elemental composition, as well as in revealing the chemical environment of the respective element found in

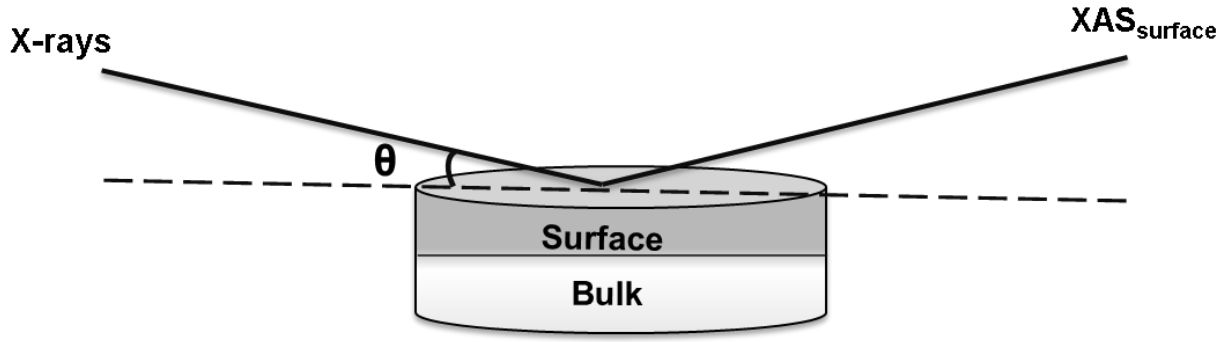

Figure 1.9 A schematic of the experimental setup for conducting glancing angle XAS experiments (GA-XAS) is shown. The angle 'θ' refers to the angle above the angle for total external reflections. In this geometry, the XAS spectra can be selectively collected from the surface regions of the material.

the top ≤10 nm of the surface of a solid.[170–173] The principle of this technique stems from the theory of the photoelectric effect proposed by Einstein which states that when a material is irradiated with a photon of energy greater than the binding energy of the core electron in the solid, electrons are ejected with a kinetic energy (KE) that is dependent on the incident energy of the photon (hυ), binding energy (BE) of the electron, and the work function of the sample (Φ_{sample}).[170] The expression that relates these terms is given in Equation 1.3.

$$BE = h\upsilon - \mathrm{KE} - \Phi_{sample} \tag{1.3}$$

Measurement of the binding energy of electrons in a solid requires referencing of the energy levels (i.e., Fermi and vacuum energy levels are chosen as the reference levels in the solid).[170,171] The concept of binding energy and work function are defined with respect to these two energy levels. The energy required to remove the electron from the core level to the Fermi level is called the binding energy.[170,171] The work function refers to the removal of electrons from the Fermi level to the vacuum level which is located away from the surface at an infinite distance where the electron is completely free from the attractive potential of the surface and exists as a free electron.[170,171] The work function of the sample (Φ_{sample}) is sample dependent.[170] In XPS, the Fermi energy levels of the sample and spectrometer are aligned to the same energy and, as a result, the work function is modified and the new work function is given in Eq. 1.4.

$$\Phi = \left(\Phi_{spectrometer} + \Phi_{sample}\right) - \Phi_{sample} = \Phi_{spectrometer} \tag{1.4}$$

The value of $\Phi_{spectrometer}$ can be found using calibration standards (e.g., Au, Ag, and Cu) possessing well-known binding energies.[170] As a result, the expression for determining the binding energy can be simplified and is provided in Eq. 1.5.

$$BE = h\upsilon - \mathrm{KE} \quad (1.5)$$

There are many sources of X-ray radiation but the most commonly employed ones are laboratory based X-ray sources (Al Kα, Mg Kα) and X-ray radiation emitted from synchrotron radiation sources.[171] It is the KE that is being measured by this technique and ultra-high vacuum (UHV) conditions are required so that the photoelectron does not encounter any air molecules on its way to the detector.[170] There are two types of energy scales used in a XPS experiment, namely the BE and KE scales.[170] In order to compare the spectra obtained using different sources of incident radiation, the BE scale is used as the observed photoelectron line energies are independent of the energy of the incident radiation used.[170] In the case of electrically conducting solids, the Fermi levels of the sample and the spectrometer align with each other and because the sample is electrically grounded to the spectrometer there is no development of positive charge on the surface of sample.[170] When the sample is insulating, alignment of the fermi levels of the sample and the spectrometer is not possible. Further, insulating samples cannot be electrically grounded and positive charges accumulate on the surface of the sample during the course of electron emission.[170] This kind of surface charging constantly shifts the binding energy scale during electron emission. Surface charging effects can be overcome using charge neutralizer which delivers low-energy electrons to the surface of the sample.[170] In a typical XPS experiment, a survey spectrum is collected from the sample over a wide energy range with a moderate step size to determine the elements present on the surface of the sample.[170] This is followed by collecting high energy resolution XPS spectra from the element of interest.[170] Representative examples of a survey scan XPS spectrum and a high-resolution P 2p XPS spectrum from $LaPO_4$ are shown in Figure 1.10.

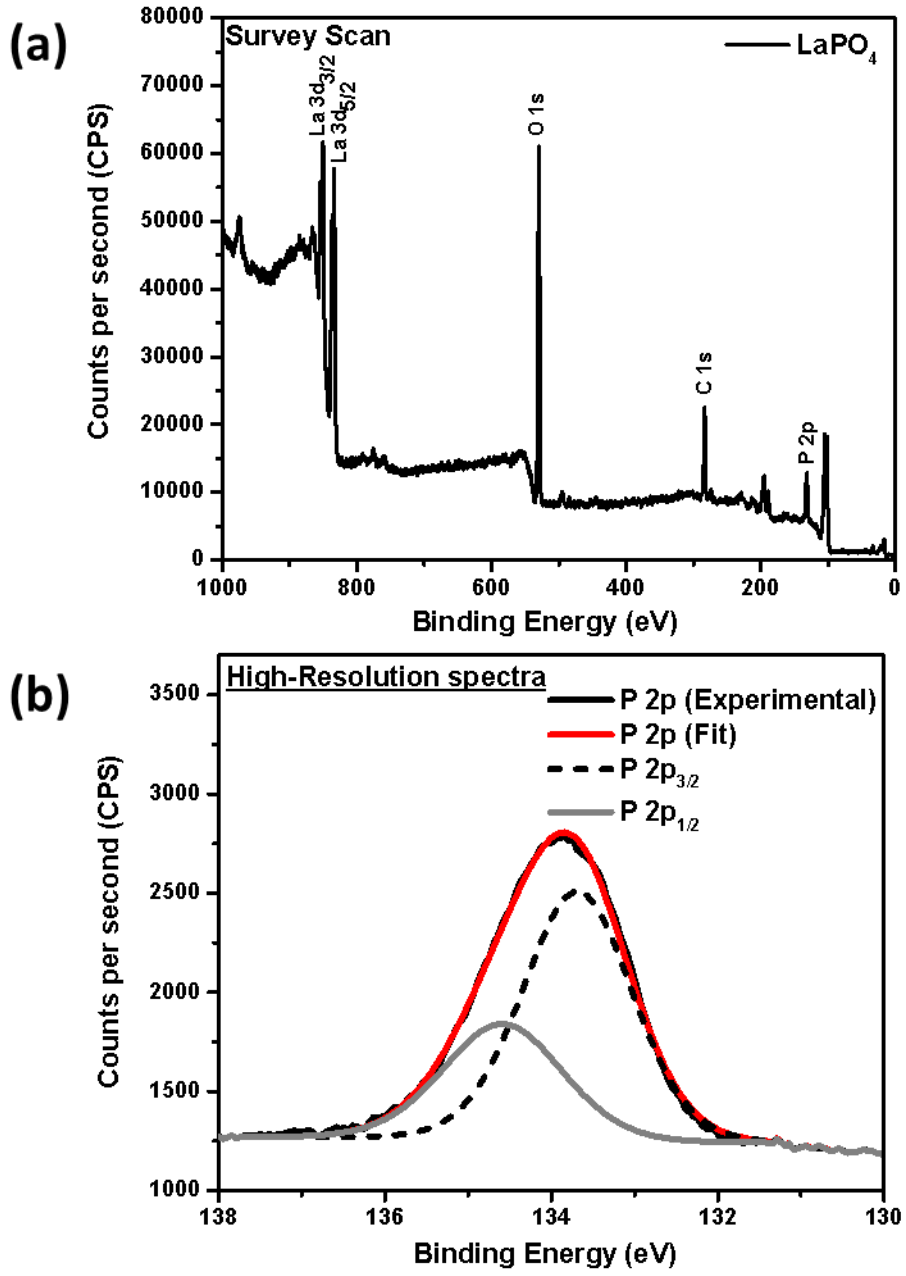

Figure 1.10 Representative (a) survey scan and (b) high-resolution P 2p XPS spectrum from $LaPO_4$ are shown. The as-obtained experimental P 2p XPS spectrum was fitted using peaks arising from spin-orbit split P 2p levels (P $2p_{3/2}$ and P $2p_{1/2}$). The solid light grey, dotted black, and solid dark gray curves represent the P $2p_{1/2}$, $2p_{3/2}$, and calculated P 2p peaks respectively.

1.7 Thesis Objectives

The first step towards the design of durable crystalline wasteforms is to gain a better understanding of the structures of proposed candidate materials at different length scales and this thesis aims to do so by providing a comprehensive structural description of monazite-, xenotime, and rhabdophane-type materials. The work presented in thesis deals with the fundamental structural investigations of these materials as well as investigating the structural response of these materials to conditions (e.g., radiation and leaching conditions) representing those experienced by a nuclear wasteform. Structural insights into these materials were obtained through the use of X-ray based diffraction and spectroscopic techniques.

The first objective of this thesis was to carry out a structural investigation of rare-earth phosphates adopting the monazite-, xenotime-, and rhabdophane-type structures and this work is presented in Chapters 2 and 3. The primary objective of the study presented in Chapter 2 was to determine how the electronic structure of materials adopting monazite- and xenotime-type structures varies as a function of composition and crystal structure. In order to meet this objective, the $RE_{1-x}RE'_xPO_4$ (RE = La, Sm; RE' = Yb, Y, Ho) materials were synthesized in the entire compositional range via conventional solid-state methods and the electronic structure of these materials was studied using X-ray spectroscopic techniques (XANES and XPS) and partial density of states (DOS) calculations. The influence of crystal structure and composition on the XANES and XPS spectra was investigated in this study through the collection and analysis of XANES (P K-, P $L_{2,3}$-, RE L_1, and RE $M_{4,5}$- edges) and XPS (P 2p, La 3d, and O 1s) spectra. Following this study, a thorough investigation of the long-range and local structures of hydrous rare-earth phosphate materials adopting the rhabdophane- and xenotime-type structures was carried out and the results obtained from this study are presented in Chapter 3. One of the

objectives of this study was to determine the crystal structure of rhabdophane-type materials and this objective was met by performing a Rietveld refinement of the powder XRD data of one of the materials adopting the rhabdophane-type structure. Another objective of this study was to determine the effect of annealing temperature on the long-range and local structure of hydrous rare-earth phosphate materials. To meet this objective, the as-synthesized hydrous rare-earth phosphate materials were annealed at various temperatures and the structural characterization of these materials were performed using powder XRD and XANES.

Following the structural investigation of hydrous and anhydrous rare-earth phosphate materials, the next objective of this thesis was to understand how these materials respond to radiation and leaching effects experienced by actinide containing wasteforms and nuclear wasteforms stored in geological repositories, respectively. In Chapter 4, the effect of radiation on the structure of monazite- and xenotime-type rare-earth phosphates was studied. The major objective of this study included the simulation of radiation damage and characterization of the surface of the materials using glancing angle XANES. The radiation studies were carried out using an external irradiation method in which the high energy α-recoil atom resulting from the decay of radioactive elements was simulated via high energy Au^- ion implantation of crystalline solids. In this study, the sintered pellets of monazite- and xenotime-type materials were bombarded with high energy Au^- ions and the resulting ion-implanted materials were characterized using glancing angle XANES and micro-XRD. This is the first study to utilize glancing angle XANES to study the structure of ion-implanted monazite- and xenotime-type rare-earth phosphates. The final objective of this thesis was to determine the chemical durability of hydrous and anhydrous rare-earth phosphate materials and this work is presented in Chapter 5. The major objective of this study was to compare the short-term dissolution behaviour of these

materials in deionized water. This objective was achieved by conducting leaching tests on powdered samples of materials adopting monazite-, xenotime-, and rhabdophane-type structures. The leaching tests were carried out in high density polyethylene (HDPE) containers filled with varying volumes of deionized water. Aliquots of water were withdrawn from the containers at regular intervals of time and were analyzed for rare-earth and P ions using Inductively Coupled Plasma – Mass Spectrometry (ICP-MS). Another objective of this study was to determine the structural response of these materials to leaching and this objective was met by determining the structure of these materials before and after exposure to water using powder XRD and XANES.

Chapter 2

AN X-RAY SPECTROSCOPIC STUDY OF THE ELECTRONIC STRUCTURE OF MONAZITE- AND XENOTIME-TYPE RARE-EARTH PHOSPHATES[1]

2.1 Introduction

Rare-earth phosphates adopting the monazite- ($REPO_4$; RE = La to Gd) and xenotime- ($RE'PO_4$; RE' = Tb to Lu & Y) type structures have been proposed as potential candidates for the sequestration of radioactive high level waste (HLW) arising from the reprocessing of spent nuclear fuel (SNF) and dismantlement of nuclear weapons.[88,121,125] Both, monazite and xenotime are naturally occurring rare-earth phosphate minerals which, depending on temperature and pressure, can coexist together in various igneous and metamorphic rocks.[174,175] The crystal structures of $CePO_4$ (monazite-type; Space group: $P2_1/n$) and YPO_4 (xenotime-type; Space group: $I4_1/amd$) are shown in Figure 1.3 and the description of these structures was provided in Section 1.5.1.[135,136,138] The cerium ion in $CePO_4$ (monazite) is coordinated to nine oxygen atoms

[1] Reproduced in part with permission from M. R. Rafiuddin, E. Mueller, A. P. Grosvenor, Journal of Physical Chemistry C (2014) 118 18000 – 18009. Copyright 2014 American Chemical Society

and the resulting CeO_9 polyhedra are connected to each other via an intervening PO_4 tetrahedron thereby leading to the formation of infinite chains of edge sharing CeO_9 and PO_4 polyhedra along the c-axis (Figure 1.3a).[135,140] In YPO_4 (xenotime), the yttrium ions are bonded to eight oxygen atoms and similar to the monazite structure, edge-sharing chains of YO_8 and PO_4 polyhedra are also present in the xenotime structure (Figure 1.3b).[135,138]

Studying synthesized solid solutions of monazite and xenotime can help develop a better understanding of the coexistence of these minerals in natural samples.[174,176,177] The variation in the crystal structure of these compounds places a limit on the solubility of monazite in xenotime, and vice versa, which results in a structural boundary between the two phases.[174,176,177] Studies of solid solutions of $Nd_xY_{1-x}PO_4$, $La_xY_{1-x}PO_4$, $Sm_xY_{1-x}PO_4$ and $Nd_xYb_{1-x}PO_4$ have revealed the compositional and temperature dependence of the structural boundary existing between the monazite and xenotime phases.[176] It is known that monazite compounds exhibit a resistance to radiation induced structural damage; however, the effect of substitution of the rare-earth element on the radiation resistance of xenotime has not been investigated. Further, the electronic structure of both monazite and xenotime materials remains unexplored.

In this study, solid solutions of monazite- and xenotime- type compounds ($La_{1-x}Yb_xPO_4$, $La_{1-x}Y_xPO_4$, and $Sm_{1-x}Ho_xPO_4$) have been synthesized and characterized by powder X-ray diffraction (XRD), X-ray absorption near-edge spectroscopy (XANES), and X-ray photoelectron spectroscopy (XPS). A phase analysis of the synthesized materials was performed by examination of powder XRD patterns. XANES was used to examine the electronic structure of the solid solutions, as this technique is sensitive to changes in the local coordination environment, the oxidation state, and the bonding environment of the absorbing atom.[152,154,158] P K-, P $L_{2,3}$-, Sm M_5-, Ho M_5-, Sm L_3-, and Ho L_3- edge XANES spectra have been collected from these solid

solutions and are reported here. Density of states calculations (DOS) were performed for $LaPO_4$ and YPO_4 to aid in the interpretation of P K- and P $L_{2,3}$- edge XANES spectra. XPS was also used to investigate these systems by collection of RE 3d, P 2p, and O 1s spectra. The focus of this study has been to establish XANES and XPS as tools for distinguishing compounds that adopt the monazite or xenotime structure in natural and synthesized samples.

2.2 Experimental

2.2.1 Synthesis and powder XRD

Solid solutions of $La_{1-x}Yb_xPO_4$, $La_{1-x}Y_xPO_4$, and $Sm_{1-x}Ho_xPO_4$ ($0 \leq x \leq 1$) were synthesized by conventional solid state methods.[25] Stoichiometric amounts of La_2O_3 (Alfa Aesar; 99.99%), Yb_2O_3 (Alfa Aesar; 99.9%), Y_2O_3 (Alfa Aesar; 99.99%), Sm_2O_3 (Alfa Aesar; 99.9%), Ho_2O_3 (Alfa Aesar; 99.9%), and $NH_4H_2PO_4$ (Alfa Aesar; 99.995%) were mixed together and placed in an alumina crucible. The crucibles were first heated in air at 1100-1200ºC for 2 days to facilitate the decomposition of $NH_4H_2PO_4$ before being quench cooled in air. The resulting mixtures were ground, pressed into pellets at 6 MPa, and heated again in air at 1100-1200ºC for a period of 6-12 days before being quench cooled in air. All materials were reground and repelleted at 2-3 day intervals. The annealing temperature used depended on the composition of the materials. The phase purity and composition of the synthesized materials was determined by powder X-ray diffraction using a PANalytical Empyrean system and either Co $K\alpha_{1,2}$ or Cu $K\alpha_{1,2}$ X-ray sources. Powder XRD patterns were collected at room temperature in the 2θ range of 10-80° and the lattice parameters and composition were determined using the HighScore Plus software package.[178] The composition of the solid solutions was determined by a simple refinement of the powder XRD patterns using the rare-earth phosphate end members as model compounds. During

this refinement, the atomic positions were held constant but the scale factors, zero shift, lattice parameters, lineshape parameters, and percent contribution of each phase were allowed to vary. The refinement procedure was performed using the HighScore Plus software package.[178]

2.2.2 XANES

2.2.2.1 P K-, Sm L_3-, and Ho L_3-edge XANES

The P K-edge XANES spectra from $La_{1-x}Yb_xPO_4$, $La_{1-x}Y_xPO_4$, and $Sm_{1-x}Ho_xPO_4$ were collected using the Soft X-ray Microcharacterization Beamline (SXRMB; 06B1-1) located at the Canadian Light Source (CLS).[179] Sm L_3- and Ho L_3- edge XANES spectra were also collected from the $Sm_{1-x}Ho_xPO_4$ series. Finely ground samples were mounted on carbon tape and the spectra were measured in vacuum. P K-edge spectra were collected in partial fluorescent yield (PFY) mode with a step size of 0.15 eV through the absorption edge. A Si (111) double crystal monochromator was used and the spectral resolution was 0.2 eV at 2145.5 eV (P K-edge). The Sm L_3- and Ho L_3- edge spectra were collected using total electron yield (TEY) mode with a step size of 0.15 eV through the absorption edge, as Sm and Ho spectra collected in PFY mode were influenced by absorption effects. The P K-edge XANES spectra were calibrated by collecting the spectrum from red P (Alfa Aesar ; 99%) with the maximum in the first derivative of the P K-edge set to 2145.5 eV.[180] Sm L_3- and Ho L_3- edge XANES spectra were calibrated against the spectrum from Fe metal by setting the maximum in the first derivative of the Fe K-edge to 7112 eV.[180] A linear combination fitting (LCF) of the P K-edge spectra was carried out to determine the relative percent of the monazite and xenotime structures that was found in each member of the solid solutions examined. All XANES spectra discussed here were analyzed using the Athena software program.[181]

2.2.2.2 P $L_{2,3}$-edge XANES

The P $L_{2,3}$-edge XANES spectra from $La_{1-x}Yb_xPO_4$, $Sm_{1-x}Ho_xPO_4$, and $La_{1-x}Y_xPO_4$ were collected using the Variable Line Spacing-Plane Grating Monochromator (VLS-PGM; 11ID-2) beamline located at the CLS.[182] A high energy grating monochromator was used to collect the P $L_{2,3}$-edge spectra and the spectral resolution was 0.01 eV at 130 eV (P L_3-edge). The samples were ground to a fine powder and mounted on carbon tape before being placed in the vacuum chamber. The spectra were collected in total fluorescence yield (TFY) mode using a step size of 0.05 eV through the absorption edge. The P $L_{2,3}$-edge spectra were calibrated using red P, with the P $L_{2,3}$-edge absorption energy set to 130 eV.

2.2.2.3 Sm M_5- and Ho M_5-edge XANES

The Sm M_5- and Ho M_5- edge XANES spectra were collected at the CLS using the Spherical Grating Monochromator (SGM; 11ID-1) beamline.[183] Finely ground samples were mounted on carbon tape and inserted into the vacuum chamber. Both the Sm M_5- and Ho M_5-edge XANES spectra were collected in TEY mode with a step size of 0.1 eV through the absorption edge. The Sm M_5- edge XANES spectra were calibrated using a zinc metal standard with the L_3- edge energy set to 1021.8 eV, and the Ho M_5- edge spectra were calibrated using a Cu metal standard with the L_3-edge set to 932.7 eV.[180]

2.2.3 XPS

XPS spectra were collected using a Kratos AXIS Ultra spectrometer and a monochromatic Al Kα X-ray source. The instrumental resolution is 0.4 eV and a X-ray spot size of 700 x 400 μm^2 was used to collect the spectra. The samples were finely ground, pressed into In foil, and then mounted on an electrically grounded sample holder. A charge neutralizer was used during the

collection of XPS spectra to overcome charging effects. High resolution P 2p, O 1s, and La 3d XPS spectra from $La_{1-x}Yb_xPO_4$ and YPO_4 were collected using a step size of 0.05 eV/step, a pass energy of 20 eV, and a collection time of 180 s per sweep. The collected XPS spectra were calibrated by setting the C 1s core-line spectrum arising from adventitious carbon to 284.8 eV. A Shirley-type function was used to remove the spectral background and the spectra were fitted using component peaks with a Gaussian (70%) and Lorentzian (30%) line profile.[184] The XPS spectra were analysed using the CasaXPS software program.[185]

2.2.4 Electronic Structure Calculations

Electronic structure calculations for the ternary monazite ($LaPO_4$) and xenotime (YPO_4) compounds were performed using a self-consistent tight-binding linear muffin tin orbital model with the atomic spheres approximation (TB-LMTO-ASA) to assist in the interpretation of P K- and P $L_{2,3}$- edge XANES spectra.[186] Overlapping Wigner-Seitz (WS) spheres are centered at each atom and the potential around these spheres is spherically symmetric in the TB-LMTO-ASA calculation. The partial Density of States (DOS) calculations were performed using the previously reported crystal structures for these materials and the lattice constants determined in this present study (see Section 2.3.1). The Brillouin zone integration was performed over a total of 512 *k*-points using a tetrahedron method.[187] The partial DOS for the P 3s, P 3p, P 3d, O 1s, O 2p, La 6s, La 6p, La 5d, La 4f, Y 5s, Y 5p, and Y 4d orbitals in these materials were calculated. The partial DOS from materials containing a partially filled 4f orbital could not be calculated adequately using the TB-LMTO-ASA package.

It should be noted that the TB-LMTO-ASA code provides only a ground state solution for these materials, as it does not account for final state relaxation effects. Nevertheless, direct comparison between the calculated partial DOS and experimental XANES spectra is still possible

for these and other compounds when the spectra are (primarily) affected by ground-state effects.[188] TB-LMTO-ASA calculations are relatively quick and straight-forward to perform unlike other packages (e.g., F*eff*) that consider both ground-state *and* final-state relaxation effects and require more computational rigour.[189] However, F*eff* calculations are necessary to simulate XANES spectra that are strongly affected by final-state relaxation effects.[189]

2.3 Results and Discussion

2.3.1 Structure

Compounds adopting the monazite- type structure crystallize in a monoclinic unit cell ($P2_1/n$) which is of a lower symmetry when compared to the tetragonal unit cell of the xenotime- type structure ($I4_1/amd$).[135,190] As a result, the powder XRD patterns from monazite-type compounds contain a larger number of diffraction peaks than the powder XRD patterns from xenotime-type compounds (Figure 2.1). All of the synthesized ternary monazite compounds ($LaPO_4$ and $SmPO_4$) were deemed to be phase pure. Small amounts of rare-earth oxides and some unknown phases were identified in the powder XRD patterns of ternary xenotime compounds ($HoPO_4$, YPO_4, and $YbPO_4$); however, these impurity phases do not alter the interpretation of the phosphorus XANES and XPS spectra. The lattice constants of the synthesized ternary monazite and xenotime compounds are presented in Table 2-1.

Solid solutions of $La_{1-x}Yb_xPO_4$, $La_{1-x}Y_xPO_4$, and $Sm_{1-x}Ho_xPO_4$ were synthesized to study the structural boundary (miscibility gap) that exists between the monazite and xenotime phases.[176] Depending on the value of 'x', the compounds can be synthesized either as a single phase or as a mixture of both phases. The solubility limit of rare-earth elements in the monazite or xenotime structure for each of the synthesized solid solutions was determined here by analysis

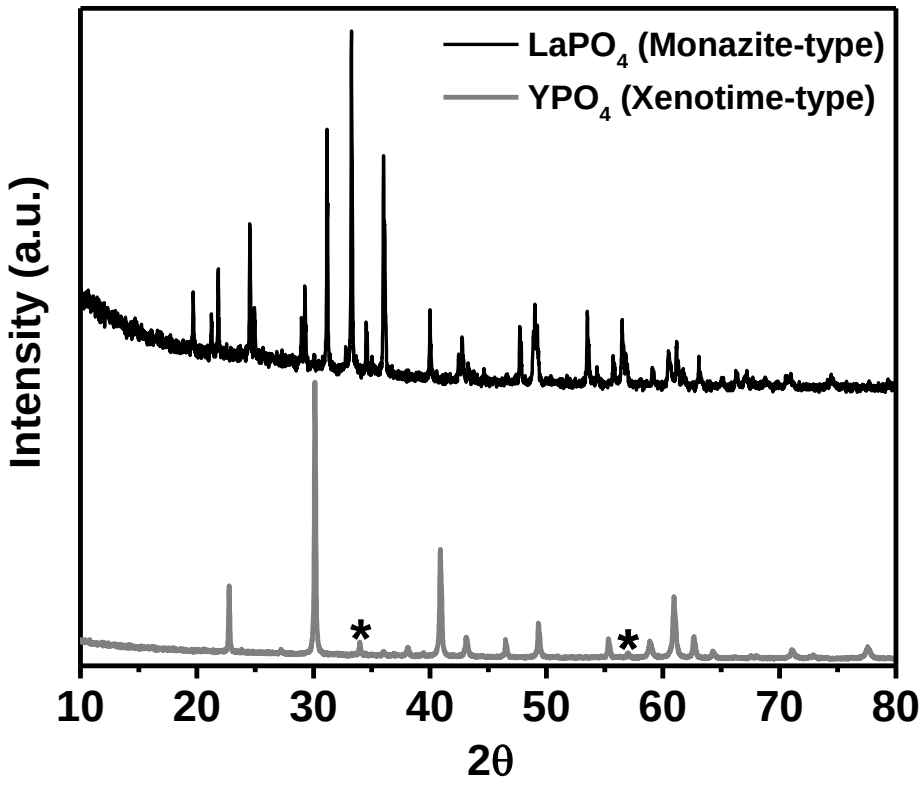

Figure 2.1 Powder XRD patterns from $LaPO_4$ (monazite-type) and YPO_4 (xenotime-type) compounds. The XRD patterns for $LaPO_4$ and YPO_4 were calculated using crystallographic information provided in reference and matched the experimental XRD patterns. The asterisk in the powder XRD pattern of YPO_4 denotes peaks from an impurity phase.

Table 2-1 Unit cell parameters from monazite and xenotime compounds

Compound	Structure	Lattice constants (Å)			β angle (degrees)
		a	b	c	
$LaPO_4$	Monazite	6.8384 (2)	7.0744 (2)	6.5097 (2)	103.281 (1)
$SmPO_4$	Monazite	6.6902 (2)	6.8915 (3)	6.3713 (2)	103.865 (2)
YPO_4[a]	Xenotime	6.8826 (2)	-	6.0199 (1)	-
$HoPO_4$	Xenotime	6.8870 (3)	-	6.0289 (3)	-
$YbPO_4$	Xenotime	6.8157 (1)	-	5.9715 (2)	-

[a] The a and b lattice constants are identical in the xenotime structure

of the powder XRD patterns. The relative concentrations of each phase, and the lattice parameters of these phases, were determined. The refined powder XRD patterns obtained from the $La_{1-x}Yb_xPO_4$ series are presented in Figure 2.2. The relative proportion of monazite and xenotime phases present in the $La_{1-x}Yb_xPO_4$ compounds, along with the lattice constants for these phases, are provided in Table 2-2. (Similar information for the $La_{1-x}Y_xPO_4$ and $Sm_{1-x}Ho_xPO_4$ series are provided in Tables A-1 and A-2 in Appendix A) The concentration of the xenotime phase increases with increasing concentration of Yb in $La_{1-x}Yb_xPO_4$. The monazite and xenotime dominated solid solutions were observed at $x < 0.5$ and $x \geq 0.5$, respectively. A similar trend was observed for the $La_{1-x}Y_xPO_4$ and $Sm_{1-x}Ho_xPO_4$ materials; however, the xenotime dominated solid solutions were only observed at $x > 0.5$, which suggests a greater solubility of Y and Ho in the monazite structure (see Tables A-1 and A-2 in Appendix A).

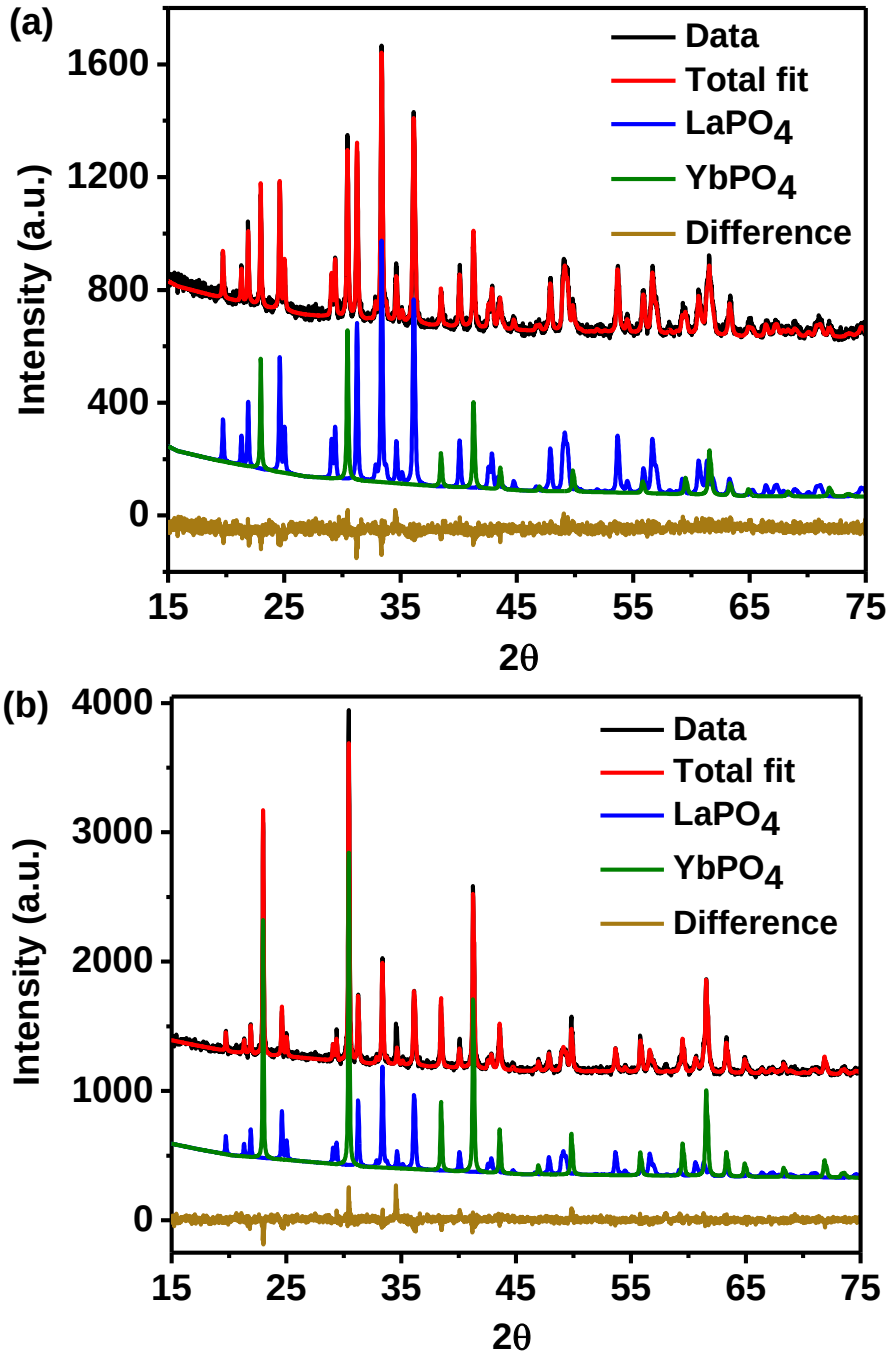

Figure 2.2 Refined powder XRD patterns from (a) $La_{0.8}Yb_{0.2}PO_4$ and (b) $La_{0.5}Yb_{0.5}PO_4$ compounds. These compounds contain a mixture of monazite and xenotime phases. The difference plots and the powder XRD patterns of the model ternary rare-earth phosphates are also presented.

Table 2-2 Unit cell parameters from $La_{1-x}Yb_xPO_4$

Compound	Monazite unit cell parameters	Xenotime unit cell parameters	Relative percent composition	Profile fit parameters[a]
$La_{0.8}Yb_{0.2}PO_4$	a = 6.8267 (3)Å	a = 6.8173 (4)Å	80% Monazite	R_p = 6.30
	b = 7.0576 (3)Å	c = 5.9726 (4)Å	20% Xenotime	R_{wp} = 8.00
	c = 6.5023 (3)Å			χ^2 = 0.98
	β = 103.333 (2)º			
$La_{0.5}Yb_{0.5}PO_4$	a = 6.8265 (4)Å	a = 6.8162 (2)Å	48% Monazite	R_p = 5.98
	b = 7.0581 (4)Å	c = 5.9718 (2)Å	52% Xenotime	R_{wp} = 7.79
	c = 6.5018 (4)Å			χ^2 = 1.43
	β = 103.335 (3)º			
$La_{0.3}Yb_{0.7}PO_4$	a = 6.8265 (5)Å	a = 6.8166 (1)Å	27% Monazite	R_p = 5.24
	b = 7.0578 (5)Å	c = 5.9719 (1)Å	73% Xenotime	R_{wp} = 6.60
	c = 6.5016 (5)Å			χ^2 = 1.38
	β= 103.314 (5)º			
$La_{0.2}Yb_{0.8}PO_4$	a = 6.8273 (8)Å	a = 6.8167 (2)Å	20% Monazite	R_p = 5.99
	b = 7.0580 (7)Å	c = 5.9720 (2)Å	80% Xenotime	R_{wp} = 7.76
	c = 6.5023 (9)Å			χ^2 = 1.93
	β = 103.302 (8)º			

[a] R_p – Profile R-factor; R_{wp} – Weighted profile R-factor; χ^2 – Goodness of Fit.

2.3.2 P K-edge XANES

The normalized P K-edge XANES spectra from ternary monazite ($LaPO_4$) and xenotime ($YbPO_4$ and YPO_4) compounds are shown in Figure 2.3a. These spectra result from the dipolar excitation of P 1s electrons into vacant P 3p orbitals. A significant difference in line-shape is observed between the monazite ($LaPO_4$) and xenotime ($YbPO_4$ and YPO_4) materials (*i.e.*, examination of these spectra can be used to distinguish between the two crystal structures).[191] The absorption energy of $YbPO_4$ (or YPO_4) increases by ~0.5 eV (~0.3 eV) with respect to $LaPO_4$, and the spectral line-shape is significantly different when comparing materials that adopt either the monazite or xenotime structure (Figure 2.3a). A shift in absorption energy can occur due to ground-state or final-state effects, or a combination of both. Prior to the absorption of a photon, the energy of P 3p conduction states in $YbPO_4$ or $LaPO_4$ may vary as a result of ground-state effects due to differences in the screening of the P nuclear charge because of both near and next nearest neighbor effects, and/or because of a change in the distribution of the conduction states that the P 1s electrons could be excited to.[192]After the absorption of a photon, the 1s electron is excited into the P 3p state and the resulting core-hole is screened either from the relaxation of electrons present above the P 1s orbital (intra-atomic effects) or from the oxygen atoms surrounding the P atom (extra-atomic effects). The contribution of intra-atomic effects to the screening of a core hole is negligible in comparison to extra-atomic effects.[192] Although the symmetry of the PO_4 tetrahedra is different in $LaPO_4$ and $YbPO_4$, the average P-O bond length is found to be similar in these compounds ($LaPO_4$ – 1.538Å; $YbPO_4$ – 1.532Å).[135] As a result, extra-atomic relaxation effects would likely be similar in these compounds. Therefore, it is not believed that the observed shift in the P K-edge absorption energy on going from $LaPO_4$ to $YbPO_4$ is a result of final-state effects. Instead, the change in the distribution of the P 3p

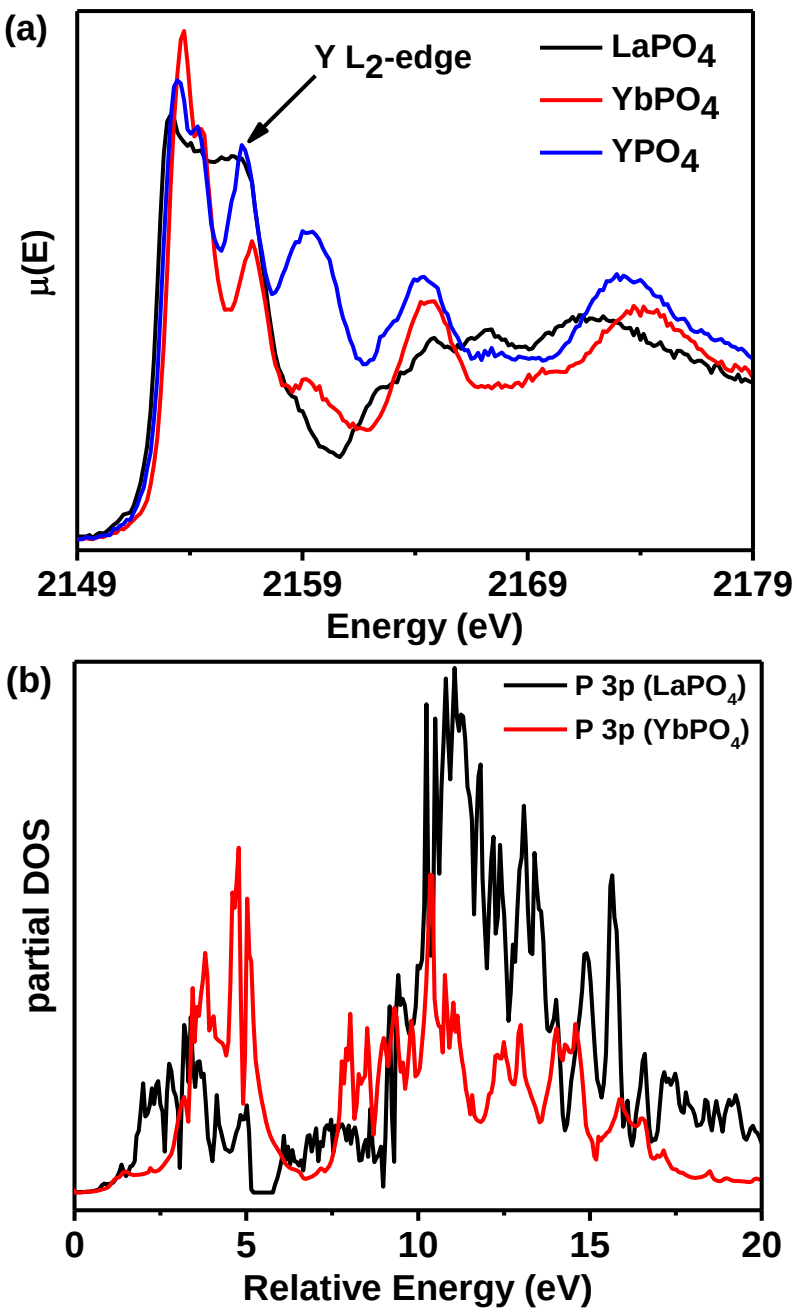

Figure 2.3 (a) Normalized P K-edge XANES spectra from $LaPO_4$, $YbPO_4$, and YPO_4 are presented along with an arrow indicating the interference of the Y L_2-edge with the P K-edge spectrum from YPO_4. (b) The P 3p partial DOS from $LaPO_4$ and YPO_4 are presented .The energies are plotted relative to the Fermi Level ($E_F = 0$).

conduction states (*i.e.*, ground-state effects) in $LaPO_4$ and $YbPO_4$ is believed to be responsible for the difference in absorption energy and lineshape of these spectra.

Partial DOS calculations were performed to confirm that the shift in absorption energy between the monazite ($LaPO_4$) and xenotime (YPO_4) compounds is due to a change in structure (Figure 2.3b). (A DOS calculation was not performed for YbPO4, as Yb contains partially occupied 4f orbitals.) Focusing on the region in the energy range of 1-8 eV in Figure 2.3b, which represents the features located between 2149 and 2156 eV in the corresponding P K-edge XANES spectra (Figure 2.3a), the distribution of the P 3p conduction states from YPO_4 is narrower and is also positioned at a higher energy, relative to the P 3p conduction states from $LaPO_4$. As a result, the xenotime compounds would be expected to have a higher P K-edge absorption energy than compounds that adopt the monazite-type structure. The change in lineshape between the P K-edge spectra from YPO_4 and $LaPO_4$ is also reflected in the P 3p partial DOS plots by a change in the distribution of unoccupied P 3p conduction states of these two materials (*cf.*, Figures 2.3a and 2.3b).

P K-edge XANES spectra were also collected from the $La_{1-x}Yb_xPO_4$ and $Sm_{1-x}Ho_xPO_4$ series to understand how the electronic structure of these solid solutions changes depending on structure and composition. The P K-edge XANES spectra were also collected from $La_{1-x}Y_xPO_4$; however, these spectra will not be discussed further because they contain a Y L_2-edge peak at ~2159 eV (see the spectrum from YPO_4 in Figure 2.3a).[180] The normalized P K-edge XANES spectra from members of the $La_{1-x}Yb_xPO_4$ series are presented in Figure 2.4a. With increasing Yb content, the line-shape of the P K-edge spectra changes gradually thereby indicating an increase in the concentration of the xenotime structure in the sample. The spectra were fitted using a linear combination fitting (LCF) method and the XANES spectra from the two ternary end-members

(*i.e.*, $LaPO_4$, and $YbPO_4$) as standards (Figure 2.5). The fitted spectra matched well with the experimentally observed P K-edge XANES spectra from the $La_{1-x}Yb_xPO_4$ series. The concentration of $LaPO_4$ and $YbPO_4$ that contributed to the linearly combined XANES spectra from the $La_{1-x}Yb_xPO_4$ series are listed in Table 2-3. The concentration of monazite and xenotime phases determined by analysis of the P K-edge XANES spectra is in close agreement to the results determined by analysis of the powder XRD patterns (c.f., Table 2-2 and Table 2-3).

The normalized P K-edge XANES spectra collected from the $Sm_{1-x}Ho_xPO_4$ series are shown in Figure 2.4b. The Sm end-member of this series (*i.e.*, x = 0) adopts the monazite structure whereas the Ho end-member (*i.e.*, x =1) adopts the xenotime structure.[135] Similar to $YbPO_4$, a difference in line-shape is observed for these compounds and the absorption energy of $HoPO_4$ is ~0.2 eV above that of $SmPO_4$. A pronounced variation in the line-shape of the P K-edge spectra occurs with increasing substitution of Ho in the $Sm_{1-x}Ho_xPO_4$ series (Figure 2.4b). A linear combination fitting was also performed for the $Sm_{1-x}Ho_xPO_4$ series using the XANES spectra from $SmPO_4$ and $HoPO_4$ as standards and a good match was observed between the fitted and experimentally observed XANES spectra (Figure A.1 in Appendix A). The concentrations of the ternary phosphates (*i.e.*, $SmPO_4$ (monazite) and $HoPO_4$ (xenotime)) that contributed to these linearly combined spectra are in good agreement with the results obtained by analysis of powder XRD patterns (c.f., Table A-1 and A-3 in Appendix A).

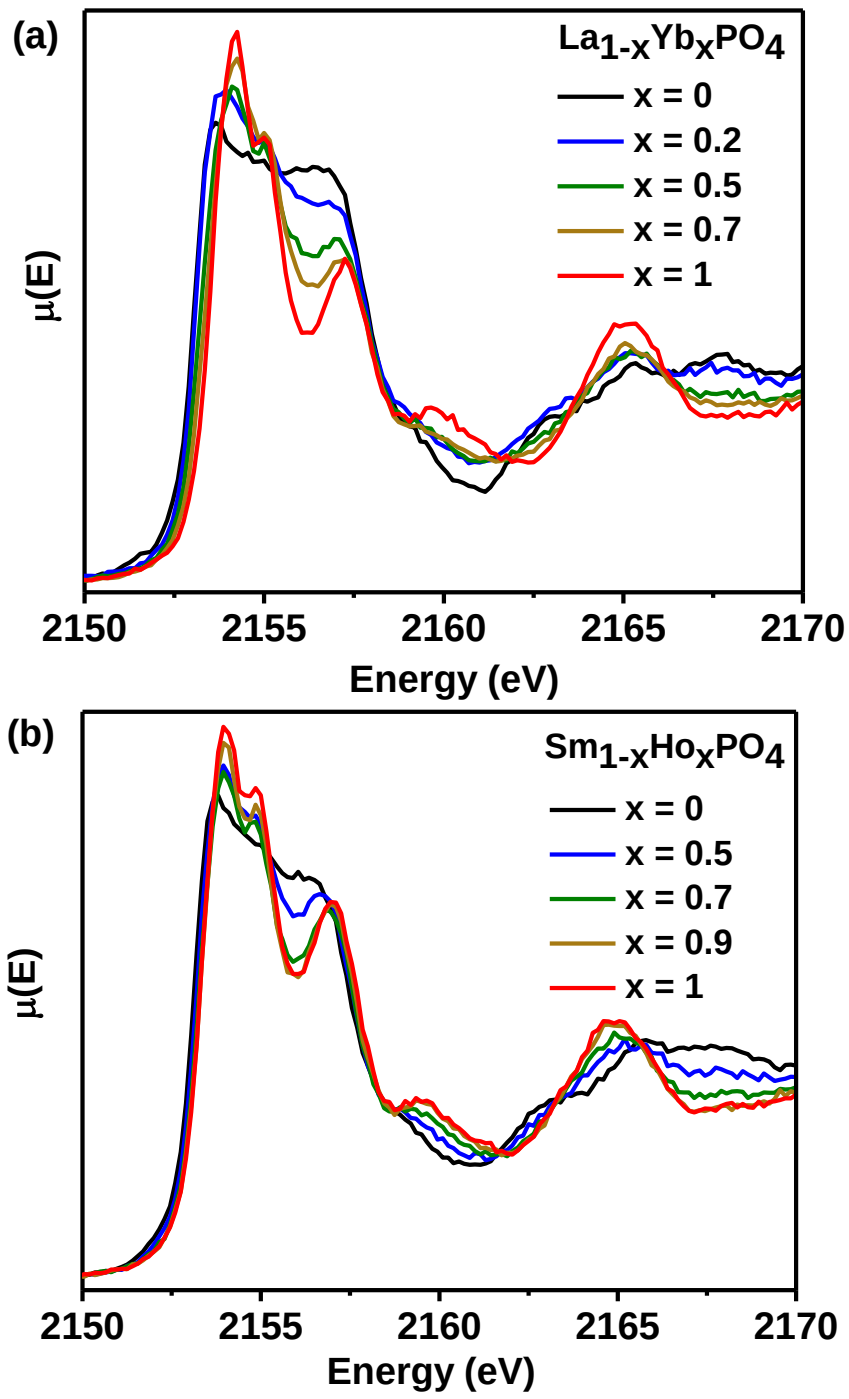

Figure 2.4 Normalized P K-edge XANES spectra from (a) $La_{1-x}Yb_xPO_4$ (x = 0, 0.20, 0.50, 0.70, and 1) and (b) $Sm_{1-x}Ho_xPO_4$ (x = 0, 0.50, 0.70, 0.90, and 1).

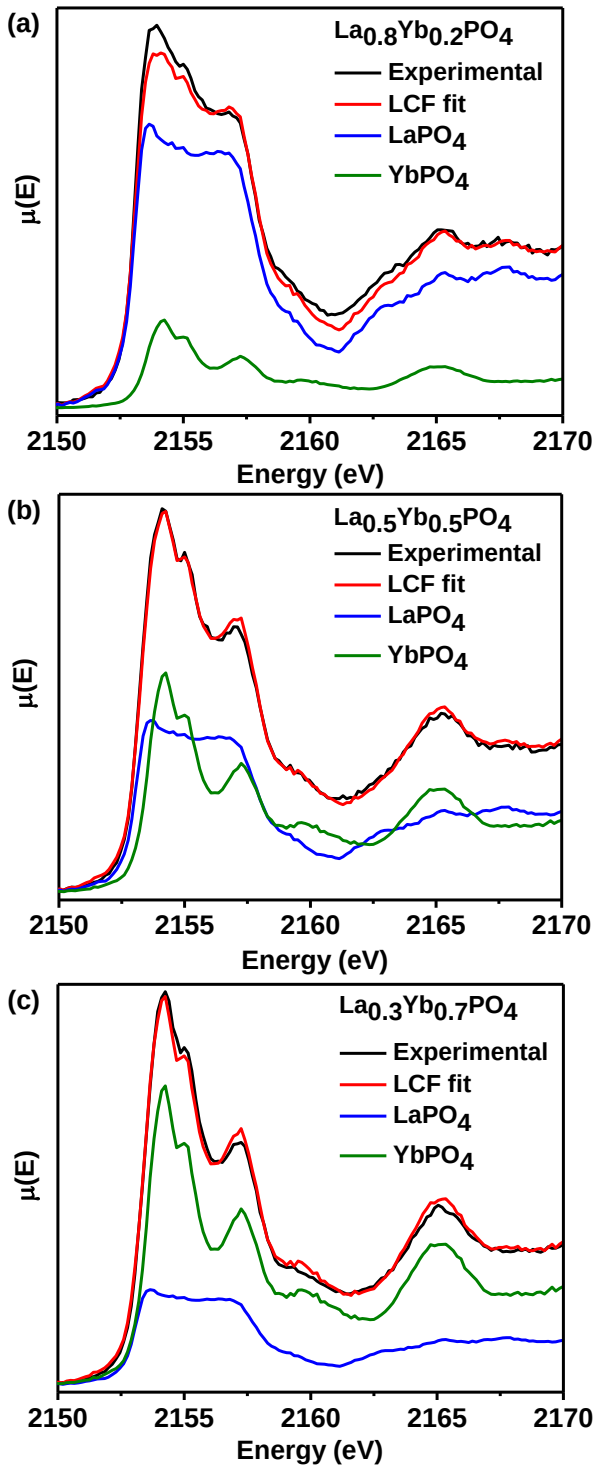

Figure 2.5 Results of the linear combination fitting of the P K-edge spectra from the $La_{1-x}Yb_xPO_4$ series [(a) x = 0.2, (b) x = 0.5, (c) x = 0.7] are shown. $LaPO_4$ and $YbPO_4$ were used to fit the spectra.

Table 2-3 Linear Combination Fitting results for the P K-edge spectra of $La_{1-x}Yb_xPO_4$

Compounds	Percent composition		Fit parameters[a]
	$LaPO_4$	$YbPO_4$	
$La_{0.8}Yb_{0.2}PO_4$	79 (2) %	21(2) %	R = 0.0082239
			χ^2 = 0.53233
$La_{0.5}Yb_{0.5}PO_4$	48 (1) %	52 (1) %	R = 0.0018217
			χ^2 = 0.10314
$La_{0.3}Yb_{0.7}PO_4$	28 (1) %	72 (1) %	R = 0.0040296
			χ^2 = 0.22292

2.3.3 P $L_{2,3}$-edge XANES

The normalized P $L_{2,3}$-edge XANES spectra collected from the monazite ($LaPO_4$) and xenotime (YPO_4) compounds are shown in Figure 2.6a. These spectra result from the excitation of 2p electrons into unoccupied 3s or 3d states.[193] Since the P 2p core-hole has a longer lifetime than its 1s counterpart, the P $L_{2,3}$-edge spectra have a higher resolution than the P K-edge spectra and more features are observed in these spectra.[194] Two distinct features, labelled as A (lower energy) and B (higher energy), are observed in the P $L_{2,3}$-edge spectra from these compounds (Figure 2.6a). Previous studies of P $L_{2,3}$-edge XANES spectra from phosphate containing compounds have identified these features as resulting from 2p → 3s (A) and 2p → 3d (B) transitions, respectively.[193,195] It is proposed here that these features actually result from more complicated transitions owing to the overlap of P 3s and 3d states, as can be observed by examination of the partial DOS from YPO_4 (Figure 2.6b).

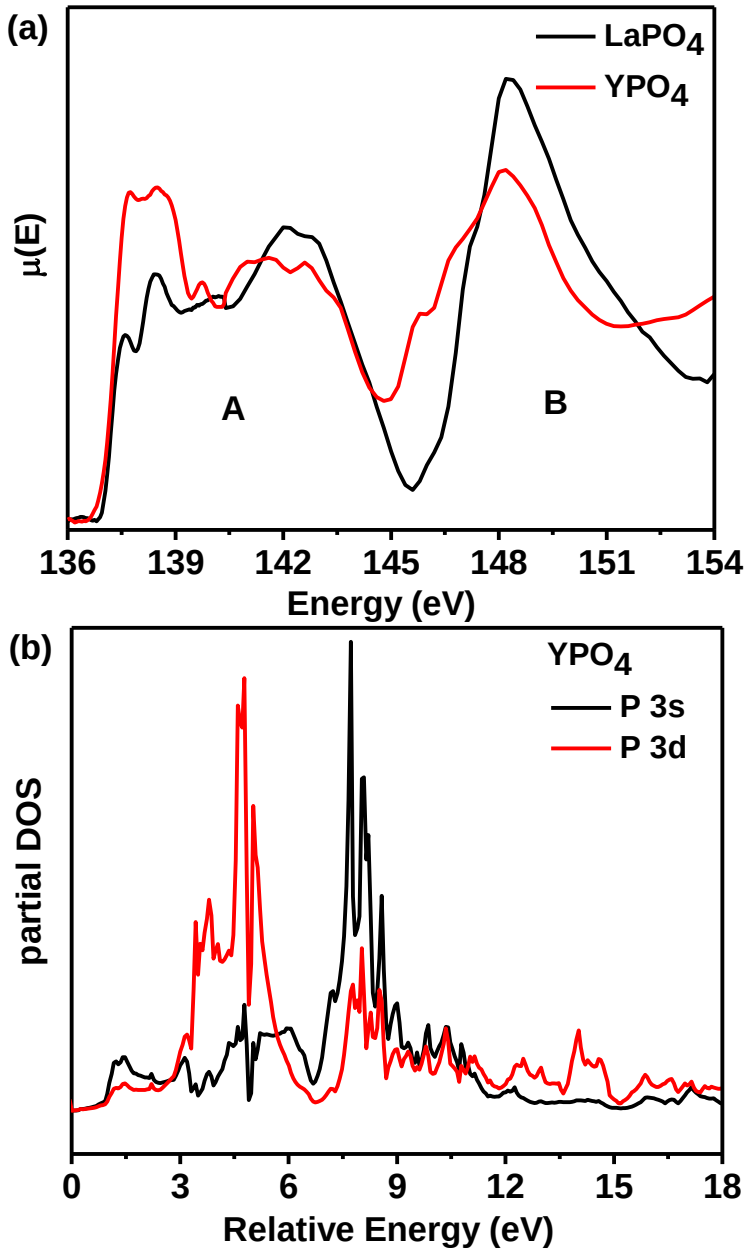

Figure 2.6 (a) Normalized P $L_{2,3}$-edge spectra from $LaPO_4$ and YPO_4 are shown. The lower and higher energy features in the spectra are labelled as A and B, respectively. (b) The partial DOS of the P 3s and P 3d conduction states from YPO_4 have been plotted relative to the Fermi level (E_F = 0). The partial DOS plots suggests that a significant overlap of P 3s and P 3d states occurs.

The effect of the substitution of the rare-earth elements on the electronic structure of the monazite or xenotime structure was studied by collecting the P $L_{2,3}$-edge XANES spectra from $La_{1-x}Y_xPO_4$ and $La_{1-x}Yb_xPO_4$. The P $L_{2,3}$-edge spectra were also collected from the $Sm_{1-x}Ho_xPO_4$ series; however, these spectra strongly overlap the Sm $N_{4,5}$-edge, which makes it impossible to compare these spectra (See Figure A.2 in Appendix A).[180] The normalized P $L_{2,3}$-edge spectra collected from the $La_{1-x}Yb_xPO_4$ series are presented in Figure 2.7. The P $L_{2,3}$-edge spectra shift to higher energy and a more pronounced fine structure is observed with increasing substitution of La^{3+} for Yb^{3+} in $La_{1-x}Yb_xPO_4$. This observation suggests an increase in the concentration of the xenotime structure. The normalized P $L_{2,3}$-edge spectra collected from the $La_{1-x}Y_xPO_4$ series also exhibited a slight variation in absorption energy and lineshape at higher values of x (see Figure A.3 in Appendix A). A linear combination fitting of the P $L_{2,3}$-edge spectra was not possible because of difficulties in normalizing the spectra; however, these observations are in general agreement with the analysis of the P K-edge XANES spectra and the powder XRD data (vide supra).

2.3.4 Sm M_5-, Ho M_5-, Sm L_3-, and Ho L_3-edge XANES

M_5- and L_3- edge XANES spectra from Sm and Ho were collected to study how substitution affected the electronic structure of the rare-earth atoms. The M_5-edge XANES spectra correspond to the transition of electrons from a 3d orbital into partially occupied 4f orbitals.[196,197] The 3d core level is split into $3d_{5/2}$ (M_5-edge) and $3d_{3/2}$ (M_4-edge) states because of spin-orbit coupling.[196,197] The normalized Sm M_5-edge XANES spectra collected from the $Sm_{1-x}Ho_xPO_4$ (x = 0, 0.1, 0.2, 0.5) series are presented in Figure 2.8a. The edge energy of the Sm M_5-edge XANES spectra remained almost invariant with increasing Ho substitution; however, the intensity of the spectra increased across the series (Figure 2.8a). It is proposed here that the

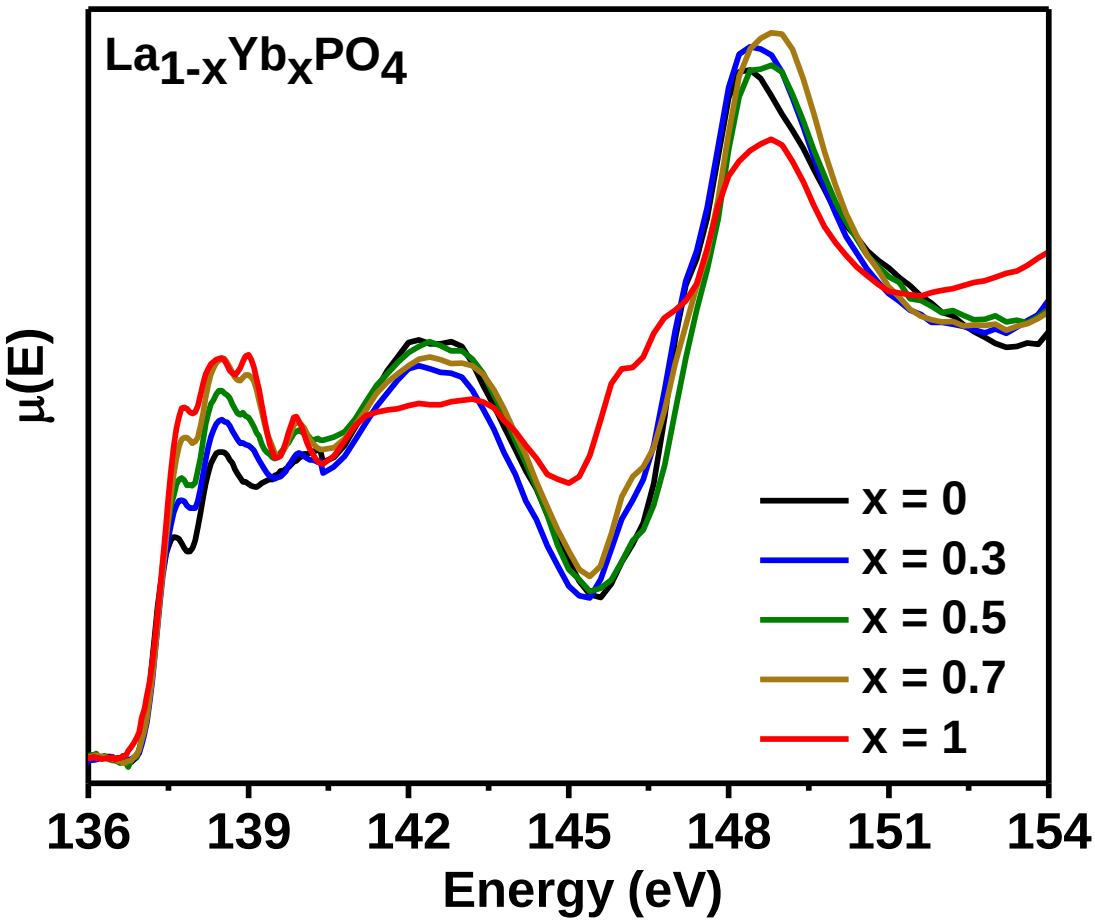

Figure 2.7 Normalized P $L_{2,3}$-edge spectra from the $La_{1-x}Yb_xPO_4$ (x = 0, 0.3, 0.5, 0.7, and 1) series are shown.

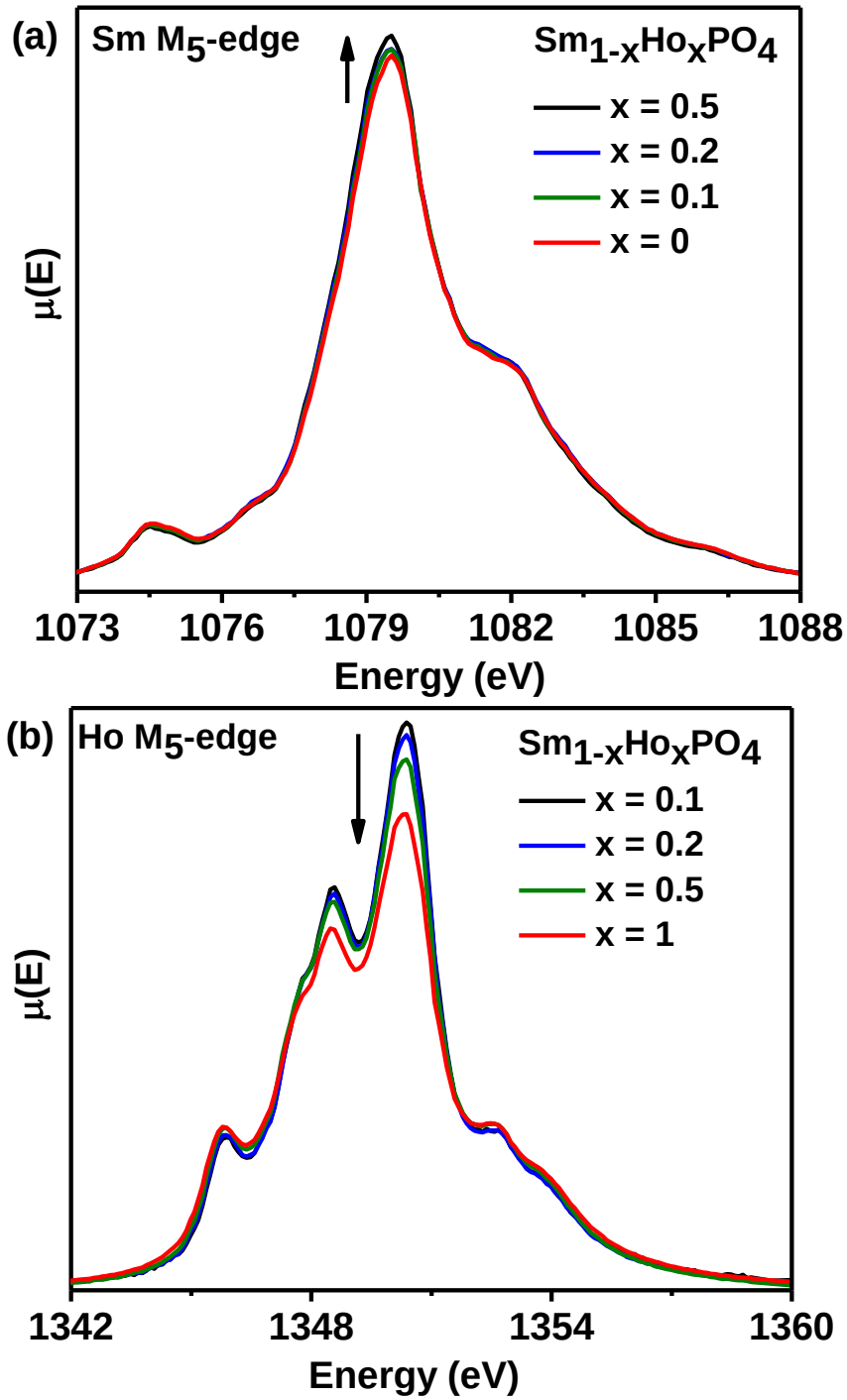

Figure 2.8 Normalized (a) Sm M_5-edge and (b) Ho M_5-edge XANES spectra from the $Sm_{1-x}Ho_xPO_4$ (x = 0, 0.1, 0.2, 0.5, and 1) series are presented. The arrows indicate the changes in the intensity of the Sm/Ho M_5-edges with increasing Ho concentration.

occupancy of the Sm valence states, which include the 4f states, decreases slightly as Ho substitutes for Sm in the $Sm_{1-x}Ho_xPO_4$ system. This change in occupancy of the Sm valence states can be understood by considering the crystal structure and the electronegativity of the rare-earth ions. From the crystal structure of $SmPO_4$, it is observed that the Sm atoms are separated from each other by a bridging O atom (Figure 1.3a). However, in the case of the $Sm_{1-x}Ho_xPO_4$ system, the substituted Ho^{3+} ion introduces a change in the electron occupation of the Sm valence states which is due to the slight difference in the electronegativity of Sm vs Ho. Sm is found to be less electronegative than Ho based on the examination of Pauling's electronegativity scale (O - 3.44; Sm - 1.17; Ho - 1.23).[198] As a result of the difference in electronegativity between Sm and Ho, O would withdraw more electrons from Sm. This would lead to a decrease in the number of occupied Sm valence states, which is observed as an increase in intensity of the Sm M_5-edge XANES spectra.

The normalized Ho M_5-edge XANES spectra from $Sm_{1-x}Ho_xPO_4$ (x = 0.1, 0.2, 0.5, and 1) provide further evidence for a change in the valence electron distribution in this system (Figure 2.8b). In contrast to the Sm M_5-edge spectra, the intensity of the Ho M_5-edge spectra decreases with increasing Ho substitution and is due to the increase in occupancy of the Ho valence states, which include the 4f states, with increasing Ho concentration. This observation is expected by considering the differences in electronegativity between Sm and Ho (Figure 2.8b). The Sm and Ho L_3-edge XANES spectra were also examined so as to confirm the observations made by examination of the M_5-edge spectra (Figure 2.9). These spectra result primarily from the excitation of 2p electrons to unoccupied 5d states. In contrast to the Sm and Ho M_5-edges, fine structure is not observed in the L_3-edge spectra, which is a result of the shorter core-hole lifetime of the excited 2p state.[194] However, the intensity trends observed in the Sm and Ho M_5-edge

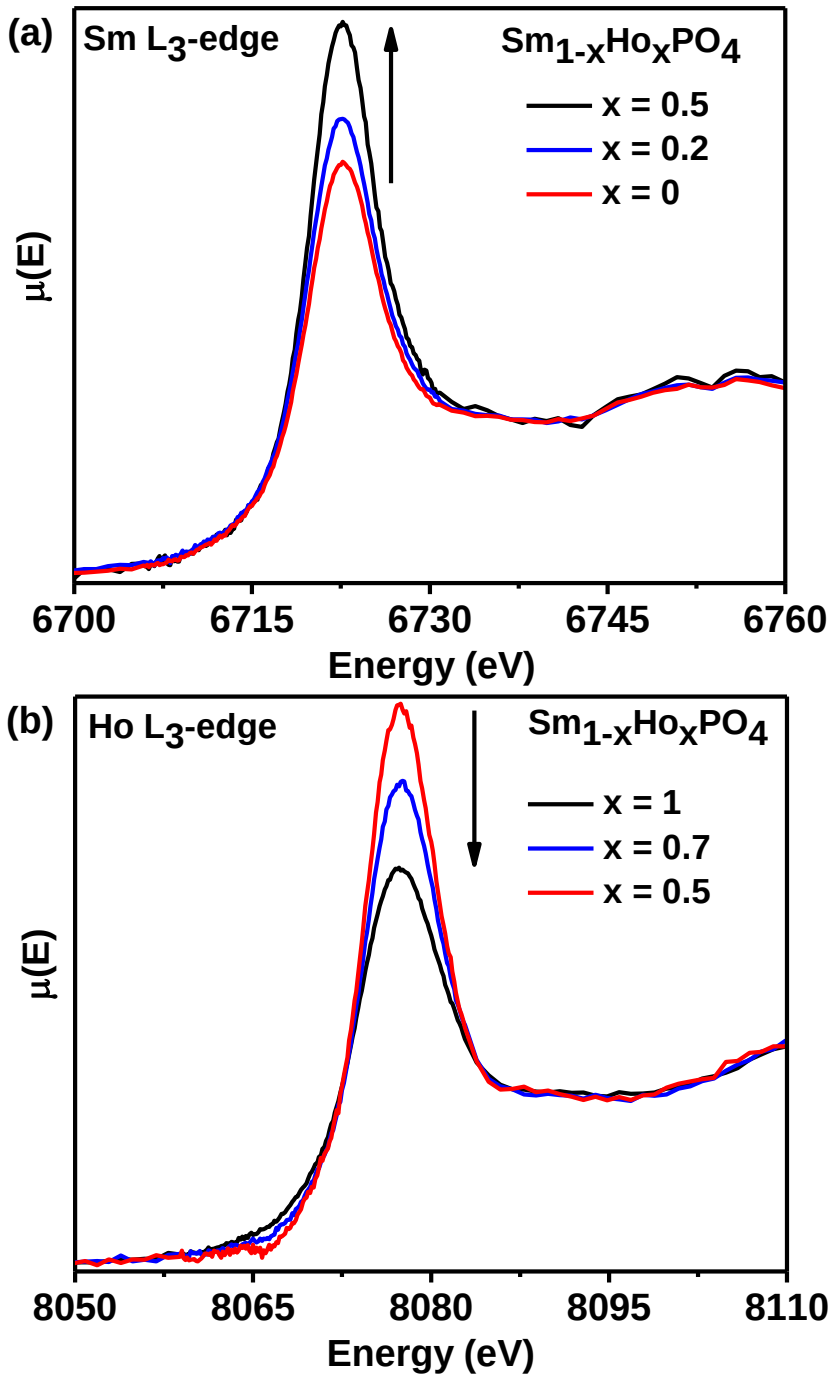

Figure 2.9 Normalized Sm L_3- and Ho L_3-edge XANES spectra from the $Sm_{1-x}Ho_xPO_4$ series are presented. The arrows indicate the changes in the intensity of Sm/Ho L_3-edges with increasing Ho concentration

XANES spectra are reproduced in the Sm and Ho L_3-edge XANES spectra, which confirms the interpretation provided above (*i.e.*, that the electron occupancy of the Sm and Ho valence states changes depending on composition).

2.3.5 P 2p, O 1s, and La 3d XPS

P 2p, O1s, and La 3d XPS spectra were collected from $La_{1-x}Yb_xPO_4$ and YPO_4 to determine if XPS can serve as a tool for determining if rare-earth phosphates adopt the xenotime or monazite structure. The P 2p XPS spectra did not exhibit any detectable binding energy (BE) shift or change in lineshape between the monazite and xenotime compounds (Figure 2.10a); however, the O 1s XPS spectra did show a minor shift in BE (~0.1 – 0.2 eV) (Figure 2.10b). The observed shift in the O 1s spectra could be a result of differences in screening of the O nuclear charge because of differences in the electronegativity of La and Yb/Y and/or because of a change in structure.[198] The La 3d XPS spectra were also collected from the $La_{1-x}Yb_xPO_4$ (x = 0, 0.3, and 0.7) series to examine if any changes occurred in the spectra (Figure 2.10c). The spectra from the quaternary phosphates ($La_{0.7}Yb_{0.3}PO_4$, and $La_{0.3}Yb_{0.7}PO_4$) were observed to shift to higher BE by ~0.17 eV relative to the ternary phosphate ($LaPO_4$). Overall, the XPS spectra were observed to be relatively insensitive to variations in the concentration of monazite and xenotime in the $La_{1-x}Yb_xPO_4$ materials.

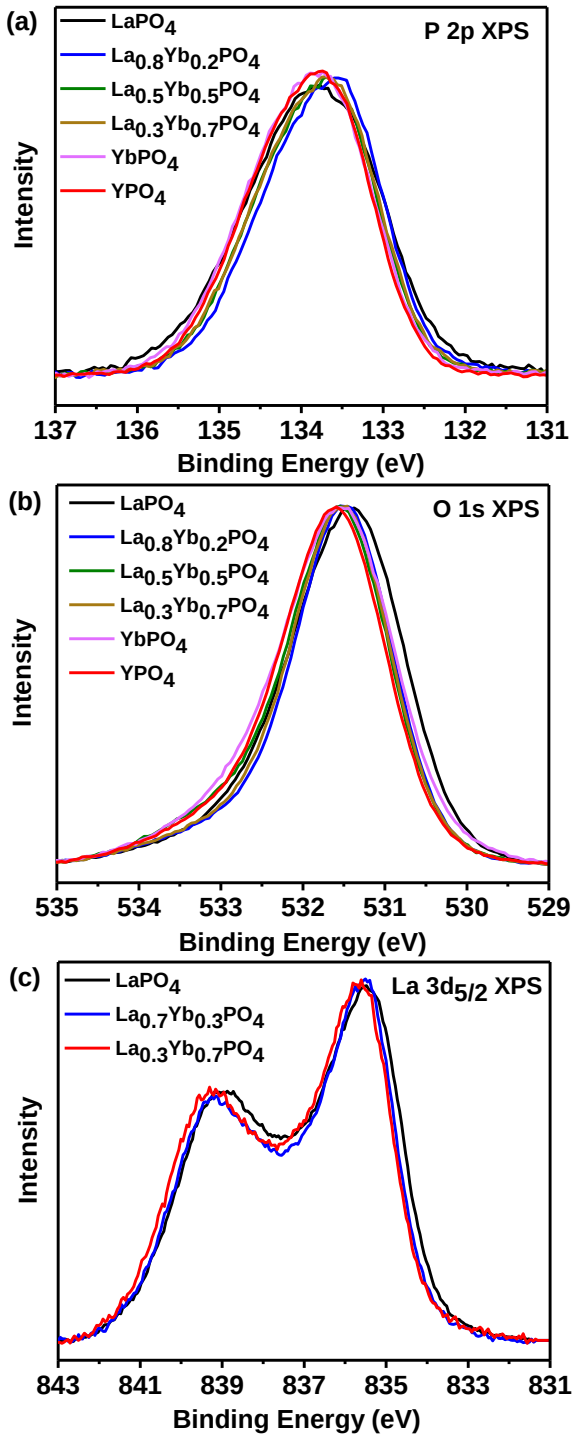

Figure 2.10 High-resolution (a) P 2p, (b) O 1s, and (c) La $3d_{5/2}$ XPS spectra from $La_{1-x}Yb_xPO_4$ and YPO_4 are presented. A distinct shift in binding energy was not observed between the monazite and xenotime compounds.

2.4 Conclusion

Multiple rare-earth phosphate solid-solutions ($La_{1-x}Yb_xPO_4$, $La_{1-x}Y_xPO_4$, and $Sm_{1-x}Ho_xPO_4$) have been synthesized. Examination of the P K-edge XANES spectra has shown that spectra from materials adopting the monazite structure have a different lineshape and energy compared to spectra from materials that adopt the xenotime structure. The quantitative linear combination fitting of the P K-edge spectra were equivalent to powder XRD analysis of the solid-solutions. Variations in the lineshape and energy of the P $L_{2,3}$-edge XANES spectra were also observed; however, a quantitative analysis of these spectra was not possible. Analysis of the P 2p, O 1s and La 3d XPS spectra revealed a minor shift in binding energy between the two crystal structures. The electronic structure of rare-earth phosphate solid-solutions was studied in greater detail by XANES and XPS in this study than has been presented previously. It was found in this investigation that P K-edge XANES spectra provide a spectroscopic fingerprint for the monazite- and xenotime- type structures, thereby making these spectra useful in determining the composition and structure of rare-earth phosphates in both geological and synthetic samples.

Chapter 3

A STRUCTURAL INVESTIGATION OF HYDROUS AND ANHYDROUS RARE-EARTH PHOSPHATES[2]

3.1 Introduction

Rare-earth phosphates are an interesting class of materials that have applications as nuclear wasteforms, in photonics, as proton conductors, as catalysts, and in biolabeling.[88,199–204] These applications stem from the structural diversity exhibited by these compounds. Depending on the water content, two classes of rare-earth phosphates exist namely the anhydrous and hydrous rare-earth phosphate materials. In the previous chapter, the crystal and electronic structures of anhydrous rare-earth phosphate materials adopting the monazite- and xenotime-type structures were discussed in detail using X-ray diffraction and X-ray spectroscopy (XANES and XPS). Of the two X-ray spectroscopic techniques, the XANES spectrum was shown to be more sensitive to changes in the crystal structures of materials. Hydrous rare-earth phosphate materials are also found in nature and, depending on the sizes of rare-earth ions and the synthetic methods used, these materials can adopt the rhabdophane- ($REPO_4.nH_2O$; RE = La to Dy) or xenotime- ($REPO_4$

[2] Reproduced in part with permission from M. R. Rafiuddin, A. P. Grosvenor, Inorganic Chemistry (2016) 55, 9685 – 9695. Copyright 2016 American Chemical Society.

& RE'PO_4.nH_2O; RE = Tb to Lu and Y; RE' = Ho to Lu and Y) type structure.[126,135] In the current chapter, a structural investigation of hydrous rare-earth phosphate materials adopting the rhabdophane- and xenotime type structure was carried out using XRD and XANES. In contrast to the monazite and xenotime structures, structural studies of the rhabdophane-type materials are rather limited due to their metastable nature.[113] The rhabdophane structure initially loses water upon heating to form an anhydrous compound followed by an irreversible structural transformation to the monazite- or xenotime- type structure depending on the rare-earth present when annealed at higher temperatures.[113] Materials adopting the rhabdophane-type structure are usually synthesized in powder form by solution based synthetic methods and no instances of single crystal growth of these materials have been reported in the literature.[205,206] The crystal structure of rhabdophane solved using an ab-initio method is presented in Figure 1.4 and a detailed description of the structure is provided in Section 1.5.2. Materials adopting the rhabdophane structure crystallize in the monoclinic crystal system.[126] The structure consists of open channels formed by the connection of two different chains of alternating SmO_n (n = 8 or 9) and PO_4 tetrahedra. The lattice water resides in the open channel oriented along the 'a' direction.[126]

A structural investigation of the hydrous and anhydrous type rare-earth phosphates was carried out in this study using powder XRD and X-ray absorption near-edge spectroscopy (XANES). The $REPO_4.nH_2O$ (RE = La, Nd, Sm, Gd, Dy, Y, Yb) and $Gd_{1-x}Dy_xPO_4.nH_2O$ (x = 0.0, 0.2, 0.4, 0.8, 1.0) materials were synthesized using a precipitation route with the crystal structure adopted by the as-synthesized materials being observed to depend on the size of the RE ion. The as-synthesized materials were annealed at various temperatures and studied by powder XRD in order to examine changes in the long-range structure of these materials. Information

about the local structure of the RE and P ions in the as-synthesized and annealed materials was obtained from the analysis of RE L_1- (RE = Gd, Dy, Sm), RE L_3-, P K-, and P $L_{2,3}$- edge XANES spectra. To the best knowledge of the author, this represents the first study to investigate variations in the local structure of $REPO_4.nH_2O$ (RE = La, Nd, Sm, Gd, Dy, Y, Yb) materials with varying annealing temperature. The primary objective of this study was to understand how the long-range and local structure of $REPO_4.nH_2O$ materials changed as a function of temperature and size of the RE ion.

3.2 Experimental

3.2.1 Synthesis and Powder XRD

The hydrated rare-earth phosphates ($REPO_4.nH_2O$ and $Gd_{1-x}Dy_xPO_4.nH_2O$ [x = 0.0, 0.2, 0.4, 0.8, 1.0]; RE = La, Nd, Sm, Gd, Dy, Y, Yb) were synthesized following the procedure developed by Kijkowska.[205] La_2O_3 (Alfa Aesar; 99.99%), Nd_2O_3 (Alfa Aesar; 99.9%), Sm_2O_3 (Alfa Aesar; 99.9%), Gd_2O_3 (Alfa Aesar; 99.99%), Dy_2O_3 (Alfa Aesar; 99.9%), Y_2O_3 (Alfa Aesar; 99.99%), Yb_2O_3 (Alfa Aesar; 99.9%), and H_3PO_4 (Fisher Scientific; 85%) were used as the starting materials. Finely ground powders of RE_2O_3 (0.0020 moles) were added to a beaker containing 13.7 mL of 14.6 M H_3PO_4 (0.200 moles) and the resulting mixture was stirred until a clear solution was obtained. A PO_4:RE_2O_3 mole ratio of 100:1 was used to synthesize these compounds. It must be noted here that the mixture containing Nd_2O_3 and H_3PO_4 remained cloudy even after stirring for long periods of time (~1 day); however, a clear solution was obtained while using other RE_2O_3 (RE = La, Sm, Gd, Dy, Y, and Yb) oxides. The clear or cloudy solution was then diluted with 100 mL of water. This solution was then transferred to a round bottomed flask and refluxed at ~130°C for 2 hours. The clear solution containing La ions became cloudy

immediately after the addition of 100 mL of water while the solutions containing other RE ions (RE = Sm, Gd, Dy, Y, Yb) remained clear. The resulting precipitate was filtered and washed using deionized water after refluxing and then dried in air overnight before being heated at 60°C for 1 hour.

The phase purity and the crystal structure of the as-synthesized materials ($REPO_4.nH_2O$ [RE = La, Nd, Sm, Gd, Dy, Y, Yb] and $Gd_{1-x}Dy_xPO_4.nH_2O$ [x = 0.0, 0.2, 0.4, 0.8, 1.0]) was determined by analysis of powder XRD patterns collected using a PANalytical Empyrean system (Co $K\alpha_{1,2}$ or Cu $K\alpha_{1,2}$ X-ray source). Powder XRD patterns were also collected from $REPO_4.nH_2O$ (RE = La, Nd, Sm, Gd, Dy, Y, Yb) materials annealed at different temperatures (500°C -1200°C) for 12h (followed by quench cooling in air) in order to study the effect of annealing temperature on the long-range order of these materials. Powder XRD patterns from the as-synthesized and annealed materials were collected in the 2θ range of 10°-80° using a step size of 0.017° and the lattice constants were determined using the HighScore Plus software program.[178] The powder XRD pattern from as-synthesized $DyPO_4.nH_2O$ (rhabdophane-type structure) was refined using the hexagonal and the monoclinic structural models to determine the best structure to describe this phase.[126,142] For refinement purposes, the powder XRD pattern from $DyPO_4.H_2O$ was collected over a wide 2θ range (5° - 120°) using a step size of 0.017° with the data being refined over the 2θ range of 10°-80°. The following parameters were varied during the refinement: scale factors, zero shift, lattice constants, profile variables, and the overall isotropic thermal factor (B_{OVL}). The atomic positions were fixed during the refinement.

3.2.2 Thermogravimetric analysis (TGA)

Thermogravimetric analysis was performed using a TA Instrument Q5000 TGA instrument to determine the total water content in the as-synthesized materials. Powdered samples of

$DyPO_4.nH_2O$ (rhabdophane-type) and $YbPO_4.nH_2O$ (xenotime-type) weighing ~17 mg were heated in air (25.0 ml/min) in a Pt pan from 25°C to 700°C at 5°C/min with the weight loss being constantly monitored.

3.2.3 XANES

3.2.3.1 P K- and P $L_{2,3}$-edge XANES

The P K-edge XANES spectra from the as-synthesized and annealed $REPO_4.nH_2O$ (RE = Sm, Gd, Dy, Yb) materials were collected using the Soft X-ray Micro-characterization Beamline (SXRMB; 06B1-1) located at the Canadian Light Source (CLS).[179] Information regarding the sample preparation and experiment was provided in Section 2.2.2.1. The P $L_{2,3}$-edge XANES spectra were also collected from as-synthesized and annealed $DyPO_4.nH_2O$ materials using the Variable Line Spacing-Plane Grating Monochromator (VLS-PGM; 11ID-2) beamline at the CLS.[182] The experimental information and sample preparation procedure was mentioned in Section 2.2.2.2. All spectra discussed in this chapter were analyzed using the Athena software program.[181]

3.2.3.2 RE L_1- and L_3-edge (RE = Sm, Gd, Dy) XANES

The RE L_1- and L_3- edge XANES spectra from $REPO_4.nH_2O$ (RE = Sm, Gd, Dy, Yb) were collected using the Sector 20 – Bending Magnet (20 BM; CLS@APS) beamline located at the Advanced Photon Source (APS; Argonne National Laboratory).[207] The spectra were collected in transmission mode using a Si (111) double crystal monochromator and 100% N_2 gas filled ionization chambers. The spectral resolution varied from 0.9 eV at 6716 eV (Sm L_3-edge) to 1.5 eV at 10486 eV (Yb L_1-edge). Fine powders of the materials were sandwiched between layers of kapton tape and the absorption signal was maximized by adjusting the number of layers. The

XANES spectra were collected using a step size of 0.15 eV through the RE L_1- and RE L_3- edges. Spectra from the calibration standards were collected from metal foils placed between the transmission and reference ionization chambers. The Gd L_3-, Dy L_3-, and Sm L_1- edge spectra were calibrated using Co metal foil (E_0 = 7709 eV). The Gd L_1-, Dy L_1-, Sm L_3-, Yb L_1- edge spectra were calibrated using Ni (E_0 = 8333 eV), Zn (E_0 = 9659 eV), Fe (E_0 = 7112 eV), and Ga (E_0 = 10367) metal foils, respectively.[180]

3.3 Results and Discussion

3.3.1 TGA and Powder XRD

The as-synthesized $REPO_4.nH_2O$ materials were found by XRD (*vide infra*) to adopt one of two structure types: rhabdophane (RE = La, Nd, Sm, Gd, Dy) or xenotime (RE = Y, Yb).[126,135] The water content 'n' in the rhabdophane and xenotime structures was determined by performing TGA on $DyPO_4.nH_2O$ and $YbPO_4.nH_2O$ (Figure B.1 in Appendix B). In accordance with previous studies, two distinct regions were observed in the TGA plot from rhabdophane and are attributed to the two-step elimination of water (Figure B.1a in the supporting information).[208] However, in materials adopting the xenotime-type structure, a continuous weight loss was observed in the temperature range of 25ºC-700°C (Figure B.1b in Appendix B).[208] The value of 'n' was determined to be ~1 for both structures and represents the total water content (i.e., no distinction was made between adsorbed and lattice water in this study). This result is in agreement with a previous investigation of these materials.[208] The total water content in the rhabdophane- and xenotime- type structures appears to be removed once the temperature reaches ~700°C.

Two different crystal structures (hexagonal and monoclinic) are reported for compounds adopting the rhabdophane structure.[126,142] The crystal structure of the rhabdophane-type materials was determined by performing a Rietveld refinement of the powder XRD data from $DyPO_4.H_2O$ using the hexagonal and monoclinic structural models (Figure 3.1).[126,142] Large differences in peak intensity were observed between the calculated and observed patterns when the hexagonal model was used (Figure 3.1a). In contrast, a significantly better fit was obtained using the monoclinic model as indicated by the residual pattern in Figure 3.2b. The lattice constants and fit parameters for $DyPO_4.H_2O$ obtained using the hexagonal and monoclinic structural models are listed in Table 3-1. It is concluded here that the rhabdophane materials studied adopt the monoclinic structure.[126]

The powder XRD patterns from materials adopting the rhabdophane ($REPO_4.H_2O$; RE = La, Nd, Sm, Gd, Dy) structure are presented in Figure 3.2a. Significant variations in peak widths and intensity were observed across the rhabdophane series. The presence of broad diffraction peaks in the XRD patterns from $LaPO_4.H_2O$ and $NdPO_4.H_2O$ indicate that these materials are poorly crystalline. On moving from $LaPO_4.H_2O$ to $DyPO_4.H_2O$, the peaks became narrower and more intense, indicating an increase in the crystallinity of these materials. This observation agrees well with an earlier report wherein similar observations were made through the analysis of scanning electron micrographs.[205] The lattice constants of the materials adopting the rhabdophane structure are listed in Table 3-2. In addition to the ternary compounds, a $Gd_{1-x}Dy_xPO_4.H_2O$ (x = 0.0, 0.2, 0.4, 0.8, 1.0) solid solution was also synthesized. The XRD patterns confirmed that all members of the solid solution adopt the rhabdophane structure (Figure 3.2b). The diffraction peaks shifted to higher 2θ with increasing Dy substitution thereby indicating a contraction in the

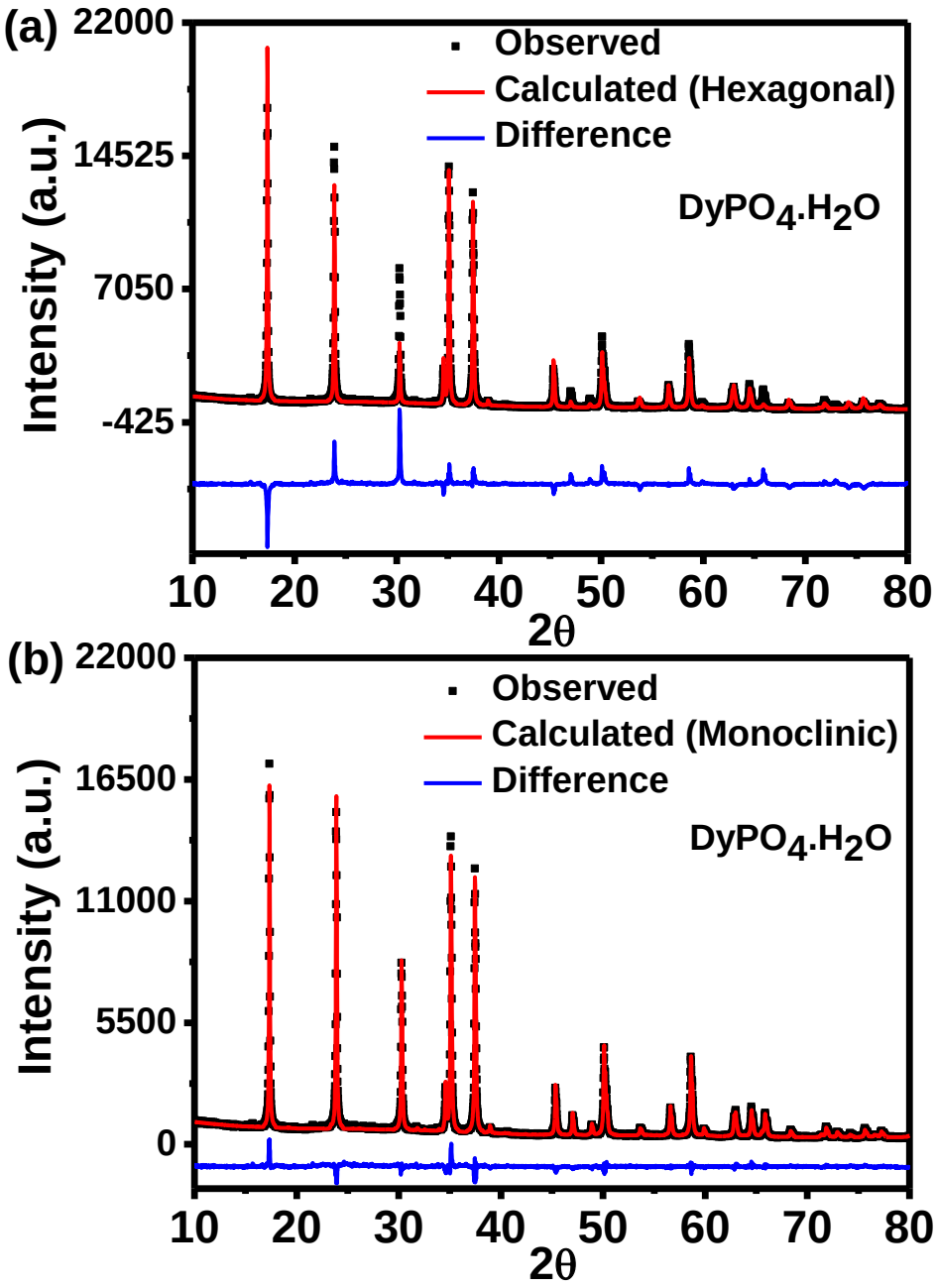

Figure 3.1 Rietveld refined powder XRD patterns from rhabdophane-type $DyPO_4.H_2O$ using the (a) hexagonal and (b) monoclinic structural models.

Table 3-1 Lattice Constants and Rietveld Refinement Results for $DyPO_4.H_2O$

Crystal system	Lattice constants (Å)	B_{OVL}	Agreement indices
Hexagonal[a]	a = 6.8476 (3)	2.81 (12)	R_{wp}[b] = 17.60
	c = 6.3084 (3)		R_p[c] = 12.91
			R_{exp}[d] = 3.48
			χ^2[e] = 25.65
Monoclinic	a = 27.874 (1)	3.77 (4)	R_{wp} = 6.65
	b = 6.8485 (5)		R_p = 5.37
	c = 11.8596 (9)		R_{exp} = 3.60
	β = 115.141 (5)		χ^2 = 3.42

[a]The a and b lattice constants are identical in the hexagonal unit cell

[b]Weighted profile R-factor, $R_{wp} = \left[\frac{\sum(w_i(y_{i(obs)}-y_{i(calc)})^2}{\sum w_i y_{i(obs)}{}^2}\right]^{1/2}$

[c]Profile R-factor, $R_P = \frac{\sum |y_{i(obs)}- y_{i(calc)}|}{\sum y_{i(obs)}}$

[d]Expected R-factor, $R_{exp} = \left[\frac{N-P}{\sum w_i y_{i(obs)}{}^2}\right]^{1/2}$

where, N = number of observations; P = number of estimated least square parameters

[e]Goodness of fit, $\chi^2 = \left[\frac{R_{wp}}{R_{exp}}\right]^2$

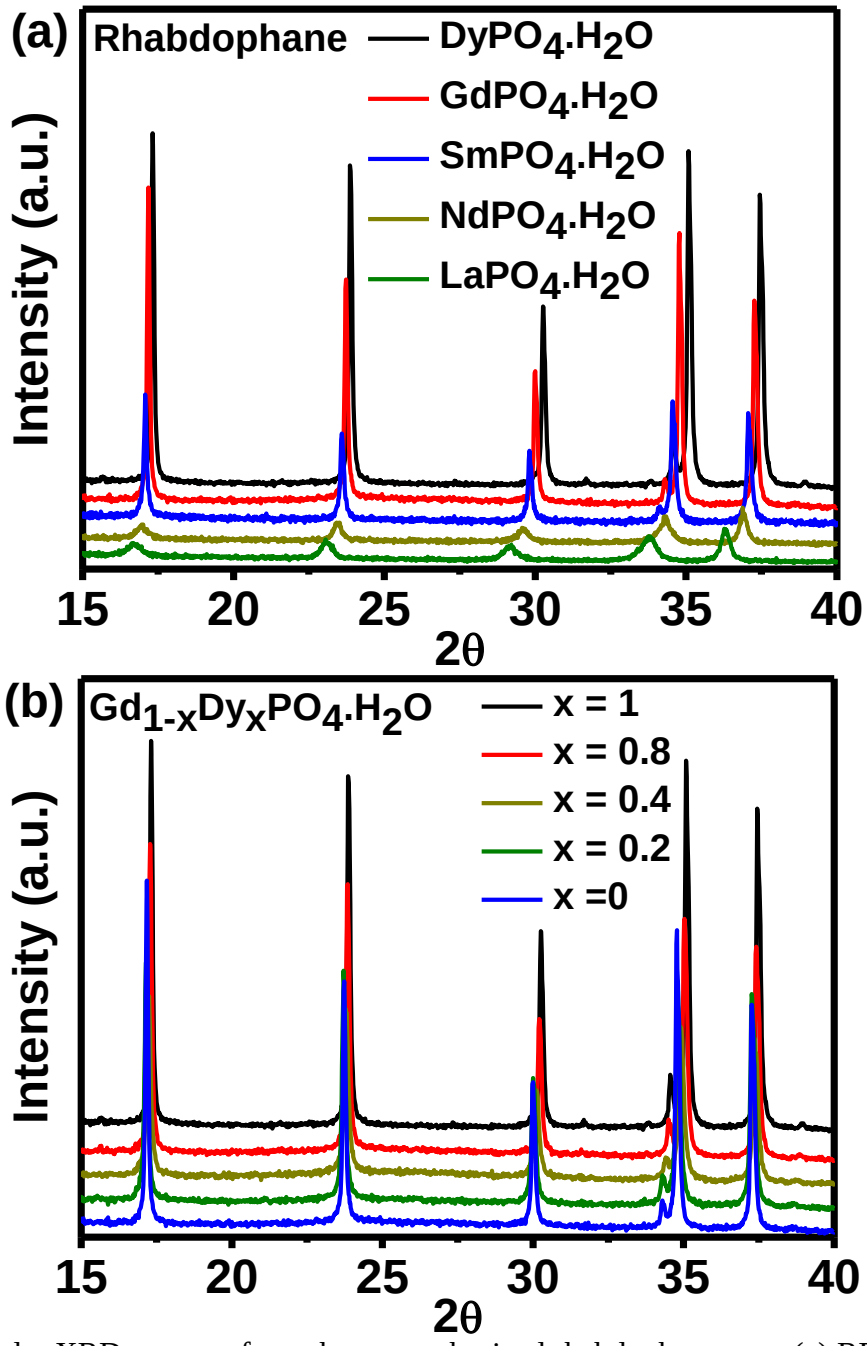

Figure 3.2 Powder XRD patterns from the as-synthesized rhabdophane-type (a) $REPO_4.H_2O$ (RE = La, Nd, Sm, Gd, Dy) and (b) $Gd_{1-x}Dy_xPO_4.H_2O$ materials.

Table 3-2 Lattice Constants from As-Synthesized Rhabdophane-Type $REPO_4.H_2O$ Materials

Compounds	a (Å)	b (Å)	c (Å)	β (degrees)
$LaPO_4.H_2O$	28.740 (5)	7.136 (1)	12.267 (2)	115.34 (2)
$NdPO_4.H_2O$	28.309 (6)	7.028 (1)	12.100 (2)	115.40 (2)
$SmPO_4.H_2O$	28.162 (3)	6.956 (1)	12.037 (2)	115.36 (1)
$GdPO_4.H_2O$	27.997 (3)	6.907 (1)	11.971 (2)	115.25 (1)
$DyPO_4.H_2O$	27.874 (1)	6.8485 (5)	11.8595 (9)	115.141 (5)

unit cell, which is in agreement with the lower ionic radius of Dy^{3+} compared to Gd^{3+} (Figure 3.2b and Table B.1 in Appendix B).[209]

The water content in the rhabdophane structure was determined to be eliminated at ~700°C by TGA (*vide supra*) and it was of interest to study how the long-range structure of rhabdophane-type materials changed upon removal of water. The long-range structure of rhabdophane was studied as a function of temperature by examining the powder XRD patterns from $DyPO_4.H_2O$ samples annealed at different temperatures (600°C-1100°C) (Figure 3.3). In comparison to the as-synthesized material, substantial changes in the powder XRD patterns from the materials annealed at 600°C and 700°C were not observed (Figure 3.3a). These results suggest that the long-range structure of rhabdophane is not significantly affected by the absence of water. At higher annealing temperatures (> 700°C), the structure of $DyPO_4$ initially transformed to a mixture of monazite- and xenotime- type structures before undergoing a final transformation to the xenotime structure at temperatures exceeding 800°C (Figure 3.3b). The temperature at which the rhabdophane → monazite and/or xenotime transformation occurs was different for the

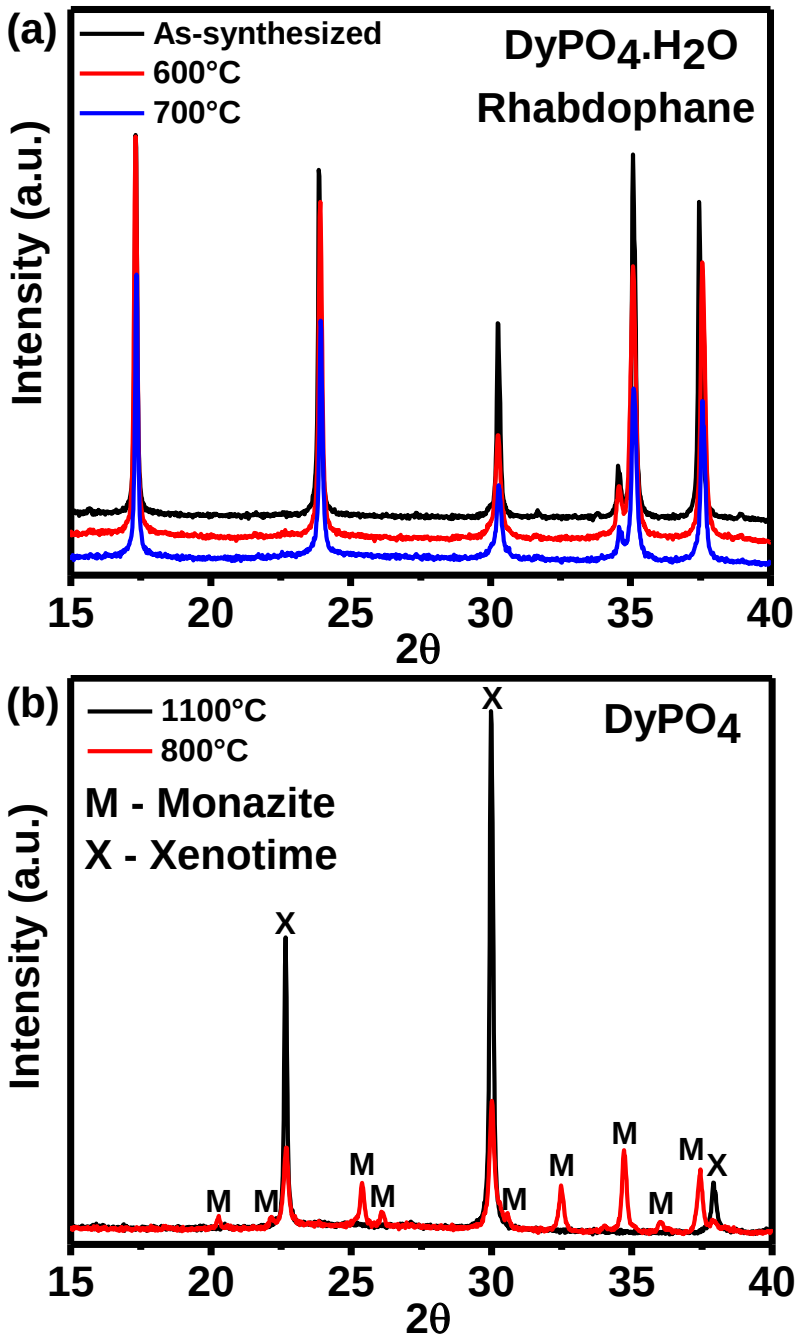

Figure 3.3 Powder XRD patterns from $DyPO_4.H_2O$ annealed to (a) 600 and 700°C and (b) 800 and 1100°C. The powder XRD pattern from the as-synthesized $DyPO_4.H_2O$ material is also presented in (a) for comparison. The labels "M" and "X" in (b) have been used to identify the peaks resulting from the monazite or xenotime structure.

compounds in the rhabdophane series (500°<T≤700°C), and was observed to increase with a decrease in the size of the rare-earth (RE = La, Sm, Gd, Dy) ions (See Figure 3.3b and Figure B.2 in Appendix B).

It has been reported that the structural transformation of $REPO_4.H_2O$ (rhabdophane-type) to $REPO_4$ (monazite- or/and xenotime-type) at high-temperature is accompanied by the formation of minor amounts of rare-earth polytrioxophosphate (REP_3O_9).[210,211] The as-synthesized precipitate may contain adsorbed H_3PO_4 that can react with $REPO_4.H_2O$ at higher temperatures to form REP_3O_9.[210,211] However, in the present study, the REP_3O_9 (RE = La, Nd, Sm, Gd, Dy) phase was not observed during the structural transformation of rhabdophane- to monazite- and/or xenotime-type structures. This is because the as-synthesized precipitates of $REPO_4.H_2O$ were washed with a large excess of water prior to annealing to remove any adsorbed phosphates.

The as-synthesized $YbPO_4.H_2O$ (and $YPO_4.H_2O$) materials were determined by analysis of powder XRD patterns to adopt the xenotime-type structure (Figure 3.4).[135] The xenotime-type structure crystallizes in a tetragonal unit cell which is of higher symmetry when compared to the monoclinic unit cell adopted by the rhabdophane structure.[126,135] The long-range structure of $YbPO_4.H_2O$ was studied as a function of temperature by collecting powder XRD patterns from $YbPO_4.H_2O$ annealed to 600°C and 1200°C (Figure 3.4). Upon heating to 600°C, the diffraction peaks become broader and shifted slightly to higher 2θ (See inset in Figure 3.4). These observations suggest a decrease in crystallinity as well as a contraction in the unit cell of the xenotime-type structure upon removal of water. Further heating to 1200°C results in an improvement in the crystallinity of the material as indicated by the presence of intense and narrow diffraction peaks (Figure 3.4). In contrast to the rhabdophane structure, the xenotime-type structure was stable at all annealing temperatures as indicated by the powder XRD patterns from

$YbPO_4.H_2O$ annealed at 600°C or 1200°C (Figure 3.4). The lattice constants of as-synthesized $YbPO_4.H_2O$ are presented in Table 3-3 along with the lattice constants from this material after annealing at 600°C or 1200°C. A slightly larger unit cell was observed for the as-synthesized material in comparison to the materials annealed to 600°C or 1200°C. These observations are consistent with an earlier report in which a similar contraction in the unit cell parameters of xenotime-type materials was observed after annealing $ErPO_4.H_2O$ (also prepared using a precipitation route) to 950°C.[208] These results indicate that the presence of water introduces changes in the xenotime crystal structure; however, more detailed studies on $YbPO_4.H_2O$ are required in order to explain how water affects the local and long-range structure.

3.3.2 XANES

The effect of annealing temperature on the long-range order of materials adopting the rhabdophane- and xenotime- type structures was discussed in Section 3.3.1 through the analysis of powder XRD data. It was shown that the powder XRD data of $DyPO_4.H_2O$ (rhabdophane-type) annealed to 700°C did not exhibit significant changes in the long-range order of the rhabdophane-type structure upon removal of water whereas distinct (although minor) changes in the powder XRD pattern of $YbPO_4.H_2O$ were observed with increasing annealing temperature. XANES spectra were collected from the $REPO_4.H_2O$ (RE = Sm, Gd, Dy, Yb) materials in order to determine how the local structures of these materials are affected by the loss of water. Temperature-induced changes in the local coordination environment of P and RE (RE = Sm, Gd, Dy, Yb) ions were probed by examination of P K-, P $L_{2,3}$-, and RE L_1- edge XANES spectra.

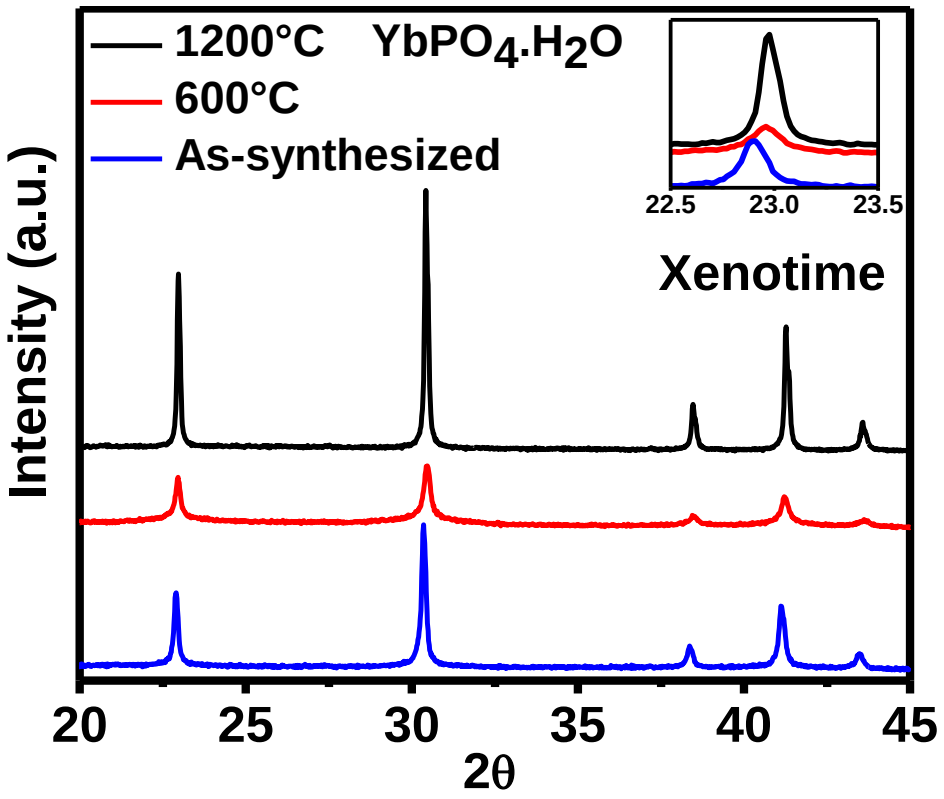

Figure 3.4 Powder XRD patterns of $YbPO_4.H_2O$ (xenotime-type structure) annealed to 600° and 1200°C along with the XRD pattern from the as-synthesized $YbPO_4.H_2O$ material.

Table 3-3 Lattice Constants from As-Synthesized and Annealed Xenotime-Type $YbPO_4.H_2O$

Sample	a (Å)	c (Å)
As-synthesized	6.8405 (4)	5.9927 (4)
Annealed at 600°C	6.8147 (8)	5.9785 (4)
Annealed at 1200°C	6.8162 (2)	5.9706 (2)

3.3.2.1 P K-edge XANES

The P K-edge XANES spectra from as-synthesized $Gd_{1-x}Dy_xPO_4.H_2O$ (x = 0, 0.2, 0.4, 0.8, 1; rhabdophane-type structure) are presented in Figure 3.5 and represent the dipole allowed excitation of P 1s electrons into unoccupied P 3p conduction states. The features that are observed in the near-edge region of P K-edge spectra reflect the distribution of P 3p conduction states in the rhabdophane structure while the high energy features in the spectra are likely a result of multiple scattering resonances. As mentioned in the Section 1.5.2, two different PO_4 tetrahedra exist in the rhabdophane structure meaning that the P K-edge spectra from these materials contain information about the local electronic structure of both P coordination environments. In other words, the P K-edge spectrum from materials adopting the rhabdophane-type structure is a weighted average of the individual spectra arising from two coordinatively distinct P ions. Minor changes in the spectral lineshape were observed as indicated by the loss of fine structure and increase in width of the main-edge region with increasing Dy concentration (Figure 3.5). This change can be explained by examination of the crystal structure of rhabdophane (Figure 1a). In rhabdophane, the REO_n (n = 8 or 9) polyhedra in chains Ch1 and Ch2 are connected to each other via an alternating PO_4 tetrahedra.[126] With increasing substitution of Dy^{3+} for Gd^{3+} in $Gd_{1-x}Dy_xPO_4$, the RE-O bond lengths decreases due to the smaller ionic radii of Dy^{3+} ($r^{[VIII]}$ = 1.027 Å; $r^{[IX]}$ = 1.083 Å) ions when compared to Gd^{3+} ($r^{[VIII]}$ = 1.053 Å; $r^{[IX]}$ = 1.107 Å) ions.[209] Therefore, the local structure of RE ion changes with increasing Dy concentration which in turn induces a slight modification in the local structure of P ions in the neighboring PO_4 tetrahedra. In the rhabdophane structure, the PO_4 tetrahedra are highly distorted due to the significant deviation of the individual O-P-O bond angles from the ideal tetrahedral angle and it is proposed here that the local symmetry around the P ion is further reduced, albeit

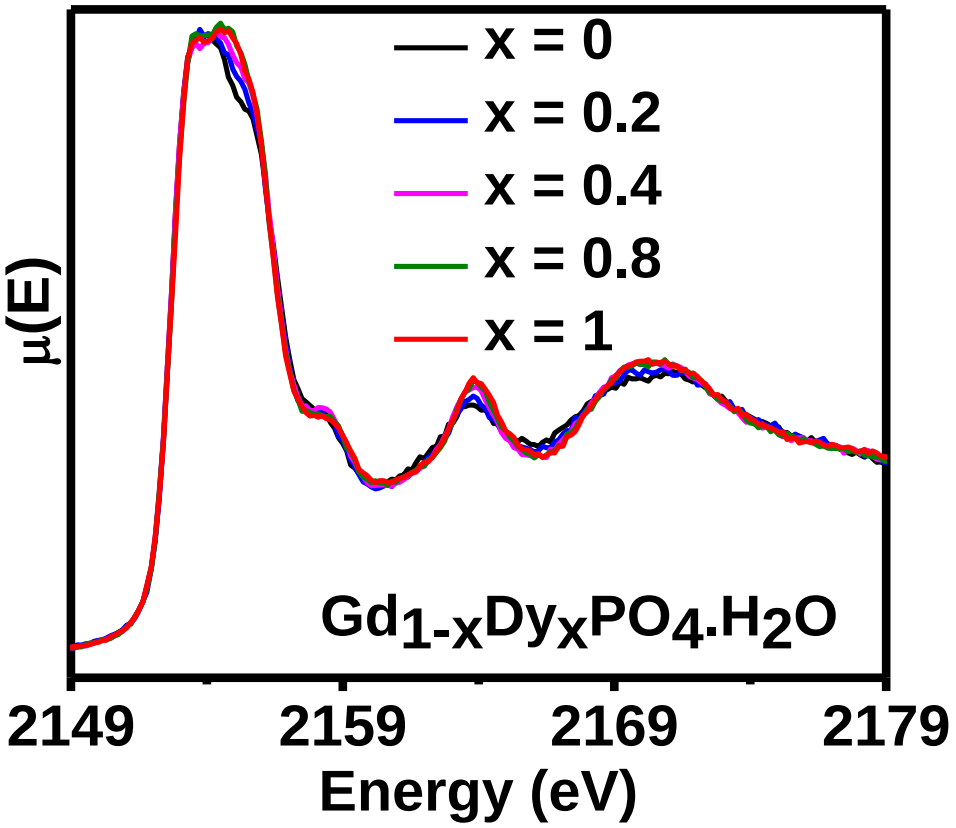

Figure 3.5 P K-edge XANES spectra from the as-synthesized $Gd_{1-x}Dy_xPO_4.H_2O$ (x = 0.0, 0.2, 0.4, 0.8, and 1.0) materials.

minor, upon substitution of Dy^{3+} for Gd^{3+} in $Gd_{1-x}Dy_xPO_4$ thereby broadening the distribution of P 3p conduction states.[126] It was shown in Chapter 2 that the differences in spectral lineshape observed between the P K-edge spectra of $LaPO_4$ (monazite-type) and $YbPO_4$ (xenotime-type) are a result of change in the distribution of P 3p conduction states induced by the differences in the local structure around P ions between these two structures. Therefore, the differences in the spectral lineshape observed between the members of the as-synthesized $Gd_{1-x}Dy_xPO_4.H_2O$ series with increasing Dy^{3+} substitution (Figure 3.5) are due to an increase in the broadness of P 3p conduction states incurred by slight changes in the local environment of P ions.

P K-edge XANES spectra were also collected from $REPO_4.H_2O$ (RE = Gd, Dy) materials annealed to 600°C to investigate how the local structure around P in the rhabdophane structure was affected by the removal of water (Figures 3.6a and 3.6b). Minor differences in the P K-edge intensity were observed between the as-synthesized materials and the materials annealed at 600°C which suggests a minor change in the local structure around the P ions as a result of the removal of water (Figures 3.6a and 3.6b). This change can be explained by examination of the rhabdophane crystal structure (Figure 1.4). In the rhabdophane structure, the RE ions in Ch1 are coordinated to nine O ions, with eight O ions provided by the PO_4 groups and the additional O ion (colored blue in Figure 1.4) being provided by water. The REO_9 polyhedra are connected to each other via PO_4 tetrahedra (Figure 1.4). The removal of water from the REO_9 polyhedra may lead to a minor rearrangement of the remaining eight O ions surrounding the RE ion, and, as a consequence, the local structure of P ions in the adjoining PO_4 tetrahedra changes. In terms of the electronic structure of P ion, the distribution of P 3p conduction states is expected to change upon removal of water from the rhabdophane structure and as a result, the P K-edge spectral lineshape of the material annealed at 600°C differs slightly from those of the as-synthesized material

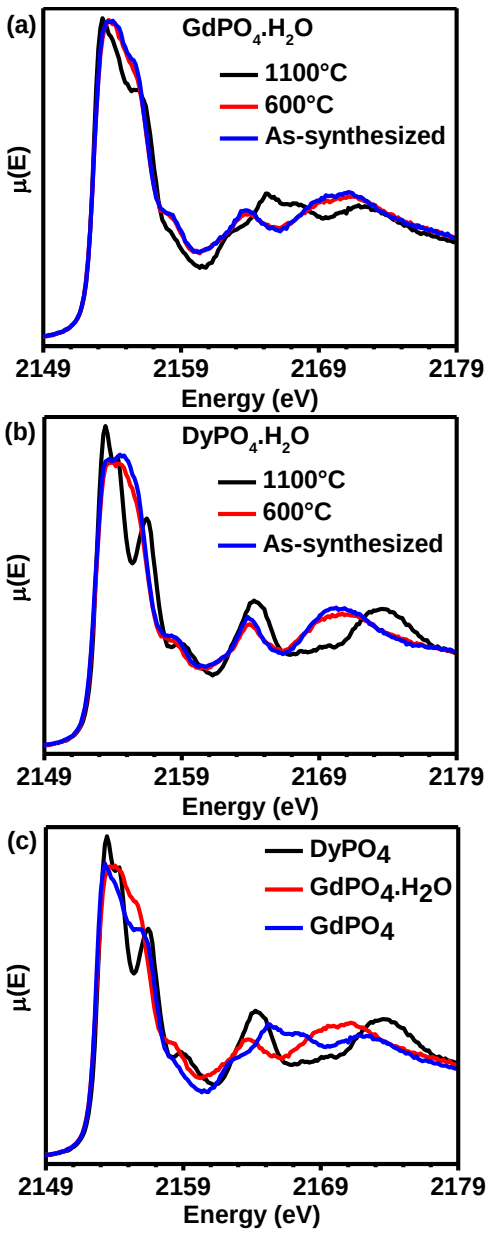

Figure 3.6 P K-edge XANES spectra from the $GdPO_4.H_2O$ material annealed at 600 and 1100°C are shown in (a) along with the spectrum from the as-synthesized material. The P K-edge XANES spectra from $DyPO_4.H_2O$ material annealed at 600 and 1100°C are shown in (b) along with the spectrum from the as-synthesized material. A comparison between the P K-edge XANES spectra from $GdPO_4$ (monazite-type), $GdPO_4.H_2O$ (rhabdophane-type), and $DyPO_4$ (xenotime-type) materials are shown in (c).

(Figure 3.6a and 3.6b). It was also reported previously that the P K- and P $L_{2,3}$-edge XANES spectra from ion-implanted $REPO_4$ (RE = La, Yb) materials exhibited a loss of both intensity and fine-structure when compared to the spectrum from as-synthesized $REPO_4$ (RE = La, Yb) materials owing to a distortion of the PO_4 tetrahedra. Likewise, the minor differences in lineshape observed in Figures 3.6a and 3.6b between the as-synthesized material and the material annealed at 600°C indicates a minimal change in the local symmetry of PO_4 tetrahedra upon removal of water from the rhabdophane structure. The P K-edge XANES spectra show changes in the local structure upon removal of water that were not observable by analysis of powder XRD data. When the $GdPO_4.H_2O$ and $DyPO_4.H_2O$ materials were annealed further to 1100°C, the P K-edge XANES spectra exhibited a significant change in lineshape when compared to the spectra from the as-synthesized materials and the materials annealed at 600°C. This large difference is due to the structural transformation of these materials to the monazite- ($GdPO_4$) or xenotime- ($DyPO_4$) type structure as a result of high-temperature annealing, and is in agreement with the powder XRD results presented in Section 3.3.1.

The local structural relationship between the rhabdophane-, monazite-, and xenotime-type structure were studied by comparing the P K-edge XANES spectra from the following materials: $GdPO_4.H_2O$ (rhabdophane-type), $GdPO_4$ (monazite-type), and $DyPO_4$ (xenotime-type) (Figure 3.6c). Significant variations in the P K-edge spectral lineshapes were observed and are due to a change in the distribution of P 3p conduction states in each of the three structures (Figure 3.6c). Focusing on the region in the energy range of 2151-2157 eV, the P K-edge spectrum from $GdPO_4.H_2O$ does not contain fine structure (see Figure 3.6c) when compared to the spectra from $GdPO_4$ and $DyPO_4$. This is because the rhabdophane structure contains highly distorted PO_4 tetrahedra, resulting in non-degenerate P 3p conduction states. In the rhabdophane structure, the

individual O-P-O bond angles in the PO_4 tetrahedra ranges from ~ 91.7° to 121.6° thereby indicating a significant deviation from the ideal tetrahedral angle (109.5°).[126] However, minor fine structure can be observed in the P K-edge spectra of $GdPO_4$ (Figure 3.6c) and indicates an increase in the number of degenerate P 3p conduction states in materials adopting the monazite structure. Although the PO_4 tetrahedra in the monazite structure is also distorted (unequal P-O bond distances and O-P-O bond angles), the magnitude of distortion in the PO_4 tetrahedra is less when compared to the rhabdophane structure due to the narrower range of O-P-O bond angles (~103.9° - 112.4°) in the monazite structure.[135] In comparison to P K-edge spectrum from $GdPO_4$ adopting the monazite-type structure, the P K-edge spectrum from $DyPO_4$ (xenotime-type) contained a more pronounced fine structure (see Figure 3.6c) which is due to the presence of a more symmetric PO_4 tetrahedra (similar P-O bond distances and two distinct O-P-O bond angles) that result in an increase in the number of degenerate P 3p conduction states available for 1s electrons to be excited to.[135] It should be noted that in the xenotime-type structure, the individual O-P-O bond angles in PO_4 tetrahedra are ~102.9° and ~112.9°.[135] Based on these observations, the changes in the spectral lineshape of the monazite-, rhabdophane-, and xenotime- type structures are observed to be a result of a change in the distribution of P 3p conduction states with the degree of PO_4 distortion that leads to these changes being arranged in the following order: rhabdophane (most distorted PO_4 tetrahedra) < monazite < xenotime (least distorted PO_4 tetrahedra).

The effect of annealing temperature on the local structure of P in $YbPO_4.H_2O$ (xenotime-type structure) was studied by collecting P K-edge XANES spectra from $YbPO_4.H_2O$ before and after annealing (Figure 3.7). The P K-edge spectrum from the as-synthesized material has a lower intensity and less pronounced fine structure than the spectrum obtained from the material

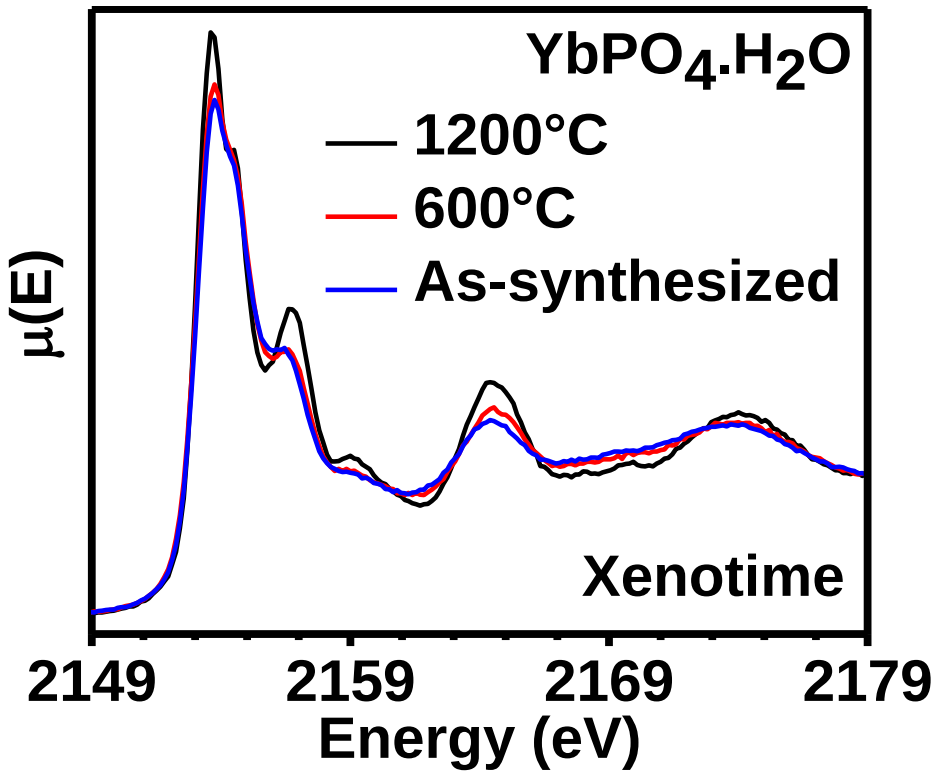

Figure 3.7 P K-edge XANES spectra from $YbPO_4.H_2O$ annealed to 600 and 1200°C along with the spectrum from the as-synthesized material.

annealed at 1200°C (Figure 3.7). It is proposed here that the presence of water in the as-synthesized $YbPO_4.H_2O$ (xenotime-type structure) introduces some local disorder around P resulting in distorted PO_4 tetrahedra leading to less pronounced fine structure in the near-edge region of the P K-edge spectrum from the as-synthesized material. Similarly, it was reported that the infrared (IR) spectrum of $ErPO_4.H_2O$ (xenotime-type structure) contained additional frequency bands that were attributed to a reduction in the site-symmetry of the PO_4 tetrahedra caused by the interaction of water with the PO_4 tetrahedra.[208] The TGA data from $YbPO_4.H_2O$ showed that water was removed after heating the material to ~700°C (Figure B.1b in Appendix B). Relative to the as-synthesized material, the P K-edge spectra from the material annealed at 600°C exhibited only a minor increase in intensity (Figure 3.7). The lack of a more pronounced fine structure in the P K-edge spectrum from the material annealed at 600°C indicates that the PO_4 tetrahedra in this material are not fully ordered (Figure 3.7). However, the P K-edge XANES spectrum from this material after being annealed at 1200°C has a higher intensity and greater fine-structure when compared to the spectra from the as-synthesized material and the material annealed at 600°C (Figure 3.7). This observation is due to a local structural transformation from distorted PO_4 tetrahedra to a more ordered PO_4 tetrahedra at higher annealing temperatures. The presence of ordered PO_4 tetrahedra leads to an increase in the number of degenerate P 3p states available for 1s electrons to be excited to, which results in the spectrum from the material annealed at 1200°C being structurally rich.

3.3.2.2 P $L_{2,3}$-edge XANES

It was shown in Section 3.3.2.1 that P K-edge XANES spectra are sensitive to temperature-induced changes in the local structure of P in materials adopting the rhabdophane- and xenotime-type structures; however, only slight changes in the lineshape of the P K-edge XANES spectra

were observed for the $REPO_4.H_2O$ (RE = Gd, Dy, Yb) materials annealed at 600°C compared to the spectra from the as-synthesized materials. P $L_{2,3}$-edge spectra, which are of higher resolution when compared to P K-edge spectra, were collected from materials adopting the rhabdophane-($DyPO_4.H_2O$) type structure to determine if there is a significant change in the P $L_{2,3}$-edge spectral lineshape of $REPO_4.H_2O$ (RE = Gd, Dy, Yb) materials annealed at 600°C (Figure 3.8). The P $L_{2,3}$-edge spectra from $DyPO_4.H_2O$ annealed at different temperatures are shown in Figure 3.8 along with the spectrum from the as-synthesized material. The P $L_{2,3}$-edge spectra represent the excitation of electrons from the 2p states into unoccupied 3s and 3d states and the different features that appear in this spectra were attributed to transitions involving the overlapped P 3s and 3d conduction states. The spectrum from the material annealed at 600°C is slightly broader when compared to the spectrum from the as-synthesized material confirming that the change that occurs in the local P environment upon annealing $DyPO_4.H_2O$ to 600°C is minor (Figure 3.8). Upon heating to 800°C, significant changes in the spectral lineshape were observed due to the structural transformation of rhabdophane to a mixture of monazite and xenotime (Figure 3.8). Similarly, the P $L_{2,3}$-edge spectra from the material annealed at 1100°C has a unique lineshape with greater fine-structure due to the transformation to a single phase xenotime-type structure containing a more symmetric PO_4 tetrahedra (Figure 3.8). It has been shown previously using partial density of states (DOS) calculations that the xenotime-type structure contains degenerate P 3s and 3d conduction states resulting in a greater fine structure being observed in the P $L_{2,3}$-edge spectrum.

3.3.2.3 RE L_3-edge XANES

The local structure of the RE (RE = Sm, Gd, Dy) ions in materials adopting the rhabdophane-type structure were studied as a function of temperature by studying the RE L_3-edge XANES spectra.

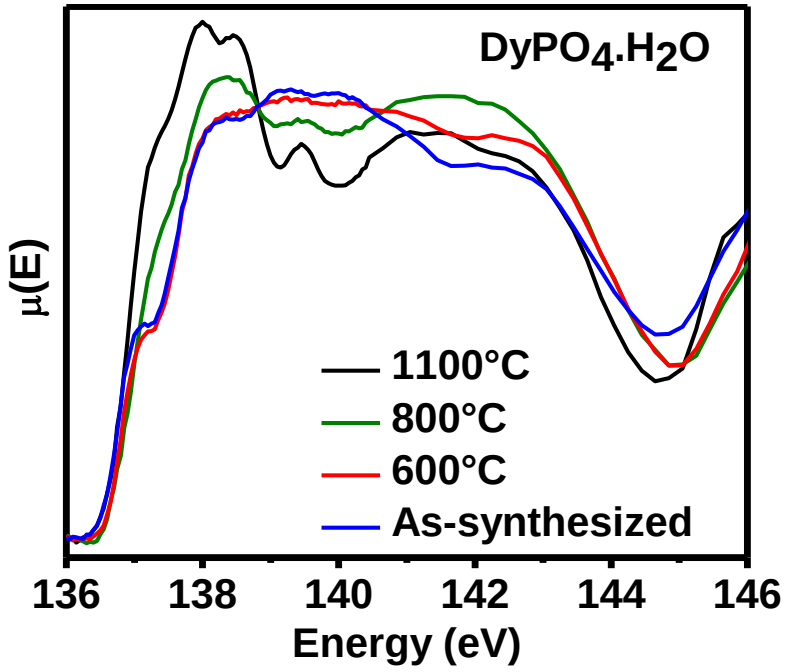

Figure 3.8 P $L_{2,3}$-edge XANES spectra from $DyPO_4.H_2O$ annealed to 600°C, 800°C, and 1100°C along with the spectrum from the as-synthesized material.

The Sm L_3-edge XANES spectra from $SmPO_4.H_2O$ annealed to 600°C and 1100°C are shown in Figure 3.9 along with the spectra from the as-synthesized material. The white line peak in the Sm L_3-edge XANES spectra corresponds to a $2p_{3/2} \rightarrow 5d$ transition.[212,213] The Sm L_3-edge XANES spectra of the material annealed at 600°C has a slightly lower intensity compared to the spectra from the as-synthesized material that may suggest a change in the local structure of Sm brought about by the removal of water (Figure 3.9). Similarly, only minor changes in lineshape were observed in the Sm L_3-edge spectra of the material annealed at 1100°C despite the structural transformation from rhabdophane (as-synthesized; 600°C) to monazite at 1100°C (Figure 3.9). Similar results were obtained from the Gd and Dy L_3-edge XANES spectra from $(Gd,Dy)PO_4.H_2O$ (Figures B.3a and B.3b in Appendix B). The observation of only minor changes in the RE L_3-edge spectra with increasing annealing temperature may suggest that these spectra are not sensitive enough to detect changes in the local structure of the RE ions in these materials.

3.3.2.4 RE L_1-edge XANES

It was suggested in Section 3.3.2.3 that the RE L_3-edge XANES spectra from the $REPO_4.H_2O$ (rhabdophane-type structure) materials were not sensitive enough to detect changes in the local structure of the RE ions. The RE L_1-edge XANES spectra, on the other hand, have been determined to be sensitive to changes in the local configuration of RE ions.[212,214,215] Sm L_1-edge spectra were collected from Sm_2O_3 and as-synthesized $SmPO_4.H_2O$ (rhabdophane-type) to determine if the Sm L_1-edge spectra can distinguish between the different coordination environments of Sm ions (Figure 3.10a). The Sm_2O_3 used in this study predominantly adopts the B-type monoclinic structure (C2/*c*) along with very minor amounts of C-type cubic structure.[216] The Sm L_1-edge spectra are characterized by main- and pre-edge peaks that result from dipole

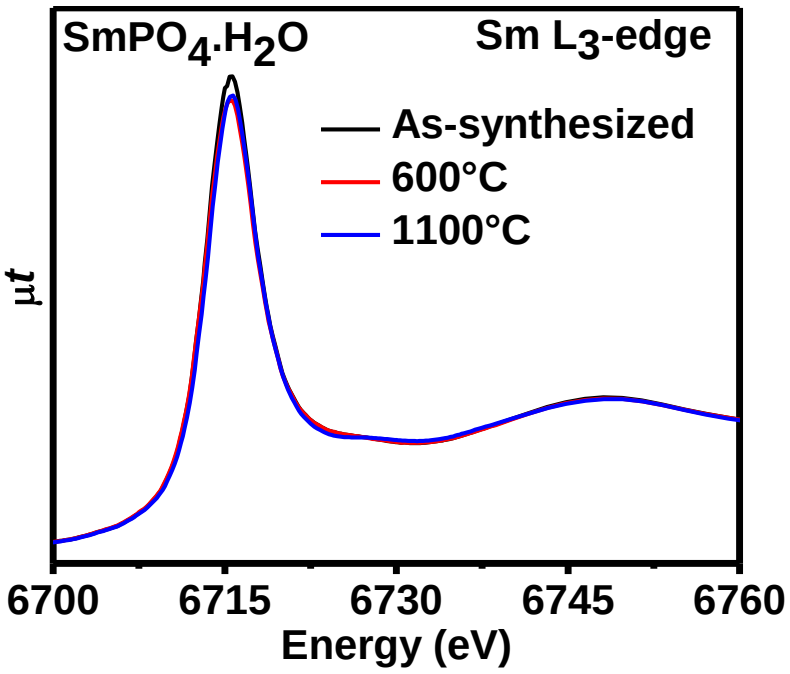

Figure 3.9 Sm L_3-edge XANES spectra from $SmPO_4.H_2O$ annealed to 600 and 1100°C along with the spectrum from the as-synthesized material.

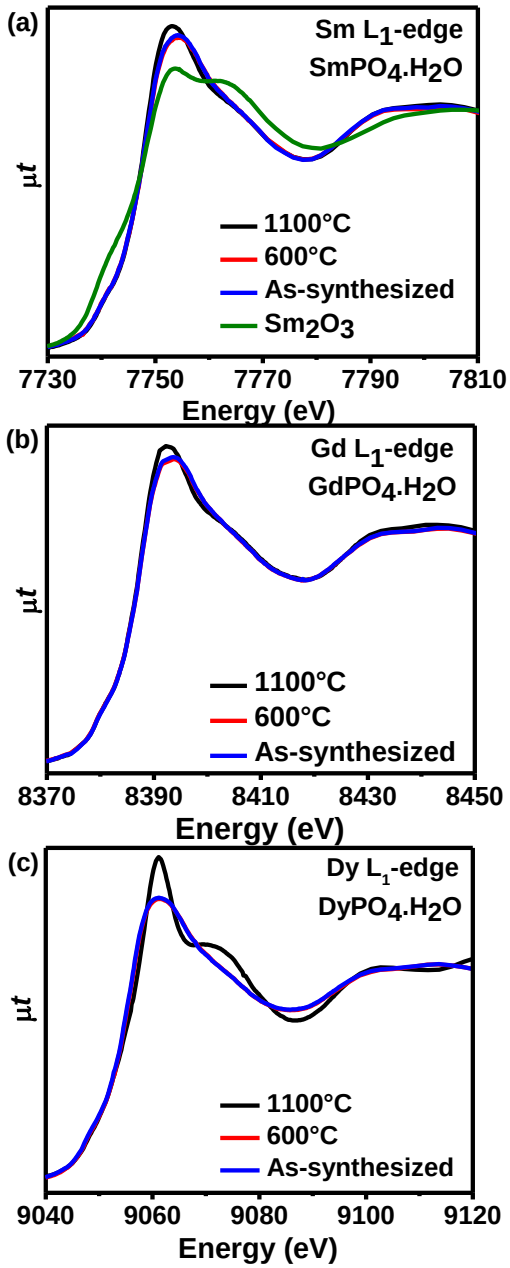

Figure 3.10 Sm L_1-edge XANES spectra from $SmPO_4.H_2O$ annealed to 600 and 1100°C are shown in (a) along with the spectrum from Sm_2O_3 and the as-synthesized material. The Gd L_1-edge XANES spectra from $GdPO_4.H_2O$ annealed to 600 and 1100°C are shown in (b) along with the spectrum from as-synthesized material. The Dy L_1-edge XANES spectra from $DyPO_4.H_2O$ annealed to 600 and 1100°C are shown in (c) along with the spectrum from the as-synthesized material.

allowed 2s → 6p transitions and 2s → 6p-5d transitions, respectively (Figure 3.10a). The pre-edge peak arises as a result of the overlap of Sm 6p and 5d states which is in turn made possible due to the presence of distorted SmO_n (n = 6 - 9) polyhedra in Sm_2O_3 and $SmPO_4.H_2O$.[160,161] It should be noted that the pre-edge feature in Sm_2O_3 is more intense when compared to $SmPO_4.H_2O$ and thereby reflects the greater extent of overlap between the Sm 6p and 5d states in Sm_2O_3. Overall, the Sm L_1-edge spectrum from Sm_2O_3 (coordination number = 6 & 7) exhibited a unique lineshape in comparison to the spectrum from $SmPO_4.H_2O$ (coordination number = 8 & 9) which confirms that these spectra are sensitive to changes in the coordination environment of RE ions.

The RE (RE = Sm, Gd, Dy) L_1-edge XANES spectra were collected from $REPO_4.H_2O$ (RE = Sm, Gd, Dy) to analyze the changes in the local structure of the RE ion with increasing annealing temperature (Figure 3.10). Minor differences in the RE L_1-edge spectral lineshape were observed between the as-synthesized materials and the materials annealed at 600°C (Figure 3.10). This observation indicates that the local structure of the RE (RE = Sm, Gd, Dy) ions is only slightly affected by the removal of water from the rhabdophane-type structure. At 1100°C, the rhabdophane-type structure transforms to the monazite- ($SmPO_4$, $GdPO_4$) or xenotime- ($DyPO_4$) type structure and is accompanied by a significant change in the RE L_1-edge spectral lineshape (Figure 3.10). In comparison to the spectra from as-synthesized $REPO_4.H_2O$ (RE = Sm, Gd), the RE L_1-edge spectra from $REPO_4$ (RE = Sm, Gd; monazite-type structure) exhibited greater fine structure suggesting a greater number of degenerate RE 6p conduction states in materials adopting the monazite structure compared to the rhabdophane-type structure (Figures 3.10a and 3.10b). This change in lineshape could be explained by analysis of crystal structures of rhabdophane and monazite. The rhabdophane structure contains six distinct RE ions and the

corresponding REO_n (n = 8 or 9) polyhedra formed by each of these RE ions having unique RE-O bond distances.[126] In contrast, the monazite-type structure only has one distinct REO_9 polyhedra; however, the 9 RE-O bond lengths are different from each other.[135] It is proposed here that the REO_9 polyhedra in the monazite-type structure are less distorted than the REO_n (n = 8 or 9) polyhedra in the rhabdophane-type structure, resulting in a greater number of degenerate RE 6p conduction states in materials that adopt the monazite-type structure.

The Dy L_1-edge spectrum from $DyPO_4$ is structurally rich as indicated by the appearance of a much more pronounced fine-structure when compared to the spectrum from $SmPO_4$ or $GdPO_4$ (cf. Figure 3.10). This observation can be explained by comparing the monazite and xenotime crystal structures (Figures 1.3a and 1.3b). In the xenotime structure, the RE ions are coordinated to 8 O atoms and the resulting REO_8 polyhedra are symmetrical (2 distinct RE-O bond distances) when compared to the REO_9 polyhedra present in the monazite structure (Figures 1.3a and 1.3b). As a result, the degeneracy of the RE 6p conduction states in the xenotime structure increases resulting in distinct fine-structure being observed in the Dy L_1-edge spectrum from $DyPO_4$ (Figure 3.10c). From this study, the degeneracy of RE 6p conduction states can be arranged in the following order: rhabdophane (most distorted REO_n [n = 8 or 9] polyhedra) < monazite < xenotime (least distorted REO_8 polyhedra).

Yb L_1-edge XANES spectra were collected from $YbPO_4.H_2O$ (xenotime-type) to examine how the annealing temperature influences the local structure of Yb (Figure 3.11). The Yb L_1-edge spectrum from the as-synthesized material has a slightly lower main-edge intensity compared to the spectrum from the materials annealed at 600°C and 1200°C (Figure 3.11). This observation indicates a slight distortion of the Yb coordination environment in the as-synthesized material caused by the presence of water. Upon annealing the as-synthesized material to 600°C and

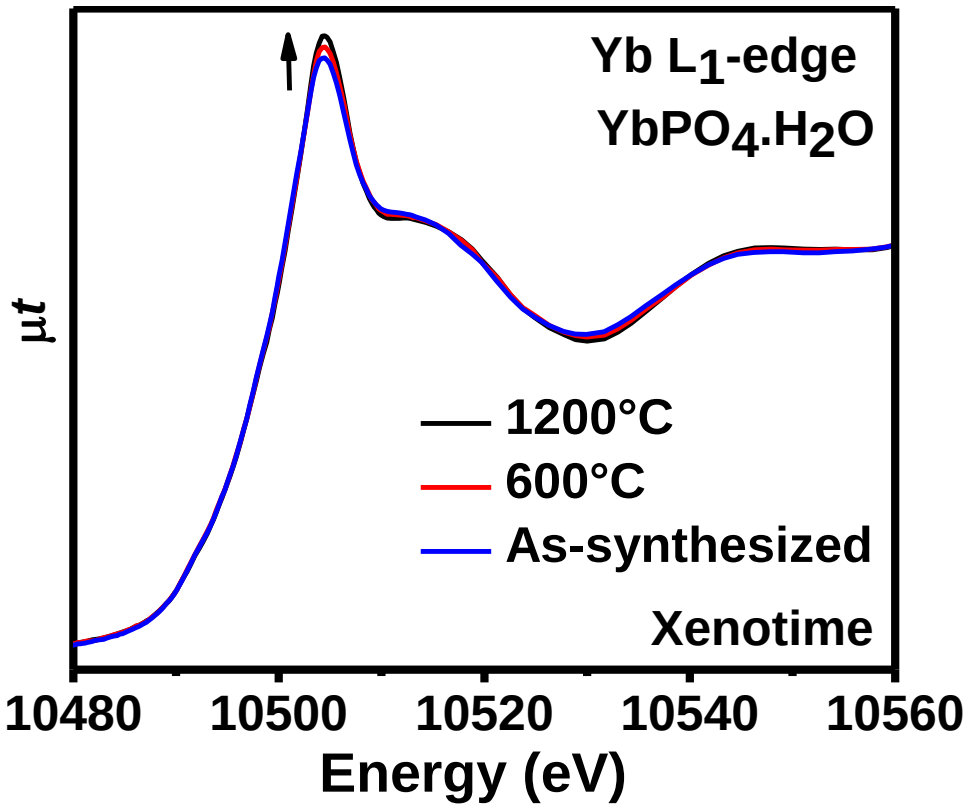

Figure 3.11 Yb L_1-edge XANES spectra from $YbPO_4.H_2O$ annealed to 600 and 1200°C along with the spectrum from the as-synthesized material. The arrow indicates an increase in the Yb L_1 main-edge intensity with increasing annealing temperature.

1200°C, a slight increase in the main-edge intensity (~10502 eV) was observed that indicates an ordering of the local environment around the Yb^{3+} ion created by the combined effects of high temperature annealing as well as the removal of water (Figure 3.11).

3.4. Conclusion

This study has provided detailed insights into the long-range and local structures of rare-earth phosphates adopting multiple structures. Examination of powder XRD data from rhabdophane-type $DyPO_4.H_2O$ has confirmed that this material adopts the monoclinic crystal system. Temperature-induced structural variations of the rhabdophane- and xenotime- type structure were also studied using TGA, powder XRD, and XANES. Powder XRD results have shown that the anhydrous rhabdophane structure can only be stabilized over a limited temperature range (e.g., 700°C<T<800°C) whereas the xenotime-type structure was stable at all temperatures studied despite the removal of water. The local structural changes that occur upon removal of water from the rhabdophane- and xenotime- type structures were studied by collection of P K-, P $L_{2,3}$-, RE L_1-, and L_3-edge XANES spectra. The XANES studies have shown that the local symmetry of the PO_4 tetrahedra and RE-O polyhedra in $REPO_4.H_2O$ materials are modified by the removal of water. The relationship between the three rare-earth phosphates structures (rhabdophane-, monazite-, and xenotime-type structures) was also established in this study. This study, for the first time, has shown how the local structure of $REPO_4.H_2O$ varies as a function of temperature and composition which will therefore aid in the optimization of these materials for photonics, biolabeling, catalytic, and nuclear wasteform applications.

Chapter 4

PROBING THE EFFECT OF RADIATION DAMAGE ON THE STRUCTURE OF RARE-EARTH PHOSPHATES[3]

4.1 Introduction

Chapters 2 and 3 of this thesis provided a fundamental understanding of the crystal and electronic structures of anhydrous and hydrous rare-earth phosphate materials. The work presented in Chapter 3 has shown that the hydrous rare-earth phosphates adopting the rhabdophane structure are metastable as revealed by their structural transformation at higher temperatures. In order for a crystalline material to be initially considered for nuclear wasteform applications, the material of interest must be structurally stable at higher temperatures. This is because actinide incorporated nuclear wasteforms will be exposed to high temperatures caused due to actinide decay and storage of wasteforms in geological repositories. The metastable nature of rhabdophane-type

[3] Reprinted in part from Journal of Alloys and Compounds, 653, M. R. Rafiuddin, A. P. Grosvenor "Probing the effect of radiation damage on the structure of rare-earth phosphates", 279 – 289, 2015, with permission from Elsevier.

materials makes them unsuitable for nuclear wasteform applications; however, as has been shown in Chapters 2 and 3, the anhydrous rare-earth phosphates adopting the monazite- or xenotime-type structures are stable at higher temperatures. Another criterion that must be considered when developing materials as nuclear wasteforms is their resistance to potential structural damage events caused by the radioactive decay of incorporated actinides. This chapter addresses this criterion by determining the structural response of monazite- and xenotime-type rare-earth phosphates to simulated radiation conditions.

Single- and multi-phase crystalline ceramics that are resistant to radiation damage have been proposed as candidate materials for encapsulating radioactive waste.[61,217,218] In this regard, monazite and xenotime are considered as host-matrices for nuclear waste because of the ability of these structures to contain actinide elements.[89,121] The crystal structures of the monazite- and xenotime-type rare-earth phosphates are presented in Figures 1.3a and 1.3b and a detailed discussion of these structure types was provided in Section 1.5.1. An actinide element incorporated in a crystalline ceramic can undergo a radioactive decay process during which it may (depending upon the decay process) transform into a new radionuclide by releasing a high-energy α-particle.[78] Because of this decay, the crystalline host matrix could experience structural damage either from the recoil energy associated with the daughter product (recoil atom) radionuclide and/or from the highly energetic α-particle.[78] Therefore, an issue surrounding actinide containing crystalline ceramics is the tendency of these materials to undergo a radiation-induced crystalline to amorphous transition in a process called metamiction.[107] A description of the radiation damage process in nuclear wasteforms and its consequences was provided in Section 1.4.

Numerous investigations on the structural stability of natural as well as synthetic monazite samples are reported in the literature.[89,104,106,120,122,123,219] The structural stability of synthetic monazite samples have been studied either by doping monazite ceramics with actinides (internal irradiation) or by simulating the long-term actinide storage by implantation of the material using high-energy ion beams (external irradiation).[89,104,107,124,125,223] Since many actinides have a very long half-life, the structural stability of a crystalline wasteform is most often determined by ion-implantation.[106] Heavy ions (such as Au^-, Kr^+, and Ar^+) are generally used to simulate the effects of the daughter product on the crystal structure of a proposed wasteform.[89,93,123,162] In an early study on the radiation resistance of the monazite structure, Karioris et al. showed the monazite structure to be unstable towards heavy ion-implantation; however, they also showed that the damaged monazite structure could be converted back to its original crystalline state after annealing the irradiated material to ~296°C for 20 hours.[122] In another study, Meldrum et al. experimentally determined the critical amorphization temperature (T_c; i.e., the temperature above which the material does not undergo metamiction) of a variety of ion-implanted ternary monazite- and xenotime-type orthophosphates and found the monazite structure to have a lower T_c than the xenotime structure.[89] This observation could suggest that the monazite structure is more resistant to radiation damage than the xenotime structure.[89] In a more recent study, Deschanels et al. performed thermal annealing experiments on Au^- ion-implanted monazite ceramics and studied them using transmission electron microscopy (TEM).[106] It was shown in this study that complete recrystallization of metamict monazite occurred after annealing the material to 300°C for 1 hour.[106] In addition to observing annealing-induced recrystallization, Deschanels et al. also observed the recrystallization of amorphous regions in damaged monazite samples under the influence of an electron beam.[106] A theoretical study of the radiation resistance of xenotime (YPO_4) by Urusov et al. shed light on the ability of recoil atoms to bring about a

cascade of atomic displacements in this structure.[220] Immediately after the creation of a cascade of atomic displacements, some of the displaced atoms returned to their original crystallographic positions which led to the partial recovery of the xenotime structure.[220]

The design of new crystalline wasteforms that are resistant to radiation damage requires a detailed understanding of the electronic structure of a material before and after exposure to radiation. In this context, the electronic structure was studied using X-ray absorption near-edge spectroscopy (XANES) as it provides information on the local coordination environment, oxidation state, and bonding environment of the absorbing atom.[221] In Chapter 2, the electronic structure of $La_{1-x}Yb_xPO_4$, $La_{1-x}Y_xPO_4$, and $Sm_{1-x}Ho_xPO_4$ were studied using XANES. It was shown in this study that the P K-edge XANES spectra provide a spectroscopic fingerprint for the monazite and xenotime structures because of the distinct change in spectral lineshape and absorption energy observed between the two structures.

The effect of Au^- ion-implantation on the structure of $La_{1-x}Yb_xPO_4$ is discussed in this chapter. The La and Yb end-members crystallize in either the monoclinic monazite (x = 0) or tetragonal xenotime (x = 1) structure, respectively. At all other values of 'x', a mixture of both monazite and xenotime phases exist, which allows for an investigation of co-mineralized samples. The Au^- ions used in the study were implanted in the near-surface region of these materials which required the use of surface-sensitive glancing angle XANES (GA-XANES) and micro X-ray diffraction (μ-XRD) to investigate the effect of ion-implantation on the local and long range structure of these materials. The extent of structural damage in $La_{1-x}Yb_xPO_4$ was studied as a function of depth by varying the X-ray angle of incidence during the GA-XANES experiments. This study has allowed for a detailed comparison of the response of the monazite and xenotime structure to ion-implantation. Although GA-XANES has been utilized in

determining the structural stability of metal oxides (zirconolites and pyrochlores), no studies exist in the literature on the use of this technique to the investigation of the structural stability of rare-earth phosphates.[162,222]

4.2 Experimental Section

4.2.1 Synthesis and Powder XRD

Rare-earth phosphates having the composition $La_{1-x}Yb_xPO_4$ (x = 0.0, 0.3, 0.7, 1.0) were synthesized by conventional solid state methods. Stoichiometric amounts of La_2O_3 (Alfa Aesar; 99.99%), Yb_2O_3 (Alfa Aesar; 99.99%), and $NH_4H_2PO_4$ (Alfa Aesar; 99.995%) were ground and mixed using a mortar and pestle before placing the mixture in an alumina crucible. The crucible containing the mixture was initially heated to 900 °C in air for 1 day to promote the decomposition of $NH_4H_2PO_4$ followed by quench cooling in air. The resulting mixture was ground, pressed into a pellet at a pressure of 6 MPa, and fired at 1100-1200 °C in air for 9 days before being quench cooled in air. The synthesis of $La_{1-x}Yb_xPO_4$ materials were carried out at 1100°C for the x = 0 material and 1200°C for all other materials (x = 0.3, 0.7, 1.0). All samples were ground and repelleted every 3 days of heating to ensure the homogeneity of the samples. The hardness of the materials was improved by pressing the materials into pellets at 8 MPa followed by annealing at 1100-1200 °C in air for 3-4 days prior to Au^- ion implantation. The phase purity of the synthesized materials was determined by powder X-ray diffraction using a PANalytical Empyrean system and a Cu $K\alpha_{1,2}$ X-ray source. The powder XRD patterns of the $La_{1-x}Yb_xPO_4$ compounds were collected at room temperature in the 2θ range of 10-80° using a step size of 0.017°. The lattice parameters and the percent composition of these materials were

determined using the HighScore Plus software program.[178] The sample plate was continuously rotated to avoid preferential orientation effects during data collection.

4.2.2 Ion Beam Implantation

Ion beam implantation experiments were carried out using the 1.7 MeV high-current Tandetron accelerator located at Interface Science Western (ISW), the University of Western Ontario. $La_{1-x}Yb_xPO_4$ (x = 0.0, 0.3, 0.7, 1.0) pellets were implanted with 2 MeV Au^- ions to a dose of $1x10^{14}$, $5x10^{14}$, or $1x10^{15}$ ions/cm^2 in order to simulate structural damage resulting from the decay of radioactive elements. The surface of the pellets was aligned normal to the incident Au^- ion beam for ion implantation. The ion-implanted $La_{1-x}Yb_xPO_4$ samples were also annealed at temperatures lower than the synthesis temperature to examine if the structure of the material was able to recover. The annealing experiments were performed by heating the ion-implanted $La_{1-x}Yb_xPO_4$ materials to 300°C or 900°C in air for 3 days.

The ion beam implantation depth profiles of $La_{1-x}Yb_xPO_4$, and the corresponding number of vacancies generated per nanometer by the Au^- ions, were calculated using the Stopping and Range of Ions in Matter (SRIM-2013) software package.[223] The calculations were performed using a total of 5000 Au^- ions and the displacement energies of the target atoms La, Yb, and P were assumed to be 25 eV and the displacement energy of O was assumed to be 28 eV.[223] The real values of the displacement energies for the target atoms (La, Yb, P, and O) are unknown so the default displacement energy values from the SRIM software program were used during the calculations.[223,224] The densities of $La_{1-x}Yb_xPO_4$ (x = 0.0, 0.3, 0.7, 1.0) that were used in these calculations were: 4.93 g/cm^3, 5.87 g/cm^3, 6.20 g/cm^3, and 6.45 g/cm^3, respectively.[225,226] These calculations have shown that the ions implant to a depth ranging between 50 and 450 nm with the maximum number of implanted Au^- ions being observed at ~275 nm (see Figure 4.1 and Figure

C.1 in Appendix C). The maximum number of vacancies produced in the materials because of implantation by high-energy Au^- ions is observed at a depth of ~200 nm below the surface (see Figure 4.1 and Figure C.1 in supporting information).

The electronic and nuclear stopping powers of $La_{1-x}Yb_xPO_4$ materials were also calculated using the SRIM-2013 software package and are presented in Table 4-1.[223] A higher electronic to nuclear stopping power (ENSP) ratio generally indicates a lower defect accumulation because of the greater delocalization of point defects.[8996] In $La_{1-x}Yb_xPO_4$, the La end-member (x = 0) adopting the monazite structure has a higher ENSP ratio than the Yb end-member (x = 1) adopting the xenotime structure (Table 4.1). This would indicate that the defect accumulation in the monazite structure is lower in comparison to the xenotime structure.[89,96]

4.2.3. Micro-X-ray diffraction (μ-XRD)

Micro-XRD was performed on the ion-implanted $La_{1-x}Yb_xPO_4$ (x = 0, 0.3, 0.7, 1) materials using a PANalytical Empyrean system and a Cu $K\alpha_{1,2}$ source to understand the stability of these materials on the long-range scale. The size of the X-ray beam was reduced to 200 μm using a monocapillary collimator in order to selectively collect the diffraction patterns from the surface of the ion-implanted pellets. It should be noted that the collected diffractograms provide information on both the surface and bulk regions of the ion-implanted materials. The pellets were mounted on a goniometer that allows for translation of the sample in x, y, and z directions. The goniometer head allows for tilting the samples. Sample alignment was performed with the help of a microscope to position the X-ray beam on the surface of the pellets. The μ-XRD patterns were collected at room temperature in the 2θ range of 10°-60° using a step size of 0.017° and analyzed using the HighScore Plus software package.[178] It should be noted that this experimental set-up

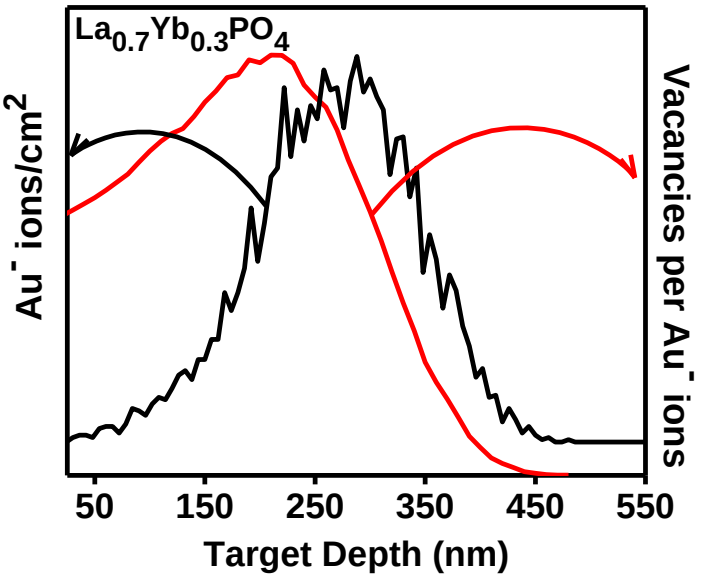

Figure 4.1 Ion-implantation depth profile of $La_{0.7}Yb_{0.3}PO_4$ (black) calculated using the SRIM-2013 software package. A total of 5000 Au^- ions having energy of 2 MeV was used during this calculation. A plot depicting the number of vacancies generated by the Au- ions as a function of depth is also presented.

Table 4-1 Calculated Electronic and Nuclear Stopping Powers for $La_{1-x}Yb_xPO_4$

Compound	**Crystal structure**	**Electronic stopping power dE/dx_e (eV/nm)**	**Nuclear stopping power dE/dx_n (eV/nm)**	**Electronic to Nuclear stopping power ratio (ENSP)**
$LaPO_4$	Monazite	2497	3873	0.645
$La_{0.7}Yb_{0.3}PO_4$	Monazite+Xenotime	2747	4483	0.613
$La_{0.3}Yb_{0.7}PO_4$	Monazite+Xenotime	2611	4571	0.571
$YbPO_4$	Xenotime	2510	4639	0.541

did not permit spinning of the sample during data collection and, therefore, preferential orientation effects could be observed in the μ-XRD patterns.

4.2.4. XANES

4.2.4.1. P K- and La L_3-edge GA-XANES

P K- and La L_3-edge GA-XANES spectra from ion-implanted $La_{1-x}Yb_xPO_4$ were collected using the Soft X-ray Microcharacterization Beamline (SXRMB; 06B1-1) located at the Canadian Light Source (CLS).[179] The ion-implanted pellets were mounted on carbon tape before being placed in the vacuum chamber. The GA-XANES spectra were collected from the surface of the pellets by allowing the X-rays to hit the sample surface at an angle greater than the critical angle for total external reflection.[169] Since the attenuation depths of X-rays depend strongly on the angle between the X-ray beam and the sample surface, XANES spectra can be collected from different regions of the material by tuning the X-ray angle of incidence. The X-ray attenuation depths, and the corresponding glancing angles, for X-rays having energies equivalent to those of the P K- and La L_3-edge were calculated using a web-based program and are presented in Table 4-2.[227] The web-based program utilizes the Beer-Lambert law (Equation 1.1) to calculate the X-ray attenuation depths.[228]

The P K- and La L_3-edge GA-XANES spectra from the ion-implanted materials were collected in partial fluorescent yield (PFY) mode and total electron yield (TEY) mode; however, the TEY signal suffered from charging effects. An attempt was made to reduce charging effects in the GA-XANES spectra collected in TEY mode by connecting the surface of the pellet to the electrically grounded Cu sample holder using Ag paint. Nevertheless, the TEY signal from the P K-edge spectra still exhibited signs of severe charging in this material. A moderate TEY signal

Table 4-2 Calculated X-ray attenuation depths and the corresponding glancing angles for the P K- and La L_3-edge GA-XANES spectra.

Compounds	**P K-edge (2145.5 eV)**		**La L_3-edge (5483 eV)**	
	Glancing angle	**X-ray attenuation depth (nm)**	**Glancing angle**	**X-ray attenuation depth (nm)**
$LaPO_4$	11.1°	250	-	-
	20.3°	450	-	-
	29.3°	638		
$La_{0.7}Yb_{0.3}PO_4$	15.7°	250	41.0°	3000
	29.1°	450	85.0°	4560
	43.6°	638		
$La_{0.3}Yb_{0.7}PO_4$	19.8°	250	36.1°	3000
	37.5°	450	85.0°	5074
	59.8°	638		
$YbPO_4$	23.0°	250	-	-
	44.6°	450	-	-
	85.0°	639		

was obtained for certain compositions in the case of the higher energy La L_3-edge spectra. It should be noted that the PFY signals from white-line La L_3-edge spectra were distorted by absorption effects so only the TEY spectra that were successfully collected were analyzed. P K-edge spectra were calibrated by collecting the spectrum from red P (Alfa Aesar; 99%) with the maximum in the first derivative of the P K-edge set to 2145.5 eV.[180] La L_3-edge XANES spectra were calibrated using the spectrum from Cr metal by setting the maximum in the first derivative of the Cr K-edge to 5989 eV.[180] All XANES spectra were analyzed using the Athena software program.[181]

4.2.4.2. P $L_{2,3}$-edge XANES

P $L_{2,3}$-edge XANES spectra were also collected from the ion-implanted $La_{1-x}Yb_xPO_4$ materials using the Variable Line Spacing-Plane Grating Monochromator (VLS-PGM; 11ID-2) beamline located at the CLS.[182] The ion-implanted pellets were mounted on carbon tape and the spectra were measured in vacuum in total fluorescence yield (TFY) mode. These spectra were not collected using glancing angle geometry. The P $L_{2,3}$-edge XANES spectra were calibrated using red P, with the P $L_{2,3}$-edge absorption energy set to 130 eV.

4.3. Results and discussion

4.3.1. Bulk and micro X-ray diffraction

Bulk powder XRD patterns from the as-synthesized $La_{1-x}Yb_xPO_4$ (x = 0.0, 0.3, 0.7, and 1.0) materials are presented in Figure 4.2 along with the μ-XRD patterns from the Au^- ion-implanted $La_{1-x}Yb_xPO_4$ materials (doses: $1x10^{14}$, $5x10^{14}$, and $1x10^{15}$ ions/cm^2). The end-members of the $La_{1-x}Yb_xPO_4$ series adopt the lower symmetry monazite (x = 0) structure or the higher symmetry

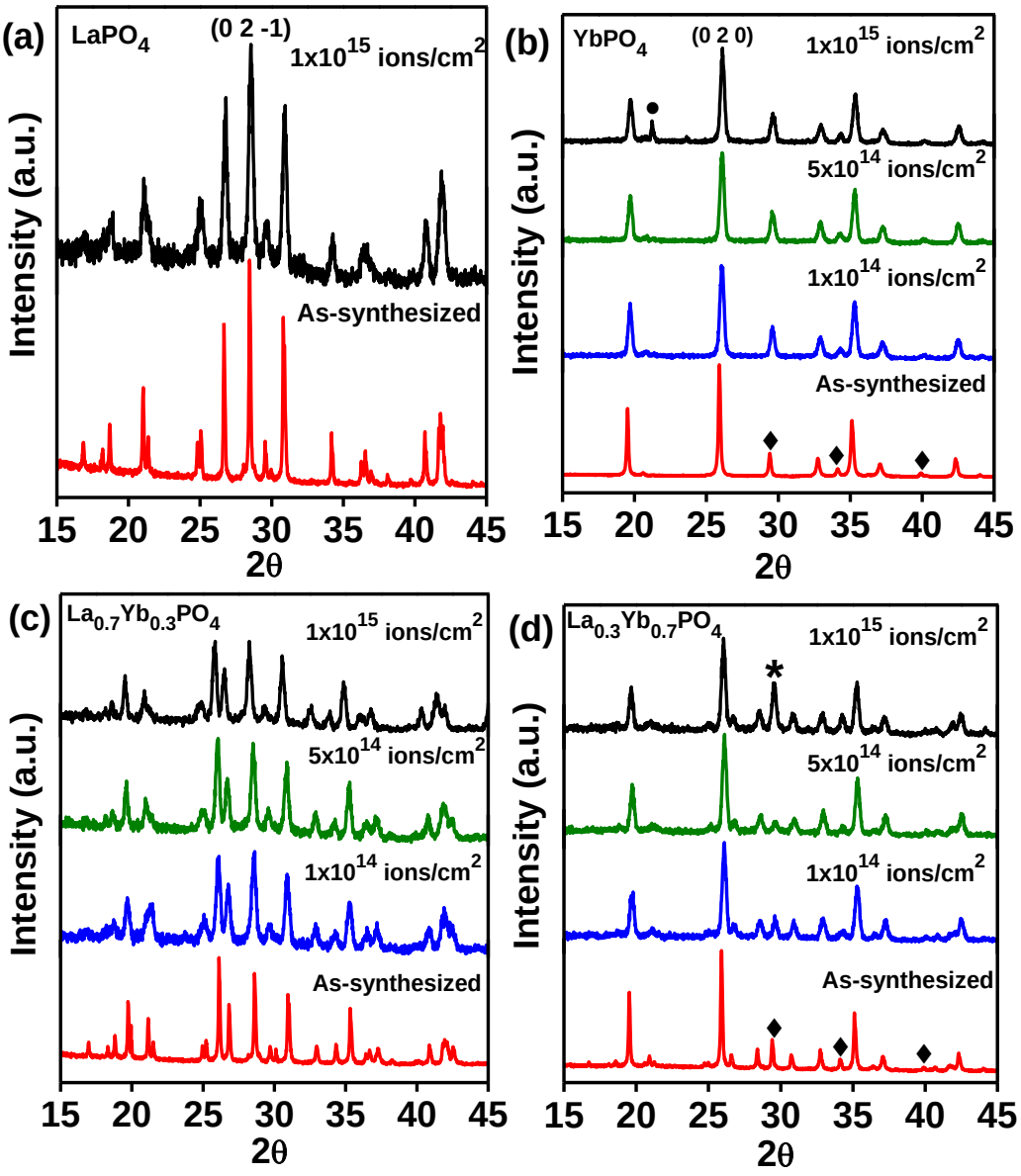

Figure 4.2 μ-XRD patterns from (a) $LaPO_4$, (b) $YbPO_4$, (c) $La_{0.7}Yb_{0.3}PO_4$, and (d) $La_{0.3}Yb_{0.7}PO_4$ materials implanted with three different doses of Au^- ions ($1x10^{14}$, $5x10^{14}$, and $1x10^{15}$ ions/cm^2) are shown. Bulk powder XRD patterns from the as-synthesized materials are also shown. The dot symbol in (b) indicates the presence of an anomalous peak. The peak labelled with an asterisk symbol in (d) arises from both the monazite phase [(0 1 -2) peak] and unreacted Yb_2O_3 [(2 2 2) peak]. Diffraction peaks from the impurity phase, Yb_2O_3 [(2 2 2) peak], observed in the pattern from $YbPO_4$ and $La_{0.3}Yb_{0.7}PO_4$ are represented by a diamond symbol.

xenotime (x = 1) structure, respectively. It is to be noted that the powder XRD pattern of $YbPO_4$ showed the presence of a minor amount of Yb_2O_3 (indicated by a diamond symbol in Figure 4.2b) in addition to the predominant xenotime phase. However, the presence of this low concentration impurity does not impact the analysis of the XANES spectra. At intermediate values of x (x = 0.3 and 0.7), the materials exist as a mixture of both the monazite and xenotime phases. Information about the lattice constants and relative concentration of monazite and xenotime phases were obtained from the Rietveld refined powder XRD data from $La_{1-x}Yb_xPO_4$ (Table C-1 in Appendix C). It was assumed in this study that the composition of the monazite structure was $LaPO_4$ while the composition of the xenotime structure was $YbPO_4$ because of the poor solubility of Yb in the monazite structure (and vice versa for La in the xenotime structure). The general trend in the $La_{1-x}Yb_xPO_4$ series is that the relative concentration of the xenotime structure increases with greater Yb concentration (see Table C-1 in the supporting information).

Powder patterns collected using the μ-XRD set-up from the ion-implanted materials allowed for a qualitative examination of how the long-range structure of these materials was affected by ion-implantation. In comparison to the powder XRD patterns from the as-synthesized materials, the μ-XRD patterns from the ion-implanted $La_{1-x}Yb_xPO_4$ materials exhibited broader diffraction peaks (Figure 4.2). This observation indicates that the structure of the materials was damaged as a result of ion-implantation. The full width at half maximum (FWHM) values of the (0 2 -1) and (0 2 0) reflections from the as-synthesized and ion-implanted $La_{1-x}Yb_xPO_4$ materials are listed in Table 4.3. The (0 2 -1) peak is characteristic of the monazite phase while the (0 2 0) peak is characteristic of the xenotime phase. The FWHM values of the characteristic peaks from the as-synthesized compounds were obtained from the bulk powder XRD data. Diffraction peaks

Table 4-3 Full width at half-maximum (FWHM) values of the (0 2 -1) [monazite] and (0 2 0) [xenotime] diffraction peaks from the damaged and as-synthesized $La_{1-x}Yb_xPO_4$ materials

Compound	Diffraction peak	FWHM as-synthesized	FWHM $1x10^{14}$ ions/cm^2	FWHM $1x10^{15}$ ions/cm^2
$LaPO_4$	(0 2 -1)	0.150°	-	0.385°
$La_{0.7}Yb_{0.3}PO_4$	(0 2 -1)	0.159°	0.374°	0.392°
	(0 2 0)	0.142°	0.399°	0.367°
$La_{0.3}Yb_{0.7}PO_4$	(0 2 -1)	0.211°	0.462°	0.465°
	(0 2 0)	0.160°	0.349°	0.368°
$YbPO_4$	(0 2 0)	0.174°	0.360°	0.336°

can broaden because of the creation of defects (e.g., interstitials and vacancies) and/or because of a reduction in the average crystallite size.[229,230] It is believed that both effects have resulted in the increased width of the diffraction peaks from the ion-implanted materials. Although peak broadening is observed in the μ-XRD patterns from ion-implanted $La_{1-x}Yb_xPO_4$ (x = 0.0, 0.3, 0.7, and 1.0), shifts in the 2θ peak positions were not observed between the ion implanted and as-synthesized materials (Figure 4.2).

One of the 2θ peaks (marked with an asterisk symbol in Figure 4.2d) in the μ-XRD pattern from $La_{0.3}Yb_{0.7}PO_4$ that was implanted with ions to the highest dose ($1x10^{15}$ ions/cm^2) was observed to be more intense in comparison to the diffraction pattern from $La_{0.3}Yb_{0.7}PO_4$ that was implanted to a lower dose. This observation may be attributed to preferential orientation effects (Figure 4.2d). Examination of the μ-XRD pattern from $YbPO_4$ that was implanted with ions at the highest dose ($1x10^{15}$ ions/cm^2) revealed the presence of an anomalous peak (marked with a dot symbol in Figure 4.2b). This peak is not due to the xenotime structure or any of the unreacted starting materials and the underlying reason for the appearance of this peak is unknown.

4.3.2. P K-edge GA-XANES: Ion implanted $La_{1-x}Yb_xPO_4$

Normalized P K-edge XANES spectra that represent the transition of electrons from the P 1s state to P 3p conduction states were collected from the ion-implanted $La_{1-x}Yb_xPO_4$ (x = 0.0, 0.3, 0.7, 1.0) materials at various glancing angles to study the extent of structural damage as a function of depth, implantation dose ($1x10^{14}$, $5x10^{14}$, and $1x10^{15}$ ions/cm^2), and composition (Figures 4.3 to 4.6). The P K-edge spectra from the as-synthesized $La_{1-x}Yb_xPO_4$ materials are also included in Figures 4.3 to 4.6.

The P K-edge GA-XANES spectra from ternary $LaPO_4$ (monazite) implanted with Au^- ions to a dose of $5x10^{14}$ and $1x10^{15}$ ions/cm^2 are presented in Figure 4.3. A significant change in the spectral lineshape is observed as a result of ion-implantation and the glancing angle used to collect the spectra; however, no significant differences in the spectra were observed depending on ion dose. Relative to the spectra from as-synthesized $LaPO_4$, the P K-edge spectra from the ion-implanted materials clearly exhibit a loss of both intensity and fine structure. The near-edge region of the spectra was broader as a result of ion-implantation, and it is proposed that this is due to a distortion of the PO_4 coordination environment (Figures 4.3a and 4.3b).

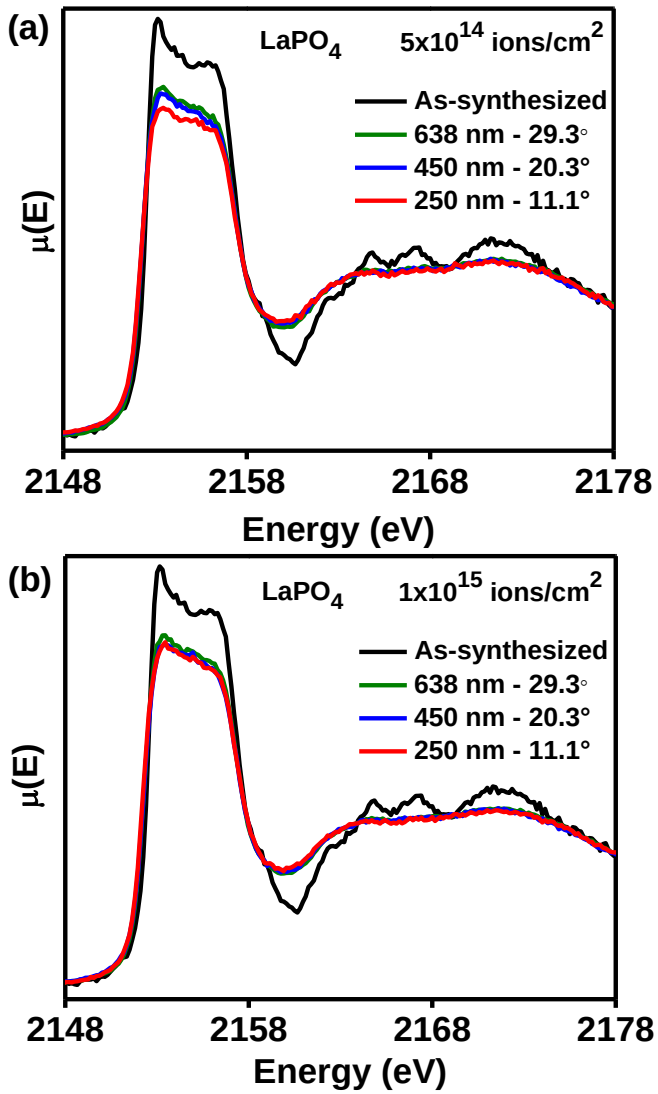

Figure 4.3 P K-edge GA-XANES spectra from $LaPO_4$ implanted with a dose of (a) 5 x 10^{14} ions/cm^2 and (b) 1 x 10^{15} ions/cm^2 are shown. The glancing angle and X-ray attenuation depths are labelled in each plot. The spectrum from the as-synthesized material is also presented for comparison.

Normalized P K-edge GA-XANES spectra from ion-implanted $YbPO_4$ (xenotime) are shown along with the spectrum from the as-synthesized material in Figure 4.4. Unlike $LaPO_4$, the structural response of $YbPO_4$ towards the lowest ($1x10^{14}$ and $5x10^{14}$ ions/cm^2) and highest ion-implantation doses ($1x10^{15}$ ions/cm^2) was found to be different (Figure 4.4). The spectral lineshape of the sample that received the highest ion-implantation dose showed some resemblance to the lineshape of the spectrum from the as-synthesized material whereas the samples that were exposed to a lower dose did not (Figure 4.4c). This observation is based on the presence of fine structure in the spectrum from $YbPO_4$ exposed to the highest ion-implantation dose, which is similar but less intense than the fine structure observed in the spectrum from as-synthesized $YbPO_4$ (see arrow in Figure 4.4c). The fine structure was observed only at the lowest glancing angles (23°- 250 nm; 44.6°- 450 nm; see Figure 4.4c). Based on these observations, it is suggested that a high flux of Au^- ions (i.e., $1x10^{15}$ ions/cm^2) may induce partial recrystallization of the damaged xenotime ($YbPO_4$) material. Although no sign of structural recovery was observed in the spectrum from $LaPO_4$ implanted to a dose of $1x10^{15}$ ions/cm^2, the possibility of partial recrystallization of the damaged monazite structure cannot be completely ruled out (Figure 4.3b). Unlike the spectrum from $YbPO_4$ which adopts the xenotime structure, the XANES spectrum from as-synthesized $LaPO_4$ is not structurally rich (i.e., less fine structure is observed), so minor changes in the spectrum depending on ion dose would be difficult to observe.

The partial self-healing of ion-implanted materials at room temperature could be explained using the "loading-unloading" effect.[231,232] It has been reported previously that nanomaterials (e.g., $MgGa_2O_4$ and ZrO_2) exhibit greater resistance to radiation-induced structural damage and theoretical studies have investigated the mechanism for the radiation-resistance of these materials.[117,231–233] Radiation-induced structural damage can lead to the production of defects

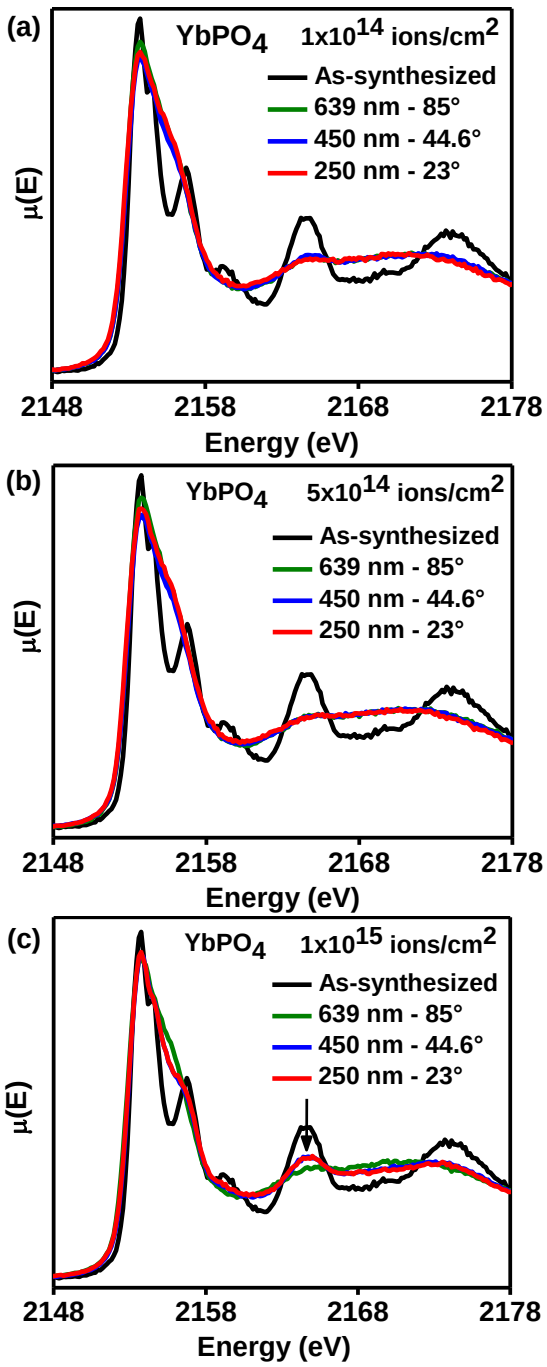

Figure 4.4 P K-edge GA-XANES spectra from $YbPO_4$ implanted with a dose of (a) 1 x 10^{14}, (b) 5 x 10^{14}, and (c) 1 x 10^{15} ions/cm^2 Au^- ions are shown. The glancing angle and X-ray attenuation depths are labelled in each plot. The spectrum from the as-synthesized material is also presented for comparison. The arrow in (c) indicates the development of fine structure in the spectrum from $YbPO_4$ that was implanted to the highest dose (1 x 10^{15} ions/cm^2).

such as interstitial atoms and vacancies.[232,234] The grain boundaries present in the material traps the interstitial atom and releases it when there are enough vacancies in the vicinity of the grain boundary.[231,232] In this way, the vacancies are annihilated and the material is able to self-heal from structural damage.[231,232] The high dose of Au^- ions ($1x10^{15}$ ions/cm^2) that were used to implant the $YbPO_4$ material may have also resulted in local heating of the sample with the accompanying rise in temperature providing enough energy for the movement of displaced atoms and the partial recovery of the structure.[235,236]

P K-edge GA-XANES spectra were also collected from ion-implanted and as-synthesized quaternary $La_{1-x}Yb_xPO_4$ (x = 0.3 and 0.7) materials to understand the effect of heavy/light rare-earth substitution on the structural stability of monazite/xenotime structures (Figures 4.5 and 4.6). The relative percent composition of monazite and xenotime phases in as-synthesized $La_{0.7}Yb_{0.3}PO_4$ (Monazite - 70%; Xenotime - 30%) and $La_{0.3}Yb_{0.7}PO_4$ (Monazite - 25%; Xenotime - 76%) compounds were determined previously by Rietveld refinement of powder XRD data as well as from a linear combination fitting (LCF) of P K-edge XANES spectra. The P K-edge XANES spectrum from as-synthesized $La_{0.3}Yb_{0.7}PO_4$ exhibited more fine structure in comparison to the spectrum from $La_{0.7}Yb_{0.3}PO_4$ due to the higher concentration of the xenotime structure. After ion-implantation, $La_{0.7}Yb_{0.3}PO_4$ and $La_{0.3}Yb_{0.7}PO_4$ were structurally damaged as observed by changes in the spectral lineshape of the P K-edge spectra (Figure 4.5 and 4.6). Similar to $LaPO_4$, the P K-edge of ion-implanted $La_{0.7}Yb_{0.3}PO_4$ did not exhibit a varied structural response to different ion-implantation doses (Figure 4.5). However, the results obtained for ion-implanted $La_{0.3}Yb_{0.7}PO_4$ are similar to those obtained for ion-implanted $YbPO_4$ (Figure 4.6). At the highest dose ($1x10^{15}$ ions/cm^2), the Yb-rich compound exhibited signs of partial structural recovery as indicated by the appearance of fine structure in the P K-edge spectra (see arrow in Figure 4.6c).

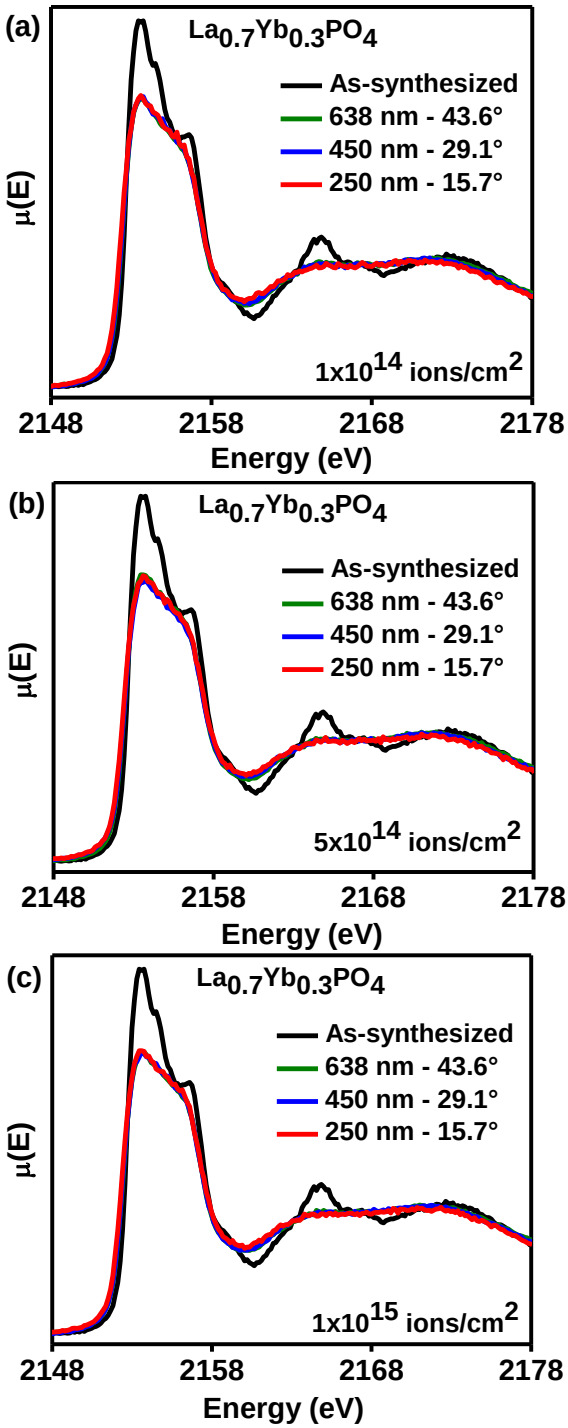

Figure 4.5 Normalized P K-edge GA-XANES spectra from $La_{0.7}Yb_{0.3}PO_4$ implanted with Au^- ions to a dose of (a) $1x10^{14}$, (b) $5x10^{14}$, and (c) $1x10^{15}$ ions/cm^2 are shown. The glancing angle and resulting X-ray attenuation depths are labelled in each plot. The spectrum from the as-synthesized material is also presented for comparison.

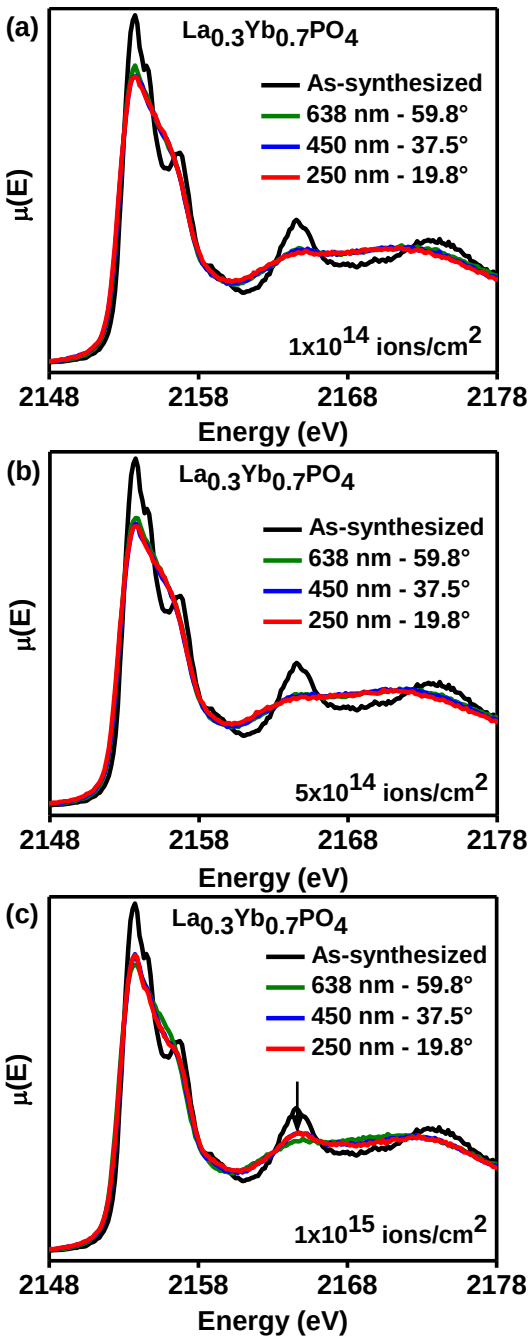

Figure 4.6 P K-edge GA-XANES spectra from $La_{0.3}Yb_{0.7}PO_4$ implanted with Au^- ions to a dose of (a) $1x10^{14}$, (b) $5x10^{14}$, and (c) $1x10^{15}$ ions/cm^2 are shown. The glancing angle and X-ray attenuation depths are labelled in each plot. The spectrum from the as-synthesized material is also presented for comparison. The arrow in Figure 4.6c indicates the development of fine structure after $La_{0.3}Yb_{0.7}PO_4$ was implanted to the highest dose ($1x10^{15}$ ions/cm^2).

No signs of structural recovery were observed when $La_{0.3}Yb_{0.7}PO_4$ was implanted to lower doses ($1x10^{14}$ and $5x10^{14}$ ions/cm^2; Figures 4.6a and 4.6b).

4.3.3. P K-edge GA-XANES: Thermal annealing of ion implanted $La_{1-x}Yb_xPO_4$

As described in Section 4.3.2, the $La_{1-x}Yb_xPO_4$ materials are not resistant to radiation-induced structural damage. Actinides, in general, produce high levels of heat during the radioactive decay process in addition to the production of high energy recoil daughter product nuclides and α-particles.[40,78] However, depending on the composition of the crystalline wasteform, the heat released during the radioactive decay process could promote structural reorganization of the damaged material.[237]

P K-edge GA-XANES spectra were collected from the ion-implanted $La_{1-x}Yb_xPO_4$ (x = 0.0, 0.3, 0.7, 1.0) materials after annealing them to 300° or 900° C to study the heat-induced recovery process of these materials. (It should be noted that not all ion-implanted materials were implanted to the same dose before annealing.) The P K-edge XANES spectra collected from the annealed materials using the lowest glancing angles are shown in Figure 4.7. The P K-edge GA-XANES spectra from ion-implanted $LaPO_4$ before and after annealing to 300° or 900° C are shown in Figure 4.7a along with the spectrum from as-synthesized $LaPO_4$. The annealed ion-implanted $LaPO_4$ samples showed signs of partial structural recovery as indicated by the increase in intensity and decrease in width of the near-edge region in comparison to the spectrum from ion-implanted $LaPO_4$. Although significant differences in the spectral lineshape were observed between the ion-implanted and annealed ion-implanted $LaPO_4$ materials, no major differences in the spectra were observed between the two annealing temperatures (i.e., 300°C vs. 900°C).

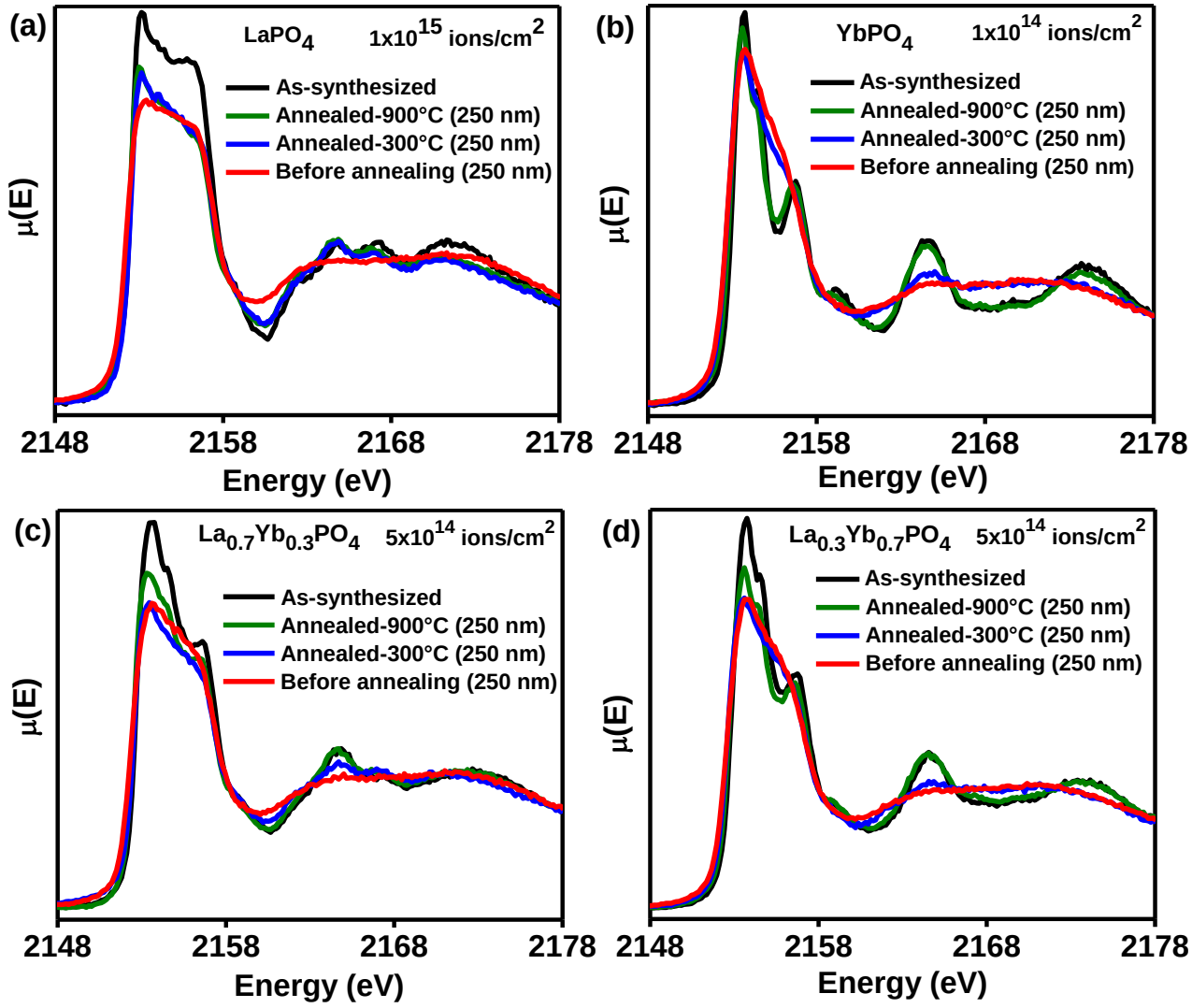

Figure 4.7 P K-edge GA-XANES spectra from ion-implanted (a) $LaPO_4$ ($1x10^{15}$ ions/cm^2), (b) $YbPO_4$ ($1x10^{14}$ ions/cm^2), (c) $La_{0.7}Yb_{0.3}PO_4$ ($5x10^{14}$ ions/cm^2), and (d) $La_{0.3}Yb_{0.7}PO_4$ ($5x10^{14}$ ions/cm^2) annealed at 300° and 900° C are shown along with the spectra from the as-synthesized and ion-implanted $La_{1-x}Yb_xPO_4$ materials before annealing. Only the spectra collected from a depth of 250 nm are shown.

The effect of temperature on the structural recovery of damaged $YbPO_4$ was also studied using P K-edge GA-XANES (Figure 4.7b). The spectrum from $YbPO_4$ annealed at 300° C revealed only minor indications of structural recovery. However, the structure of $YbPO_4$ was observed to recover to its original state after annealing the material to 900° C (see Figure 4.7b). The difference in behaviour between $LaPO_4$ and $YbPO_4$ may be attributed to the $LaPO_4$ sample receiving a higher dose of ions as well as the different structures adopted by these materials. The P K-edge GA-XANES spectra from the $La_{0.7}Yb_{0.3}PO_4$ and $La_{0.3}Yb_{0.7}PO_4$ materials that were ion-implanted to the same dose ($5x10^{14}$ ions/cm^2) and then annealed also displayed signs of structural recovery (Figures 4.7c and 4.7d). Had there been any surface segregation of phases in these quaternary compounds it would be expected that only one phase would recover from the structural damage. However, both the monazite and xenotime structures partially recover from structural damage as indicated by the similarity of the spectral lineshape to that of the as-synthesized material. The signs of recovery were more evident in the spectra from the ion-implanted materials annealed at the highest temperature (900°C); however, structural recovery was not complete. This conclusion is a result of the differences in the intensity of the P K-edge GA-XANES spectra between the as-synthesized and annealed ion-implanted materials (See Figures 4.7c and 4.7d).

4.3.4 P $L_{2,3}$-edge XANES

The normalized P $L_{2,3}$-edge XANES spectra from ion-implanted $La_{1-x}Yb_xPO_4$ are shown in Figure 4.8 along with the spectra from the as-synthesized materials. The P $L_{2,3}$-edge spectrum generally represents the transition of electrons from the P 2p state to P 3s and 3d conduction states.[238] In Chapter 2, the two distinct features observed in the P $L_{2,3}$-edge spectra from as-synthesized $La_{1-x}Yb_xPO_4$ (A and B) were assigned to the transition of P 2p electrons into the

overlapping P 3s and 3d states. Similar to P K-edge GA-XANES spectra, the P $L_{2,3}$-edge spectra were observed to be sensitive to changes in the local coordination environment of P as a result of ion-implantation. Relative to the as-synthesized materials, the lineshape of the spectra from the ion-implanted $La_{1-x}Yb_xPO_4$ (x = 0, 0.3, 0.7, 1.0) materials changed significantly (see Figure 4.8). The increased broadness of the spectra from the ion-implanted materials implies that the degeneracy of the P conduction states is lost as a result of ion-implantation.

The P $L_{2,3}$-edge spectra from the ion-implanted $La_{1-x}Yb_xPO_4$ (x = 0.3 and 0.7) materials that were annealed at 300° and 900°C are shown in Figure 4.9. The near-edge region in the P $L_{2,3}$-edge spectra from the ion-implanted $La_{1-x}Yb_xPO_4$ (x = 0.3 and 0.7) materials becomes narrower with increasing annealing temperature, which is a result of the partial recovery of the structure of these materials. Considerable differences in the spectral lineshape were observed between the two annealing temperatures and it was observed that the spectral lineshape of ion-implanted $La_{0.7}Yb_{0.3}PO_4$ and $La_{0.3}Yb_{0.7}PO_4$ annealed at the highest temperature (900° C) closely resembled that of the as-synthesized material (Figure 4.9). These observations are in agreement with those obtained by the examination of the P K-edge GA-XANES spectra from the annealed ion-implanted materials (See Section 4.3.3).

4.3.5. La L_3-edge XANES

La L_3-edge GA-XANES spectra were collected from the ion-implanted $La_{1-x}Yb_xPO_4$ materials to examine changes in the local coordination environment of La. The La L_3-edge partial fluorescent yield (PFY) spectra were distorted because of severe absorption effects so the total electron yield (TEY) mode was the preferred method of detection.[239,240] The TEY La L_3-edge XANES spectra from the ion-implanted $La_{0.7}Yb_{0.3}PO_4$ and $La_{0.3}Yb_{0.7}PO_4$ materials are shown in Figure 4.10 along with the spectra from the as-synthesized materials. The white-line feature in the La L_3-edge

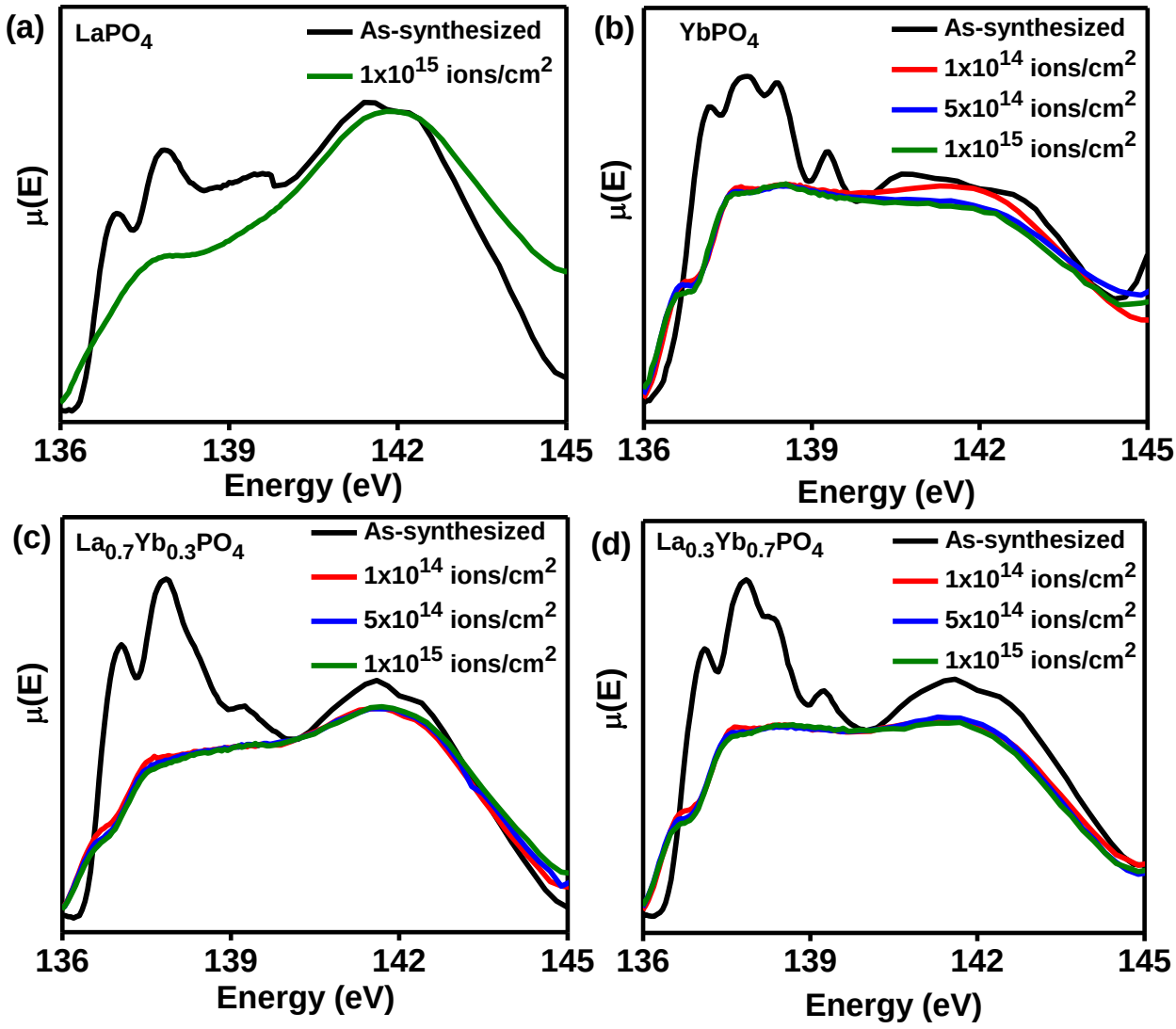

Figure 4.8 Normalized P $L_{2,3}$-edge XANES spectra from ion-implanted (a) $LaPO_4$, (b) $YbPO_4$, (c) $La_{0.7}Yb_{0.3}PO_4$, and (d) $La_{0.3}Yb_{0.7}PO_4$ materials are shown along with the spectra from the as-synthesized materials.

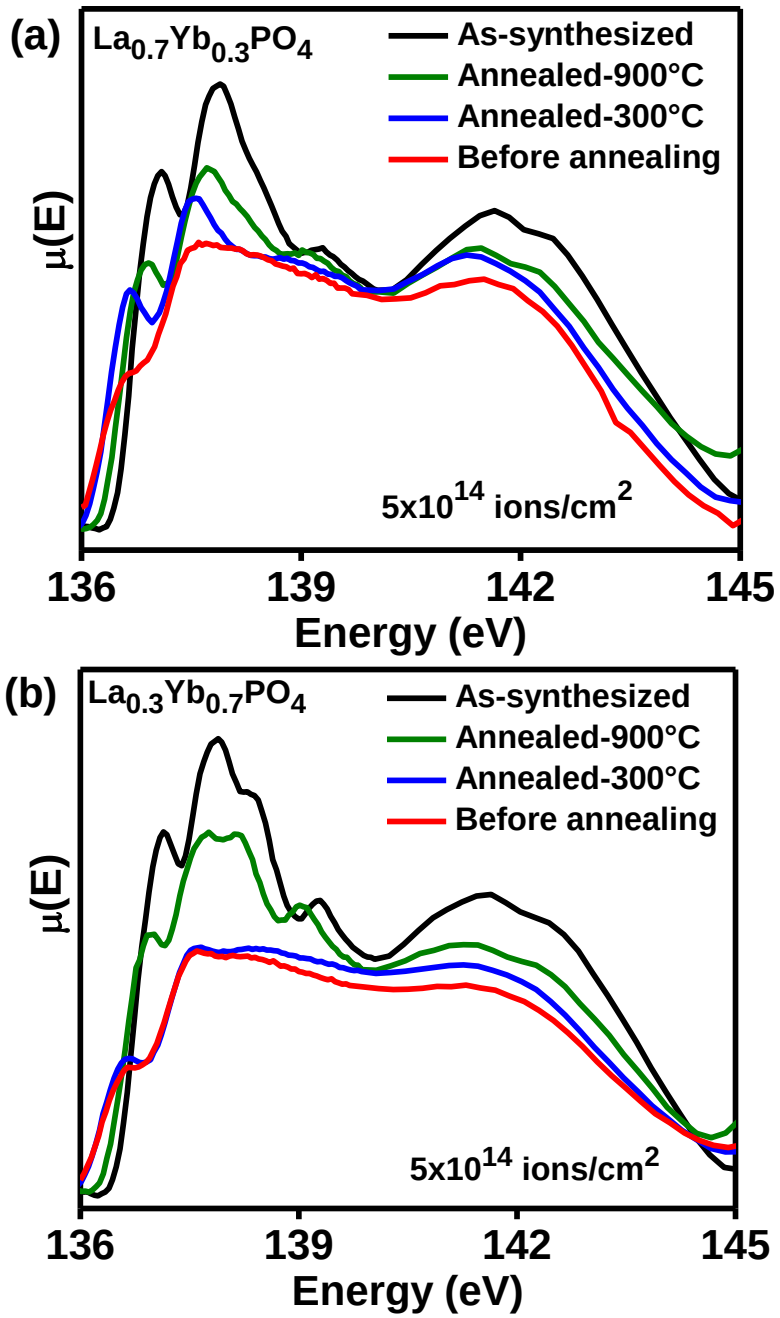

Figure 4.9 Normalized P $L_{2,3}$-edge XANES spectra from ion-implanted (a) $La_{0.7}Yb_{0.3}PO_4$ and (b) $La_{0.3}Yb_{0.7}PO_4$ compounds annealed at 300° or 900° C are presented along with the spectra from the as-synthesized materials and ion-implanted materials before annealing.

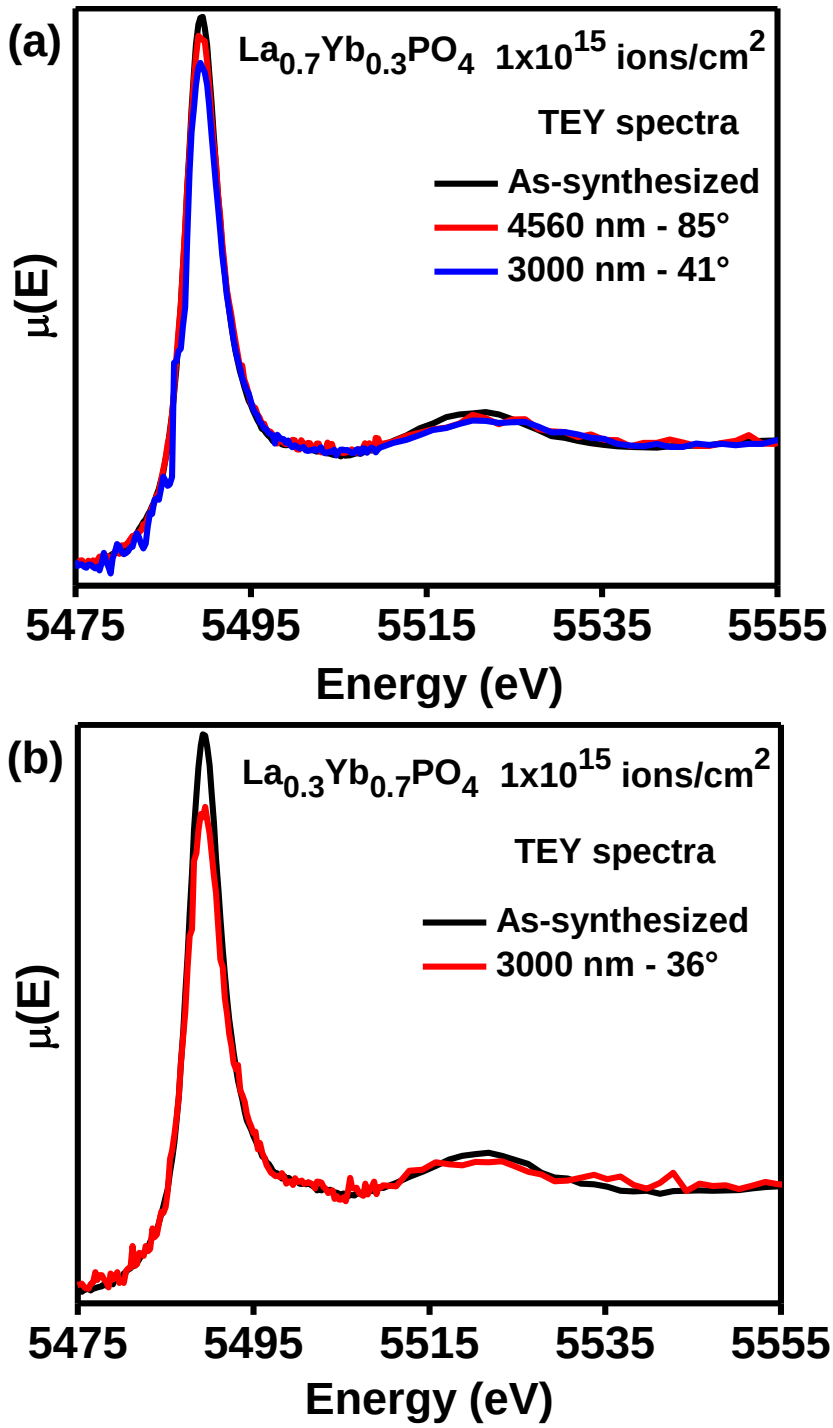

Figure 4.10 Normalized La L_3-edge GA-XANES spectra from ion-implanted $La_{1-x}Yb_xPO_4$ (x = 0.3 and 0.7) materials are shown along with the spectra from as-synthesized materials.

spectra represents a 2p → 5d excitation.[215] After ion-implantation, the intensity of the La L_3-edge decreased relative to the as-synthesized material and the spectra became broader.[214,215] This observation suggests a distortion of the La coordination environment in the ion-implanted materials (Figures 4.10a and 4.10b).[214,215] Since the changes in the intensity of the La L_3-edge between the as-synthesized and ion-implanted materials were observed to be minor, Yb L_3-edge spectra were not collected from the ion-implanted materials as they would be expected to give similar information as the La L_3-edge spectra.

4.4. Conclusion

The effect of Au^- ion-implantation on the long- and short-range order of $La_{1-x}Yb_xPO_4$ materials was studied using μ-XRD and GA-XANES. The μ-XRD data revealed the loss of long-range order in the $La_{1-x}Yb_xPO_4$ materials that were implanted with 2 MeV Au^- ions. The P K-, P $L_{2,3}$-, and La L_3-edge XANES spectra clearly showed that the $La_{1-x}Yb_xPO_4$ materials are susceptible to radiation-induced structural damage. The P K- and La L_3-edge GA-XANES and P $L_{2,3}$-edge XANES spectra were observed to be very sensitive to changes in the structure of these materials as a result of ion-implantation. The P K-edge GA-XANES spectra provided evidence for the occurrence of partial recrystallization of the structure of the $La_{0.3}Yb_{0.7}PO_4$ and $YbPO_4$ materials that were implanted to Au^- ions to the highest dose (1×10^{15} ions/cm^2). Annealing studies of the ion-implanted $La_{1-x}Yb_xPO_4$ materials have shown the ability of these materials to recover (either partially or completely depending on composition) from structural damage caused by the implantation of high-energy Au^- ions. It was found in this study that the ability of ion-implanted rare-earth phosphates to recover from a damaged state is dependent on the ion-dose received and the temperature that these materials are exposed to post implantation.

Chapter 5

A SHORT TERM INVESTIGATION OF THE CHEMICAL DURABILITY OF HYDROUS AND ANHYDROUS RARE-EARTH PHOSPHATES

5.1 Introduction

In Chapters 2 and 3, fundamental structural aspects of hydrous and anhydrous rare-earth phosphates were discussed and in Chapter 4, the structural stability of monazite- and xenotime-type materials when exposed to simulated radiation conditions was determined. For permanent disposal of nuclear waste elements, the wasteforms are packed within multiple containers, which are intended for storage in a deep geological repository.[40,49,50,53] However, under a failed container situation the wasteforms could be exposed to groundwater present in the geological repository. In this scenario, the radionuclides contained in a wasteform could leach out of the material and reach the biosphere through groundwater migration.[23] Materials proposed for nuclear wasteform applications must be leach resistant in addition to being radiation resistant. The current chapter is focused on determining the chemical durability of hydrous and anhydrous rare-earth phosphate materials in deionized water so as to understand the leaching behaviour of these materials.

Rare-earth phosphates adopting the monazite- ($REPO_4$; RE = La - Gd) and xenotime-type (RE'PO_4; RE' = Tb - Lu & Y) structures are considered as promising materials for the immobilization of actinides and several studies in relation to the structure and properties of these materials have been reported in the literature.[78,88,89,121,190] Leaching studies of synthetic and natural monazite samples under basic conditions have shown that the surface of the monazite can be chemically altered to produce a hydrous layer adopting the rhabdophane ($REPO_4.nH_2O$; RE = La - Dy) structure.[126,128–132] This hydrous rare-earth phosphate mineral (rhabdophane) is expected to play a vital role in controlling or stopping the release of actinides from monazite.[126] The crystal structures of materials adopting monazite- ($CePO_4$; space group - $P2_1/n$), xenotime- (YPO_4; space group - $I4_1/amd$), and rhabdophane-($SmPO_4.0.667H_2O$; space group - $C2$) type structures are presented in Figures 1.3 and 1.4.[126,135]

Leaching studies of nuclear wasteforms are generally carried out using standard protocols such as the materials characterization center tests (MCC), the single-pass flow through tests (SPFT), the product consistency tests (PCT), or the international atomic energy agency (IAEA) tests.[241–244] These leaching tests can be conducted in either static or dynamic conditions.[245] Under static conditions, the leachant solution which is in contact with the wasteform, is partially withdrawn from the test vessel at regular intervals of time and these tests mimic the low flow-rates of groundwater in geological repositories.[245] Under dynamic leaching conditions, the leachant solution is completely withdrawn and replaced with fresh solution at regular time intervals.[245] As a result, dynamic leaching tests will prevent the formation of any secondary phases on the surface of wasteform and provide an accurate picture of the leaching behavior of a wasteform.[245] With the exception of a few studies, leaching studies on rare-earth phosphate based wasteforms reported in the literature have been focused mostly on materials adopting the

monazite-type structure.[245–249] Early investigations into the leaching behaviour of glass and monazite based wasteforms in deionized water have revealed that the monazite matrix is chemically more durable when compared to borosilicate glass.[250] Therefore, monazite ceramics serve as a potential alternative to borosilicate glass wasteforms used for immobilization of nuclear wastes.[250]

The objective of this chapter was to conduct a investigation (short-term) of the chemical durability of monazite- ($LaPO_4$), xenotime- ($YbPO_4$), and rhabdophane- ($GdPO_4.nH_2O$) type materials in deionized water. The concentration of RE and P ions in the solution was determined using inductively coupled plasma – mass spectrometry (ICP-MS). The long-range and local structures of $REPO_4$ and $REPO_4.H_2O$ materials before and after exposure to deionized water was studied using X-ray diffraction (XRD) and X-ray absorption near-edge spectroscopy (XANES), respectively. Information regarding the local structure around P and RE ions was obtained by analysis of P K-, P $L_{2,3}$-, and RE L_1-edge XANES spectra. This is the first study to compare the leaching behaviour of monazite-, xenotime-, and rhabdophane-type rare-earth phosphates.

5.2. Experimental

5.2.1. Synthesis

The rare-earth phosphates adopting the monazite- ($LaPO_4$), xenotime- ($YbPO_4$), and rhabdophane- ($GdPO_4.H_2O$) type structures were synthesized using the procedure discussed in Chapters 2 and 3. The $REPO_4.H_2O$ (RE = La, Yb, Gd) materials was synthesized using a precipitation route as described in Chapter 3. The as-synthesized precipitates were filtered using a Grade 42 Whatman quantitative filter paper (pore size – 2.5 µm) and washed with large volumes of water to remove any soluble impurities. The as-synthesized precipitates were dried in air for 1

day before drying the precipitates at 60°C for 1 h. In order to obtain anhydrous $REPO_4$ (RE = La, Yb) adopting the monazite- and xenotime-type structure, the as-synthesized $REPO_4.H_2O$ (RE = La, Yb) precipitates were initially annealed at 1100°C (LaPO4) or 1200°C (YbPO4) for 1 day followed by quench cooling in air. Post-annealing, the powders of $LaPO_4$ and $YbPO_4$ were then pressed into pellets at 6 MPa and annealed at 1100°C or 1200°C for 2 days before being quench cooled in air. The $LaPO_4$, $YbPO_4$, and $GdPO_4.H_2O$ powders were ground and sieved using a 90 micron sieve in order to obtain particles with a similar range of particle sizes (≤ 90 μm) prior to the leaching experiments.

The specific surface areas ($SA_{specific}$) of the powders were calculated using Equation 5.1 by assuming the particles to be spherical in shape.[251]

$$Specific\ Surface\ Area, SA_{specific}\ \left(\frac{cm^2}{g}\right) = \frac{Area\ of\ Sphere}{Mass} = \frac{\pi d^2}{\rho \times Volume\ of\ Sphere} = \frac{6}{\rho \times d} \quad (5.1)$$

In Equation 5.1, ρ and d represents the density of the wasteform and the diameter of the particle (or particle size), respectively. The densities (ρ) of the $LaPO_4$, $YbPO_4$, and $GdPO_4.H_2O$ powders are 5.08 g/cm^3, 6.44 g/cm^3, and 5.01 g/cm^3.[126,135] Since the as-synthesized $REPO_4.H_2O$ (RE = La, Yb, Gd) precipitates were initially filtered using a 2.5 micron filter paper, the probable lower and upper limit of the particle sizes of the $LaPO_4$, $YbPO_4$, and $GdPO_4.H_2O$ powders was 2.5 μm and 90 μm; however, the distribution of particle sizes in the aforementioned powders was not determined and, as a result, the average particle size was not determined in this study. The particle size (d), therefore, was assumed to be 90 μm in this study. The calculated specific surface areas ($SA_{specific}$) of the $LaPO_4$, $YbPO_4$, and $GdPO_4.H_2O$ materials are listed in Table 5-1. It should be noted that the calculated $SA_{specific}$ could be different from the measured $SA_{specific}$ obtained using Brunauer-Emmett-Teller (BET) technique.

Table 5-1 Calculated total surface area (SA) of $YbPO_4$, $LaPO_4$, and $GdPO_4.H_2O$ materials

Compounds	**Density (g/cm^3)**	**Calculated specific surface area ($SA_{specific}$)(cm^2/g)**	**Calculated total surface area (SA_{total}) (cm^2)**	**Volume of water required (mL; $SA_{total}/V = 0.3$ cm^{-1})**
$YbPO_4$	6.44	104	24.0	80
$LaPO_4$	5.08	131	30.1	100.3
$GdPO_4.H_2O$	4.93	133	30.6	104.6

5.2.2. Leaching Test

The leaching experiments were conducted at room temperature using deionized water as the leachant. About 0.23 g of the powdered $REPO_4$ (RE = La, Yb) and $GdPO_4.H_2O$ materials were used for the leaching tests and the total surface area (SA_{total}) of these powders are presented in Table 5-1. The SA_{total} of $REPO_4$ (RE = La, Yb) and $GdPO_4.H_2O$ was obtained by multiplying the $SA_{specific}$ of the respective material by the mass of the material (m = 0.23 g). Powders of these materials were placed inside separate high-density polyethylene (HDPE) containers and were filled with varying volumes of deionized water such that the ratio of calculated total surface area (SA_{total}) to the volume of water (V) was 0.3 cm^{-1}. A SA_{total}/V ratio of 0.3 cm^{-1} indicates that the volume of leachant is approximately three times the calculated total surface area of the test material. It should be noted that the ratio of calculated total surface area to the volume of water that was used in this study is higher than the ratio (0.1 cm^{-1}) reported in standard leaching test

methods.[261] According to standard leaching protocols, the volume of leachant must be ten times the total surface area of the specimen. Using this ratio would mean that large volumes of water are required for conducting leaching studies and this requirement places a limit on the type of wasteform that can be studied. For wasteforms that possess very low leach rates, the concentration of the leached elements in the solution will be very low; hence, in order to generate measurable solution concentration of the leached elements, ratios higher than 0.1 cm^{-1} are generally used. The volumes of deionized water required to fill the HDPE vessels containing the $REPO_4$ (RE = La, Yb) and $GdPO_4.H_2O$ materials are listed in Table 5-1.

Two series of leaching experiments were conducted in order to analyze the leaching behaviour of rare-earth phosphates in deionized water, and to determine the effect of leaching on the long-range and local structure of the test materials. In the first set of leaching experiments, the leaching behaviour was studied by performing triplicate experiments on each test material under semi-static conditions in which 5 mL of the leachant solution was withdrawn from the test vessel according to the schedule shown in Table 5-2 and renewed with the same volume of fresh deionized water. Each test vessel was shaken manually once every day during the entire three month period in order to speed up the leaching process. After stirring, the solution was left undisturbed until the solids settled. The withdrawn leachant solution was tested for the presence of RE (RE = La, Yb, Gd) and P ions using an ICP-MS instrument (Perkin Elmer NexION 300D) located in the Aqueous Geochemistry Laboratory, Department of Geological Sciences, University of Saskatchewan (Saskatoon, Canada). It should be noted that the withdrawn leachant solution was not filtered prior to ICP-MS analysis. The ICP-MS data was collected from the leachant solution over a period of two months. The instrumental detection limits for the P, La, Gd, and Yb ions in solution are 100 ppb, 0.40 ppb, 1.00 ppb, and 0.04 ppb, respectively. ICP-MS analysis

was also performed on a blank solution (i.e., deionized water) to determine the concentration of RE and P elements in the deionized water used during this study. It was found that the RE and P ions, if present in the blank solution, have concentrations that are below the detection limits of the instrument.

Table 5-2 Schedule for ICP-MS data collection

Leachant collection/renewal schedule
1st Week (Day 1, 3, 5, 7)
Once/week for three weeks
Once/month for two months

The normalized leach (or release) rates of RE and P ions from $LaPO_4$, $YbPO_4$, and $GdPO_4.H_2O$ materials were calculated using Equation 5.2:[245]

$$Normalized\ Leach\ Rate = \frac{m}{f \times SA_{Total} \times t} \quad (5.2)$$

In Equation 5.2, *m* indicates the mass (in g) of the leached ion in the leachate, *f* is the mass ratio of the leached ion in the wasteform, SA_{total} (in m^2) represents the calculated total surface area of the material, and *t* indicates the time interval (in days) in which the leachant solution was collected. The mass (*m*) of the ions in the leachate were derived by multiplying the concentration of RE and P ions in the leachate with the volume of the leachant.

A second set of leaching experiments were carried out under static conditions (i.e., the leachant solution was not withdrawn during the three month time period) to determine the

structural response of $REPO_4$ (RE = La, Yb) and $GdPO_4.H_2O$ materials after exposure to deionized water for one, two, and three months. The structural response of $REPO_4$ (RE = La, Yb) and $GdPO_4.H_2O$ materials when exposed to water for a longer time period was also determined in this study by recovering the $REPO_4$ (RE = La, Yb) and $GdPO_4.H_2O$ materials from the first set of leaching experiments after exposure to deionized water for six and seven months.

5.2.3. Powder XRD

The long-range structure of $REPO_4$ and $REPO_4.H_2O$ materials before and after leaching was determined by obtaining powder XRD patterns from these materials using a PANalytical Empyrean system employed with a Co $K\alpha_{1,2}$ source. The samples were finely ground and the powder XRD patterns were collected from 10° to 80° using a step size of 0.017°. The lattice constants of the $REPO_4$ (RE = La, Yb) and $GdPO_4.H_2O$ materials were determined using the HighScore Plus software program.[178] The crystallite sizes of $GdPO_4.H_2O$, $LaPO_4$, and $YbPO_4$ materials were calculated using the Scherrer equation shown in Equation 5.3:

$$B = \frac{K\lambda}{D\cos\theta} \tag{5.3}$$

In Equation 5.3, B denotes the full width at half maxima (FWHM; in degrees) of the diffraction peak, K represents the shape factor, λ is the wavelength of the Co Kα X-ray source, and D refers to the crystallite size (in nm). The broadening observed in a diffraction peak contains contributions from the sample and instrument. In order to eliminate the effects of instrumental broadening, powder XRD patterns were collected from a polycrystalline silicon disk to determine the instrumental FWHM. The peak broadening due to the sample was calculated by subtracting the instrumental FWHM from the FWHM of the observed diffraction peak. In this study, the

particles were assumed to be spherical in shape and so a K value of 0.9 was used in the calculation.

5.2.4 XANES

5.2.4.1 P K-edge XANES

The P K-edge XANES spectra were collected from the as-synthesized and leached samples of $REPO_4$ (RE = La, Yb) and $GdPO_4.H_2O$ materials using the Sector 9 – Bending Magnet (9 BM) beamline located at the Advanced Photon Source (APS) and the Soft X-ray Micro-characterization Beamline (SXRMB; 06B1-1) located at the Canadian Light Source (CLS).[179] Monochromatic X-rays were obtained using a Si (111) monochromator and the energy resolution of the P K-edge (E_0 = 2145.5 eV) spectrum was 0.2 eV. Finely ground powders of $REPO_4$ and $GdPO_4.H_2O$ materials were spread uniformly over carbon tape and placed inside the sample chamber. At the 9 BM beamline, the sample chamber was filled with 100% Helium gas whereas at the SXRMB beamline the sample chamber was held under vacuum. The P K-edge XANES spectra were obtained in partial fluorescent yield (PFY) mode using a step size of 0.15 eV through the absorption edge. It must be noted that the P K-edge spectra of $GdPO_4.H_2O$ collected in PFY mode exhibited signs of absorption effects at the near-edge region. Therefore, the P K-edge spectra of $GdPO_4.H_2O$ collected in TEY mode was used for analysis as the TEY signal is devoid of absorption effects. The TEY signal was also obtained for the $REPO_4$ (RE = La, Yb) materials; however, the P K-spectra obtained in PFY and TEY modes were observed to be similar and so the spectra collected in PFY mode was used for analysis. The P K-edge spectra were calibrated by collecting the spectra from red P and setting the maximum in the first derivative

from the red P P K-edge spectrum to 2145.5 eV.[180] All XANES spectra discussed in this study were analyzed using the Athena software program.[181]

5.2.4.2 P $L_{2,3}$-edge XANES

The P $L_{2,3}$-edge XANES spectra were collected from the as-synthesized and leached $REPO_4$ (RE = La, Yb) and $GdPO_4.H_2O$ materials using the Variable Line Spacing – Plane Grating Monochromator (VLS-PGM; 11ID-2) beamline at the CLS.[182] The entrance and exit slit sizes for the X-rays to travel through were set to 50 µm. Further details about the experiment and sample preparation were provided in Section 2.2.2.2. The P $L_{2,3}$-edge spectra were collected in a TFY mode with the step size being 0.05 eV through the absorption edge.

5.2.4.3 RE L_1-edge (RE = La, Yb, Gd) XANES

The RE L_1-edge (RE = La, Yb, Gd) XANES spectra were collected from the $REPO_4$ (RE = La, Yb) and $GdPO_4.H_2O$ materials before and after exposure to leaching conditions using the Sector 9 BM beamline located at the APS. The spectra were collected in both transmission and fluorescence modes and the ionization chambers (I_0, I_T, and I_{ref}) were filled with 100% N_2 gas. The fluorescence signal was detected using a 4 element vortex detector. The spectra obtained in transmission mode were used in this study for analysis as the fluorescence signals are prone to absorption effects. The experimental details and sample preparation procedure were discussed in Section 3.2.3.3. The RE (RE = La, Yb, Gd) L_1-edge spectra were collected using a step size of 0.15 eV through the absorption edge. The energy resolution of the RE L_1-edge spectra varied from 0.6 eV (La L_1-edge) to 1.0 eV (Yb L_1-edge). Calibration of the spectra was performed by collecting the K-edge spectra from metal foils placed between the I_T and I_{ref} chambers and setting the maximum in the first derivative of the metal K-edge spectra to their respective absorption

energy. Calibration of the La L_1-, Yb L_1-, and Gd L_1- edge spectra was done using Mn (E_0 = 6539 eV), Ga (E_0 = 10367 eV), and Ni (E_0 = 8333 eV) metal foils, respectively.[180]

5.3 Results and Discussion

5.3.1. Powder XRD: Before Leaching

Prior to the leaching experiment, powder XRD patterns were collected from the as-synthesized $LaPO_4$ (monazite-type), $YbPO_4$ (xenotime-type), and $GdPO_4.H_2O$ (rhabdophane-type) materials in order to determine the phase purity of these materials (Figure 5.1). The powder XRD patterns shown in Figure 5.1 reveal the phase purity of the as-synthesized materials. The lattice constants of $LaPO_4$, $YbPO_4$, and $GdPO_4.H_2O$ materials are listed in Table 5-3. When compared to the powder XRD patterns from the $LaPO_4$ and $YbPO_4$ materials, the powder XRD pattern of $GdPO_4.H_2O$ materials contains broader diffraction peaks (Figure 5.1). The diffraction peaks in powder XRD patterns could broaden due to the presence of smaller sized crystallites and/or lattice strain in the crystalline solid. Since the $GdPO_4.H_2O$ materials were synthesized at a temperature much lower than that required for the synthesis of $LaPO_4$ and $YbPO_4$ materials, it is more likely that the peak broadening observed in the powder XRD pattern of $GdPO_4.H_2O$ is due to the presence of smaller sized crystallites in the $GdPO_4.H_2O$ material. The crystallite sizes of the $GdPO_4.H_2O$, $LaPO_4$, and $YbPO_4$ materials were calculated using Equation 5.3 assuming negligible contribution of strain towards peak broadening, and are listed in Table 5-3. As shown in Table 5-3, the crystallite size of the $GdPO_4.H_2O$ material is lower than that of $LaPO_4$ or $YbPO_4$.

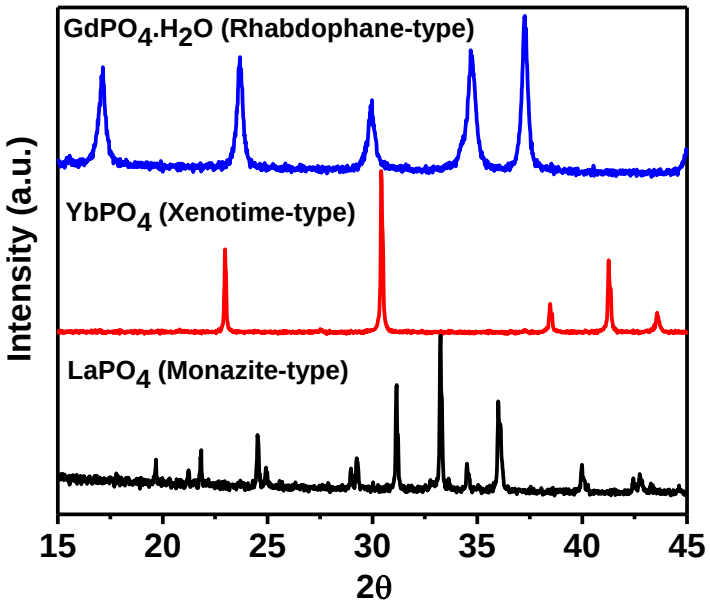

Figure 5.1 Powder XRD patterns of as-synthesized $LaPO_4$, $YbPO_4$, and $GdPO_4.H_2O$ materials collected before leaching are presented.

Table 5-3 Lattice constants and average crystallite sizes of $LaPO_4$, $YbPO_4$, and $GdPO_4.H_2O$

Compounds	Lattice constants	Average crystallite size (nm)
$LaPO_4$	a = 6.5084 (4) Å	156
	b = 7.0742 (5) Å	
	c = 8.2869 (5) Å	
	β = 126.574 (3)°	
$YbPO_4$	a = b = 6.8156 (2) Å	152
	c = 5.9708 (2) Å	
$GdPO_4.H_2O$	a = 27.964 (7) Å	22
	b = 6.925 (1) Å	
	c = 11.931 (2) Å	
	β = 115.26 (3)°	

5.3.2. ICP-MS: Leaching behaviour of $REPO_4$ and $REPO_4.H_2O$

The chemical durability of the $LaPO_4$ (monazite-type), $YbPO_4$ (xenotime-type), and $GdPO_4.H_2O$ (rhabdophane-type) materials upon exposure to deionized water was studied by withdrawing aliquots of deionized water from the respective test vessel at regular time intervals (See Table 5-2) and analyzing the leachate solution for RE (RE = La, Yb, Gd) and P ions using ICP-MS. The elemental concentration of RE (RE = La, Yb, Gd) and P ions in the leachate determined using ICP-MS are plotted as a function of time and are presented in Figure 5.2. The ICP-MS data obtained on Day 1 indicated that the $GdPO_4.H_2O$ material (rhabdophane-type) released higher amounts of RE (RE = Gd) and P ions to the leachant solution when compared to those released by $LaPO_4$ (monazite-type) and $YbPO_4$ (xenotime-type) (Figure 5.2). However, the $LaPO_4$ and $YbPO_4$ materials were found to exhibit similar chemical behaviour on Day 1. The differential chemical response of these materials in deionized water is attributed to the differences in the crystal structure, crystallinity, and solubility of the as-synthesized $LaPO_4$, $YbPO_4$, and $GdPO_4.H_2O$ materials.[252]

In terms of crystal structure, the rhabdophane structure consists of infinite channels oriented along the 'a' direction and the water of crystallization associated with this structure resides in this channel (See Figure 1.4).[126] In this study, it is proposed that the leachant solution (i.e. deionized water) may diffuse through these channels and interact with the RE and P elements present in the rhabdophane structure which might allow for a greater leaching of the rhabdophane-type material. The crystallinity of the materials prior to the leaching experiment may also have an effect on the leaching process. In Section 5.3.1, it was shown using powder XRD that the rhabdophane-type material is less crystalline when compared to materials adopting the monazite- and xenotime- type structure (See Table 5-3). The individual crystallites within a

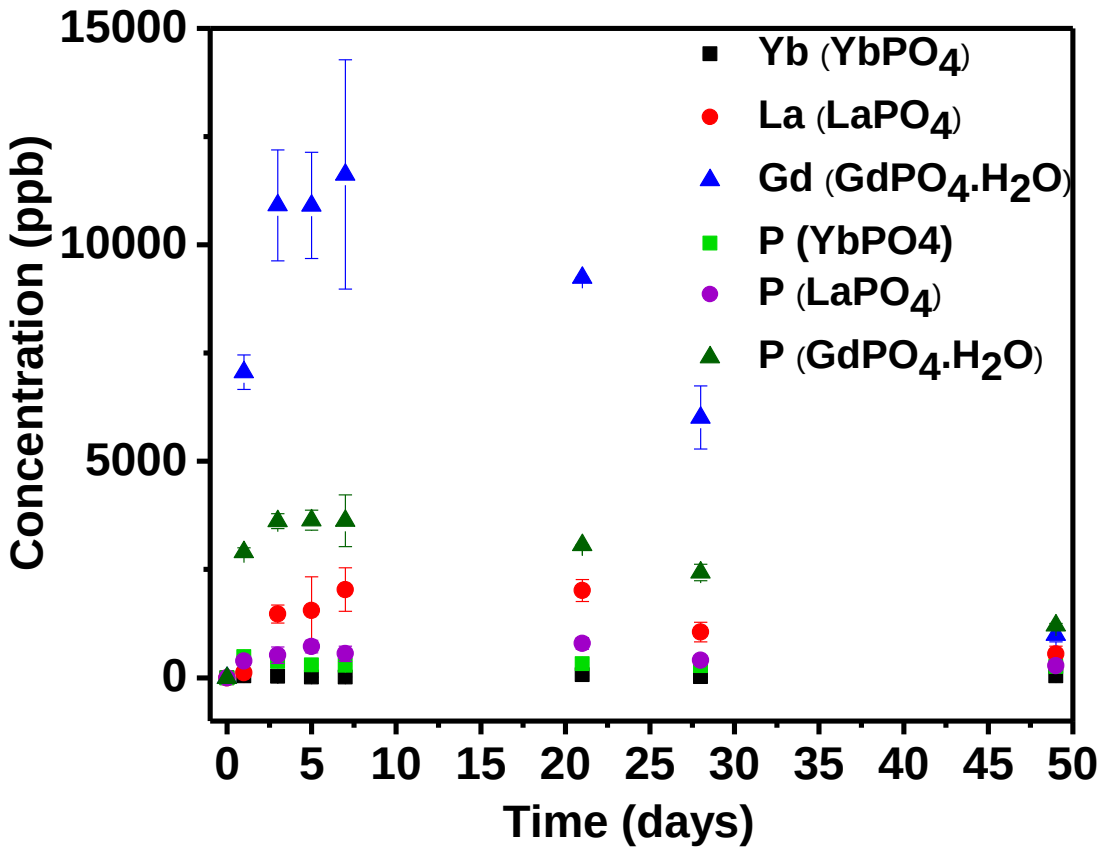

Figure 5.2 The concentration of RE (RE = La, Yb, Gd) and P ions in leachate solutions withdrawn from vessels containing $LaPO_4$, $YbPO_4$, and $GdPO_4.H_2O$ materials plotted against time are presented. The concentration of ions in the leachate was obtained using ICP-MS.

polycrystalline material are separated by a grain boundary and a study by Rakesh et al. has shown that during leaching experiments, these grain boundaries will serve as a preferred site for chemical attack.[253] The number of grain boundaries in a material generally varies inversely with the crystallite size. Therefore, the presence of smaller sized crystallites in rhabdophane-type material will increase the number of grain boundaries which in turn may allow for a greater leaching of the rhabdophane-type material in deionized water.

The concentration of RE (RE = La, Gd) and P ions in the leachate solution released by the $LaPO_4$ and $GdPO_4.H_2O$ materials displayed a similar increasing trend during the first week. However, in the case of $YbPO_4$, the concentration of Yb and P ions in the leachate solution did not change significantly during the first week and were found to be similar. These observations could suggest the establishment of equilibrium between $YbPO_4$ and its constituent ions at an early stage of the leaching experiment. It is also observed in Figure 5.2 that the concentration of RE (RE = La, Gd) and P ions in the leachate were not similar despite the 1:1 stoichiometry of RE and P in $LaPO_4$ and $GdPO_4.H_2O$ materials. Bois et al. investigated the leaching behaviour of $La_{0.3}Zr_2(PO_4)_3$ and $LaPO_4$ ceramics in deionized water and found that the concentration of P ions in the leachant solution is greater than the concentration of La and Zr ions.[254] The authors of that study proposed that the dissimilarity in concentration could arise from the presence of residual phosphoric acid adhering to the solid and/or due to the precipitation of secondary phases on the surface of solid as a result of leaching.[254] In the present study, the presence of phosphoric acid adhering to the solid's surface could be dispelled as the solids were washed with large volumes of water (followed by drying) prior to leaching. Similarly, the XRD analysis of the as-synthesized materials confirmed the absence of any crystalline phosphorus and/or rare-earth containing impurities and it is proposed that the differences in the concentration of RE and P ions in the

solution are most likely not associated with the presence of impurities. Leaching studies on other wasteforms have also reported a similar non-stoichiometric dissolution of solids and have ascribed the dissimilarities in the concentration of constituent ions in the leachant solution to incongruency in the leach rates of the ions.[255,256] Therefore, the observed dissimilarities in the concentration of RE and P ions in solution could also be a result of the incongruent dissolution of $REPO_4$ and $REPO_4.H_2O$ materials in deionized water (i.e., the RE and P elements may leach out at different rates upon contact with the leachant solution). Incongruent leaching of wasteforms could arise from a multitude of factors (chemical composition of the wasteform, surface roughness, and porosity of the wasteform).[252] It, is therefore difficult to account for the observed differences in the concentration of RE and P ions in the leachant solution.

It is observed in Figure 5.2 that the concentration of RE and P ions in the leachate solution collected from the test vessel containing $LaPO_4$ and $GdPO_4.H_2O$ materials decreased after one week which suggests that the release of RE and P ions into the water solution slowed and that the decrease in concentration is most likely a result of dilution of these ion concentrations caused by the addition of water to the test vessel in order to offset the removal of solution for ICP-MS analysis so as to keep the total volume constant. Similar observations were made for the $YbPO_4$ material although the decrease in the concentration of the Yb and P ions were observed after Day 1. These results could suggest the creation of an equilibrium between the solid and its constituent ions within the first week of the leaching experiment. The normalized leach rates of the $REPO_4$ and $GdPO_4.H_2O$ materials were calculated using Equation 5.2 and are plotted in Figure 5.3. An exponential decrease in the leach rates was observed for all materials. The plot of normalized leach rate versus time clearly depicts the stabilization of the concentration of RE and P ions in the leachate solution attained after the first week of leaching. The decrease in the leach rates as a

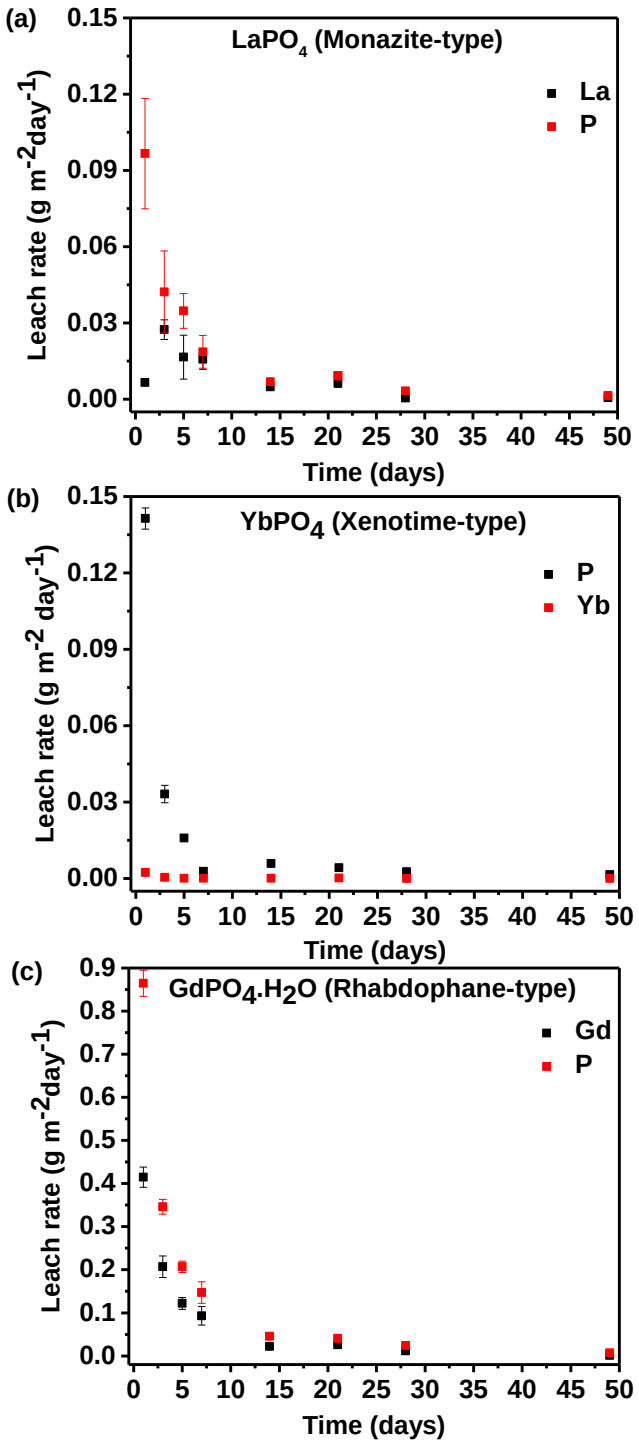

Figure 5.3 Normalized leach rates of (a) $LaPO_4$, (b) $YbPO_4$, and (c) $GdPO_4.H_2O$ versus time are shown. The leach rates of these materials drop-off with increasing time.

function of time could also be attributed to the development of a film on the surface of these materials owing to their prolonged exposure to deionized water. It should be noted that the normalized leach rates presented in this study were obtained using the calculated total surface area (SA_{total}) and the true leach rates of these materials will vary from what is shown here.

5.3.3. Powder XRD: Effect of leaching on the long-range structure

The structural response of materials to leaching was determined at different stages of the leaching experiment by obtaining powder XRD patterns from $LaPO_4$, $YbPO_4$, and $GdPO_4.H_2O$ materials every month for a total duration of seven months (Figure 5.4). The absence of secondary phases in the powder XRD pattern of $LaPO_4$, $YbPO_4$, and $GdPO_4.H_2O$ materials obtained after leaching indicates that the long-range structure of these materials is preserved after exposure to deionized water. It must be noted that in the case of $GdPO_4.H_2O$, slight broadening of the diffraction peak was observed after leaching which indicates a slight loss in the crystallinity of the material. However, no significant changes in the peak widths were observed for the $LaPO_4$ and $YbPO_4$ materials after leaching.

5.3.4. XANES: Effect of leaching on the local structure

It was shown in the previous section using powder XRD that the long-range structure of the $LaPO_4$, $YbPO_4$, and $GdPO_4.H_2O$ materials remained unaffected under aqueous leaching conditions. While XRD analysis has confirmed the absence of crystalline impurity or secondary phases after leaching, it did not offer any information about the presence of amorphous secondary phases (if any) as well as the changes in local structure upon exposure of the materials to deionized water. XANES spectra are sensitive to changes in the local structure of materials.

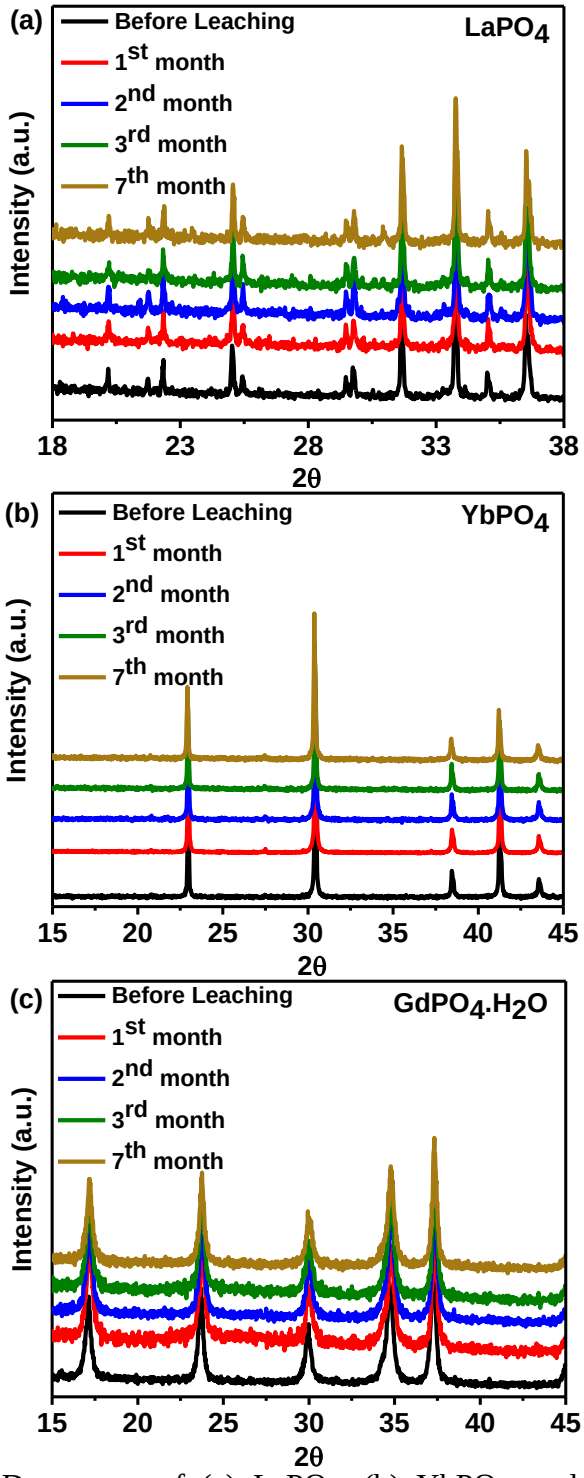

Figure 5.4 Powder XRD patterns of (a) $LaPO_4$, (b) $YbPO_4$, and (c) $GdPO_4.H_2O$ materials obtained before and after leaching are presented.

Therefore, P K-, P $L_{2,3}$-, and RE L_1-edge XANES spectra were collected from $LaPO_4$, $YbPO_4$, and $GdPO_4.H_2O$ materials before and after exposure to deionized water.

5.3.4.1. P K-edge XANES

The P K-edge spectra from the $LaPO_4$, $YbPO_4$, and $GdPO_4.H_2O$ materials collected before and after leaching were normalized and are presented in Figure 5.5. The intense near-edge region in the XANES spectra corresponds to the dipole allowed P 1s → 3p transition. The difference in spectral lineshapes observed between the $LaPO_4$, $YbPO_4$, and $GdPO_4.H_2O$ materials are a result of the change in the distribution of P 3p conduction states as a result of the different crystal structures that these materials adopt. It can be observed from Figure 5.5 that the local structure of P ions in these materials also remain unaffected after leaching as indicated by the similarity of the P K-edge spectra of the leached materials to those from the as-synthesized materials; however, there is a caveat to this conclusion. Since the surface of the material is in direct contact with deionized water, it is expected that the magnitude of changes (if any) in the local structure would be larger in the surface region when compared to the bulk regions of the material. The absorption energy corresponding to the P K-edge is high enough that it provides local structural information from both the bulk and surface regions of the material. Hence, the P K-edge spectra collected from $LaPO_4$, $YbPO_4$, and $GdPO_4.H_2O$ materials after leaching do not exclusively reflect the local structure of P at the surface.

5.3.4.2. P $L_{2,3}$-edge XANES

In the previous section, it was proposed that the changes in the local structure of a material (if any) caused by leaching will be higher in the surface region of the material and that the P K-edge spectrum does not provide local structural information exclusively from the surface of the

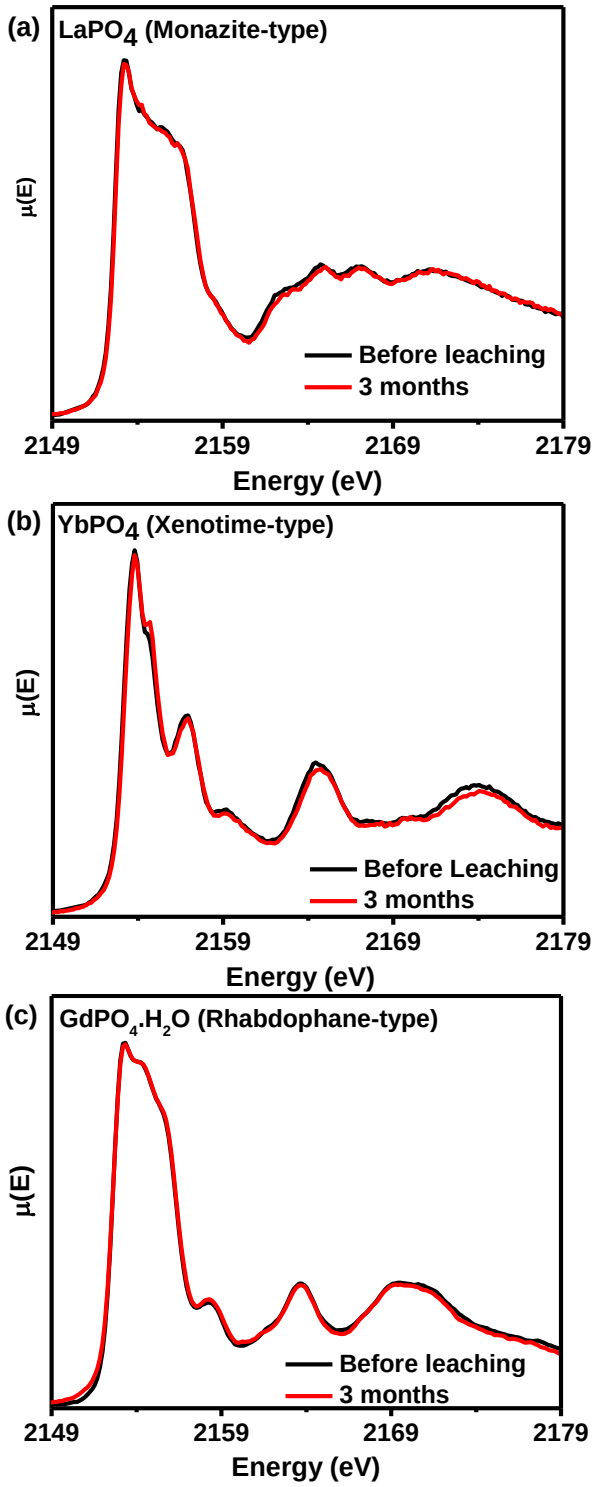

Figure 5.5 P K-edge XANES spectra of (a) $LaPO_4$, (b) $YbPO_4$, and (c) $GdPO_4.H_2O$ materials obtained before and after leaching are shown

material. P $L_{2,3}$-edge spectra were collected from $LaPO_4$, $YbPO_4$, and $GdPO_4.H_2O$ materials before and after leaching in order to obtain surface specific local structural information (Figure 5.6). The P $L_{2,3}$-edge XANES spectra are surface sensitive due to the low energy of P $L_{2,3}$-edge. The P $L_{2,3}$-edge spectra result from the transition of electrons from the spin-orbit split 2p states into unoccupied 3d and 3s states. The P $L_{2,3}$-edge spectra are structurally rich and contain various features representing the transition of electrons from the 2p state into overlapping 3d and 3s conduction states. The higher energy features present in the P $L_{2,3}$-edge spectra of $GdPO_4.H_2O$ are due to the overlap of the Gd N-edge with the P $L_{2,3}$-edge spectra. It can be observed from Figure 5.6 that the P $L_{2,3}$-edge spectra of leached samples are similar to the spectra from the as-synthesized materials. These results confirm that the local structure of the surface regions do not change significantly as a result of leaching.

5.3.4.3. RE L_1-edge XANES

The RE L_1-edge spectra were collected from $LaPO_4$, $YbPO_4$, and $GdPO_4.H_2O$ materials before and after leaching in order to determine the changes in the local structure of the RE ion (Figure 5.7). The near-edge region in the RE L_1-edge spectra represent the RE 2s → 6p transition. In the pre-edge region, a small shoulder is observed as a result of a RE 2s → 6p-5d transition. The pre-edge feature is sensitive to the local symmetry of the RE ion and the intensity of this feature generally increases with decreasing local symmetry around the RE ion. The pre-edge shoulder observed in the Yb L_1-edge spectra is less pronounced when compared to the pre-edge regions in the La L_1- and Gd L_1-edge spectra (Figure 5.7) because the YbO_8 polyhedra in $YbPO_4$ are more symmetrical when compared to the LaO_9 and GdO_n (n = 8 and 9) polyhedra in the $LaPO_4$ and $GdPO_4.H_2O$ materials.[126,135] Similar to the results obtained from analysis of the P K- and P $L_{2,3}$-

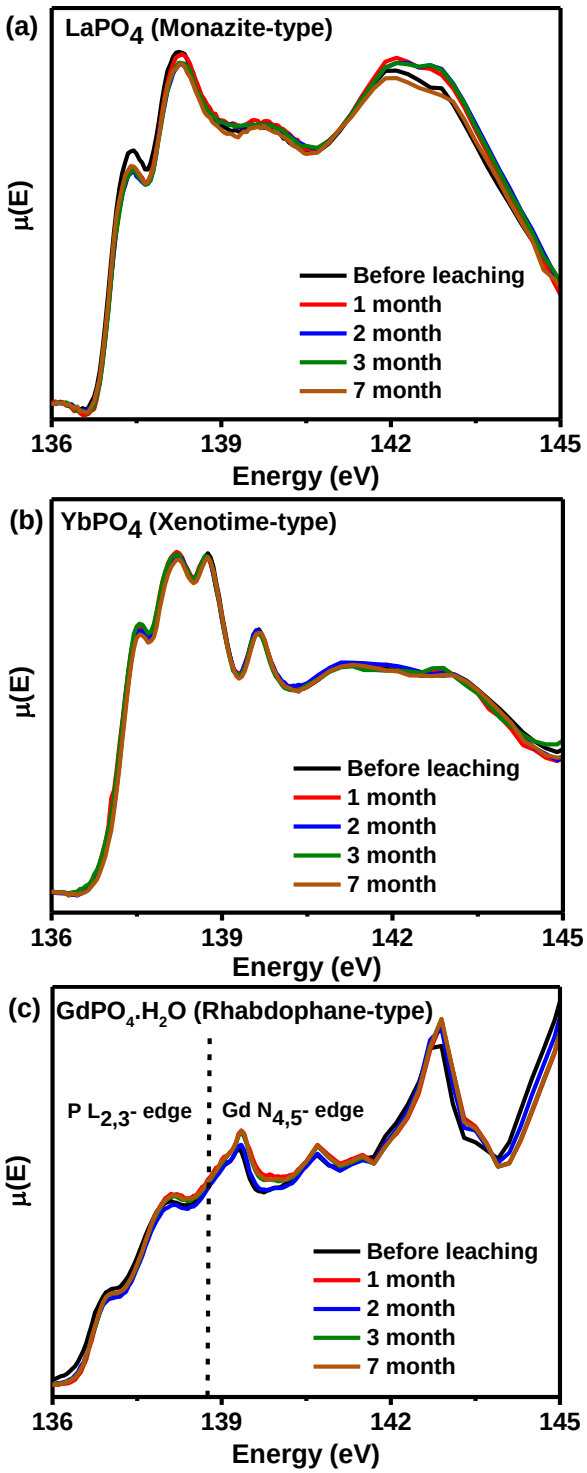

Figure 5.6 P $L_{2,3}$-edge XANES spectra of (a) $LaPO_4$, (b) $YbPO_4$, and (c) $GdPO_4.H_2O$ materials obtained before and after leaching are shown. The high energy region of the P $L_{2,3}$-edge spectra of $GdPO_4.H_2O$ is masked due to interference from the Gd $N_{4,5}$-edge.

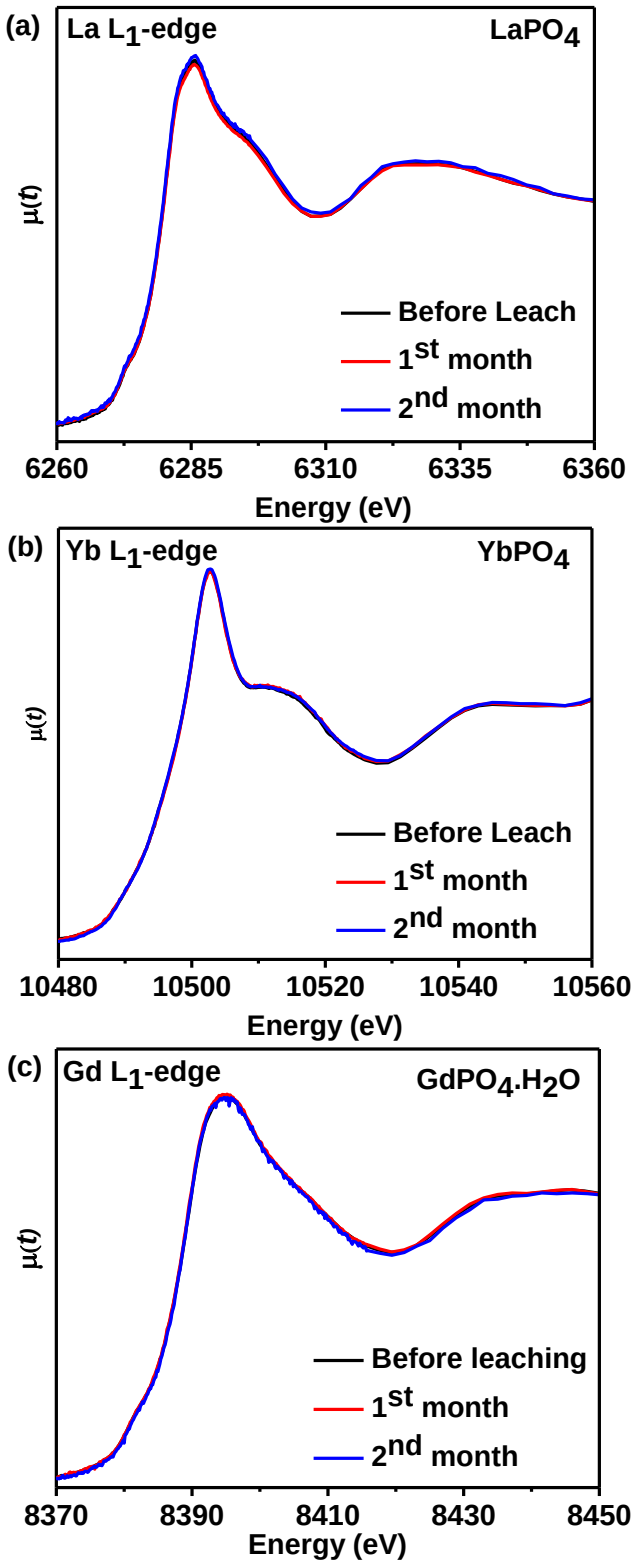

Figure 5.7 RE L_1-edge XANES spectra of (a) $LaPO_4$, (b) $YbPO_4$, and (c) $GdPO_4.H_2O$ materials obtained before and after leaching are presented.

edge spectra, no significant changes in the local structure of the RE ions were observed after leaching.

5.4 Conclusion

This study has investigated the room temperature chemical durability of monazite-, xenotime-, and rhabdophane-type rare-earth phosphates by conducting the leaching experiments in deionized water under semi-static conditions. In terms of chemical response, the material adopting the rhabdophane structure was found to dissolve more in deionized water when compared to materials adopting the monazite- and xenotime-type structures. A stabilization in the concentration of RE and P ions in the water solution was attained for all three materials after one week of leaching. Examination of the long-range and local structures of these materials before and after leaching was carried out using powder XRD and XANES, respectively. No significant changes in the powder XRD pattern and XANES spectra of the leached samples were observed when compared to those of as-synthesized samples. This observation is ascribed to the fact that the concentration of the leached ions in solution are only in the ppb – ppm range. Therefore, these materials exhibit little to no change in their long-range and local structure after leaching. This study, for the first time, has provided a comparison of the dissolution behaviour of monazite-, xenotime-, *and* rhabdophane-type materials in an aqueous environment and has shown that the structures of these materials remain intact after seven months of leaching. This study has provided the basis for conducting future leaching experiments on these materials under harsh chemical conditions including conditions that simulate the groundwater in a geological repository.

Chapter 6

CONCLUSIONS AND FUTURE WORK

6.1. Conclusions and Significance

The studies presented in this thesis have contributed to a much broader understanding of the structural properties of monazite-, xenotime-, and rhabdophane-type rare-earth phosphate materials and how these materials would respond to conditions simulating the effects of radiation in nuclear wasteforms as well as conditions simulating a failed container situation in a geological repository (i.e., the metal container that holds the nuclear wasteform fails and groundwater enters the container and interacts with the nuclear wasteform). The results that were presented in this thesis will add to a growing body of fundamental research work on various crystalline materials proposed for nuclear waste sequestration applications. This research will assist in the selection process of potential candidate materials for storing nuclear waste.

In Chapter 2, a fundamental understanding of the crystal and electronic structure of monazite- and xenotime-type rare-earth phosphates was obtained using X-ray diffraction and spectroscopic techniques. Naturally occurring rare-earth phosphate minerals reveal the existence of monazite-xenotime solid solutions, and, in Chapter 2, the solubility limit for the substitution of smaller sized rare-earth (RE) ions into the larger sized RE site in the monazite-type structure was

studied by synthesizing $RE_{1-x}RE'_xPO_4$ (RE = La, Sm; RE' = Yb, Y, Ho) materials via a conventional solid-state method. The end-members of the $RE_{1-x}RE'_xPO_4$ series adopt the monazite- (x = 0) and xenotime-type (x = 1) structures. Powder X-ray diffraction (XRD) analysis of these materials indicated the formation of a solid solution over a narrow compositional range ($0.1 \leq x \leq 0.2$). The electronic structure of these materials was investigated using X-ray absorption near-edge spectroscopy (XANES) and X-ray photoelectron spectroscopy (XPS). While the XPS spectra exhibited very minor changes in binding energy between the two structures, significant differences in absorption energy and spectral lineshape were observed in the P K-edge XANES spectra of materials adopting either monazite or xenotime structures. This study has shown that the XANES spectra are influenced by changes in the crystal structure of these materials and that P K-edge XANES spectra could be used as a spectroscopic fingerprint for the identification of monazite- and xenotime-type structures in natural and synthetic samples.

The long-range and local structures of hydrous rare-earth phosphates ($REPO_4.H_2O$) adopting the rhabdophane- (RE = La - Dy) and xenotime-type (RE = Tb – Lu & Y) structures were investigated in detail using powder XRD and XANES and the results obtained from this study was presented in Chapter 3. The $REPO_4.H_2O$ materials were synthesized using a low temperature precipitation route in which RE_2O_3 was dissolved in concentrated H_3PO_4 and the clear solution was refluxed at temperatures above the boiling point of water to obtain the $REPO_4.H_2O$ precipitate. The crystal structure of the rhabdophane materials was determined by performing a Rietveld refinement of the XRD data and it was found that the rhabdophane materials adopts the monoclinic structure rather than the most often reported hexagonal structure. Thermogravimetric analysis (TGA) of the $REPO_4.H_2O$ materials has confirmed the removal of water at specific temperatures and this study determined the structure of these materials after the

removal of water by annealing the as-synthesized $REPO_4.H_2O$ materials at a variety of temperatures. The structure of the resulting products was determined ex-situ using powder XRD and XANES. It was found through this study that the rhabdophane-type structure is metastable and transforms into thermodynamically stable monazite- or xenotime-type structures at higher temperatures depending on the size of RE ion. The xenotime-type $REPO_4.H_2O$ material was found to be structurally stable at all temperatures studied although minor variations in the powder XRD and XANES spectra were observed upon removal of water molecules. This study, for the first time, has provided detailed insights into the structure of $REPO_4.H_2O$ materials and how these materials would respond to changes in temperature. In terms of nuclear wasteform applications, understanding the structure of $REPO_4.H_2O$ materials is important as these phases are proposed to form during the aqueous alteration of monazite- and xenotime-type rare-earth phosphates.[128–132]

An actinide element incorporated in a crystalline ceramic can undergo a radioactive decay process during which the crystalline matrix could experience structural damage from the high recoil energies associated with daughter product radionuclide. Therefore, the radiation damage due to recoil atom was simulated by implanting high energy Au^- ions (2 MeV) of varying ion doses (ions/cm^2) into pellets of $La_{1-x}Yb_xPO_4$ and the structural response of these materials to ion-implantation was determined and was discussed in Chapter 4. The Au^- ions were implanted in the surface regions of the pellet. Glancing angle XANES (GA-XANES) and μ-XRD were used to obtain the structural information from the ion-implanted regions of the pellet. In this study, the GA-XANES was shown to be an effective technique in obtaining local structural information from materials in which the chemical environment surrounding the element of interest at the surface region is different from those present in the bulk region. The P K-edge GA-XANES

spectra obtained from ion-implanted monazite- and xenotime-type materials reveal a distortion in the local structure around P ion after ion implantation. However, the P K-edge GA-XANES spectra from xenotime-type materials implanted with a high dose of Au^{-} ions exhibited signs of partial structural recovery as indicated by the partial resemblance of the GA-XANES spectra from the ion-implanted material to those obtained before ion-implantation. The high ion dose could cause local heating of the ion-implanted material which therefore induces a partial recrystallization of the material. This is an important result for nuclear wasteform applications because actinides emit heat during the radioactive decay process and the emitted heat could restore the structural order in a structurally damaged crystalline host matrix. This study also investigated the effect of radioactive decay heat on the structure of ion-implanted monazite- and xenotime-type materials by annealing the ion-implanted materials to 300°C and 900°C and investigating the structural response to these temperatures using GA-XANES. Depending on the annealing temperature and composition, the structures of ion-implanted monazite and xenotime materials were found to recover either partially or completely upon annealing. The results obtained from this study point out the structural resilience of monazite- and xenotime-type materials thereby making them an ideal candidate for storing radioactive waste.

Assessing the chemical durability of nuclear wasteforms is of the utmost importance and results obtained from the short-term leaching studies on monazite-, xenotime-, and rhabdophane-type materials were presented in Chapter 5. Deionized water was used as a leaching medium and powders of as-synthesized materials were exposed to deionized water at room temperature for a total period of three months. The elemental concentration in the leachate (i.e., deionized water) was determined using ICP-MS. Based on the ICP-MS data, it was found that materials adopting the rhabdophane structure leach at a faster rate when compared to monazite- and xenotime-type

materials. Structural characterization of materials before and after leaching was performed using powder XRD and XANES. Both the long-range and local structures of these materials were found to remain unaltered after leaching. This preliminary study has determined the chemical and structural response of hydrous and anhydrous rare-earth phosphates to aqueous conditions at room temperature and in doing so provides the groundwork for carrying out advanced leaching studies (i.e., leaching under basic and acidic conditions; temperature-dependent leaching study etc.) on these materials.

This thesis discussed the structure, radiation stability, and chemical durability of rare-earth phosphate materials proposed for nuclear waste sequestration applications. The work presented in Chapters 2 and 3 showcases the rich structural chemistry of monazite-, xenotime-, and rhabdophane-type rare-earth phosphates by providing a comprehensive understanding of the long-range and local structures of monazite-, xenotime-, and rhabdophane-type materials using powder XRD and XANES. One of the major findings from these studies is that the P K-edge XANES spectra from these materials have a distinct spectral lineshape which allows for the detailed elucidation of the local environment around the P ion in these materials. The structural richness of P K-edge XANES spectra was exploited in Chapter 4 of this thesis wherein the structural response of monazite- and xenotime-type materials to high energy Au^- ion-implantation was monitored primarily using P K-edge XANES spectra collected in a glancing angle mode. In this Chapter, the structural stability of monazite- and xenotime-type materials to radiation events caused by actinide incorporation in crystalline materials was studied by simulating these events in a laboratory through high energy heavy ion implantation in solids. This method of study allowed for a quick determination of structural response of materials to radiation events accumulated as a result of at least 100 years of actinide storage. Through the use of GA-XANES,

this study has shown that the monazite- and xenotime-type ceramics lose local order after ion-implantation but can be restored back to their original structure either partially or completely upon annealing to temperatures ≥ 300°C. Having determined the structure and radiation stability of rare-earth phosphate materials, the final chapter of this thesis addressed the chemical durability of monazite-, xenotime-, and rhabdophane-type structures upon exposure to deionized water. In this study, a comparison of the dissolution behaviour of these materials was made and it was found that the materials adopting the rhabdophane-type structure dissolves more when compared to materials adopting the monazite- and xenotime-type structures. All of the studies that were presented in this thesis have provided a greater understanding of the structure of rare-earth phosphate materials from both a fundamental and practical standpoint.

6.2. Future Work

A great deal of information about the structure and properties of monazite-, xenotime-, and rhabdophane-type rare-earth phosphate materials has been presented in this thesis. The work presented in this thesis discussed the long-range, local, and electronic structure of hydrous and anhydrous rare-earth phosphate materials in addition to discussing the effect of radiation damage and leaching on the structure of these materials. The complex structure and structural transformations of rhabdophane-type materials presented in Chapter 3 of this thesis opens up new possibilities for carrying out solid state exploratory research. Similarly, the results obtained from the radiation (Chapter 4) and leaching (Chapter 5) studies of rare-earth phosphates materials can be used as a basis for further research explorations. Some of the proposed future work plans for the research presented in Chapters 3, 4, and 5 will be discussed below.

It was shown in Chapter 3 that the materials adopting the rhabdophane-type structure are sensitive to changes in temperature as indicated by the loss of water with increasing temperature. Upon complete loss of water, the rhabdophane structure can be stabilized over a narrow temperature range (e.g. 700°C < T < 800°C). Beyond this temperature range, the rhabdophane-type structure transforms into either the monazite- or xenotime-type structure thereby revealing the metastable nature of rhabdophane. The metastability of the rhabdophane phase therefore makes it an ideal system to study under extreme pressure conditions. The use of extreme pressures could open up new pathways for obtaining novel crystal structures with exotic properties and no studies have yet been reported in the literature on the effect of pressure on the structure of rhabdophane. This study is purely exploratory in nature and the major objective of this study would be to determine how the crystal structure of rhabdophane materials varies as a function of pressure. The high-pressure route could potentially lead to the formation of new materials which may not be accessible via high temperature methods. To this end, the extreme pressures required for conducting this study would be achieved through the use of a Diamond Anvil Cell (DAC). The DAC allows for the study of materials over a wide-range of pressures ranging from a few GPa to pressures typically found in the Earth's core (~ 380 GPa).[257] The structural response of these materials to varying pressures (e.g., 1 GPa – 100 GPa) can be monitored using X-ray based diffraction and spectroscopic techniques (e.g., XANES).

The effect of energetic α-recoil nuclei (daughter products) on the structure of monazite- and xenotime-type rare-earth phosphates was studied by simulating the radiation events in these materials via high energy Au^{-} ion implantation in Chapter 4. This study has successfully demonstrated the use of GA-XANES to obtain selective local structural information from the ion-implanted regions of the material and the resulting GA-XANES spectra indicate a change in the

local structure of these materials after ion-implantation. In an α-decay event, the actinide element incorporated within a wasteform decays via production of high energy α-recoil nuclei and α-particles. Therefore, the role played by α-particles on the structure of crystalline wasteform must also be taken into account while conducting radiation studies on proposed materials of interest. This can be done by implanting high-energy He ions into the surface of sintered pellets of materials adopting the monazite- and xenotime-type structures and the structural characterization can be performed using glancing angle XRD and XANES. Some studies in the literature have provided evidence of structural recovery of heavy ion implanted ceramics upon irradiating the ion-implanted material with high energy electron beams.[89,104,106] To this end, the sintered pellets of monazite and xenotime materials could be exposed to 2 MeV Au^- ion beams at a specified dose (ions/cm^2) followed by exposure to a similar dosage of 2 MeV He ions. This study would determine the combined effects of α-particles and α-recoil atoms on the structure of monazite- and xenotime-type materials.

In the concluding study of this thesis, preliminary leaching experiments were conducted on materials adopting the monazite-, xenotime-, and rhabdophane-type structure and the results were presented in Chapter 5. This study has shown that the structure (bulk and surface) of these materials remain unaltered after exposure to deionized water for three months. In a failed container situation in a geological repository, the wasteform could be exposed to groundwater for very long periods of time. Depending on the location of the geological repository, the groundwater could be either acidic or basic or neutral. Accordingly, the chemical durability of rare-earth phosphate materials under those conditions can be studied by conducting the leaching experiments in harsh media (e.g., acidic and basic solutions). The use of acidic and basic solutions also speeds up the leaching of the materials and would effectively simulate the long-

term exposure of wasteforms to groundwater.[249,258,259] The leaching studies can also be conducted using natural groundwater samples collected from sites proposed for geological repository construction. It is reported in the literature that the rhabdophane mineral grows on the surface of monazite minerals as a result of aqueous alteration of the latter.[126,128–134] Therefore, it is important to determine if the surface of the synthetic monazite samples could be chemically altered in a reasonable time scale to produce a thick surface layer with a chemical composition resembling that of rhabdophane. This study could be conducted by exposing the pellets of synthetic analogues of monazite material to strong basic or acidic solutions for long periods of time. After the leaching experiments, the surface of the pellets could be examined using glancing angle XRD and XANES. Formation of the rhabdophane phase on the surface of monazite material can be confirmed by comparing the glancing angle XRD and XANES data of the surface of the pellet with that of a standard rhabdophane material.

REFERENCES

(1) United Nations, Department of Economic and Social Affairs, Population Division (2015). *World Population Prospects: The 2015 Revision, Key Findings and Advance Tables*. Working Paper No. ESA/P/WP.241

(2) Asif, M.; Muneer, T. *Renew. Sustain. Energy Rev.* **2007**, *11*, 1388–1413.

(3) Franco, S.; Mandla, V. R.; Ram Mohan Rao, K. *Renew. Sustain. Energy Rev.* **2017**, *71*, 898–907.

(4) Höök, M.; Tang, X. *Energy Policy* **2013**, *52*, 797–809.

(5) Newbold, K. B. 2017. Population Growth. The *International Encyclopedia of Geography. 1-6.*

(6) Wang, J.; Feng, L.; Tang, X.; Bentley, Y.; Höök, M. *Futures* **2017**, *86*, 58–72.

(7) Hoffert, M. I.; Caldeira, K.; Benford, G.; Criswell, D. R.; Green, C.; Herzog, H.; Jain, A. K.; Kheshgi, H. S.; Lackner, K. S.; Lewis, J. S.; Lightfoot, H. D.; Manheimer, W.; Mankins, J. C.; Mauel, M. E.; Perkins, L. J.; Schlesinger, M. E.; Volk, T.; Wigley, T. M. L. *Science* **2002**, *298*, 981–987.

(8) Menyah, K.; Wolde-Rufael, Y. *Energy Policy* **2010**, *38*, 2911–2915.

(9) Dresselhaus, M. S.; Thomas, I. L. *Nature* **2001**, *414*, 332–337.

(10) Panwar, N. L.; Kaushik, S. C.; Kothari, S. *Renew. Sustain. Energy Rev.* **2011**, *15*, 1513–1524.

(11) Lund, H. *Energy* **2007**, *32*, 912–919.

(12) Eerkens, J. W. Renewable Energy Sources and Their Limitations. *The Nuclear Imperative: A Critical Look at the Approaching Energy Crisis (More Physics for Presidents)*, 2nd Edition; Springer: Netherland, 2010; pp 65-75.

(13) Evans, A.; Strezov, V.; Evans, T. J. *Renew. Sustain. Energy Rev.* **2009**, *13*, 1082–1088.

(14) Painuly, J. P. *Renew. Energy* **2001**, *24*, 73–89.

(15) Zinkle, S. J.; Was, G. S. *Acta Mater.* **2013**, *61*, 735–758.

(16) Jewell, J. *Energy Policy* **2011**, *39*, 1041–1055.

(17) Sims, R. E. H.; Rogner, H. H.; Gregory, K. *Energy Policy* **2003**, *31*, 1315–1326.

(18) International Energy Agency. *Key World Energy Statistics*; Paris, 2016.

(19) Pękala, Ł. M.; Tan, R. R.; Foo, D. C. Y.; Jeżowski, J. M. *Appl. Energy* **2010**, *87*, 1903–1910.

(20) Abbott, D. *Proc. IEEE* **2010**, *98*, 42–66.

(21) Ewing, R. C. *Can. Mineral.* **2001**, *39*, 697-715.

(22) Sellin, P.; Leupin, O. X. *Clays Clay Miner.* **2014**, *61*, 477-498.

(23) Ewing, R. C.; Whittleston, R. A.; Yardley, B. W. D. *Elements* **2016**, *12*, 233-237.

(24) Ewing, R. C. *Proc. Natl. Acad. Sci.* **1999**, *96*, 3432–3439.

(25) McCloy, J. S.; Goel, A. *MRS Bull.* **2017**, *42*, 233–240.

(26) Montel, J.-M. *Comptes Rendus Geosci.* **2011**, *343*, 230–236.

(27) Hubbert, M. K. Nuclear Energy and The Fossil Fuel. Presented at the Spring Meeting of the Southern District, Division of Production, American Petroleum Institute, San Antonio, Texas, March 7-9, 1956.

(28) Ewing, R. C. *Can. Mineral.* **2005**, *43*, 2099–2116.

(29) *The nuclear fuel cycle : from ore to wastes*; Wilson, P. D., Ed.; Oxford University Press: New York, 1996.

(30) Dreicer, M.; Tort, V.; Margerie, H. *Nuclear Fuel Cycle: Implementation in France*; Final Report Prepared for Directorate General XII of the Commission of the European Communities in the Framework of the ExternE Project, Contract No. CCE/ARMINES JOU2-CT92-0236; August, 1995.

(31) Lenzen, M. *Energy Convers. Manag.* **2008**, *49*, 2178–2199.

(32) Lehmann, B. *Rev. Econ. Geol.* **2008**, No. 2, 16–26.

(33) Raffensperger, J. P.; Garven, G. *Am. J. Sci.* **1995**, *295*, 639–696.

(34) OECD Nuclear Energy Agency. *Uranium 2007: Resources, Production and Demand*; A Joint Report by the OECD Nuclear Energy Agency and the International Atomic Energy Agency; OECD, Paris, 2008.

(35) OECD Nuclear Energy Agency. *Trends in the Nuclear Fuel Cycle: Economic, Environmental and Social Aspect*, OECD, Paris, 2001

(36) Rosman, K. J. R.; Taylor, P. D. P. *Pure Appl. Chem.* **1998**, *70*, 217–235.

(37) International Atomic Energy Agency. *Nuclear Fuel Cycle Information System: A Directory of Nuclear Fuel Cycle Facilities*; IAEA-TECDOC-1613; IAEA, Vienna, 2009.

(38) Bruno, J.; Ewing, R. C. *Elements* **2007**, *2*, 343-349.

(39) Bunn, M.; Holdren, J. P.; Pickett, S. E.; Weeks, J.; Macfarlane, A. *Interim Storage of Spent Nuclear Fuel: A Safe, Flexible, and Cost-Effective Approach to Spent Fuel Management*; Cambridge: Managing the Atom Project, Harvard University and Project on Sociotechnics of Nuclear Energy, University of Tokyo, 2001

(40) Ewing, R. C. *Nat Mater* **2015**, *14*, 252–257.

(41) International Atomic Energy Agency. *Estimation of Global Inventories of Radioactive Waste and Other Radioactive Materials*; IAEA-TECDOC-1591, IAEA, Vienna, 2008.

(42) International Atomic Energy Agency. *Survey of Wet and Dry Spent Fuel Storage*; IAEA-TECDOC-1100; IAEA, Vienna, 1999.

(43) International Atomic Energy Agency. *Geological Disposal Facilities for Radioactive Waste*; Specific Safety Guide No. SSG-14; IAEA, Vienna, 2011.

(44) Macfarlane, A. *Annu. Rev. Energy Environ.* **2001**, *26*, 201–235.

(45) Sovacool, B. K. *Energy Policy* **2008**, *36*, 2950–2963.

(46) Bodansky, D. *Phys. Today* **2006**, *59*, 80–81.

(47) Ewing, R. C.; Runde, W.; Albrecht-Schmitt, T. E. *MRS Bull.* **2010**, *35*, 859–866.

(48) Kuno, M.; Hamada, M. Radioactive Waste Treatment and Disposal Technique. In *Earthquake Engineering for Nuclear Facilities*; Hamada M., Kuno, M., Eds.; Springer,

Singapore, 2017; pp 211-228.

(49) Plodinec, M. J. *Glas. Technol.* **2000**, *41*, 186–192.

(50) Weber, W. J.; Navrotsky, A.; Stefanovsky, S.; Vance, E. R.; Vernaz, E. *MRS Bull.* **2009**, *34*, 46–53.

(51) Harrison, M. T. *Procedia Mater. Sci.* **2014**, *7*, 10–15.

(52) Lee, W. E.; Ojovan, M. I.; Stennett, M. C.; Hyatt, N. C. *Adv. Appl. Ceram.* **2006**, *105*, 3–12.

(53) Apted, M.; Ahn, J. Multiple-barrier geological repository design and operation strategies for safe disposal of radioactive materials. In *Geological Repository Systems for Safe Disposal of Spent Nuclear Fuels and Radioactive Waste;* Ahn, J., Apted, M. J., Eds.; Woodhead Publishing Series in Energy, 2010; Vol. 9, pp 3–28.

(54) Hedin, A.; Olsson, O. *Elements* **2016**, *12*, 247–252.

(55) Grambow, B. *Elements* **2016**, *12*, 239–245.

(56) Metlay, D. S. *Elements* **2016**, *12*, 269-274.

(57) Johnson, B.; Newman, A.; King, J. *Ann. Oper. Res.* **2017**, *253*, 733–755.

(58) Ewing, R. C.; Weber, W. J. Nuclear Waste Management and Disposal. In *Fundamentals of Materials for Energy and Environmental Sustainability*; Ginley, D. S., Cahen, D., Eds.,; Cambridge University Press: New York, 2012; pp 178–193.

(59) Donald, I.; Metcalfe, B. L.; Taylor, R. N. J. *J. Mater. Sci.* **1997**, *32*, 5851–5887.

(60) Ewing, R. C. *Proc. Natl. Acad. Sci. U. S. A.* **1999**, *96*, 3432–3439.

(61) Lumpkin, G. R. *Elements* **2007**, *2*, 365-372.

(62) Gin, S.; Abdelouas, A.; Criscenti, L. J.; Ebert, W. L.; Ferrand, K.; Geisler, T.; Harrison, M. T.; Inagaki, Y.; Mitsui, S.; Mueller, K. T.; Marra, J. C.; Pantano, C. G.; Pierce, E. M.; Ryan, J. V; Schofield, J. M.; Steefel, C. I.; Vienna, J. D. *Mater. Today* **2013**, *16*, 243–248.

(63) Fournier, M.; Gin, S.; Frugier, P. *J. Nucl. Mater.* **2014**, *448*, 348–363.

(64) Poinssot, C.; Gin, S. *J. Nucl. Mater.* **2012**, *420*, 182–192.

(65) Ojovan, M. I.; Lee, W. E. Immobilization of Radioactive Wastes in Glass. In *An Introduction to Nuclear Waste Immobilisation*; Ojovan, M. I., Lee, W. E., Eds.; Elsevier: Oxford, 2005; pp 213–249.

(66) Ojovan, M. I.; Batyukhnova, O. G. Glasses for Nuclear Waste Immobilization. *Proceedings of the WM'07 Conference, Tucson, AZ, February 25 - March 1, 2007*

(67) Mesko, M. G.; Day, D. E. *J. Nucl. Mater.* **1999**, *273*, 27–36.

(68) Bohre, A.; Avasthi, K.; Pet'kov, V. I. *J. Ind. Eng. Chem.* **2017**, *50*, 1–14.

(69) Grambow, B. *Elements* **2007**, *2*, 357-364.

(70) Vienna, J. D.; Ryan, J. V; Gin, S.; Inagaki, Y. *Int. J. Appl. Glas. Sci.* **2013**, *4*, 283–294.

(71) Jantzen, C. M.; Brown, K. G.; Pickett, J. B. *Int. J. Appl. Glas. Sci.* **2010**, *1*, 38–62.

(72) Weber, W. J. *Procedia Mater. Sci.* **2014**, *7*, 237–246.

(73) Connelly, A. J.; Hand, R. J.; Bingham, P. A.; Hyatt, N. C. *J. Nucl. Mater.* **2011**, *408*, 188–

193.

(74) Utton, C. A.; Swanton, S. W.; Schofield, J.; Hand, R. J.; Clacher, A.; Hyatt, N. C. *Mineral. Mag.* **2013**, *76*, 2919-2930.

(75) Barkatt, A.; Barkatt, A.; Pehrsson, P. E.; Szoke, P.; Macedo, P. B. *Nucl. Chem. Waste Manag.* **1981**, *2*, 151–164.

(76) Gin, S. *Procedia Mater. Sci.* **2014**, *7*, 163–171.

(77) Ringwood, A. E.; Willis, P. *Nature* **1984**, *311*, 735–737.

(78) Weber, W. J.; Ewing, R. C.; Catlow, C. R. A.; de la Rubia, T. D.; Hobbs, L. W.; Kinoshita, C.; Matzke, H.; Motta, A. T.; Nastasi, M.; Salje, E. K. H.; Vance, E. R.; Zinkle, S. J. *J. Mater. Res.* **1998**, *13*, 1434–1484.

(79) Farnan, I.; Cho, H.; Weber, W. J. *Nature* **2007**, *445*, 190–193.

(80) Hatch, L. P. *Am. Sci.* **1953**, *41*, 410–421.

(81) Lumpkin, G. R.; Smith, K. L.; Gieré, R.; Williams, C. T. *Geol. Soc. London, Spec. Publ.* **2004**, *236*, 89-111.

(82) Stefanovsky, S. V; Yudintsev, S. V; Gieré, R.; Lumpkin, G. R. *Geol. Soc. London, Spec. Publ.* **2004**, *236*, 37-63.

(83) Ringwood, A. E.; Oversby, V. M.; Kesson, S. E.; Sinclair, W.; Ware, N.; Hibberson, W.; Major, A. *Nucl. Chem. Waste Manag.* **1981**, *2*, 287–305.

(84) Kessoft, S. E.; Sinclair, W. J.; Ringwood, A. E. *Nucl. Chem. Waste Manag.* **1983**, *4*, 259–265.

(85) Ringwood, a. E. *Mineral. Mag.* **1985**, *49*, 159–176.

(86) Ringwood, A. E.; Oversby, V. M.; Sinclair, W. The Effects of Radiation Damage on Synroc. In *Scientific Basis for Nuclear Waste Management*; Northrup, C. J. M., Ed.; Springer: Boston, 1980; Vol.2, pp 273–280.

(87) Vance, E. R. *MRS Bull.* **1994**, *19*, 28–32.

(88) Oelkers, E. H.; Montel, J.-M. *Elements* **2008**, *4*, 113–116.

(89) Meldrum, a.; Boatner, L.; Ewing, R. *Phys. Rev. B* **1997**, *56*, 13805–13814.

(90) Bailey, D. J.; Stennett, M. C.; Hyatt, N. C. *Procedia Chem.* **2016**, *21*, 371–377.

(91) Wang, S. .; Wang, L. .; Ewing, R. .; Was, G. .; Lumpkin, G. . *Nucl. Instruments Methods Phys. Res. Sect. B Beam Interact. with Mater. Atoms* **1999**, *148*, 704–709.

(92) Schlenz, H.; Heuser, J.; Neumann, A.; Schmitz, S.; Bosbach, D. *Z. Kristallog. Cryst. Mater.* **2013**, *228*, 113-123.

(93) Meldrum, A.; Boatner, L. A.; Weber, W. J.; Ewing, R. C. *Geochim. Cosmochim. Acta* **1998**, *62*, 2509–2520.

(94) Lian, J.; Zu, X. T.; Kutty, K. V. G.; Chen, J.; Wang, L. M.; Ewing, R. C.; Ewing, R. C. *Phys. Rev. B - Condens. Matter Mater. Phys.* **2002**, *66*, 541081–541085.

(95) Yudintsev, S. V.; Lizin, A. a.; Livshits, T. S.; Stefanovsky, S. V.; Tomilin, S. V.; Ewing, R. C. *J. Mater. Res.* **2015**, *7*, 1–13.

(96) Trachenko, K. *J. Phys. Condens. Matter* **2004**, *16*, R1491–R1515.

(97) Urusov, V. S.; Grechanovsky, A. E.; Eremin, N. N. *Glas. Phys. Chem.* **2012**, *38*, 55–62.

(98) Men, D.; Patel, M. K.; Usov, I. O.; Toiammou, M.; Monnet, I.; Pivin, J. C.; Porter, J. R.; Mecartney, M. L. *J. Nucl. Mater.* **2013**, *443*, 120–127.

(99) Ewing, R. C.; Weber, W. J.; Clinard, F. W. *Prog. Nucl. Energy* **1995**, *29*, 63–127.

(100) Ewing, R. C.; Weber, W. J. Actinide Waste Forms and Radiation Effects. In *The Chemistry of the Actinide and Transactinide Elements*; Morss, L. R., Edelstein, N. M., Fuger, J., Eds.; Springer: Dordrecht, 2011; Vol. 6, pp 3813–3887.

(101) Stanek, C. R.; Uberuaga, B. P.; Scott, B. L.; Feller, R. K.; Marks, N. A. *Curr. Opin. Solid State Mater. Sci.* **2012**, *16*, 126–133.

(102) Thomé, L.; Debelle, A.; Garrido, F.; Mylonas, S.; Décamps, B.; Bachelet, C.; Sattonnay, G.; Moll, S.; Pellegrino, S.; Miro, S.; Trocellier, P.; Serruys, Y.; Velisa, G.; Grygiel, C.; Monnet, I.; Toulemonde, M.; Simon, P.; Jagielski, J.; Jozwik-Biala, I.; Nowicki, L.; Behar, M.; Weber, W. J.; Zhang, Y.; Backman, M.; Nordlund, K.; Djurabekova, F. *Nucl. Instruments Methods Phys. Res. Sect. B Beam Interact. with Mater. Atoms* **2013**, *307*, 43–48.

(103) Ewing, R. C. *Comptes Rendus Geosci.* **2011**, *343*, 219–229.

(104) Picot, V.; Deschanels, X.; Peuget, S.; Glorieux, B.; Seydoux-Guillaume, A. M.; Wirth, R. *J. Nucl. Mater.* **2008**, *381*, 290–296.

(105) McVay, G. L.; Weber, W. J.; Pederson, L. R. *Nucl. Chem. Waste Manag.* **1981**, *2*, 103–108.

(106) Deschanels, X.; Seydoux-Guillaume, A. M.; Magnin, V.; Mesbah, A.; Tribet, M.; Moloney, M. P.; Serruys, Y.; Peuget, S. *J. Nucl. Mater.* **2014**, *448*, 184–194.

(107) Ewing, R. C.; Meldrum, A.; Wang, L.; Wang, S. *Rev. Mineral. Geochemistry* **2000**, *39*, 319–361.

(108) Interface Science Western http://www.isw.physics.uwo.ca/facilities_techniques/ion_implantation.html (Accessed October 28, 2017).

(109) Naab, F. U.; Toader, O. F.; Was, G. S. *Phys. Procedia* **2015**, *66*, 632–640.

(110) Long, K. R.; Van Gosen, B. S.; Foley, N. K.; Cordier, D. *The principal rare earth elements deposits of the United States - A summary of domestic deposits and a global perspective*; U.S. Geological Survey Scientific Investigations Report 2010-5220; USGS: Virginia, 2010

(111) Zepf, V. Rare Earth Elements: What and Where They Are. In *Rare Earth Elements*. *Springer Theses (Recognizing Outstanding Ph.D. Research)*; Springer: Heidelberg, 2013; pp 11–39.

(112) Voncken, J. H. L. The Ore Minerals and Major Ore Deposits of the Rare-Earths. In *The Rare Earth Elements*; SpringerBriefs in Earth Sciences, Springer: Cham, 2016; pp 15–52.

(113) Boatner, L. A. *Rev. Mineral. Geochemistry* **2002**, *48*, 87–121.

(114) Forster, H. J. *Am. Mineral.* **1998**, *83*, 1302–1315.

(115) van Emden, B.; Thornber, M. R.; Graham, J.; Lincoln, F. J. *Can. Mineral.* **1997**, *35*, 95-

104.

(116) Spear, F. S.; Pyle, J. M. *Rev. Mineral. Geochemistry* **2002**, *48*, 293-335.

(117) Lu, F.; Shen, Y.; Sun, X.; Dong, Z.; Ewing, R. C.; Lian, J. *Acta Mater.* **2013**, *61*, 2984–2992.

(118) Hikichi, Y.; Nomura, T.; Tanimura, Y.; Suzuki, S.; Miyamoto, M. *J. Am. Ceram. Soc.* **1990**, *73*, 3594–3596.

(119) Tomašić, N.; Gajović, A.; Bermanec, V.; Su, D. S.; Rajić Linarić, M.; Ntaflos, T.; Schlögl, R. *Phys. Chem. Miner.* **2006**, *33*, 145.

(120) Seydoux-Guillaume, A. M.; Wirth, R.; Nasdala, L.; Gottschalk, M.; Montel, J. M.; Heinrich, W. *Phys. Chem. Miner.* **2002**, *29*, 240–253.

(121) Vance, E. R.; Zhang, Y.; McLeod, T.; Davis, J. *J. Nucl. Mater.* **2011**, *409*, 221–224.

(122) Karioris, F. G.; Gowda, K. A.; Cartz, L. *Radiat. Eff. Lett.* **1981**, *58*, 1–3.

(123) Meldrum, A.; Boatner, L. A.; Wang, L. M.; Ewing, R. C. *Nucl. Instruments Methods Phys. Res. Sect. B-Beam Interact. with Mater. Atoms* **1997**, *127*, 160–165.

(124) Meldrum, A.; Wang, L. M.; Ewing, R. C. *Nucl. Instruments Methods Phys. Res. Sect. B Beam Interact. with Mater. Atoms* **1996**, *116*, 220–224.

(125) Dacheux, N.; Clavier, N.; Podor, R. *Am. Mineral.* **2013**, *98*, 833-847.

(126) Mesbah, A.; Clavier, N.; Elkaim, E.; Gausse, C.; Kacem, I. Ben; Szenknect, S.; Dacheux, N. *Cryst. Growth Des.* **2014**, *14*, 5090–5098.

(127) Qin, D.; Mesbah, A.; Gausse, C.; Szenknect, S.; Dacheux, N.; Clavier, N. *J. Nucl. Mater.* **2017**, *492*, 88–96.

(128) Nagy, G.; Draganits, E.; Demény, A.; Pantó, G.; Árkai, P. *Chem. Geol.* **2002**, *191*, 25–46.

(129) Du Fou de Kerdaniel, E.; Clavier, N.; Dacheux, N.; Terra, O.; Podor, R. *J. Nucl. Mater.* **2007**, *362*, 451–458.

(130) Ochiai, A.; Utsunomiya, S. *Minerals* **2017**, *7*, 84.

(131) Krenn, E.; Finger, F. *Lithos* **2007**, *95*, 130–147.

(132) Berger, A.; Gnos, E.; Janots, E.; Fernandez, A.; Giese, J. *Chem. Geol.* **2008**, *254*, 238–248.

(133) Jonasson, R. G.; Bancroft, G. M.; Boatner, L. A. *Geochim. Cosmochim. Acta* **1988**, *52*, 767–770.

(134) Clavier, N.; Dacheux, N.; Podor, R. *Inorg. Chem.* **2006**, *45*, 220–229.

(135) Ni, Y.; Hughes, J. M.; Mariano, A. N. *Am. Mineral.* **1995**, *80*, 21–26.

(136) Clavier, N.; Podor, R.; Dacheux, N. *J. Eur. Ceram. Soc.* **2011**, *31*, 941–976.

(137) Kolitsch, U.; Holtstam, D. *Eur. J. Mineral.* **2004**, *16*, 117–126.

(138) Milligan, W. O.; Mullica, D. F.; Beall, G. W.; Boatner, L. A. *Inorganica Chim. Acta* **1982**, *60*, 39–43.

(139) Beall, G. W.; Boatner, L. A.; Mullica, D. F.; Milligan, W. O. *J. Inorg. Nucl. Chem.* **1981**, *43*, 101–105.

(140) Mullica, D. F.; Milligan, W. O.; Grossie, D. A.; Beall, G. W.; Boatner, L. A. *Inorganica*

Chim. Acta **1984**, *95*, 231–236.

(141) Mooney, R. C. L. *J. Chem. Phys.* **1948**, *16*, 1003.

(142) Mooney, R. C. L. *Acta Crystallogr.* **1950**, *3*, 337–340.

(143) Ferhi, M.; Horchani-Naifer, K.; Férid, M. *J. Lumin.* **2008**, *128*, 1777–1782.

(144) Lu, S.; Zhang, J.; Zhang, J.; Zhao, H.; Luo, Y.; Ren, X. *Nanotechnology* **2010**, *21*, 365709.

(145) Di, W.; Li, J.; Shirahata, N.; Sakka, Y.; Willinger, M.-G.; Pinna, N. *Nanoscale* **2011**, *3*, 1263–1269.

(146) Wang, X.; Gao, M. *J. Mater. Chem.* **2006**, *16*, 1360–1365.

(147) Buissette, V.; Moreau, M.; Gacoin, T.; Boilot, J. P.; Chane-Ching, J. Y.; Le Mercier, T. *Chem. Mater.* **2004**, *16*, 3767–3773.

(148) Momma, K.; Izumi, F. *J. Appl. Crystallogr.* **2008**, *41*, 653–658.

(149) Rehr, J. J.; Kas, J. J.; Vila, F. D.; Newville, M. Theory and Analysis of XAFS. In *XAFS Techniques for Catalysts, Nanomaterials, and Surfaces*; Iwasawa, Y., Asakura, K., Tada, M., Eds.; Springer: Cham, 2017; pp 13–50.

(150) Balerna, A.; Mobilio, S. Introduction to Synchrotron Radiation. In *Synchrotron Radiation: Basics, Methods and Applications*; Mobilio, S., Boscherini, F., Meneghini, C., Eds.; Springer: Heidelberg, 2015; pp 3–28.

(151) Willmott, P. Spectroscopic Techniques. In *An Introduction to Synchrotron Radiation*; John Wiley & Sons, Ltd: Chichester, 2011; pp 223–302.

(152) Newville, M. *Rev. Mineral. Geochemistry* **2014**, *78*, 33-74.

(153) Penner-Hahn, J. E. *Coord. Chem. Rev.* **1999**, *190*, 1101–1123.

(154) Schnohr, C. S.; Ridgway, M. C. Introduction to X-ray Absorption Spectroscopy. In *X-Ray Absorption Spectroscopy of Semiconductors;* Schnohr, C. S., Ridgway, M. C., Eds.; Springer Series in Optical Sciences, Springer: Heidelberg, 2015; Vol. 190, pp 1–26.

(155) Willmott, P. The Interaction of X-rays with Matter. In *An Introduction to Synchrotron Radiation*; John Wiley & Sons, Ltd: Chichester, 2011; pp 15–37.

(156) Wende, H. *Reports Prog. Phys.* **2004**, *67*, 2105–2181.

(157) Yano, J.; Yachandra, V. K. *Photosynth. Res.* **2009**, *102*, 241.

(158) Penner-Hahn, J. E. X-ray Absorption Spectroscopy. *eLS* **2005,** 1-4.

(159) Henderson, G. S.; de Groot, F. M. F.; Moulton, B. J. A. *Rev. Mineral. Geochemistry* **2014**, *78*, 75-138.

(160) Yamazoe, S.; Hitomi, Y.; Shishido, T.; Tanaka, T. *J. Phys. Chem. C* **2008**, 112, 6869–6879.

(161) Yamamoto, T. *X-Ray Spectrom.* **2008**, *37*, 572–584.

(162) Aluri, E. R.; Hayes, J. R.; Walker, J. D. S.; Grosvenor, A. P. *J. Phys. Chem. C* **2014**, *118*, 7910–7922.

(163) Bunker, G. *Introduction to XAFS: A Practical Guide to X-ray Absorption Fine Structure Spectroscopy*; Cambridge University Press, 2010.

(164) Willmott, P. Synchrotron Physics. In *An Introduction to Synchrotron Radiation*; John Wiley & Sons, Ltd: Chichester, 2011; pp 39–86.

(165) Aquilanti, G.; Vaccari, L.; Plaisier, J. R.; Goldoni, A. Instrumentation at Synchrotron Radiation Beamlines. In *Synchrotron Radiation: Basics, Methods and Applications*; Mobilio, S., Boscherini, F., Meneghini, C., Eds.; Springer: Heidelberg, 2015; pp 65–104.

(166) Willmott, P. Beamlines. In *An Introduction to Synchrotron Radiation*; John Wiley & Sons, Ltd: Chichester, 2011; pp 87–131.

(167) Margaritondo, G. Characteristics and Properties of Synchrotron Radiation. In *Synchrotron Radiation: Basics, Methods and Applications*; Mobilio, S., Boscherini, F., Meneghini, C., Eds.; Springer: Heidelberg, 2015; pp 29–63.

(168) Fornasini, P. Introduction to X-ray Absorption Spectroscopy. In *Synchrotron Radiation: Basics, Methods and Applications*; Mobilio, S., Boscherini, F., Meneghini, C., Eds.; Springer: Heidelberg, 2015; pp 181–211.

(169) Waychunas, G. A. *Rev. Mineral. Geochemistry* **2002**, *49*, 267-315.

(170) van der Heide, P. Introduction. In *X-Ray Photoelectron Spectroscopy: An Introduction to Principles and Practices*; John Wiley & Sons, Inc.: Hoboken, NJ, USA, 2011; pp 1–12.

(171) Hüfner, S.; Schmidt, S.; Reinert, F. *Nucl. Instruments Methods Phys. Res. Sect. A Accel. Spectrometers, Detect. Assoc. Equip.* **2005**, *547*, 8–23.

(172) Sarma, D. D.; Santra, P. K.; Mukherjee, S.; Nag, A. *Chem. Mater.* **2013**, *25*, 1222–1232.

(173) Weimer, J. J. X-ray Photoelectron Spectroscopy. In *Characterization of Materials*; John

Wiley & Sons, Inc., 2002; pp 1-43.

(174) Gratz, R.; Heinrich, W. *Am. Mineral.* **1997**, *82*, 772-780.

(175) Heinrich, W.; Rehs, G.; Franz, G. *J. Metamorph. Geol.* **1997**, *15*, 3–16.

(176) Van Emden, B.; Thornber, M. R.; Graham, J.; Lincoln, F. J. Solid Solution Behaviour of Synthetic Monazite and Xenotime from Structure Refinement of Powder Data. *Advances in X-ray Analysis - Proceedings of the 45th Annual X-ray Conference, Denver, Colarado, USA*; 1997.

(177) Andrehs, G.; Heinrich, W. *Chem. Geol.* **1998**, *149*, 83–96.

(178) Degen, T.; Sadki, M.; Bron, E.; König, U.; Nénert, G. *Powder Diffr.* **2014**, *29*, S13–S18.

(179) Hu, Y. F.; Coulthard, I.; Chevrier, D.; Wright, G.; Igarashi, R.; Sitnikov, A.; Yates, B. W.; Hallin, E. L.; Sham, T. K.; Reininger, R. *AIP Conf. Proc.* **2010**, *1234*, 343–346.

(180) Thompson, A.; Attwood, D.; Gullikson, E. M.; Howells, M.; Kim, K.--J.; Kirz, J.; Kortright, J.; Lindau, I.; Yanwei, L.; Pianetta, P.; Robinson, A.; Scofield, J.; Underwood, J.; Williams, G.; Winick, H.; Thompson, A.; Attwood, D.; Gullikson, E. M.; Howells, M.; Kortright, J.; Robinson, L. F.; Underwood, J.; Kim, K.--J.; Kirz, J.; Lindau, I.; Pianetta, P.; Winick, H.; Williams, G.; Scofield, J. *X-ray data booklet*; Lawrence Berkeley National Laboratory: Berkeley 2009.

(181) Ravel, B.; Newville, M. *J. Synchrotron Radiat.* **2005**, *12*, 537–541.

(182) Hu, Y. F.; Zuin, L.; Reininger, R.; Sham, T. K. *AIP Conf. Proc.* **2007**, *879*, 535–538.

(183) Regier, T.; Krochak, J.; Sham, T. K.; Hu, Y. F.; Thompson, J.; Blyth, R. I. R. *Nucl.*

Instruments Methods Phys. Res. Sect. A Accel. Spectrometers, Detect. Assoc. Equip. **2007**, *582*, 93–95.

(184) Martin, R. L.; Shirley, D. A. *J. Chem. Phys.* **1976**, *64*, 3685.

(185) Fairley, N. *CasaXPS Version 2.3.16 ; Casa Software Ltd (www.casaxps.com)*. 2011.

(186) Andersen, O. K.; Jepsen, O. *Phys. Rev. Lett.* **1984**, *53*, 2571–2574.

(187) Blöchl, P. E.; Jepsen, O.; Andersen, O. K. *Phys. Rev. B* **1994**, *49*, 16223–16233.

(188) Hayes, J. R.; Grosvenor, A. P. *J. Phys. Condens. Matter* **2011**, *23*, 465502.

(189) Tromp, M.; Moulin, J.; Reid, G.; Evans, J. *AIP Conf. Proc.* **2007**, *882*, 699–701.

(190) Clavier, N.; Podor, R.; Dacheux, N. *J. Eur. Ceram. Soc.* **2011**, *31*, 941–976.

(191) Ingall, E. D.; Brandes, J. A.; Diaz, J. M.; de Jonge, M. D.; Paterson, D.; McNulty, I.; Elliott, W. C.; Northrup, P. *J. Synchrotron Radiat.* **2011**, *18*, 189–197.

(192) Gaultois, M. W.; Grosvenor, A. P. *J. Phys. Chem. C* **2010**, *114*, 19822–19829.

(193) Kruse, J.; Leinweber, P.; Eckhardt, K.-U.; Godlinski, F.; Hu, Y.; Zuin, L. *J. Synchrotron Radiat.* **2009**, *16*, 247–259.

(194) de Groot, F. *Coord. Chem. Rev.* **2005**, *249*, 31–63.

(195) Li, D.; Bancroft, G. M.; Kasrai, M.; Fleet, M. E.; Feng, X. H.; Tan, K. H. *Am. Mineral.* **1994**, *79*, 785–788.

(196) Thole, B. T.; van der Laan, G.; Fuggle, J. C.; Sawatzky, G. A.; Karnatak, R. C.; Esteva, J.-M. *Phys. Rev. B* **1985**, *32*, 5107–5118.

(197) Kaindl, G.; Kalkowski, G.; Brewer, W. D.; Perscheid, B.; Holtzberg, F. *J. Appl. Phys.* **1984**, *55*, 1910–1915.

(198) Allred, A. L. *J. Inorg. Nucl. Chem.* **1961**, *17*, 215–221.

(199) Ewing, R. C.; Wang, L. *Rev. Mineral. Geochemistry* **2002**, *48*, 673–699.

(200) Li, H.; Zhu, G.; Ren, H.; Li, Y.; Hewitt, I. J.; Qiu, S. *Eur. J. Inorg. Chem.* **2008**, *2008*, 2033–2037.

(201) Wang, L.; He, D.; Feng, S.; Yu, C.; Hu, L.; Qiu, J.; Chen, D. *Sci. Rep.* **2015**, *5*, 8490.

(202) Kitamura, N.; Amezawa, K.; Tomii, Y.; Yamamoto, N. *Solid State Ionics* **2003**, *162–163*, 161–165.

(203) Onoda, H.; Nariai, H.; Moriwaki, A.; Maki, H.; Motooka, I. *J. Mater. Chem.* **2002**, *12*, 1754–1760.

(204) Meiser, F.; Cortez, C.; Caruso, F. *Angew. Chemie Int. Ed.* **2004**, *43*, 5954–5957.

(205) Kijkowska, R. *J. Mater. Sci.* **2003**, *8*, 229–233.

(206) Mayence, A.; Navarro, J. R. G.; Ma, Y.; Terasaki, O.; Bergstro, L. *Inorg. Chem.* **2014**, *53*, 5067–5072.

(207) Heald, S. M.; Brewe, D. L.; Stern, E. A.; Kim, K. H.; Brown, F. C.; Jiang, D. T.; Crozier, E. D.; Gordon, R. A. *J. Synchrotron Radiat.* **1999**, *6*, 347–349.

(208) Kijkowska, R. *Thermochim. Acta* **2003**, *404*, 81–88.

(209) Shannon, R. D. *Acta Crystallogr. Sect. A* **1976**, *32*, 751–767.

(210) Lucas, S.; Champion, E.; Bregiroux, D.; Bernache-Assollant, D.; Audubert, F. *J. Solid State Chem.* **2004**, *177*, 1302–1311.

(211) Lucas, S.; Champion, E.; Bernache-Assollant, D.; Leroy, G. *J. Solid State Chem.* **2004**, *177*, 1312–1320.

(212) Asakura, H.; Shishido, T.; Fuchi, S.; Teramura, K.; Tanaka, T. *J. Phys. Chem. C* **2014**, *118*, 20881–20888.

(213) Ishii, M.; Crowe, I. F.; Halsall, M. P.; Hamilton, B.; Hu, Y.; Sham, T.-K.; Harako, S.; Zhao, X.-W.; Komuro, S. *J. Appl. Phys.* **2013**, *114*, 133505.

(214) Asakura, H.; Shishido, T.; Teramura, K.; Tanaka, T. *J. Phys. Chem. C* **2015**, *119*, 8070–8077.

(215) Asakura, H.; Shishido, T.; Teramura, K.; Tanaka, T. *Inorg. Chem.* **2014**, *53*, 6048–6053.

(216) Kennedy, B. J.; Avdeev, M. *Solid State Sci.* **2011**, *13*, 1701–1703.

(217) Lee, W. E.; Gilbert, M.; Murphy, S. T.; Grimes, R. W. *J. Am. Ceram. Soc.* **2013**, *96*, 2005–2030.

(218) Men, D.; Patel, M. K.; Usov, I. O.; Toiammou, M.; Monnet, I.; Pivin, J. C.; Porter, J. R.; Mecartney, M. L. *J. Nucl. Mater.* **2013**, *443*, 120–127.

(219) Burakov, B. E.; Yagovkina, M. A.; Garbuzov, V. M.; Kitsay, A. A.; Zirlin, V. A. *MRS Proc.* **2004**, *824*.

(220) Urusov, V. S.; Grechanovsky, A. E.; Eremin, N. N. *Glas. Phys. Chem.* **2012**, *38*, 55–62.

(221) De Groot, F. *Chem. Rev.* **2001**, *101*, 1779–1808.

(222) Reid, D. P.; Stennett, M. C.; Ravel, B.; Woicik, J. C.; Peng, N.; Maddrell, E. R.; Hyatt, N. C. *Nucl. Instruments Methods Phys. Res. Sect. B Beam Interact. with Mater. Atoms* **2010**, *268*, 1847–1852.

(223) Ziegler, J. F.; Ziegler, M. D.; Biersack, J. P. *Nucl. Instruments Methods Phys. Res. Sect. B Beam Interact. with Mater. Atoms* **2010**, *268*, 1818–1823.

(224) Nasdala, L.; Grötzschel, R.; Probst, S.; Bleisteiner, B. *Can. Mineral.* **2010**, *48*, 351-359.

(225) Zhang, F. X.; Lang, M.; Ewing, R. C.; Lian, J.; Wang, Z. W.; Hu, J.; Boatner, L. A. *J. Solid State Chem.* **2008**, *181*, 2633–2638.

(226) Rustad, J. R. *Am. Mineral.* **2012**, *97*, 791-799.

(227) X-ray Attenuation lengths http://henke.lbl.gov/optical_constants/atten2.html.

(228) Avci, R.; Davis, B. H.; Wolfenden, M. L.; Kellerman, L. R.; Lucas, K.; Martin, J.; Deliorman, M. *Corros. Sci.* **2015**, *93*, 9–18.

(229) Balzar, D. *J. Res. Natl. Inst. Stand. Technol.* **1998**, *98*, 321–353.

(230) Ungár, T. *Scr. Mater.* **2004**, *51*, 777–781.

(231) Ackland, G. *Science* **2010**, *327*, 1587-1588.

(232) Bai, X.-M.; Voter, A. F.; Hoagland, R. G.; Nastasi, M.; Uberuaga, B. P. *Science* **2010**, *327*, 1631-1634.

(233) Shen, T. D.; Feng, S.; Tang, M.; Valdez, J. A.; Wang, Y.; Sickafus, K. E. *Appl. Phys. Lett.* **2007**, *90*, 263115.

(234) Watkins, G. D. *Phys. Rev. Lett.* **1974**, *33*, 223–225.

(235) Tan, H. H.; Jagadish, C.; Williams, J. S.; Zou, J.; Cockayne, D. J. H.; Sikorski, A. *J. Appl. Phys.* **1995**, *77*, 87–94.

(236) Margalit, S.; Nemirovsky, Y.; Rotstein, I. **1993**, *6386*, 1–5.

(237) Prieur, D.; Vigier, J.-F.; Wiss, T.; Janssen, A.; Rothe, J.; Cambriani, A.; Somers, J. *J. Solid State Chem.* **2014**, *212*, 7–12.

(238) Kruse, J.; Leinweber, P.; Eckhardt, K. U.; Godlinski, F.; Hu, Y.; Zuin, L. *J. Synchrotron Radiat.* **2009**, *16*, 247–259.

(239) Tröger, L.; Arvanitis, D.; Baberschke, K.; Michaelis, H.; Grimm, U.; Zschech, E. *Phys. Rev. B* **1992**, *46*, 3283–3289.

(240) Achkar, A. J.; Regier, T. Z.; Wadati, H.; Kim, Y.-J.; Zhang, H.; Hawthorn, D. G. *Phys. Rev. B* **2011**, *83*, 81106.

(241) Strachan, D. M.; Turcotte, R. P.; Barnes, B. O. *Nucl. Technol.* **1982**, *56*, 306–312.

(242) ASTM C1285-02. *ASTM, Conshohocken, USA, 2002*. ASTM International 2002, pp 1–26.

(243) ASTM-C1662-10. *ASTM, Conshohocken, USA, 2010*. ASTM International 2010, pp 1–13.

(244) Hespe, E. D. *At. Energy Rev.* **1971**, *9*, 195–207.

(245) Dacheux, N.; Clavier, N.; Podor, R. *Am. Mineral.* **2013**, *98*, 833–847.

(246) Gausse, C.; Szenknect, S.; Qin, D. W.; Mesbah, A.; Clavier, N.; Neumeier, S.; Bosbach, D.; Dacheux, N. *Eur. J. Inorg. Chem.* **2016**, *2016*, 4615–4630.

(247) Teng, Y.; Wang, X.; Huang, Y.; Wu, L.; Zeng, P. *Ceram. Int.* **2015**, *41*, 10057–10062.

(248) Kumar, S. P.; Gopal, B. *J. Nucl. Mater.* **2015**, *458*, 224–232.

(249) Teng, Y.; Zeng, P.; Huang, Y.; Wu, L.; Wang, X. *J. Nucl. Mater.* **2015**, *465*, 482–487.

(250) Sales, B. C.; White, C. W.; Boatner, L. A. *Nucl. Chem. Waste Manag.* **1983**, *4*, 281–289.

(251) ASTM C1285-14. *ASTM, Conshohocken, USA, 2014*. ASTM International 2014, pp 1–27.

(252) Stone, J. A. *Nucl. Chem. Waste Manag.* **1981**, *2*, 113–118.

(253) Kumar, R.; Das, S.; Ray, R. K.; Biswas, A. K. *Hydrometallurgy* **1993**, *32*, 39–59.

(254) Bois, L.; Guittet, M. J.; Carrot, F.; Trocellier, P.; Gautier-Soyer, M. *J. Nucl. Mater.* **2001**, *297*, 129–137.

(255) Szenknect, S.; Finkeldei, S.; Brandt, F.; Ravaux, J.; Odorico, M.; Podor, R.; Lautru, J.; Dacheux, N.; Bosbach, D. *J. Nucl. Mater.* **2017**, *496*, 97–108.

(256) Finkeldei, S.; Brandt, F.; Rozov, K.; Bukaemskiy, A. A.; Neumeier, S.; Bosbach, D. *Appl. Geochemistry* **2014**, *49*, 31–41.

(257) Grochala, W.; Hoffmann, R.; Feng, J.; Ashcroft, N. W. *Angew. Chemie - Int. Ed.* **2007**, *46*, 3620–3642.

(258) Angeli, F.; McGlinn, P.; Frugier, P. *J. Nucl. Mater.* **2008**, *380*, 59–69.

(259) ASTM C1308-08. *ASTM, Conshohocken, USA, 2008*. ASTM International 2008, pp 1–14.

Appendix A

SUPPORTING TABLES AND FIGURES FOR CHAPTER 2

Table A-1 Unit cell parameters of $Sm_{1-x}Ho_xPO_4$

Compound	**Monazite unit cell parameters**	**Xenotime unit cell parameters**	**Relative percent composition**	**Profile fit parameters[a]**
$Sm_{0.8}Ho_{0.2}PO_4$	a = 6.6744 (5)Å		100% Monazite	R_p = 5.41
	b = 6.8754 (5)Å			R_{wp} = 6.83
	c = 6.3596 (5)Å			χ^2 = 1.19
	β = 103.920 (3)º			
$Sm_{0.5}Ho_{0.5}PO_4$	a = 6.6673 (8)Å	a = 6.9007 (8)Å	60% Monazite	R_p = 7.63
	b = 6.8715 (9)Å	c = 6.0398 (8)Å	40% Xenotime	R_{wp} = 9.92
	c = 6.3557 (9)Å			χ^2 = 1.35
	β = 103.900 (8)º			
$Sm_{0.3}Ho_{0.7}PO_4$	a = 6.661 (1)Å	a = 6.8939 (4)Å	30% Monazite	R_p = 5.98
	b = 6.867 (1)Å	c = 6.0343 (4)Å	70% Xenotime	R_{wp} = 7.73
	c = 6.351 (1)Å			χ^2 = 1.70
	β = 103.85 (1)º			
$Sm_{0.1}Ho_{0.9}PO_4$	a = 6.670 (4)Å		11% Monazite	R_p = 6.95
	b = 6.875 (4)Å		89% Xenotime	R_{wp} = 9.86
	c = 6.368 (5)Å		1% Ho_2O_3	χ^2 = 3.22
	β = 103.79 (5)º			

[a] R_p – Profile R-factor; R_{wp} – Weighted profile R-factor; χ^2 – Goodness of Fit.

Table A-2 Unit cell parameters of $La_{1-x}Y_xPO_4$

Compound	Monazite unit cell parameters	Xenotime unit cell parameters	Relative percent composition	Profile fit parameters[a]
$La_{0.9}Y_{0.1}PO_4$	a = 6.8238 (5)		100% Monazite	R_p = 7.62
	b = 7.0526 (5)			R_{wp} = 9.98
	c = 6.4997 (5)			χ^2 = 1.14
	β = 103.356 (3)			
$La_{0.6}Y_{0.4}PO_4$	a = 6.802 (1)	a = 6.8831 (7)	74% Monazite	R_p =7.72
	b = 7.026 (1)	c = 6.0203 (7)	26% Xenotime	R_{wp} = 9.90
	c = 6.481 (1)			χ^2 = 1.53
	β = 103.434 (5)			
$La_{0.5}Y_{0.5}PO_4$	a = 6.7964 (9)	a = 6.8840 (7)	63% Monazite	R_p = 7.80
	b = 7.020 (1)	c = 6.0213 (6)	37% Xenotime	R_{wp} = 9.70
	c = 6.476 (1)			χ^2 = 1.60
	β = 103.456 (6)			
$La_{0.4}Y_{0.6}PO_4$	a = 6.8017 (9)	a = 6.8837 (4)	47% Monazite	R_p = 7.61
	b = 7.026 (1)	c = 6.0220 (3)	53% Xenotime	R_{wp} = 9.46
	c = 6.480 (1)			χ^2 = 1.54
	β = 103.440 (7)			

[a] R_p – Profile R-factor; R_{wp} – Weighted profile R-factor; χ^2 – Goodness of Fit.

Table A-3 Linear combination fitting results for the $Sm_{1-x}Ho_xPO_4$ P K-edge XANES spectra

Solid solution	**Percent composition**		**Fit parameters**[a]
	$SmPO_4$	**$HoPO_4$**	
$Sm_{0.5}Ho_{0.5}PO_4$	60 (1) %	40 (1) %	R factor = 0.0005987 χ^2 = 0.03561
$Sm_{0.3}Ho_{0.7}PO_4$	29 (2) %	71 (2) %	R-factor = 0.0053668 χ^2 = 0.28548
$Sm_{0.1}Ho_{0.9}PO_4$	7 (1) %	93 (1) %	R-factor = 0.0024635 χ^2 = 0.13905

[a] R – R-factor; χ^2 – Goodness of Fit.

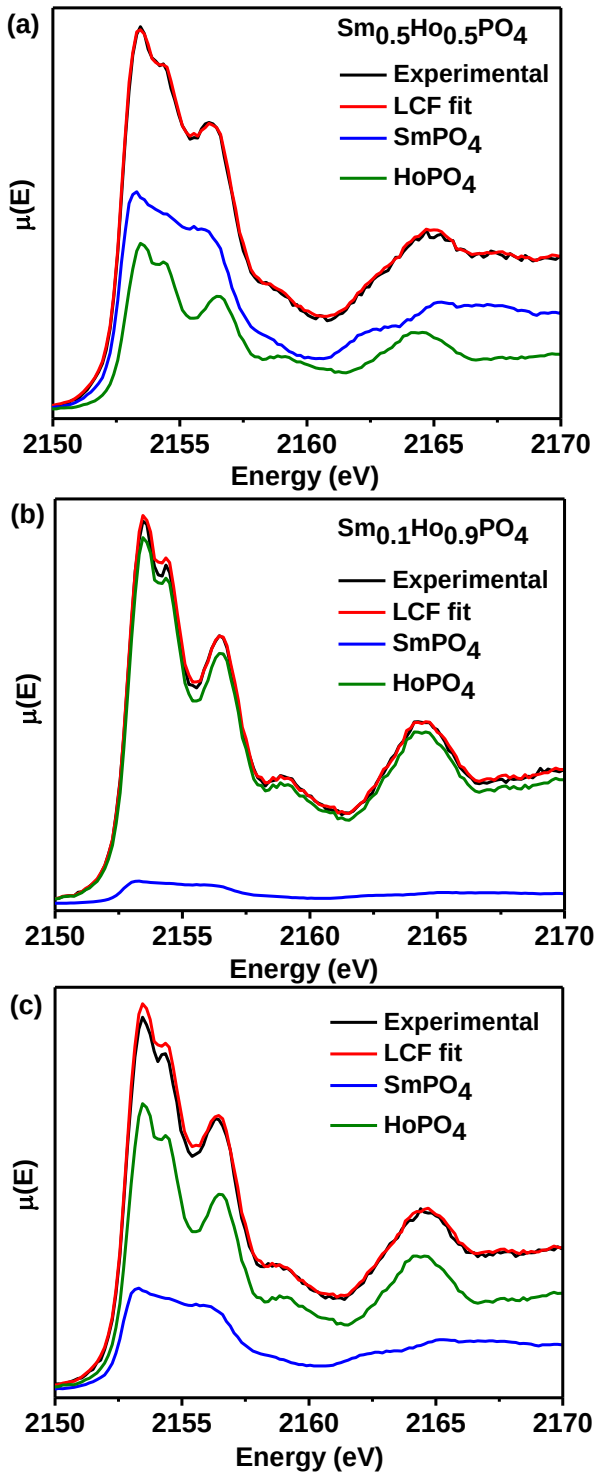

Figure A.1 Linear combination fitting of the P K-edge spectra from $Sm_{1-x}Ho_xPO_4$ series ((a) x = 0.5, (b) x = 0.7, (c) x = 0.9) is shown. The standards used in the LCF fitting were $LaPO_4$ and $YbPO_4$.

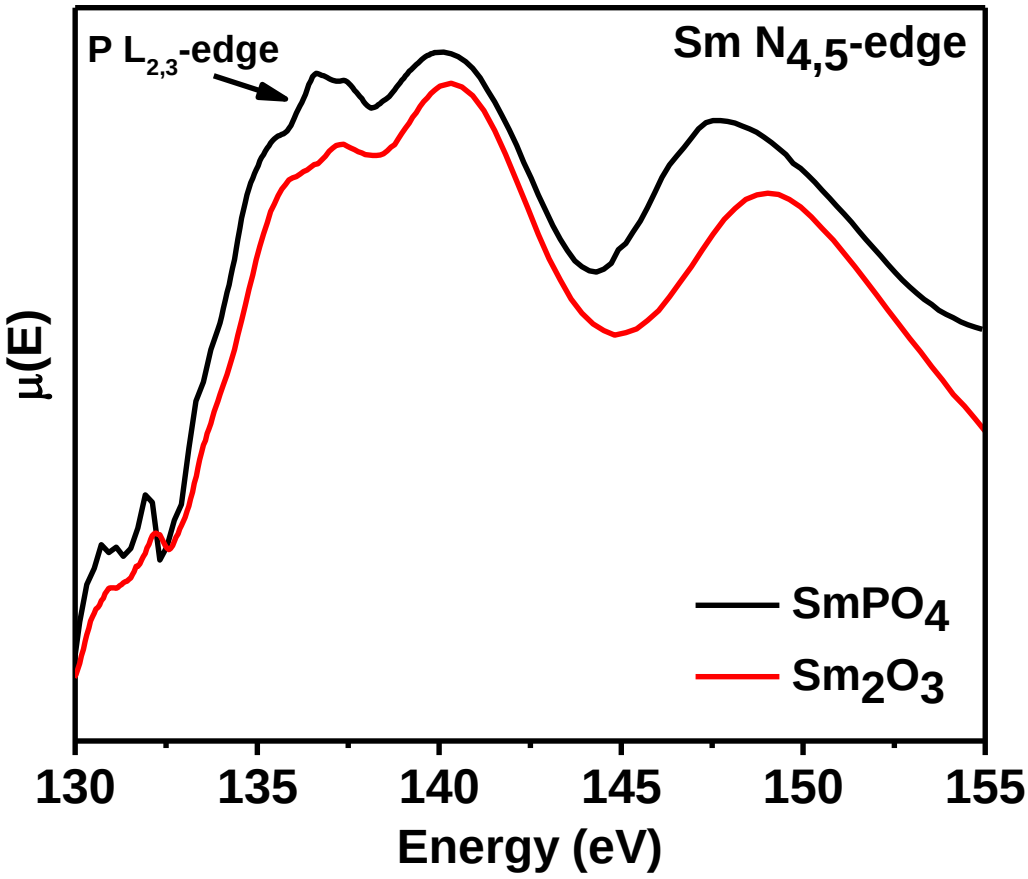

Figure A.2 The Sm $N_{4,5}$-edge XANES spectra from $SmPO_4$ (black) is presented along with the Sm $N_{4,5}$-edge XANES spectra from Sm_2O_3 (red). The P $L_{2,3}$-edge in the spectra of $SmPO_4$ is indicated by an arrow.

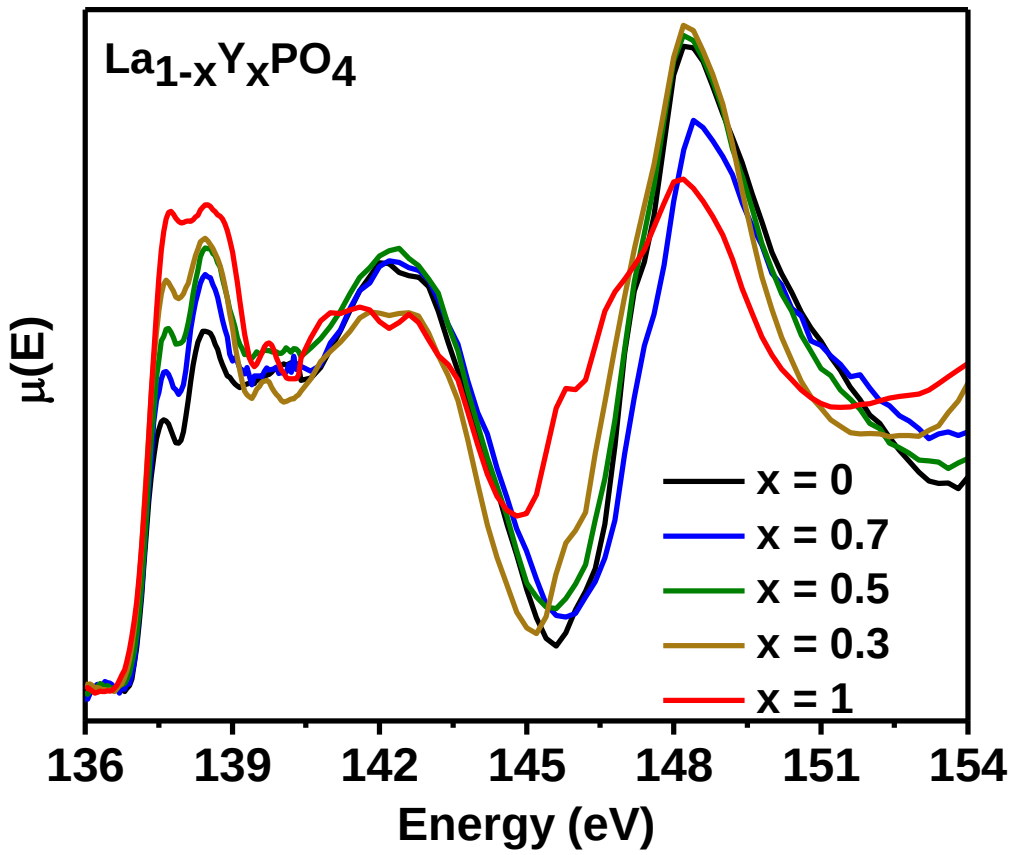

Figure A.3 Normalized P $L_{2,3}$-edge XANES spectra from $La_{1-x}Y_xPO_4$ (x = 0, 0.30, 0.50, 0.70, and 1) series are shown.

Appendix B

SUPPORTING TABLES AND FIGURES FOR CHAPTER 3

Table B-1 Lattice constants from as-synthesized rhabdophane-type $Gd_{1-x}Dy_xPO_4.H_2O$ ($0 < x < 1$) materials

x	a (Å)	b (Å)	c (Å)	β (degrees)
0.0	27.997 (3)	6.907 (1)	11.971 (2)	115.25 (1)
0.2	27.979 (5)	6.894 (2)	11.944 (3)	115.33 (2)
0.4	27.830 (9)	6.892 (3)	11.909 (5)	114.78 (4)
0.8	27.892 (5)	6.859 (1)	11.874 (2)	115.22 (2)

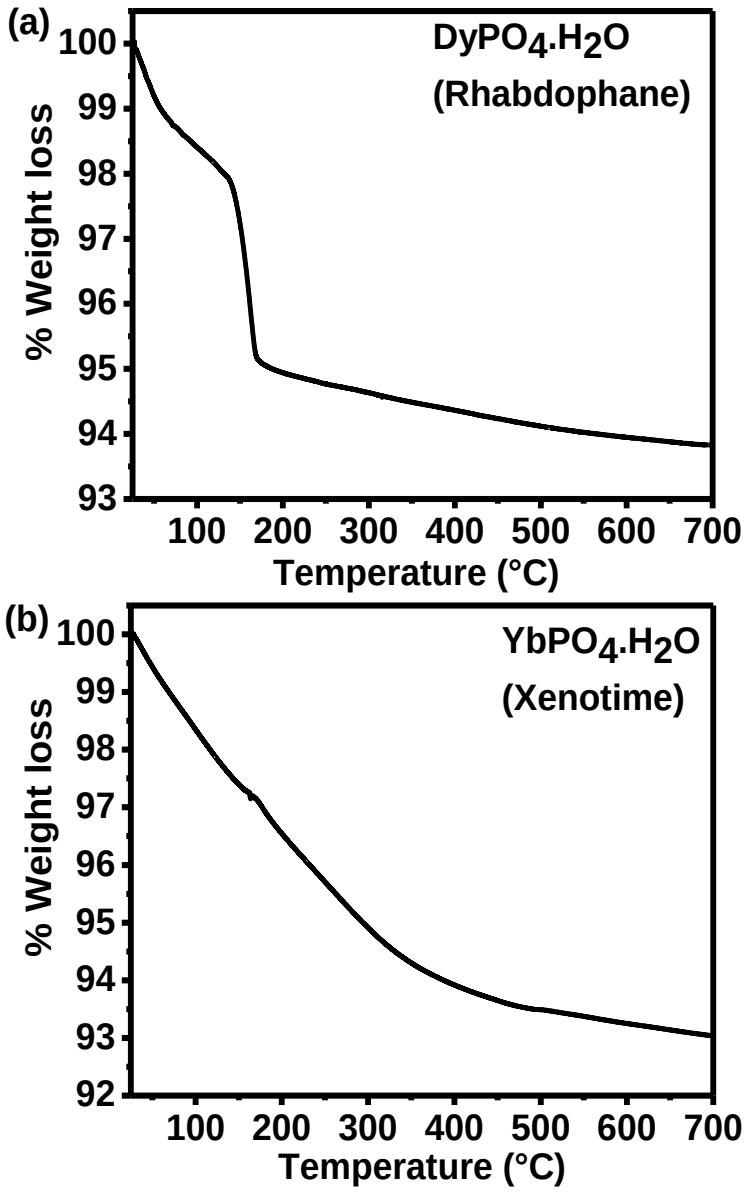

Figure B.1 TGA plots from the (a) rhabdophane-type $DyPO_4.H_2O$ and (b) xenotime-type $YbPO_4.H_2O$ materials are shown.

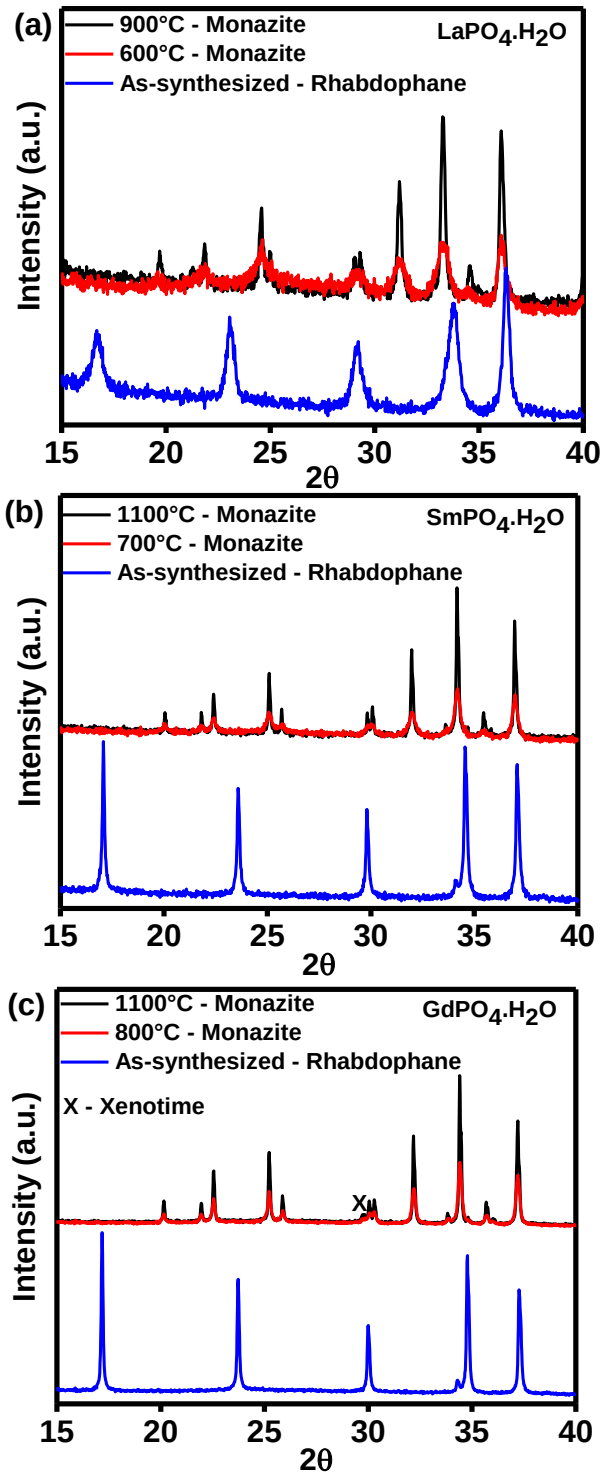

Figure B.2 Powder XRD patterns from (a) $LaPO_4.H_2O$, (b) $SmPO_4.H_2O$, and (c) $GdPO_4.H_2O$ annealed to different temperatures.

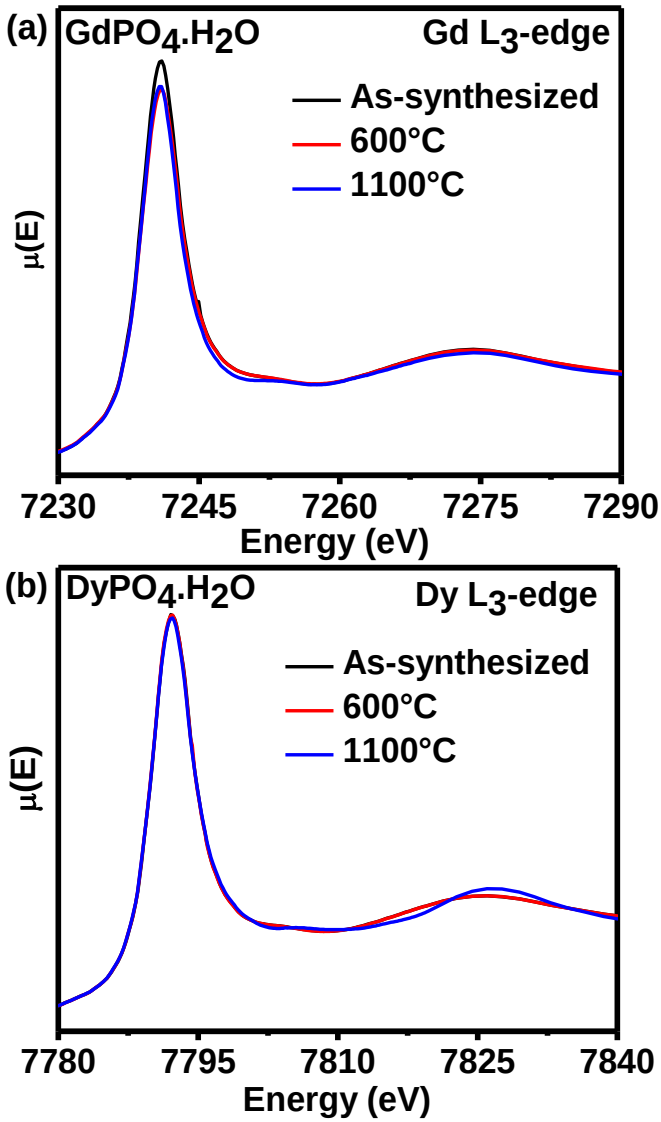

Figure B.3 RE (RE = Gd, Dy) L_3-edge XANES spectra from $REPO_4.H_2O$ (RE = Gd, Dy) annealed to 600°C and 1100°C are presented along with the spectrum from the as-synthesized material.

Appendix C

SUPPORTING TABLES AND FIGURES FOR CHAPTER 4

Table C-1 Rietveld refinement results from $La_{1-x}Yb_xPO_4$ (x = 0, 0.3, 0.7, 1.0)

compound	monazite unit cell constants	xenotime unit cell constants	relative percent composition	profile fit parameters[a]
$LaPO_4$	a = 6.8373 (2)Å		100% Monazite	R_{wp} = 11.65
	b = 7.0737 (2)Å			R_{exp} = 9.21
	c = 6.5073 (2)Å			χ^2 = 1.60
	β = 103.281 (1)°			
$La_{0.7}Yb_{0.3}PO_4$	a = 6.8250 (3)Å	a = 6.8171 (3)Å	70% Monazite	R_{wp} = 8.96
	b = 7.0591 (3)Å	c = 5.9719 (3)Å	30% Xenotime	R_{exp} = 8.75
	c = 6.5011 (3)Å			χ^2 = 1.05
	β = 103.324 (2)°			
$La_{0.3}Yb_{0.7}PO_4$	a = 6.8260 (7)Å	a = 6.8179 (3)Å	24.4% Monazite	R_{wp} = 11.21
	b = 7.0583 (7)Å	c = 5.9726 (3)Å	75.1% Xenotime	R_{exp} = 7.18
	c = 6.5002 (8)Å		0.5% Yb_2O_3	χ^2 = 2.43
	β = 103.327 (6)°			
$YbPO_4$		a = 6.8118 (2)Å	90% Xenotime	R_{wp} = 9.78
		c = 5.9675 (2)Å	10% Yb_2O_3	R_{exp} = 5.86
				χ^2 = 2.79

[a] R_{wp}, weighted profile R-factor; R_{exp}, expected profile R-factor; χ^2, goodness of fit.

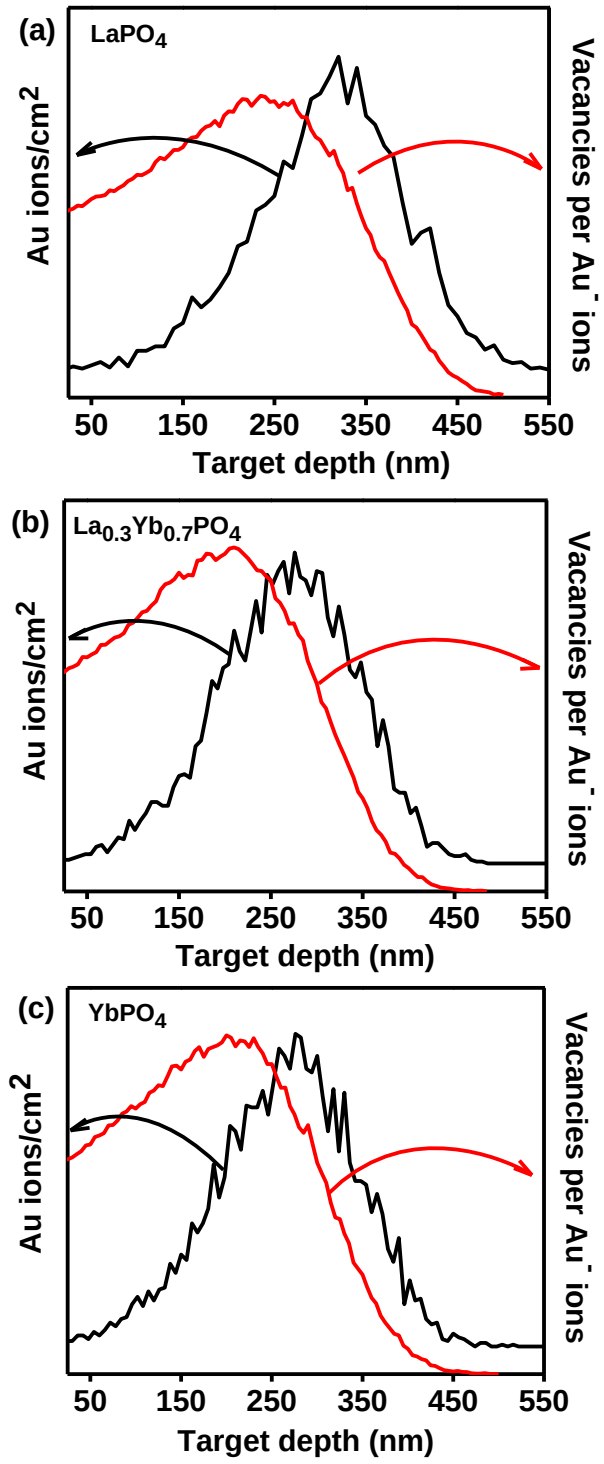

Figure C.1 Au^- ion-implantation depth and vacancy profile of (a) $LaPO_4$, (b) $La_{0.3}Yb_{0.7}PO_4$, and (c) $YbPO_4$ compounds.